SOME PROBLEMS IN GLOBAL TOMOGRAPHY:

Modeling the core-mantle boundary and statistical analysis of travel-time data

Thesis by

Olafur Gudmundsson

In Partial Fulfillment of the Requirements

of the Degree of Doctor of Philosophy

California Institute of Technology

Pasadena, California

1990

(submitted August 8th, 1989)

Acknowledgements

I would like to thank the faculty of the Seismological Laboratory for offering me the opportunity to acquire an excellent education through dynamic research and many outstanding courses, and for giving me financial support throughout my stay at the lab. In particular, I thank my advisor, Professor Robert W. Clayton, for his advice and support. He invested in me the trust that allowed me to pursue the projects of my fancy. His advice was always sound on a professional level and compassionate on a personal level.

My thanks go to the students of the Seismo Lab for their many contributions to my education. In particular, I thank Huw Davies, who has been a friend and a collaborator throughout my stay at the lab. My discussions with him were often informative and always stimulating. I also thank Doug Dreger for being a fun and understanding office mate and Brad Woods for laughing at my jokes.

The completion of this thesis would have been impossible without the understanding and support of my wife, Bryndis, who always stood at my side. My infant son, Einar Birnir, has been a source of joy in these last grueling months and a means of escape from my worries.

I thank my parents, Gudmundur Bjornsson and Gudlaug Olafsdottir for their infallible support. They gave me an interest in science and the single most important quality to complete the Ph.D., persistence.

This thesis is dedicated to my father, Professor Gudmundur Bjornsson (1925-1988), who taught me more about values, culture, science and life than could be put in one thesis. He anticipated the completion of this thesis as much as I have, but did not live to see it finished.

Abstract

Core-mantle boundary (CMB) structure is mapped with travel-time data in the International Seismological Centre (ISC) catalog. Different subsets of ISC data yield inconsistent results for CMB topography. Correlations of anomalies in well covered areas indicate a common source of signal above the CMB. Allowing for heterogeneity above the CMB yields models of 4 km peak-to-peak CMB topography and 2.5% velocity variations in the D'' layer. The models contain a large degree-two, zonal component. This agrees with the results of a stacking procedure employed in search of an axisymmetric pattern in the ISC data. It is concluded that the axisymmetric pattern in antipodal PKIKP data must at least in part be explained by CMB structure.

A method is developed to extract estimates of random data-errors and statistical measures of the earth's structure from global, travel-time data. Application of this method to teleseismic P-wave data yields an estimate of the signal-to-noise ratio in excess of unity. Heterogeneity is found to be strongly concentrated near the earth's surface. It extends over a wide range of scales in the upper mantle, but is restricted to relatively large scales in the lower mantle. The root-mean-square level of heterogeneity is found to be of the order of 0.1% in the lower mantle, but several times higher at its top and bottom.

Synthetic (2D) tests of lower-mantle and CMB travel-time inversions indicate only partial success for the lower mantle and a 5 to 10 km uncertainty in CMB mapping. This is consistent with the inconsistencies in the ISC data, when mapped onto the CMB, and suggests that the above results pertaining to CMB structure may be obscure.

Table of Contents

1 INTRODUCTION

The research presented in this thesis utilizes data from the International Seismological Centre (ISC) catalog to study the aspherical structure of the earth on a global scale. Much of this effort has been devoted to an attempt to evaluate the quality of the models that we and previous workers have constructed.

The ISC catalog contains over twenty years of worldwide travel-time readings of many seismic phases. This database of more than nine million picks is being actively used to map the aspherical structure of the earth's interior on a global scale as well as regional lateral velocity variations near the earth's surface. As time has progressed the global studies have sought to image ever deeper structure. Clayton and Comer (1983) (see also Hager and Clayton 1989) and Dziewonski (1984) used fifteen years of ISC mantle P-wave data to map the lower mantle. Creager and Jordan (1986b) and Morelli and Dziewonski (1987) used compressional core-phases to map the core-mantle boundary. Morelli et al. (1986) and Shearer et al. (1988) used PKIKP-waves to map anisotropy in the inner core. The regional studies have concentrated on the structure of subducting slabs (e.g., Creager and Jordan 1984, Zhou and Clayton 1989). These studies together with surface-wave tomography and long-period, body-wave synthesis provide important constraints on the style and scale of mantle convection, on the workings of the geodynamo, and on the evolution of the earth.

There are, however, some concerns about the ISC data and the techniques used to analyze them. The uncertainty of measurement is high compared with the signal attributable to aspherical structure. The data are contaminated by systematic errors that are due to misidentification of phases,

earthquake mislocation, earthquake time-function complexity, and potentially biased picking. The geometrical coverage of the data is uneven, because of the clustering of seismic sources in tectonically active regions and the lack of recording stations in the oceans. The images suffer from complex artifacts, which depend on the particular technique employed, because of the uneven coverage. The strong small-scale velocity variations in the earth's outermost layers are simplistically accounted for by station corrections. The severity of these problems is currently poorly understood.

This research was initiated by a class project in Professor Anderson's class, Physics of the earth's interior, which involved mapping the core-mantle boundary (CMB) using ISC PcP travel-time residuals. From there the subject developed to include other subsets of the ISC data to map the CMB, and to study the hypothesis of anisotropy in the earth's inner core. Two papers have been published in recent years on each of these subjects (Creager and Jordan (1986b), Morelli and Dziewonski (1987) on CMB structure, and Morelli et al. (1986), Shearer et al. (1988) on inner-core anisotropy). Inconsistencies between the results of these papers and the results presented in this thesis led us to focus on the accuracy of the results and potential causes of the inconsistencies. We subsequently developed a technique to measure statistical characteristics of the perturbations to a hydrostatically ellipsoidal earth in the mantle, and, finally, undertook a synthetic study of the resolution power of global, travel-time tomography.

This thesis is divided into four somewhat independent chapters in addition to this introduction and a summary at the end. Chapter 2, entitled "Mapping the core-mantle boundary," presents the results that we get for CMB topography or structure from compressional travel-time residuals in the

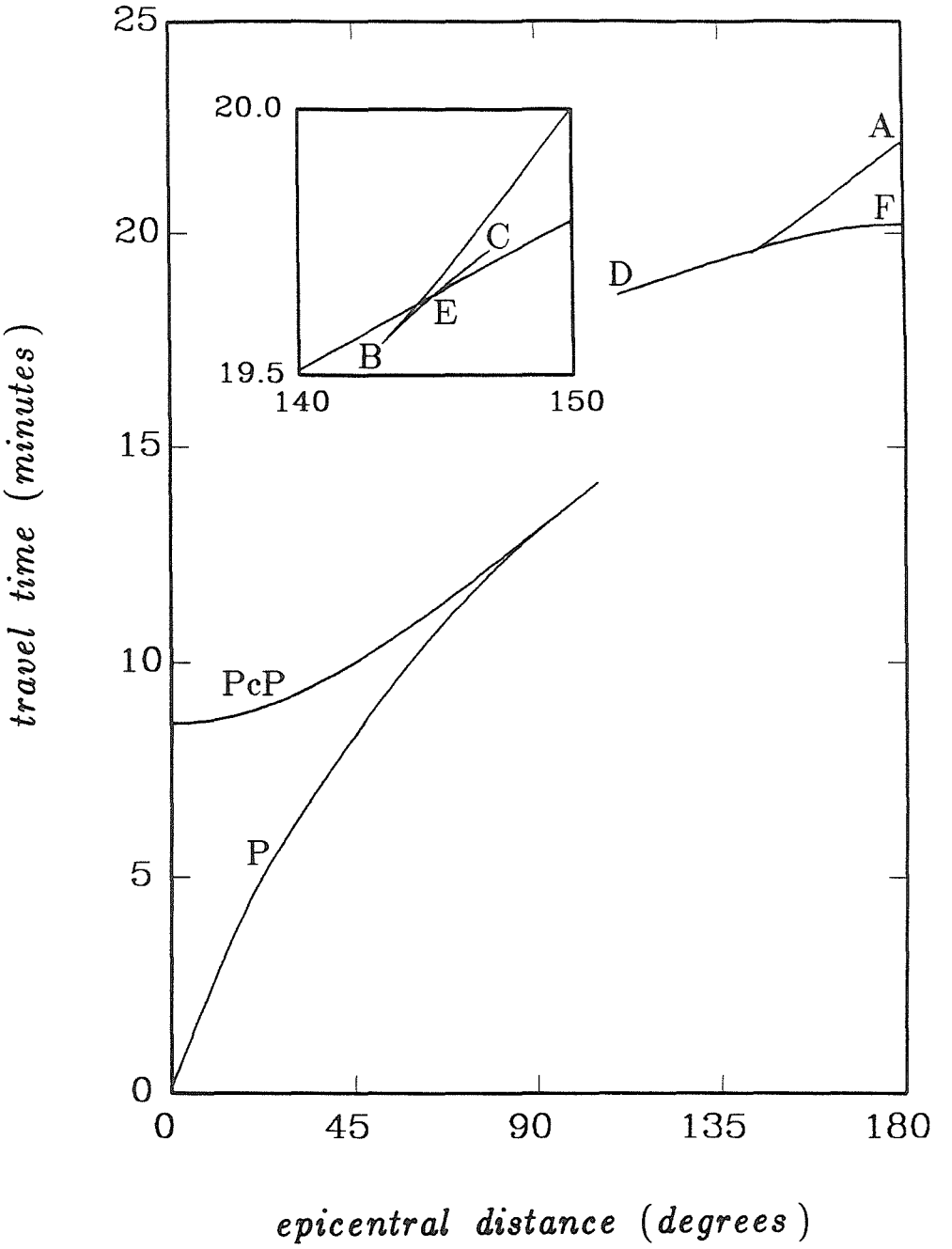

Figure 1.1 Travel time as a function of epicentral distance for surface focus and the reference model of Jeffreys and Bullen. Only those branches that are used in this study are included. The small figure in the upper left-hand corner is an enlargement of the section of the PKP curve, which contains the BC branch.

ISC catalog. Chapter 3, entitled "Core-mantle boundary structure or core anisotropy?," presents the results of a search for an anisotropic pattern in the travel-time residuals of the same compressional data. Chapter 4, called "Stochastic analysis of global, travel-time data," outlines a method of extracting statistical parameters of the earth's slowness field from travel-time data and the results for the earth's mantle obtained by applying it to P-wave data in the ISC catalog. Work for this chapter was in part done in cooperation with Huw Davies. Finally, Chapter 5, entitled "A synthetic study of global, travel-time tomography," discusses the results of synthetic tests of recoverability of artificial, earth models by deterministic, travel-time inversion.

Before embarking on the main body of this thesis, it may be useful to some of its readers to define the terminology used to discuss the different subsets of the ISC data. All the data used here are compressional-wave data. We use mantle P-waves in Chapters 4 and 5. In Chapters 2, 3, and 5 we use the compressional core-phases. Their travel-time curves and a ray diagram depicting their ray geometry are shown in Figures 1.1 and 1.2. Reflections off the CMB are named PcP-waves according to convention. The naming conventions of the other (true) core phases are both mixed and more complex. These include all compressional waves that refract at the CMB and enter the earth's core. They are collectively called PKP-waves or P'-waves. We will stick with the former. The subdivisions of these waves is often according to the alphabetical names of the extremes and caustics on their travel-time curves (see Figure 1.1); i.e., PKPab represents waves that fall between the points A and B on the travel-time curve. One notable exception is that of PKPdf-waves. These waves refract at the inner core boundary (ICB) into the inner core, and are accordingly sometimes named PKIKP-waves. We will use

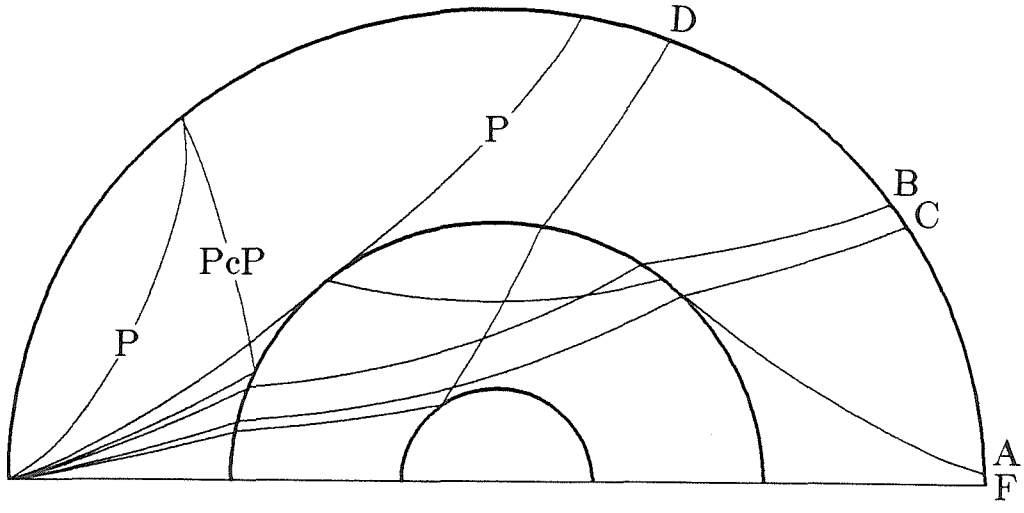

Figure 1.2 A ray diagram for the data used in this study. Labeling is analogous to that in Figure 1.1. P and PcP rays are ad hoc examples. PKP rays correspond to the labeled extremes on the PKP travel-time curves (see Figure 1.1).

the alphabetical names in the text of this thesis. In figures and tables we will sometimes abbreviate the names (AB = PKPab, BC = PKPbc etc.), and sometimes use the PKIKP name. The point "E" marked on the travel-time curves in Figure 1.1 at the intersection of the PKPbc and PKPdf branches is sometimes used to subdivide PKIKP-waves into two sets, PKPde and PKPef. We will use this convention in the text. Figures in Chapter 3 will use PKIKP1 and PKIKP2, respectively, for this subdivision. In summary, P-waves are compressional waves in the earth's mantle. PcP-waves are compressional reflections off the CMB. PKPab-waves are compressional waves that bottom or turn in the central third of the outer core, PKPbc-waves turn in the bottom third of the outer core, PKPde-waves (PKIKP1) turn on the bottom side of the ICB and PKPef-waves (PKIKP2) traverse the body of the inner core. PKPdf-waves (PKIKP) is a collective term for PKPde and PKPef.

Finally, we use the term D''' in Chapter 2 to refer to the region on the core side of the CMB. This is not according to any convention and is simply done for the lack of a better name. The term D'' is conventionally used for the mantle side of the CMB (originally a thin layer of low, radial, velocity gradient in the model of Jeffreys and Bullen (JB), (Bullen 1979). This unconventional term thus renders the two boundary layers adjacent to the CMB of similar names, but it is inconsistent with the naming scheme of Bullen, of which D'' is part.

2 MAPPING THE CORE-MANTLE BOUNDARY

2.1 Introduction

The core-mantle boundary (CMB) is the sharpest discontinuity in the earth. It represents a 4.3 g/cm^3 density contrast, a 5.5 km/sec compressional velocity contrast, a major chemical discontinuity, with silicates on one side and an iron alloy on the other, and a sharp transition from a solid above to a liquid below. It is fair to say that the CMB in many ways resembles the free surface of the earth, although physical conditions in terms of pressure and temperature are vastly different. It is the interface between two radically different regimes; the core, where the source of the geodynamo lies, and the mantle, which through convection controls many of the features of surface tectonics. In the structure of the CMB lie the answers to many questions pertaining to the coupling of these two regimes, such as heat flux, chemical reactions, and dynamical effects. The nature and structure of the CMB has a strong bearing on the thermal and chemical evolution of the earth. It is clearly of much geophysical interest to map its structure.

Seismology has provided the best tool for studying the structure of the CMB. The absolute timing of seismic waves reflected off the CMB has long since provided good estimates of the depth to the CMB. Gutenberg's (1914) estimate of 2900 km and Jeffreys' (1939) estimate of 2898 $\pm$ 2.5 km are remarkably close to the 2889 $\pm$ 4 km estimate of Dziewonski and Anderson (1981). Other estimates have ranged from a depth of about 2885 km to 2900 km. The recent estimates are based on free oscillation data as well as body-wave travel-times. As early as 1939, the presence of a thin layer (

$\approx 200\ km$ thick) of a low, radial velocity gradient immediately above the CMB was identified by Gutenberg and Richter (1939) and Jeffreys (1939). Bullen (1949) later termed this layer D''.

The decrease in the radial velocity gradients in D'' in global velocity-models has been explained in terms of a simple, thermal boundary-layer between the mantle and core (e.g., Stacey and Loper 1983). Doornbos et al. (1986) pointed out that reversed velocity gradients may be consistent with a simple, thermal boundary-layer. On the other hand, Brown (1986) pointed out that allowing for uncertainties of a number of physical parameters, radial heterogeneity cannot be ruled out. Williams et al. (1987) presented evidence for higher core temperatures than previously assumed, which implies higher heat flow through the CMB, a more pronounced thermal boundary-layer, and thus lends support to seismic models involving reversed velocity gradients immediately above the CMB. Jeanloz et al. (1988) discussed evidence for higher mantle temperatures, which would alleviate this effect of increased core temperatures. Zarkov et al. (1985) discussed a model of a complex, thermal boundary-layer in D'', which is thermally heterogeneous (laterally) and temporally unstable. Other suggested mechanisms for heterogeneity around the CMB include dynamically sustained CMB topography (Hager et al. 1985), isostatic topography on the CMB that is due to chemical heterogeneity in D'' (Creager and Jordan 1986b) and mantle dregs aggregated at the CMB and modulated by the flow of the overlying mantle (Davies and Gurnis 1986). Jeanloz et al. (1988) predicted vigorous chemical reactions between mantle and core across the CMB, and Stevenson (1988) suggested interaction via infiltration, dissolution, and underplating.

The basic structure of a solid-liquid interface and an overlying D'' layer, has served as a guideline for studies of the CMB for decades. Recently (the last 15 years), however, much data have been gathered that indicate relatively subtle, but significant, changes to the basic, radially-symmetric structure of D'', as well as strong lateral heterogeneity at or around the CMB. Studies of the apparent velocity of diffracted waves, which is sensitive to the velocity at the base of the mantle, in the late sixties yielded low estimates of D'' velocity, and thus introduced a positive, radial velocity-gradient above the CMB (Sacks 1967, Bolt 1970 and 1972, Cleary 1969, and Bolt et al. 1970). These studies did, however, suffer from disregard for the dispersive nature of diffracted waves. More recent studies have applied waveform modeling to diffracted waves, and thus utilize amplitude information as well as timing, and account for dispersive effects (Alexander and Phinney 1966, Mondt 1977, Doornbos and Mondt 1979a and 1979b, Mula and Muller 1980, Mula 1981, and Doornbos 1983). These studies are localized in nature and give widely varying results or a large degree of scatter when scattered samples are grouped together. Some prefer a positive, radial velocity gradient in D'' (e.g., Doornbos and Mondt 1979b). Ruff and Helmberger (1982) used short period P-wave amplitude-data from the arctic region to construct a series of acceptable models, all with a small low-velocity zone at the top of D''. Young and Lay (1988) used the same kind of data as Ruff and Helmberger (including the same) from three different regions to argue against positive radial velocity gradients in D'' and for strong lateral heterogeneity (approx 1%). Wright (1973b), Wright and Lyons (1975 and 1981), and Wright et al. (1985) used short-period, array data of deeply refracted P-waves to infer the complication of a triplication due to a sharp, but small (2%), velocity

increase about 180 km above the CMB. Lay and Helmberger (1983b and 1983c), Zhang and Lay (1984), and Young and Lay (1987a) show long-period, SH-wave data from four distinct regions, which show a waveform complication consistent with a reflection (Scd) off a small (2.75%) velocity increase some 280 km above the CMB. Schlittenhardt et al. (1985) showed that a shear velocity discontinuity like that proposed by Lay and others is inconsistent with long-period observations of SH waveforms from a number of regions, few of which overlap with those of Lay and others. Garnero et al. (1988) presented SH-wave data from a fifth (central Pacific) region, which show no evidence for the reflected Scd phase of Lay and Helmberger (1983b and 1983c). They used anomalous, differential travel-times between S-waves, SKS-waves, and SKKS-waves to argue that the anomalous D'' models of Lay and others for regions surrounding the Pacific fade out in the central Pacific.

The different local models for D'' may be indications of lateral heterogeneity in this region and are indeed often interpreted as such. Many of the above studies have, however, been subject to justified, albeit inconclusive, criticism. Cormier (1985) points out the importance of considering the potential effects of lower-mantle heterogeneity, in particular the possibility of contamination from SKS scattering in the data shown by Lay, Helmberger, and Young, giving rise to an Scd type signal. Haddon and Buchbinder (1986 and 1987) point to inconsistencies in the Scd data and nonuniqueness in their interpretation. They point out that a minor apparent phase like the Scd phase may be due to scattering off localized, smooth, velocity anomalies in the lower mantle. Both the above rebuttals have been vigorously refuted by Lay (1986) and Young and Lay (1987a). The high degree of scatter in observations of the amplitude decay of diffracted signals has given rise to

suspicions about contamination from shallow structure. Menke (1986a) showed that scatterers in D'' may significantly affect the decay rate of diffracted waves, without invoking a change in the overall velocity structure of D''.

Precursors to PKP-waves have proven to give valuable information about the CMB region. These small, variable wiggles precede PKPdf-waves in the distance range from $\Delta \approx 125^o$ to 143^o. They were originally explained as a distinctive phase (PKPgh), that was caused by a velocity discontinuity near the base of the outer core (Bolt 1962 and 1964), but are now attributed to scattering at the CMB (Cleary and Haddon 1972, Doornbos 1974, Doornbos and Vlaar 1973, Haddon and Cleary 1974, King et al. 1974, Wright 1975, and Husebye et al. 1976). The characteristic scale of the scatterers is tens of km; they are velocity perturbations of the order of 1% in rms (root-mean-square) amplitude distributed through a thin ($<$ 200 km) layer above the CMB, or undulations on the CMB of height of the order of hundreds of meters, depending on the study. Sacks et al. (1979) used variations in the amplitude ratios of PKPab- and PKPdf-waves to argue that the scatterering characteristics of the D'' layer are laterally variable; specifically, they identified a region of high scattering with a correlation length of 150 km and 1% velocity variations and another region of much lower scattering. Precursors to PKKP-waves are consistent with the estimates of CMB topography from PKP precursors (Doornbos 1978 and 1980, and Chang and Cleary 1978). Menke (1986b) showed by physical modeling that small-scale corrugations on the CMB (2 - 50 km in scale) would drastically affect the apparent reflection coefficient of PcP-waves, were they any bigger than few hundred meters in size. This would in turn contradict observations (Frasier and

Chowdhury 1974).

Inversions of body-wave, travel-time residuals of mantle P-waves have consistently resulted in an increase in the level of heterogeneity at the base of the mantle, indicating that the D'' layer is highly heterogeneous (Sengupta and Toksoz 1977, Sengupta et al. 1981, Clayton and Comer 1983 (see also Hager and Clayton 1989), and Dziewonski 1984). These studies generally resolve only very large-scale structure and are thus not directly comparable with the scattering results. We provide later in this thesis (Chapters 4 and 5) evidence that implies that these studies may suffer significantly from noisy data. One particularly relevant observation presented in Chapter 4 is that of a marked increase in the incoherent scatter of global travel-time data at epicentral distances sensitive to the D'' region. This noise in the data may contribute to the high level of heterogeneity in D'' in global mantle-models (see chapter 5). Body-wave, travel-time residuals have also been used to map the very large-scale topography on the CMB (Creager and Jordan 1986b, Morelli and Dziewonski 1987, hereafter referred to as CJ and MD, respectively, and Gudmundsson et al. 1986). These studies have resulted in peak-to-peak amplitudes of CMB topography of the order of 10 km. Large discrepancies exist between the locations of the major anomalies. It is with this approach that we concern ourselves in this chapter. We present the results of inversions of all of the subsets of PKP and PcP data from the ISC catalog for CMB topography as well as the results from combined data sets and for a layered structure around the CMB. It is of particular interest to us to discern the degree to which inconsistencies arise between the different data sets and what their cause may be.

In summary, the array of models that have been proposed for the D'' and CMB region is perplexing. Some of the differences are explainable by discounted scattering effects in the lower mantle and near the earth's surface. Other differences are best explained as manifestations of lateral heterogeneity on relatively large scales. There is ample evidence that the lower mantle is heterogeneous, particularly at depth (D'') and at small scales.

2.2 Data processing

We use the travel-time residuals of the ISC catalog (1964 - 1982), which are referenced to the spherically-symmetric earth-model of Jeffreys and Bullen (JB). The ellipticity correction of the ISC is replaced by the more accurate corrections provided by Dziewonski and Gilbert (1975). We then omit all observations exceeding five seconds in absolute value, as well as all observations from events or stations with fewer than 50 primary picks (first arrival picks). Static station and event corrections are computed iteratively from the ellipticity-corrected residuals of P-waves and then applied to the core data. Then baseline shifts and linear trends in the average residual as a function of epicentral distance are removed.

Each of the subsets of data that we use has some problems associated with it. The travel-time curve of PcP data crosses with that of S-waves at around 20^o epicentral distance, and that of PP- and PPP-waves at about 45^o. It then merges with the travel-time curve of P-waves at the core shadow at $\approx 100^o$ (see Figure 1.1). The cross-overs with S-waves and PP-waves are windowed out of the data set. The time separation of PcP- and P-waves remains larger than 5 seconds out to about 85^o epicentral distance. It should

be possible to pick PcP out to that distance. We did, however, notice spurious streaking of residuals along the time axis between 70^o and 75^o epicentral distance and opted to cut off the set at 70^o. Note that the reflection coefficient of PcP-waves at the CMB starts falling off rapidly at about $\Delta = 70^o$. If a triplication exists in the travel-time curve for P-waves (Wright 1973b, Wright and Lyons 1975 and 1981, and Wright et al. 1985), it could introduce difficulty in picking PcP at large ranges. The total number of individual picks in this data set is 9784.

PKPdf-waves are first arrivals throughout the range from about 115^o to 180^o, except for the short span of the PKPbc branch from about 143^o to 145^o. This is again with the exceptions of diffracted waves, which extend into the core shadow from mantle P-waves, and also extend the B-caustic of PKP-waves toward 140^o. As discussed in the introduction, these waves are preceded by precursors at distances less than $\Delta = 143^o$. The rms amplitude of the precursors does, however, decay rapidly away from the B-caustic, by about an order of magnitude at $\Delta = 130^o$ (see Figures 2 and 3 in Haddon and Cleary 1974). We use data from the distance range form 115^o to 130^o to avoid the precursors, and term this subset PKPde. We also use data in the range from $\Delta = 155^o$ to 180^o, and term that subset PKPef. Theoretically, the BC branch of PKP-waves extends out only to 147^o for the JB model. The extent of this branch is, however, quite model-dependent (it goes out to 154^o for PREM), and diffractions around the inner-core boundary (ICB) may extend it further yet. The travel-time separation of the PKPbc and PKPef branches reaches 5 seconds at about 152^o. To avoid contamination from the high-amplitude BC branch, we use data at ranges larger than 155^o only. The numbers of data in the PKPde and PKPef data set are 104989 and 35514,

respectively.

PKPbc-waves are the highest amplitude, compressional core-waves, as they are focused in a very small epicentral distance range. They are the front branch of a caustic at B (see Figure 1.1) with PKPab-waves as the back branch. For the JB model PKPbc-waves are a first arrival between $\Delta = 143^o$ and $\approx 145^o$. This branch is crossed by the DF branch, which becomes the first arrival at 145^o. The BC branch is almost an order of magnitude higher in amplitude than the DF branch (see Muller 1973). Anderssen and Cleary (1980) reported that between $\Delta = 144^o$ and 148^o PKPbc arrivals are several times higher in amplitude than PKPdf arrivals and that 85% of the picks in this interval in the ISC catalog are PKPbc. We thus take the same approach as MD and interpret all arrivals in this interval as being PKPbc. It is likely that where PKPbc is a first arrival, the relative picking frequency of PKPbc is higher than the overall picking frequency. We truncate the PKPbc subset of data at $\Delta = 147^o$, since the JB travel-time tables extend no farther. This also has the advantage that at greater ranges the differential travel-time of the two phases becomes significant, and while PKPbc picks may be much more abundant than PKPde picks, the latter provide large outlyers to the distribution of data. Furthermore, the amplitude ratio of the two phases becomes more even and the relative picking frequency is likely to even at larger ranges. The ISC residuals in this PKPbc range are referenced to the PKPdf travel-time. We have rereferenced the data to the appropriate phase. The number of data in this data set is 56348.

The last subset of data that we use in this study is that of PKPab-waves. We truncate this set at $\Delta = 155^o$, where the travel-time separation

of it and the other core phases exceeds ten seconds. These waves are grazing at the CMB and thus are very sensitive to D'' heterogeneity. They suffer from the complications of tunneling effects at the CMB discontinuity (Richards 1976). The number of PKPab data is 10229.

We form summary rays on an equal-area grid of 15x15^o at the equator. We then correct the summary rays for contributions from harmonic degrees 1 through 3 of the mantle model of Clayton and Comer (1983). We limit this correction to the lowest harmonics because of the lack of correlation between the model of Clayton and Comer (1983) and Dziewonski (1984) at higher degrees (see Hager et al. 1985). Finally, it has been suggested on the basis of the travel-time residuals of PKPef-waves and free-oscillation data that the inner core is anisotropic (Morelli et al. 1986, Woodhouse et al. 1986, and Shearer et al. 1988). We correct the PKIKP data for the anisotropic inner-core model of Shearer et al. (1988), but also retain the data that are not anisotropy corrected for our inversions.

Table 2.1 summarizes the numbers of data in the different subsets as individual picks, as summary rays and as summary rays with at least five composite rays. Table 2.2 summarizes the variances of the individual sets at stages in the data-reduction process. The PKPbc and PKPde data sets stand out in terms of numbers of data and low scatter. The secondary phases (PcP and PKPab) are present in considerably fewer numbers than the primary phases (PKPbc, PKPde, and PKPef). It is interesting to note that the anisotropy correction increases the variance of the PKPef data set when we restrict ourselves to summary rays with at least five picks. This is because much of the polar antipodal data in the set, which contain the strongest anisotropic signal, have but a few individual picks per summary ray.

Phase	picks	srays n > 0	srays n > 4
PcP	9784	810	300
PKPab	10229	362	150
PKPbc	56348	761	422
PKPde	104989	1300	790
PKPef	35514	588	329

Table 2.1 Numbers of data in the different subsets of core data from the ISC catalog. The first column indicates numbers of individual picks, the second column the total number of summary rays, and the last column the number of summary rays with at least five contributing rays.

		Mantle correction		Anisotropy corrected	
Phase	picks	srays n > 0	srays n > 4	srays n > 0	srays n > 4
PcP	2.89	2.39	0.61	xxxx	xxxx
PKPab	2.50	2.10	0.72	xxxx	xxxx
PKPbc	1.77	1.01	0.55	xxxx	xxxx
PKPde	1.90	1.14	0.48	1.14	0.48
PKPef	3.28	2.07	0.95	1.95	1.05

Table 2.2 Variances (sec^2) of the five subsets of ISC core data at different stages in the data processing. The first column shows the variance of all individual picks taken together, the next two columns show the variance of all summary rays after mantle correction, and the last two columns show the summary-ray variance after the PKPdf data have been corrected for the model of Shearer et al. (1988) for inner-core anisotropy. The minimum number of contributing rays to a summary ray is indicated above columns 2 through 5.

2.3 Method

The travel-time residual of PcP-waves, δt, is related to a small perturbation in CMB radius, δh, by the simple expression:

$$\delta t = -2\delta h \cos(\theta)/V_m, \tag{2.1}$$

where θ is the angle of incidence at the CMB and V_m is the compressional velocity at the base of the mantle. The analogous expression for refracted waves is:

$$\delta t = \delta h \left[\frac{\cos(\theta_c)}{V_c} - \frac{\cos(\theta_m)}{V_m} \right], \tag{2.2}$$

where V_m is as before the velocity at the base of the mantle, V_c is the velocity at the top of the core, and θ_m and θ_c are the angles of incidence at the mantle and core sides of the CMB, respectively. Note that waves that refract through the CMB do so at two loci, whereas reflected waves sense only one region of the CMB. Travel-time residuals that are due to small velocity anomalies above or below the CMB, δV, are:

$$\delta t = -\frac{\delta V}{V^2} dS, \tag{2.3}$$

where dS is the path length within the anomalous region. When mapping CMB topography with PcP data, we simply need to project the data along their ray paths to the CMB. When using the refracted core phases, we are, on the other hand, faced with an inherent inverse problem due to the intercoupling of the data as they relate to the model, because of the double sampling.

We divide the model space into 192 equal area patches, equivalent to a 15x15^o square on the equator. The same equal area grid is used to group

summary rays. We compute ray geometry by power-law ray-tracing (see Bullen 1979) through the JB model. Each summary ray is defined by the average epicentral distance of the composite rays and the azimuth of the center of one grid cell as seen from the other. Denote the patches containing the refraction points of the i-th datum by k and l. Assuming a constant model value within each patch we write:

$$\delta t_i = (\delta h_k + \delta h_l) \left[\frac{\cos(\theta_{ci})}{V_c} - \frac{\cos(\theta_{mi})}{V_m} \right]. \tag{2.4}$$

Grouping all these linear equations, we have the matrix equation:

$$\mathbf{d}_i = \mathbf{G}_{ij} \mathbf{x}_j, \tag{2.5}$$

where $\mathbf{x}_j = \delta h_j$, $\mathbf{D}_i = \delta t_i$, and

$$\mathbf{G}_{ij} = \frac{\cos(\theta_{ci})}{V_c} - \frac{\cos(\theta_{mi})}{V_m}, \tag{2.6}$$

where $j = k$ or l, and zero elsewhere. We can similarly translate Equation 2.3 into a linear matrix equation of the form of Equation 2.5 with $x_j = \delta V_j$ and

$$\mathbf{G}_{ij} = -dS_{ij} / V^2, \tag{2.7}$$

where dS_{ij} is the path length of the i-th ray in the j-th grid cell. We compute the path lengths explicitly for a layer thickness of 200 km above and below the CMB, rather than use the analytical limit $dS = H/\cos(\theta)$ at the CMB ($H = 200\ km$). Finally, we normalize the topography kernels by $1/V_m$ and the velocity kernels by $\frac{200\ km}{V^2}$, such that both are dimensionless and of order 1.

A range of inversion procedures are at our disposal. CJ used a variant of the stochastic-inverse method, MD used a least-squares inversion for the coefficients of a truncated expansion in terms of spherical harmonics, Gudmundsson et al. (1986) used an iterative back-projection scheme. The model size (192 parameters for one layer, 576 parameters for three) does not call for an iterative scheme. The distribution of data over the CMB is very uneven (see figures of resolution in the next section). The data are quite redundant for some regions, notably between New Zealand and Europe and under the Americas, but very sparse in others, notably the Pacific ocean and the southern hemisphere. This distribution of data calls for localized smoothing in the solution, rather than an expansion in terms of relatively few, smooth, global functions as MD did. We find the stochastic inverse scheme of CJ appealing, since it constrains the solution to be smooth, and allows for trade-off between the enforcement of the constraint and the fitting of the data. Their choice of a cosine, model-covariance function renders the smoothing constraint not strictly local. We use instead a Gaussian of 25^o width.

This variant of the stochastic inverse solution to the inverse problem stated in Equation 2.5 may be written on the form:

$$\bar{\mathbf{x}} = \left[\mathbf{C}\mathbf{G}^T\mathbf{G} + \alpha\mathbf{I}\right]^{-1}\mathbf{C}\mathbf{G}^T\mathbf{d}, \tag{2.8}$$

where $\mathbf{C}$ is the presumed model-covariance matrix, $\bar{\mathbf{x}}$ is the solution approximating the true model, $\mathbf{x}$, and $\mathbf{G}$ and $\mathbf{d}$ are defined as before. α is a dimensionless parameter used to trade off between model variance and resolution. The resolution matrix is:

$$\mathbf{R} = \left[\mathbf{C}\mathbf{G}^T\mathbf{G} + \alpha\mathbf{I}\right]^{-1}\mathbf{C}\mathbf{G}^T\mathbf{G}, \tag{2.9}$$

and the covariance matrix of model estimates is:

$$\mathbf{S} = \left[\mathbf{C}\mathbf{G}^T\mathbf{G} + \alpha\mathbf{I}\right]^{-1}\mathbf{C}\mathbf{G}^T\mathbf{\Omega}\mathbf{G}\mathbf{C}^T\left[\mathbf{G}^T\mathbf{G}\mathbf{C}^T + \alpha\mathbf{I}\right]^{-1}, \qquad (2.10)$$

where Ω is the data-covariance matrix. This method deviates from the standard stochastic-inverse scheme in that the data-covariance matrix does not enter the solution explicitly. (see Aki and Richards 1980, and references therein). This is because of the choice of not weighing the data inversely to their estimated error. We estimate the data variances by computing the average variance within summary rays in each of the five data sets and assigning that value divided by the number of composite rays in each summary ray. Weighing the data inversely to the estimated data variances would defeat the purpose of summary rays, which is partly to even the distribution of data and reduce the dominance of densely sampled, shallow features. In our construction of Ω we assume that the data errors are not correlated. These error estimates are not a complete description of errors in the data, simply a reflection of the randomness.

In the solutions presented in the following section we followed the example of CJ and selected the trade-off parameter α such that the number of degrees of freedom in the solution was fixed. The degrees of freedom may be computed from the trace of the resolution matrix. We chose to fix the degrees of freedom at twenty-five, which equals the number of parameters in a harmonic expansion that is truncated at degree four (MD). In the cases where we solve for more than one layer (including heterogeneity above and below the CMB), we fix the degrees of freedom in the CMB-topography layer at twenty-five. In these cases we did not couple the presumed model covariances for the different layers in the solution (i.e., we used a block diagonal, laterally-Gaussian model-covariance). In our solutions to the single layer problem (CMB topography), we define resolution length, ϕ, measured in

degrees, according to

$$\mathbf{R}_{ii} = \frac{1 - \cos(15^o)}{1 - \cos(\phi_i)}, \tag{2.11}$$

where $\mathbf{R}_{ii}$ are the diagonal elements of the resolution matrix. This assumes that the resolution function for each model parameter may be simplified as a function of constant value inside a circular area of radius ϕ on a sphere, that its value is zero outside the area, and that it integrates to unity. In the multiple layer cases we define a simple measure of resolution of the i-th model parameter according to:

$$t = \frac{\mathbf{R}_{ii} - \sum \mathbf{R}_{ij} / N_i}{\mathbf{R}_{ii}^2 + \sum \mathbf{R}_{ij}^2}, \tag{2.12}$$

where the sum is taken over nearest neighbors in the case of lateral resolution and the adjacent elements of the other two layers of the solution in the case of vertical resolution. The number of elements participating in the sum is denoted by N_i.

Finally, we comment that we find the above parameterization of an inverse problem for the structure of a continuum, with no known or presumed discontinuities, appealing. An effectively over-parameterized solution with local smoothness constraints yields a smooth (continuous if one wishes and goes to the expense) model, which avoids discretization artifacts. Local smoothness constraints avoid potential artifacts that are due to uneven sampling of a global smoothing function.

2.4 Results

We present a large array of models in this section; models obtained by the inversion of individual subsets of the ISC data, models obtained from data including a correction for inner-core anisotropy, and models obtained by simultaneous inversions of all the data for a one-, two-, and three-layer structure at the CMB. The reader can thus get a flavor of the inconsistencies in the data and the effects of varying the above parameters. All the models are presented as harmonic expansions of the direct inversion results, with degrees 1 through 4 included. All measures of solution goodness (model standard-error and measures of resolution) are presented in a smoothed form as harmonic expansions out to degree 8. This is done for display purposes only, since the smoothed versions of model error and resolution maps make it easier to discern regions of good resolution from regions of poor resolution. When referring to individual harmonic coefficients, they are relevant to fully normalized, spherical harmonics, normalized according to:

$$\int_{globe} X_{lm}^2 \, dA = 1,$$

where X_{lm} is the normalized spherical-harmonic basis-function for degree l and order m, and the integral is taken over the area of a globe.

Figures 2.1 through 2.6 show the results of inversions for CMB topography using the different subsets of the data. The top frames are the models, the middle frames are the diagonal elements of the covariance of model estimates, and the bottom frames are the resolution lengths as defined by Equation 2.11. Figure 2.1 shows the results for the PKPef data set. The model is dominated by a degree-two, zonal harmonic ($C_2^0 \approx 9.5\ km$) and has a peak-to-peak amplitude of 15 km. This model is similar to the model

Figures 2.1 - 2.6 Top: Model of CMB topography in km. Contours are at 0.0, $\pm$ 0.4, $\pm$ 1.2, and $\pm$ 2.0 km. Striped areas are topographic highs; dotted areas are topographic lows. The data set used is indicated at top. Middle: Square root of the diagonal elements of the covariance matrix of the model estimates. Contours are at 0.33, 0.67, and 1.0 km. Densely striped areas are areas of much uncertainty. Bottom: Resolution length measured in degrees as defined in text. Contours are at 35, 45, and 55 degrees. The minimum possible value of 15 is indicated. Densely striped areas are areas of wide lateral smoothing.

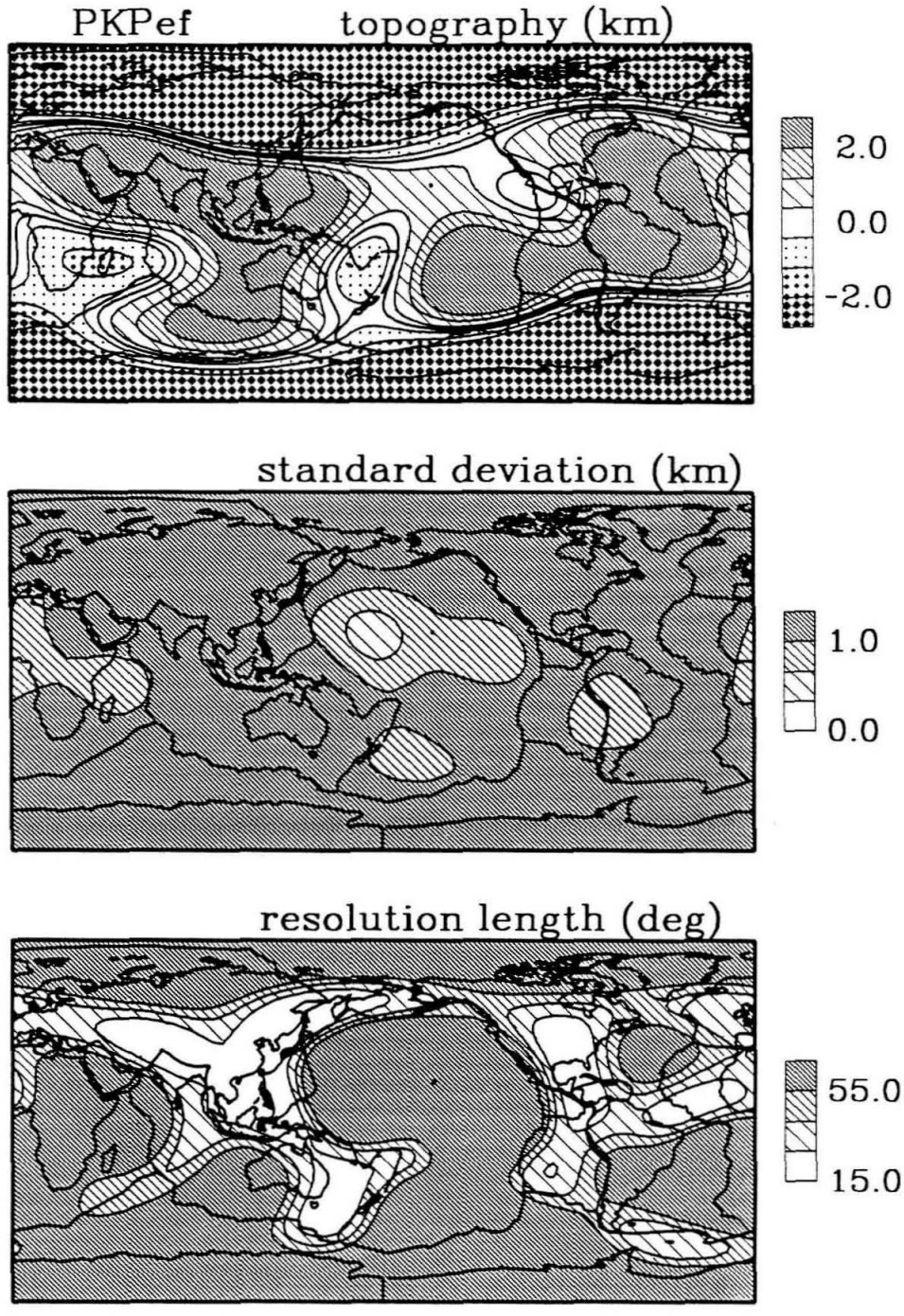

Figure 2.1 Results for CMB topography from the PKPef data set. Data have not been corrected for inner-core anisotropy.

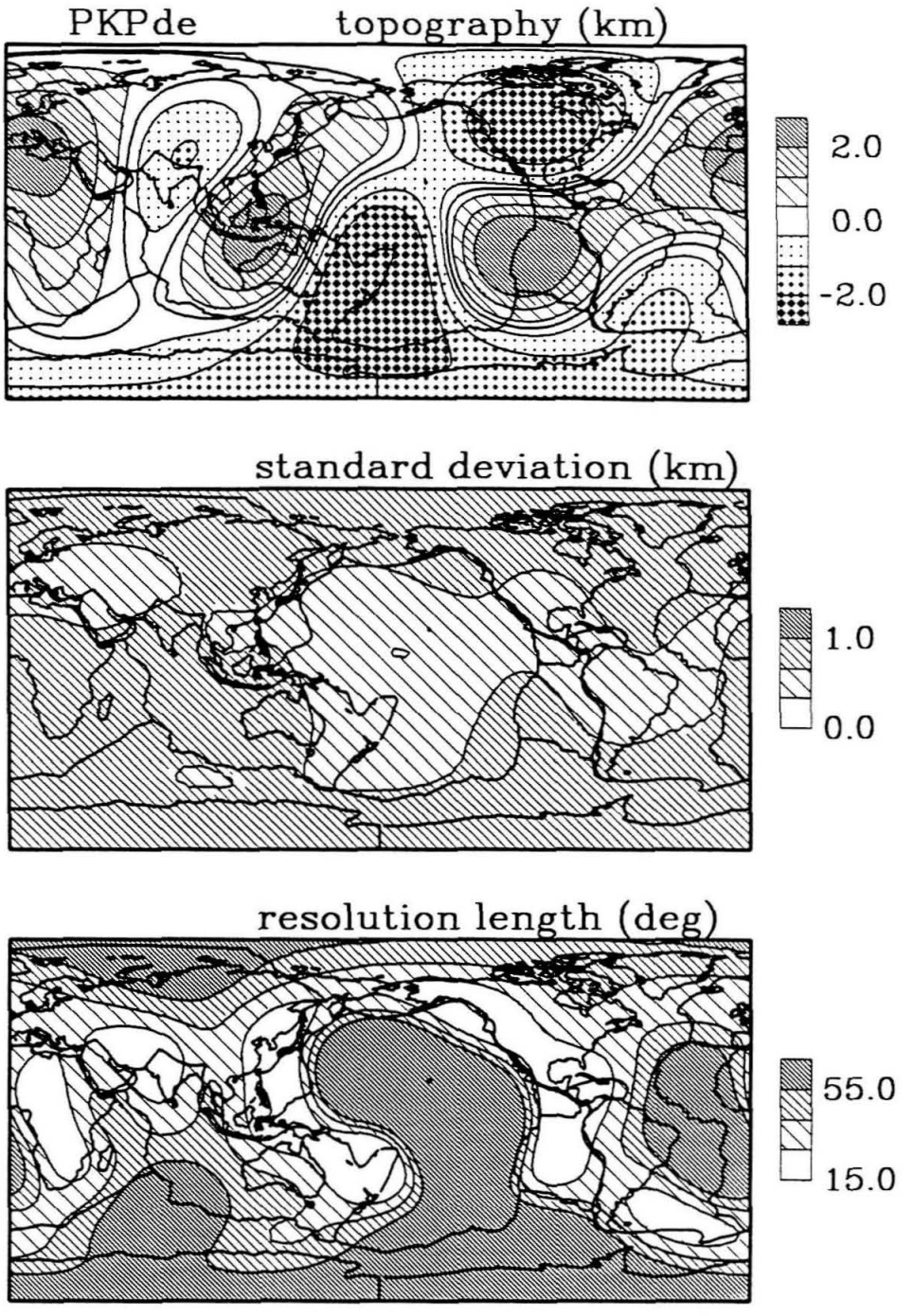

Figure 2.2 Results for CMB topography from the PKPde data set. Data have not been corrected for inner-core anisotropy.

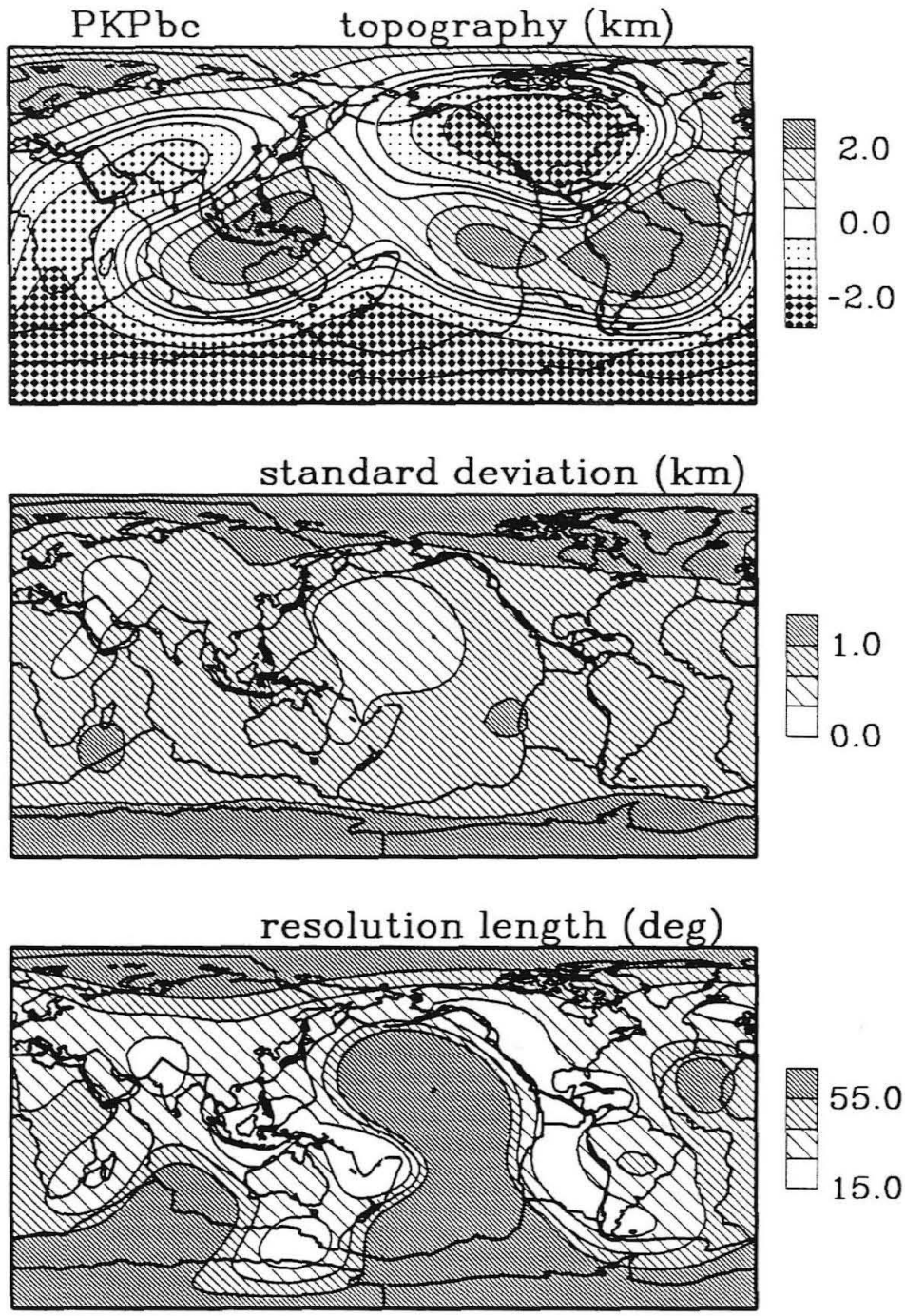

Figure 2.3 Results for CMB topography from the PKPbc data set.

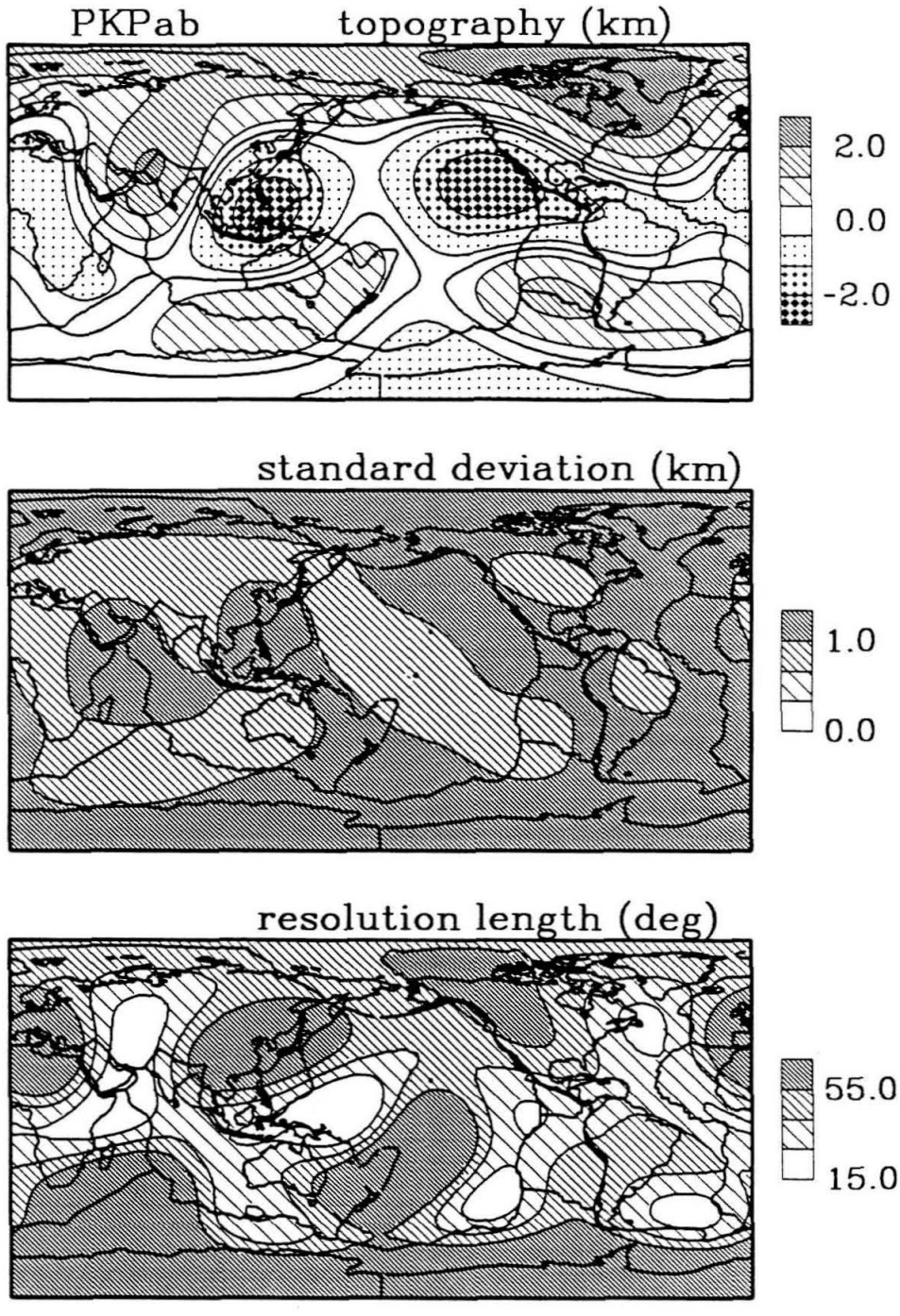

Figure 2.4 Results for CMB topography from the PKPab data set.

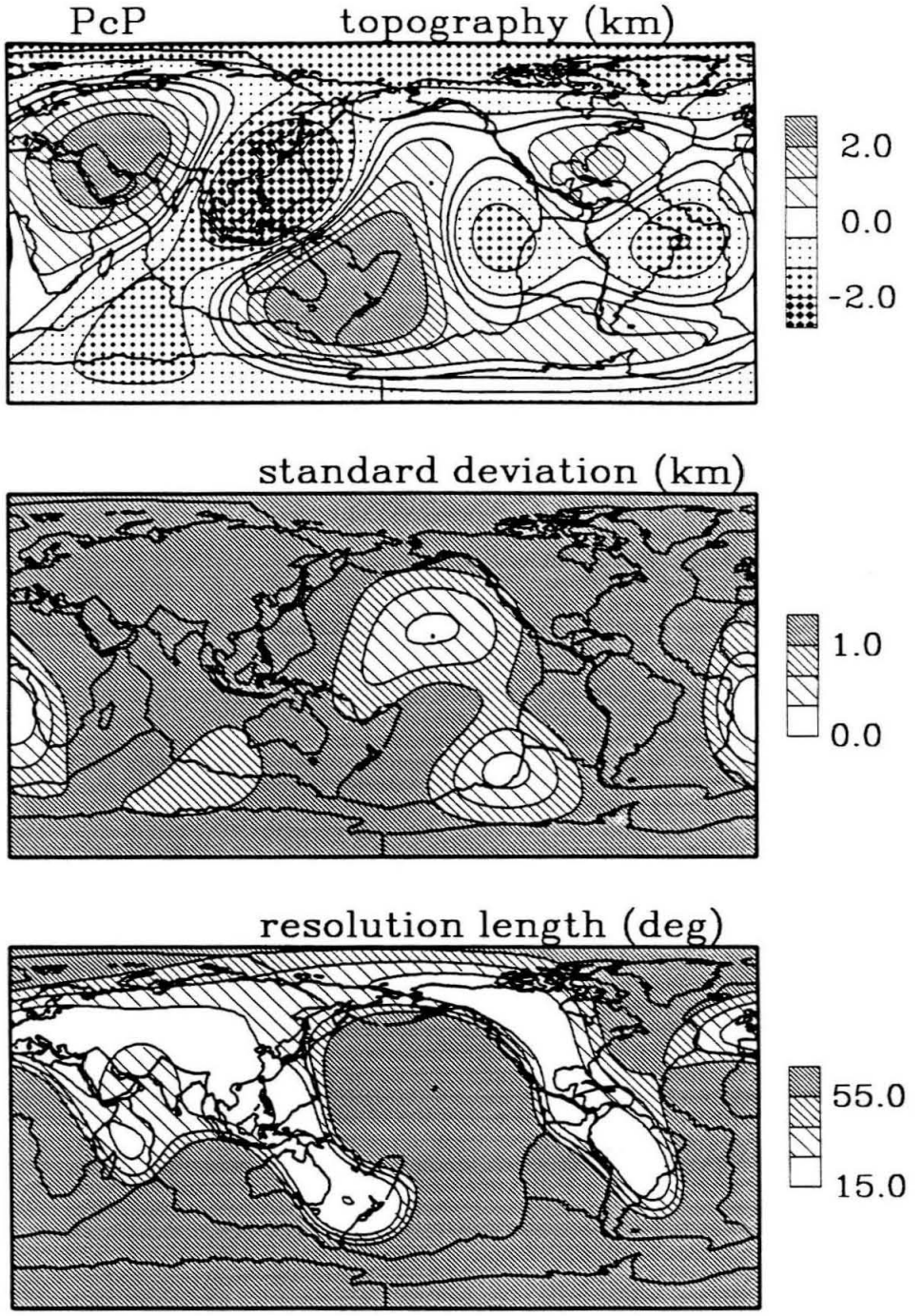

Figure 2.5 Results for CMB topography from the PcP data set.

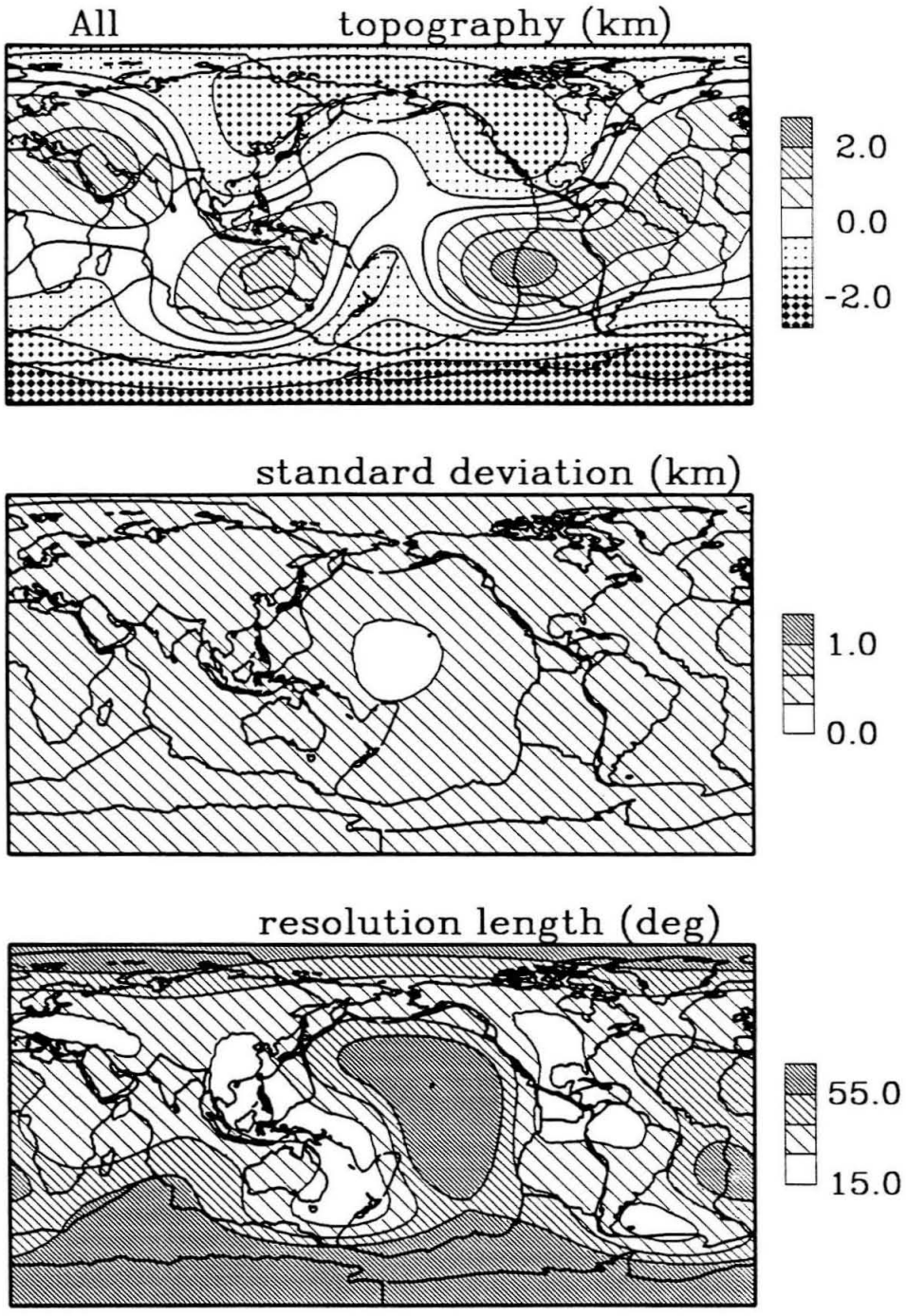

Figure 2.6 Results for CMB topography from simultaneous inversion of all data sets. Data have not been corrected for inner-core anisotropy.

obtained by CJ (Figure 1) and the expansion of travel-time residuals presented by Morelli et al. (1986, Figure 1). Both are based partly on the same data. Note that the lateral resolution (roughly equivalent to density of coverage) is poor for most of the globe. Regions of good resolution extend from New Zealand through southeast Asia towards Europe and the island arcs of the northwest Pacific, and along the Americas. The level of error in this model is high (>1 *km*). Figure 2.2 shows the results for the PKPde data set. Similar results from this data set have not been published. We have in this case a much better constrained model with random error less than 1 km and overall better resolution. Note that the regions of good resolution are much the same as for PKPef. The model, however, is drastically different. There is a significant degree-two, zonal harmonic ($C_2^o \approx 2.0$ *km*). The peak-to-peak amplitude of this map is about 6 km. Figure 2.3 shows the results from PKPbc data. This model bears little resemblance to the results obtained by MD (Figure 5) from similar data. Here the peak-to-peak amplitude is about 8 km. This far exceeds the standard error of the model. This model has a significant, degree-two, zonal component ($C_2^o \approx 3.0$ *km*), although not as dominating as the PKPef model. The pattern of good resolution is similar to the previous cases, but more dispersed. Figure 2.4 presents the results from PKPab data. This model does not correlate well with analogous results by CJ (Figure 1). Here the peak-to-peak amplitude is about 6 km. The level of the standard error is relatively high. The pattern of good resolution is somewhat different than before and much more dispersed. Figure 2.5 shows the results from PcP data. Again we have a major discrepancy with the previous study of MD (Figure 3). The peak-to-peak amplitude is about 8 km. Standard errors are high. The resolution

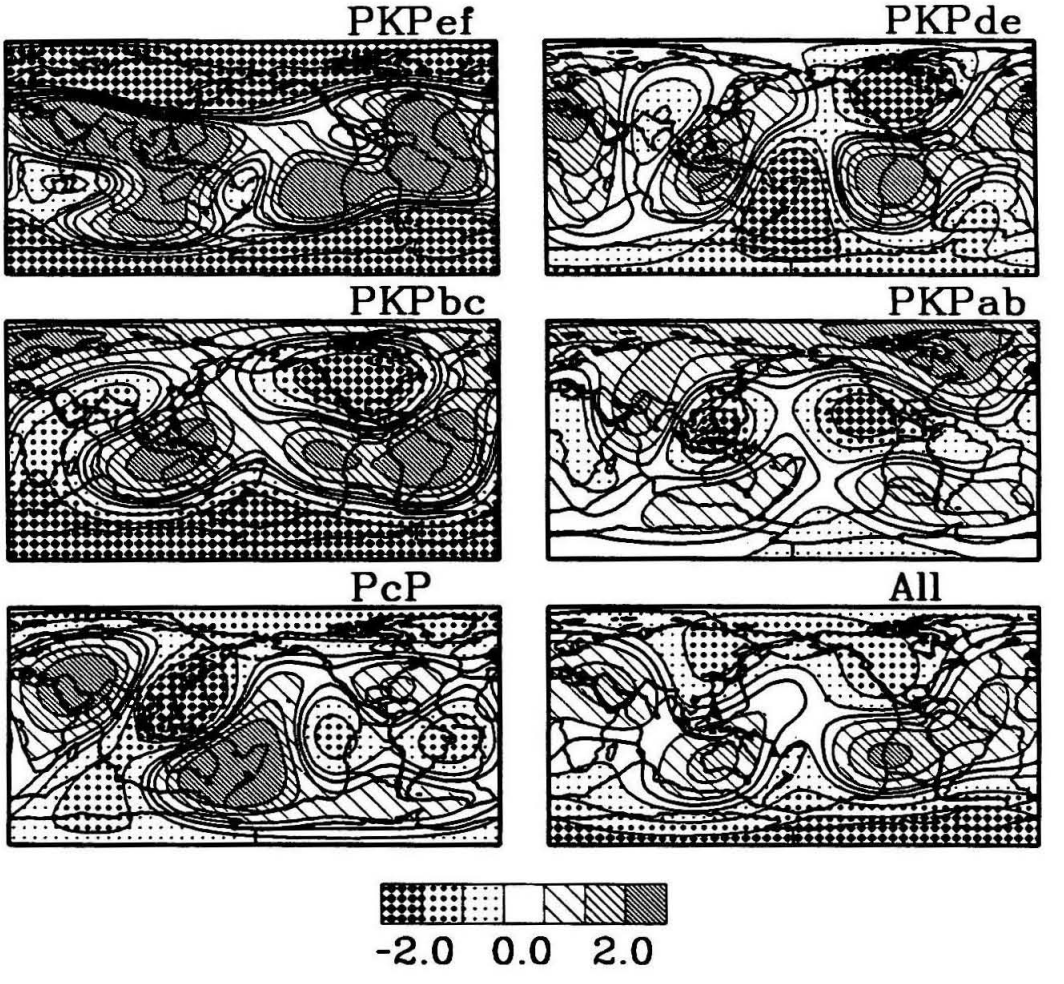

Figure 2.7 A summary of results for CMB topography from data that have not been corrected for inner-core anisotropy.

pattern is similar to the previous cases. Figure 2.6 presents the results obtained by simultaneous inversions of all of the above subsets of data. Once again the pattern of resolution is similar, but the standard error of the model is much reduced. This is because we design the solution such that the overall resolution is fixed. The inconsistencies between the models in Figures 2.1 through 2.5 yield a model in this case with a somewhat reduced peak-to-peak variation of 5 km. The degree-two, zonal pattern of the PKPef, PKPde and, PKPbc models survives the averaging and is perhaps the most prominent feature of this model ($C_2^0 \approx 2.2\ km$). Figure 2.7 summarizes the results presented in Figures 2.1 through 2.6. There is no clear common feature to all of these models. It is worth concentrating on the common regions of good resolution. In the narrow band of good resolution extending from New Zealand to Europe, the PcP model has its three biggest anomalies. They are a large high under New Zealand and eastern Australia, a deep low under southeast Asia and a high under southwest Asia. On the other hand, the PKPde model has this pattern almost perfectly reversed. The pattern in this region of the PKPbc model is similar to the PKPde pattern, except that the New Zealand anomaly is an indentation in a steep gradient. The New Zealand low is a clear feature in the PKPef model. The pattern in this part of the PKPab model is similar to that in the PcP model. Under the Americas all the refracted core phases (PKPef, de, bc, and ab) have a topographic high under S. America and a low under N. America, although less clear for PKPab than the other models. On the other hand, the PcP model has a high under N. America and a low under S. America and the East Pacific Rise. The kernels for CMB topography are reversed in sign for PcP relative to the other phases (see Equations 2.1 and 2.2). Thus, this apparent reverse correlation in

Figures 2.8 - 2.10 Top: Model of CMB topography in km. Contours are at 0.0, $\pm$ 0.4, $\pm$ 1.2, and $\pm$ 2.0 km. Striped areas are topographic highs; dotted areas are topographic lows. The data set used is indicated at top. Middle: Square root of the diagonal elements of the covariance matrix of the model estimates. Contours are at 0.33, 0.67, and 1.0 km. Densely striped areas are areas of much uncertainty. Bottom: Resolution length measured in degrees as defined in text. Contours are at 35, 45, and 55 degrees. The minimum possible value of 15 is indicated. Densely striped areas are areas of wide lateral smoothing.

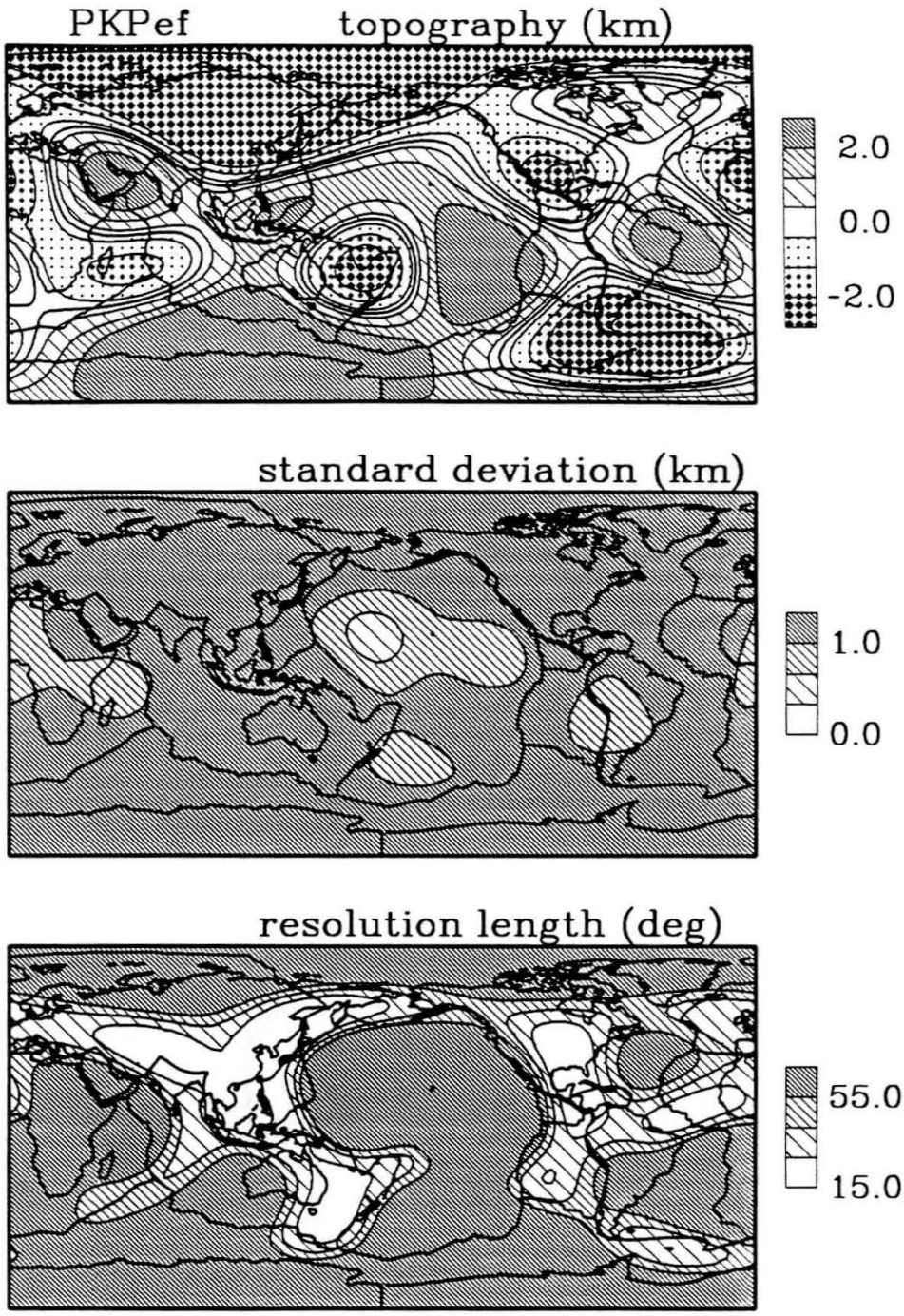

Figure 2.8 Results for CMB topography from the PKPef data set. Data have been corrected for inner-core anisotropy.

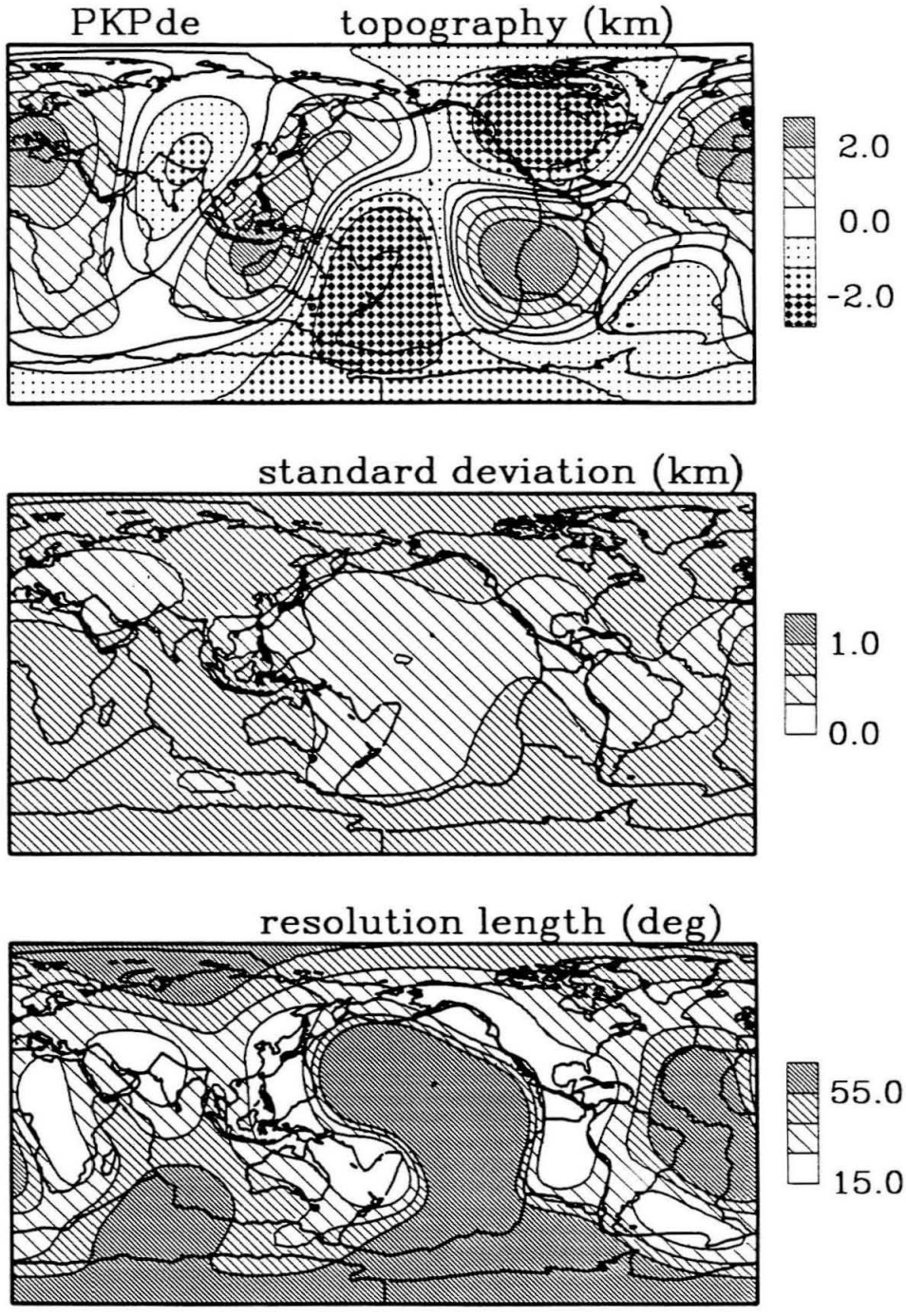

Figure 2.9 Results for CMB topography from the PKPde data set. Data have been corrected for inner-core anisotropy.

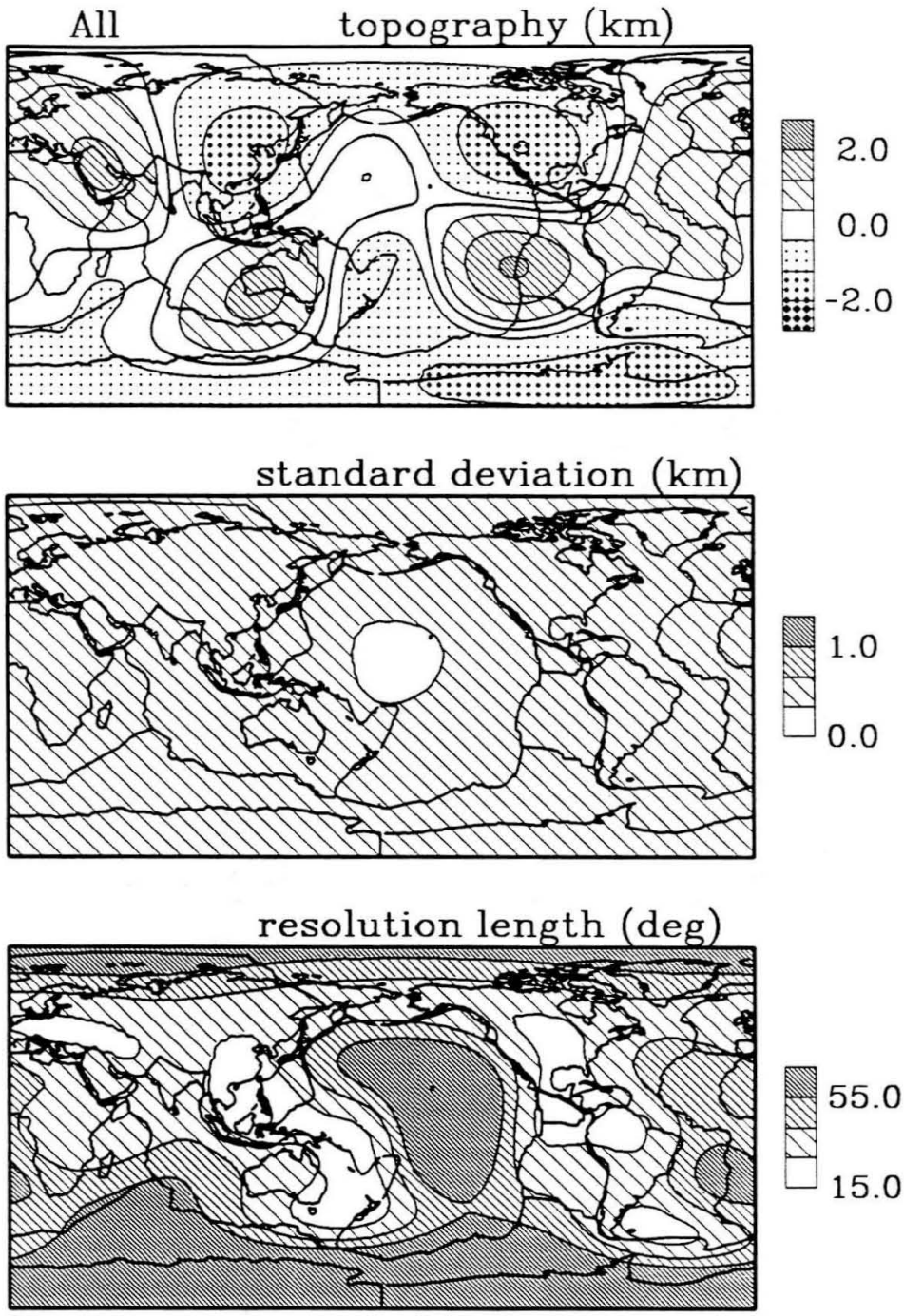

Figure 2.10 Results for CMB topography from simultaneous inversion of all data sets. Data have been corrected for inner-core anisotropy.

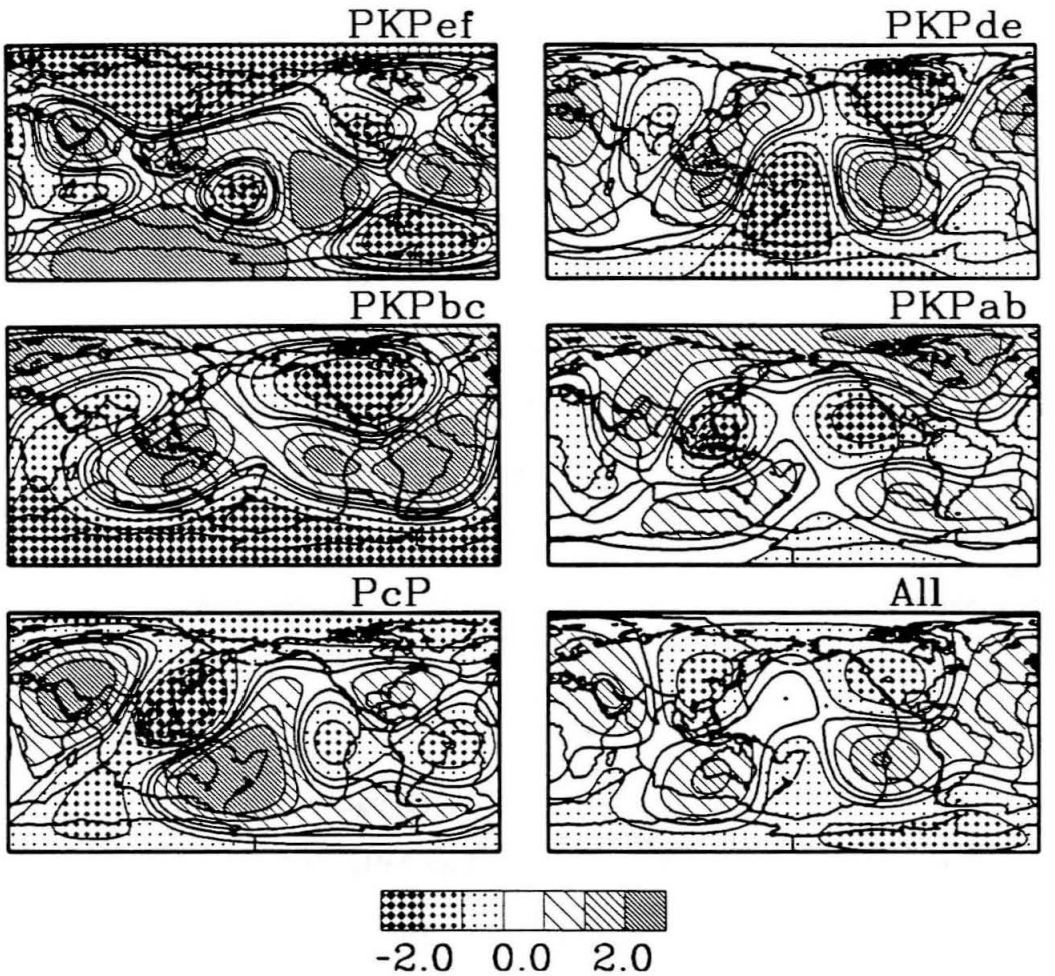

Figure 2.11 A summary of results for CMB topography from data that have been corrected for inner core anisotropy.

the models between PcP on one hand, and particularly PKPef, de, and bc on the other, implies a positive correlation of time residuals, indicating a common source for the residuals above the CMB. The most prominent of the anticorrelated features is perhaps the anomaly underlying New Zealand. There the sense of the anomaly indicates fast travel-time residuals, leading to the suspicion of contamination from the Fiji-Tonga subducting slab. This subduction zone is the most active seismic zone on earth and provides numerous events in the ISC catalog. On the other hand, the anticorrelated anomalies under S. America are due to slow residuals, despite the Andean slab. It is also possible that the discrepancies between the above models are due to structure immediately above the CMB. While we have corrected our data for lower-mantle structure (model of Clayton and Comer 1983), the correction may be lacking at the base of the mantle because of relatively poor coverage there.

Figures 2.8 through 2.10 show results analogous to Figures 2.1 - 2.6, where the PKIKP (PKPef and PKPde) data have been corrected for a proposed model for anisotropy in the inner core (Shearer et al. (1988)). The strong degree-two, zonal harmonic in PKPef data is one of two main arguments for this proposition, the other being observations of normal-mode splitting. Figure 2.11 summarizes the results from all subsets of data with an anisotropy correction applied. The only striking difference between Figures 2.11 and 2.7 is the absence of the degree-two, zonal harmonic in the PKPef model. The anisotropy corrected PKPef model is not strikingly correlated with any of the other models, although some similarities exist between it and the PKPde model. The composite model in Figure 2.10 is only slightly affected by the anisotropy correction (compared with Figure 2.6) and still

Variances (s*s) for summary rays at N > 0

Phase	initial	CMB.phase	CMB.all	DCMB.all	DCD.all
PcP	2.39	2.24 (6.3%)	2.38 (0.4%)	2.24 (6.3%)	2.20 (7.9%)
PKPab	2.10	1.85 (11.9%)	2.05 (2.4%)	2.05 (2.4%)	1.99 (5.2%)
PKPbc	1.01	0.88 (12.9%)	0.97 (4.0%)	0.92 (8.9%)	0.91 (9.9%)
PKPde	1.14	1.04 (8.8%)	1.11 (2.6%)	1.06 (7.0%)	1.04 (8.8%)
PKPef	2.07	1.65 (20.3%)	1.98 (4.3%)	1.89 (8.7%)	1.80 (13.0%)
cPKPde	1.14	1.04 (8.8%)	1.10 (3.5%)	1.06 (7.0%)	1.04 (8.8%)
cPKPde	1.95	1.61 (17.4%)	1.90 (2.6%)	1.92 (1.5%)	1.81 (7.2%)
All	1.61	1.57 (2.5%)	1.57 (2.5%)	1.51 (6.2%)	1.47 (8.7%)
cAll	1.59	1.56 (1.9%)	1.56 (1.9%)	1.50 (5.7%)	1.47 (7.5%)

Table 2.3. Variances (sec^2) of the various subsets of data before and after inversion. The data set is specified in the first column. The prefix "c" refers to data that have been corrected for anisotropy. The first numerical column gives the initial variance of the data set. The column labeled "CMB.phase" gives the residual variance after inversion for a one-layer structure (CMB topography) using the given data set only. The column labeled "CMB.all" gives the residual variances after inversion for a one-layer structure using all data. The column labeled "DCMB.all" gives the residual variances after inversion for a two-layer structure (D'' and CMB) using all data. The column labeled "DCD.all" gives the residual variances after inversion for a three-layer structure (D'', CMB, and D'''). The variance reduction is given in brackets. This table is based on data sets that include all summary rays.

Variances (s*s) for summary rays at N > 4

Phase	initial	CMB.phase	CMB.all	DCMB.all	DCD.all
PcP	0.61	xxxx (x.x%)	0.66 (-8.2%)	0.46 (24.6%)	0.45 (26.2%)
PKPab	0.72	xxxx (x.x%)	0.66 (8.3%)	0.55 (23.6%)	0.51 (29.2%)
PKPbc	0.55	xxxx (x.x%)	0.49 (10.9%)	0.42 (23.6%)	0.41 (25.5%)
PKPde	0.48	xxxx (x.x%)	0.43 (10.4%)	0.36 (25.0%)	0.35 (27.1%)
PKPef	0.95	xxxx (x.x%)	0.84 (11.6%)	0.74 (22.3%)	0.70 (26.3%)
cPKPde	0.48	xxxx (x.x%)	0.42 (12.5%)	0.36 (25.0%)	0.35 (27.1%)
cPKPde	1.05	xxxx (x.x%)	0.93 (11.4%)	0.88 (16.2%)	0.83 (21.0%)
All	0.61	0.56 (8.2%)	0.56 (8.2%)	0.46 (24.6%)	0.45 (26.2%)
cAll	0.63	0.57 (9.5%)	0.57 (9.5%)	0.49 (22.2%)	0.47 (25.4%)

Table 2.4. Variances (sec^2) of the various subsets of data before and after inversion. The data set is specified in the first column. The prefix "c" refers to anisotropy-corrected data. The first numerical column gives the initial variance of the data set. The column labeled "CMB.phase" gives the residual variance after inversion for a one-layer structure (CMB topography) using the given data set only. The column labeled "CMB.all" gives the residual variances after inversion for a one-layer structure using all data. The column labeled "DCMB.all" gives the residual variances after inversion for a two-layer structure (D'' and CMB) using all data. The column labeled "DCD.all" gives the residual variances after inversion for a three-layer structure (D'', CMB, and D'''). The variance reduction is given in brackets. This table is based on data sets that include all summary rays with at least five composite rays.

contains a significant C_2^0 term (1.1 km), although not dominant. This is to be expected since PKPef data are only 15% of the entire data set and the only subset to be significantly affected by the anisotropy correction.

A number of the above models of CMB topography would be deemed significant, at least in parts, if one were to assume that the standard error of the model estimates were a full description of the error. We have good resolution over limited regions of the globe and model amplitudes that exceed the standard error. However, the inconsistencies of the models imply that the physical model of CMB topography is not consistent with the signal in the data. Furthermore, the variance reduction of data by these models is rather low.

Tables 2.3 and 2.4 list the variances of the individual data sets, the residual variances after inversion and the percentage variance reduction by different models. The CMB topography models inverted from individual subsets of data yield variance reductions of the order of 10% to 20%. When all the data are used simultaneously to map a single layer structure on the CMB, the variance reduction is only 2%. This is very small and is indicative of the inconsistencies between the individual data sets.

Summary rays are applied in order to even the distribution of data over the globe, to reduce the relative weight of clustered data that sense a potentially discounted anomaly outside of model space, and to reduce the problem size. But summary rays also give us means to estimate random errors in the data. The random error of summary rays is high when the number of composite rays is low for two reasons. Firstly, redundancy within a summary ray suppresses random noise in the individual data. Secondly, a populous, even distribution of data over the area of a summary ray filters out signal from

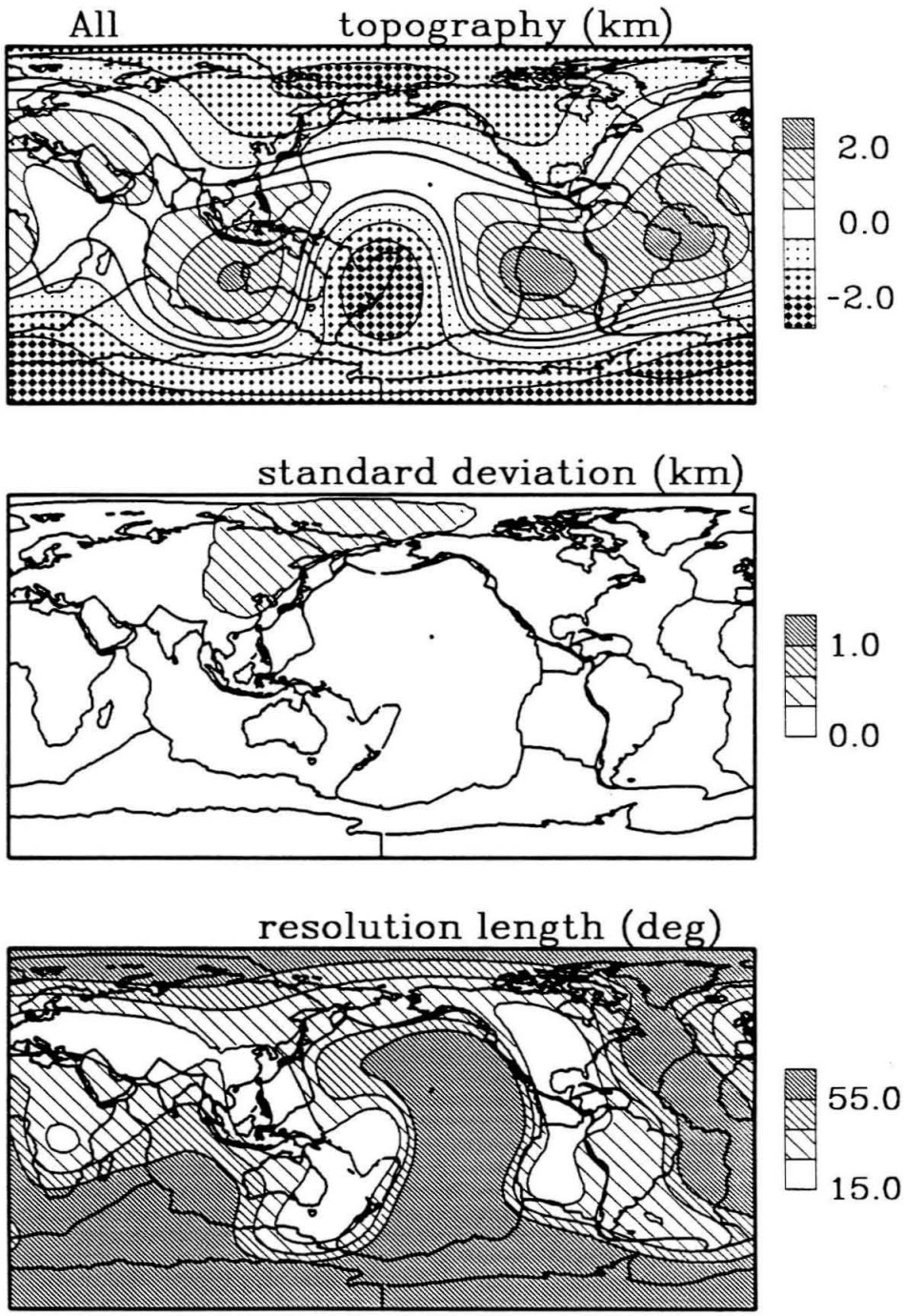

Figure 2.12 Results for CMB topography from simultaneous inversion of all summary rays with at least 5 composite rays. Data have not been corrected for core anisotropy. Legend same as for Figures 2.1 through 2.6.

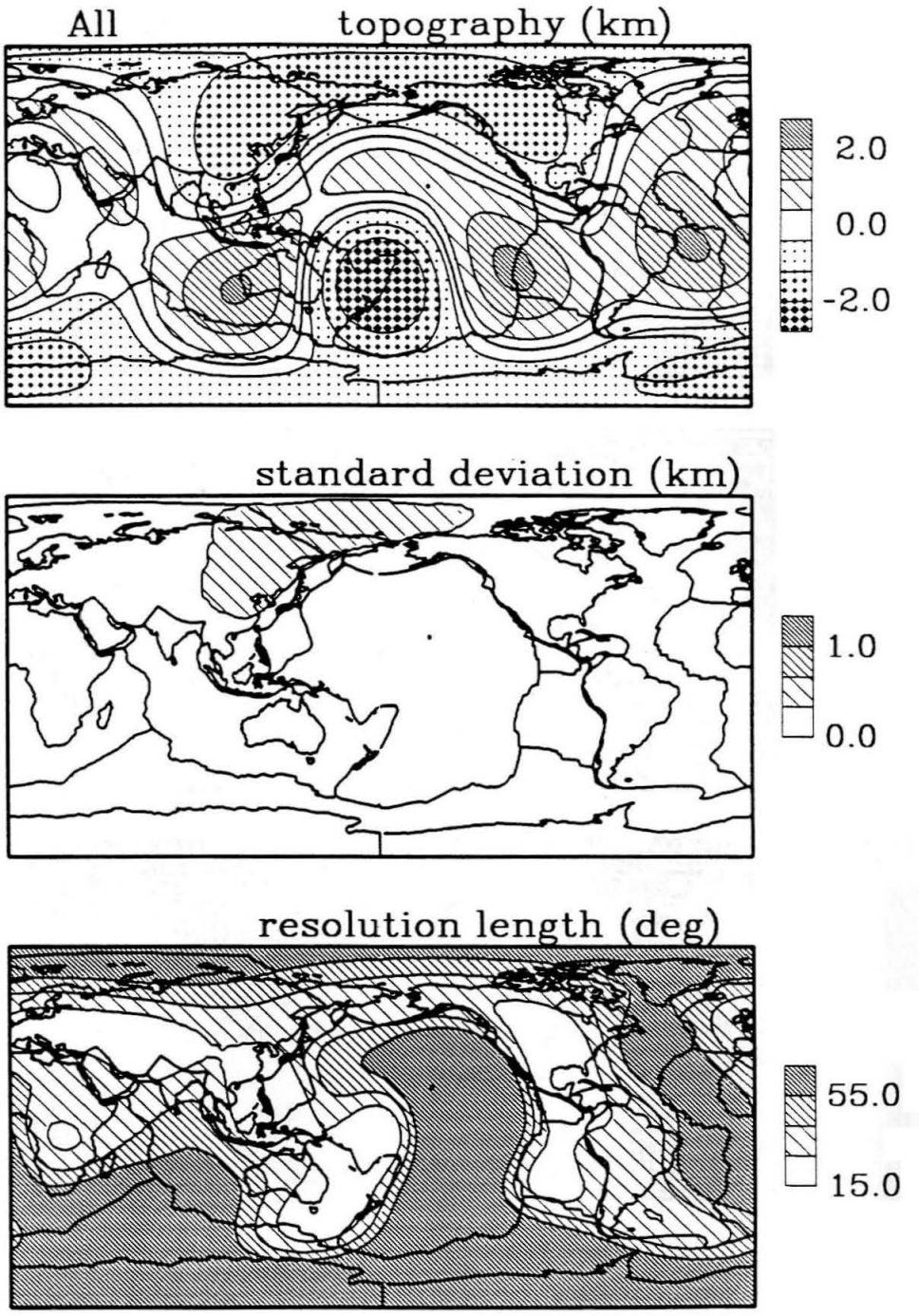

Figure 2.13 Results for CMB topography from simultaneous inversion of all summary rays with at least 5 composite rays. Data have been corrected for core anisotropy. Legend same as for Figures 2.1 through 2.6.

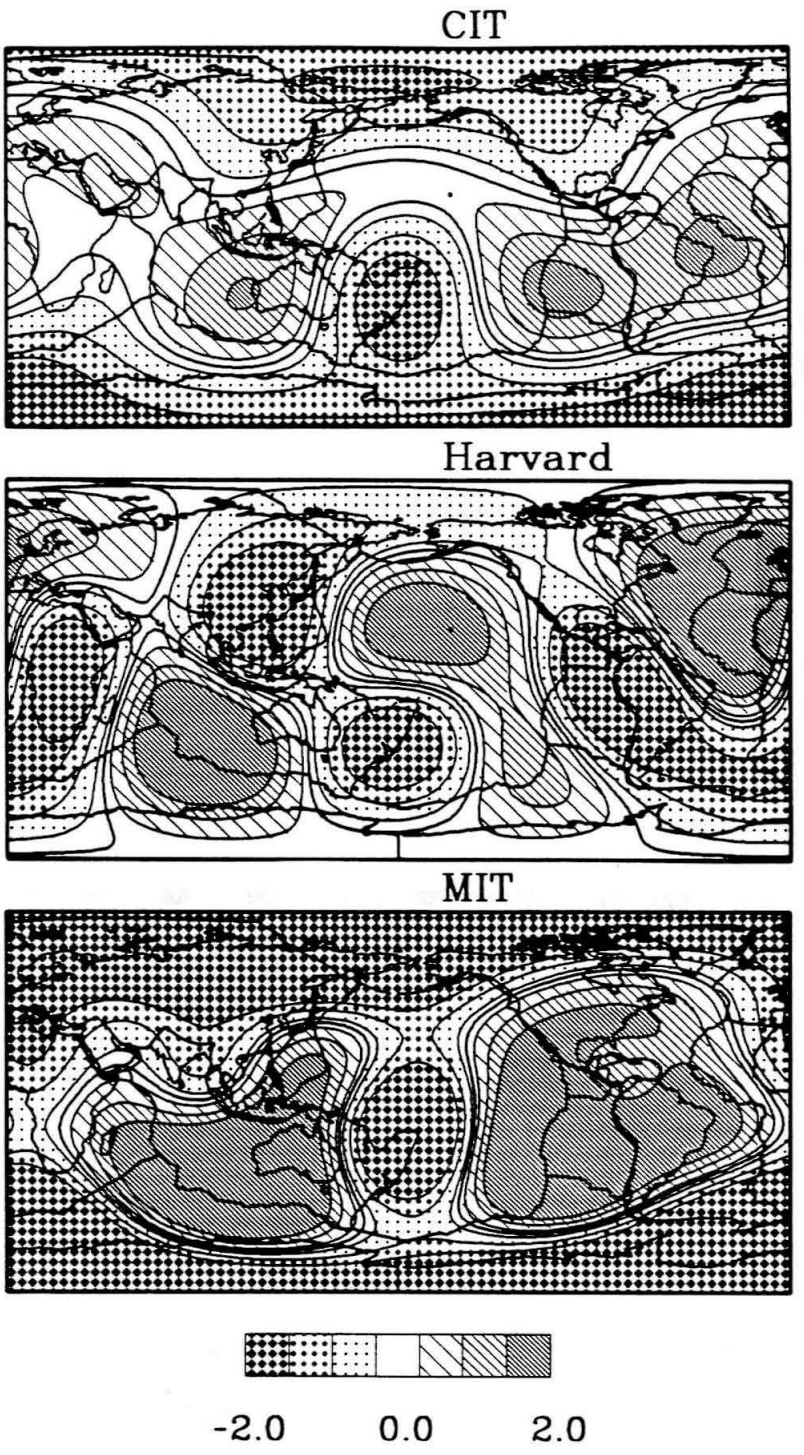

Figure 2.14 A comparison of the present results for CMB topography and previous results. Model CIT is the present result from summary rays with at least 5 composite rays. Model HARVARD is from Morelli and Dziewonski (1987), model MIT from Creager and Jordan (1986b).

	PcP	AB	BC	DE	EF	All1	All5	cDE	cEF	cAll1	cAll5
PcP	1.00	0.28	-0.36	-0.44	0.04	0.07	-0.27	-0.44	-0.01	0.08	-0.28
PKPab		1.00	-0.18	-0.26	-0.33	-0.03	-0.21	-0.23	-0.20	0.10	-0.17
PKPbc			1.00	0.57	0.25	0.67	0.66	0.54	0.04	0.59	0.56
PKPde				1.00	0.26	0.66	0.72	0.99	0.11	0.66	0.71
PKPef					1.00	0.68	0.63	0.23	0.71	0.47	0.49
All-1						1.00	0.84	0.63	0.42	0.91	0.74
All-5							1.00	0.72	0.41	0.75	0.93
cPKPde								1.00	0.13	0.67	0.73
cPKPef									1.00	0.48	0.49
cAll-1										1.00	0.78
cAll-5											1.00

	Oth	PcP	AB	BC	DE	EF	All1	All5	cDE	cEF	cAll1	cAll5
Harvard	0.20	-0.06	0.12	0.18	0.11	0.12	0.24	0.29	0.16	0.26	0.35	0.42
MIT	0.20	-0.19	-0.24	0.36	0.38	0.64	0.59	0.75	0.37	0.49	0.47	0.68

Table 2.5. Correlation coefficients of the various CMB models. The models are named after the data sets that are used to compute them, as in the text. The prefix "c" is used to refer to data that have been corrected for inner-core anisotropy. The models HARVARD and MIT are after Morelli and Dziewonski (1987) and Creager and Jordan (1986b), respectively.

small-scale structure. From the point of view of random uncertainty it may be advantageous to discard the poorest data. We tried selecting data according to the criterion that any given summary ray have at least five composite rays. This omits unstable data points based on only a few individual picks. Note the reduction in data variance by the application of this selection in Table 2.2. However, another effect of this data selection is to reduce redundancy, and in some cases to cancel coverage of entire large geographical areas. Figures 2.12 and 2.13 show the results of inverting all these data for CMB topography. In Figure 2.13 an anisotropy correction has been applied. Note how similar the two models are, and how low the estimates of model error are. The similarity of the two models is enhanced because polar antipodal PKIKP data are lacking in redundancy. They are thus excluded from the data. But those are the data that contain the strongest anisotropy signal. Note that the variance of the selective PKPef data set is increased by the application of an anisotropy correction (see Table 2.2). The models in Figures 2.12 and 2.13 have a strong degree-two, zonal component, ($C_2^0 \approx 2.5$ *km* and 1.6 *km*, respectively) with a major disruption in a topographic low under New Zealand. A topographic high along the equator is also disrupted by a saddle point under India. It is interesting to note that if we could discount the deep, topographic low under New Zealand as contamination from the Fiji-Tonga subduction slab, the remaining model would correlate with the predicted CMB topography of Hager et al. (1985). Furthermore, only a minor amplitude discrepancy would remain. These models yield an overall variance reduction of 8% and 9% respectively.

In Figure 2.14 we compare the model in Figure 2.12 with the models of MD and CJ. This is not to be taken as our preferred model of CMB

Figures 2.15 - 2.22 Results from inversions for a two-layer structure at the CMB (CMB topography and D'' velocity variations). Top: Model of CMB topography in km or D'' velocity anomalies in percent relative deviation from the JB reference model as indicated at top. Contours are at 0.0, $\pm$ 0.4, $\pm$ 1.2, and $\pm$ 2.0 km or percent. Striped areas are positive (topographic highs or fast regions); dotted areas are negative (topographic lows or slow). Second from top: Square root of the diagonal elements of the covariance matrix of the model estimates. Contours are at 0.25, 0.50, and 0.75 km or percent. Densely striped areas are areas of much uncertainty. Second from bottom: Vertical resolution (unitless) as defined in text. Contours are at 0.25, 0.50, and 0.75. Densely striped areas are regions of good vertical resolution. Bottom: Lateral resolution (unitless) as defined in text. Contours are at 0.25, 0.50, and 0.75. Densely striped areas are regions of good lateral resolution.

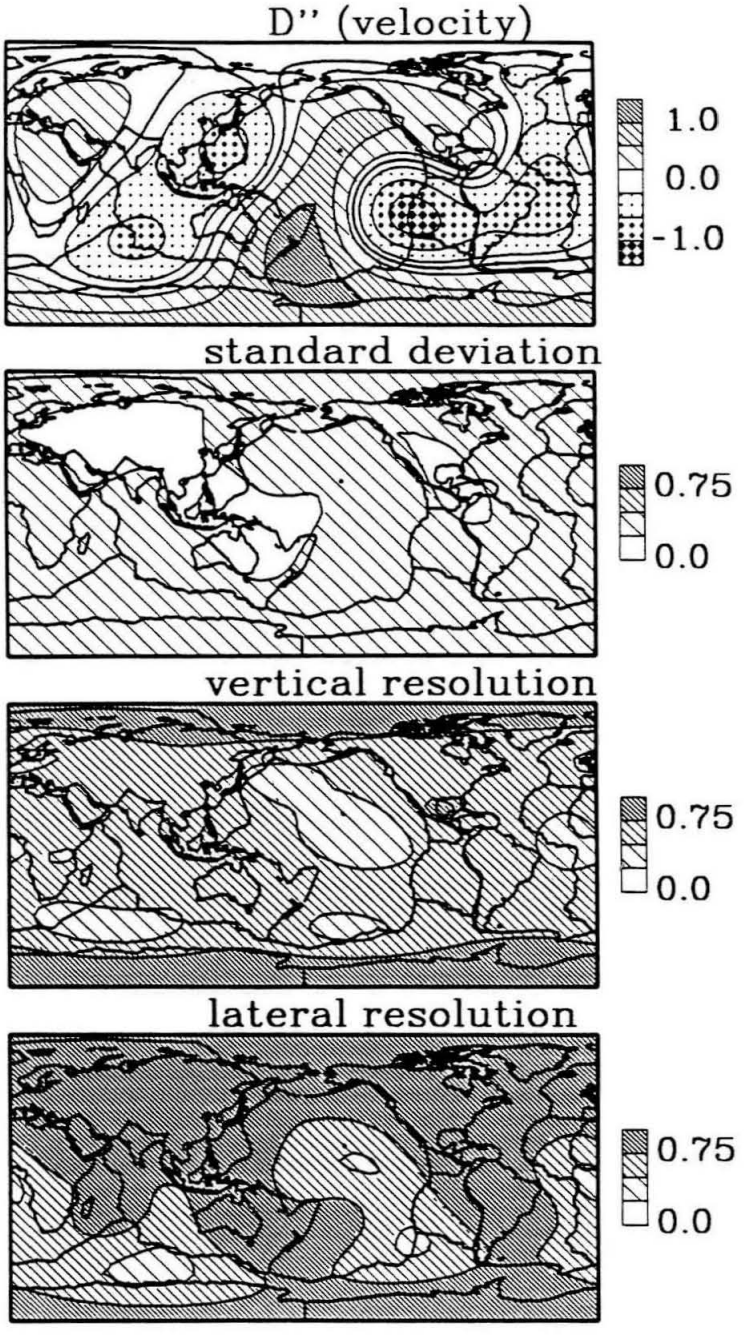

Figure 2.15. Results for D'' velocity variations. Data were not corrected for inner-core anisotropy. All summary rays were included.

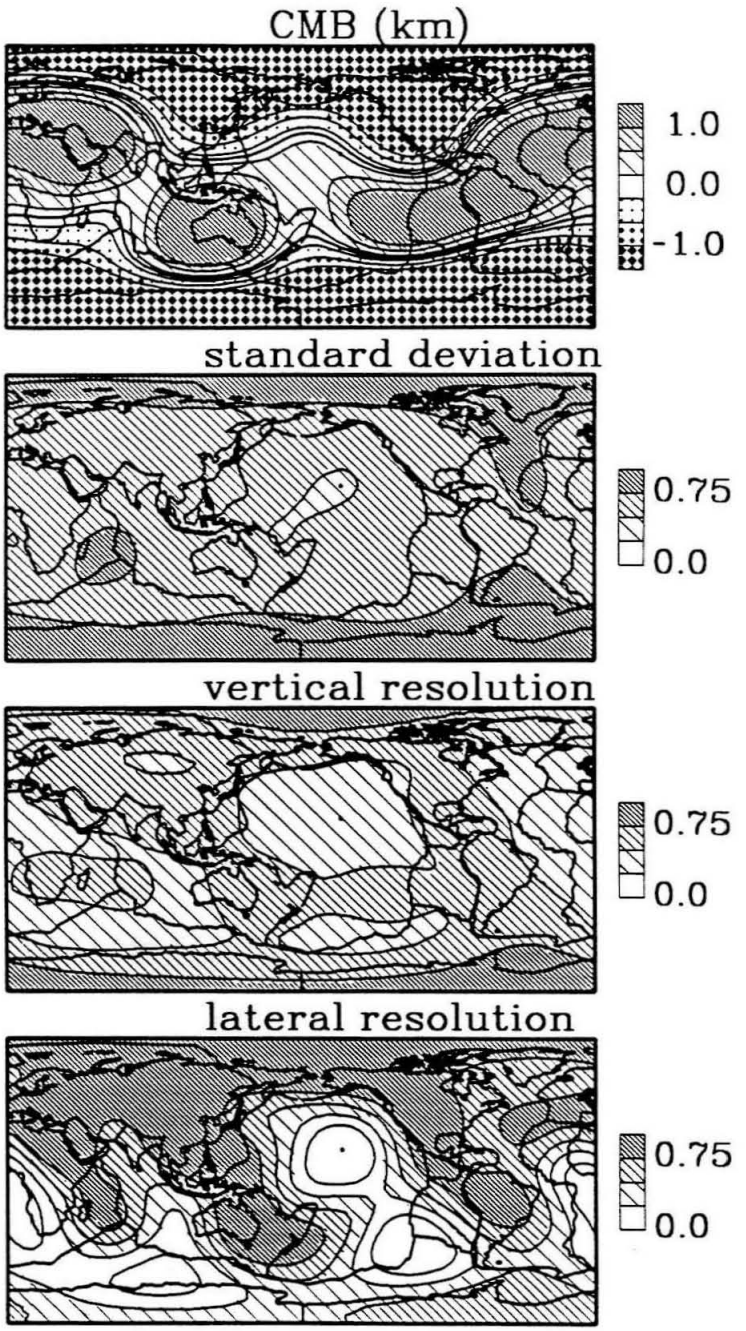

Figure 2.16. Results for CMB topography. Data were not corrected for inner-core anisotropy. All summary rays were included.

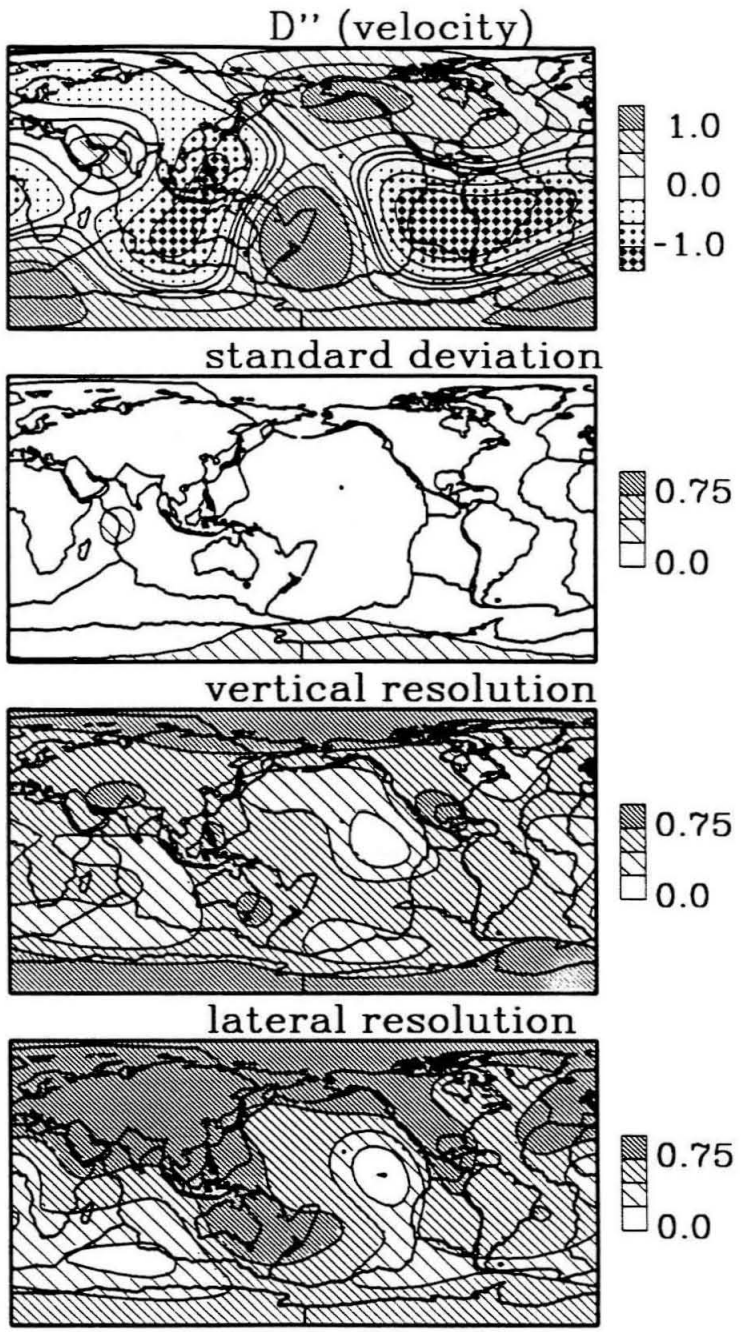

Figure 2.17. Results for D'' velocity variations. Data were not corrected for inner-core anisotropy. All summary rays with at least five composite rays were included.

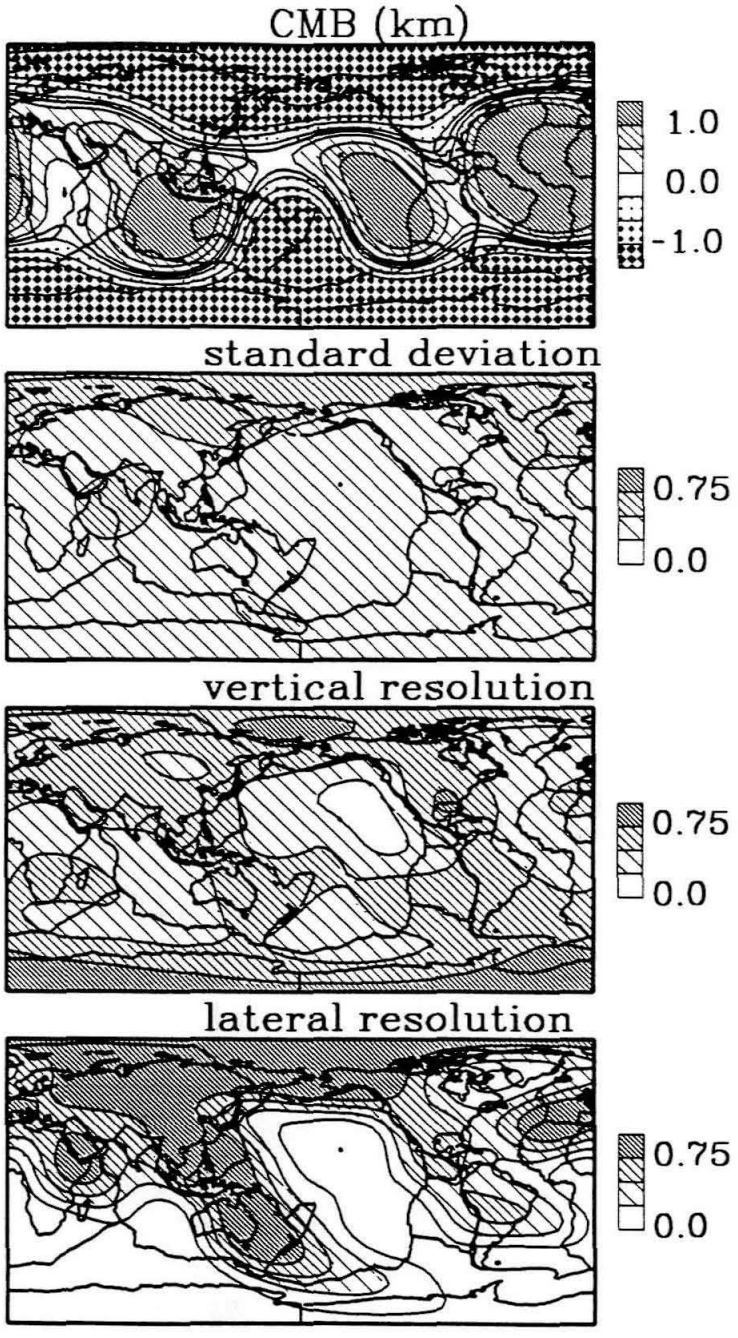

Figure 2.18. Results for CMB topography. Data were not corrected for inner-core anisotropy. All summary rays with at least five composite rays were included.

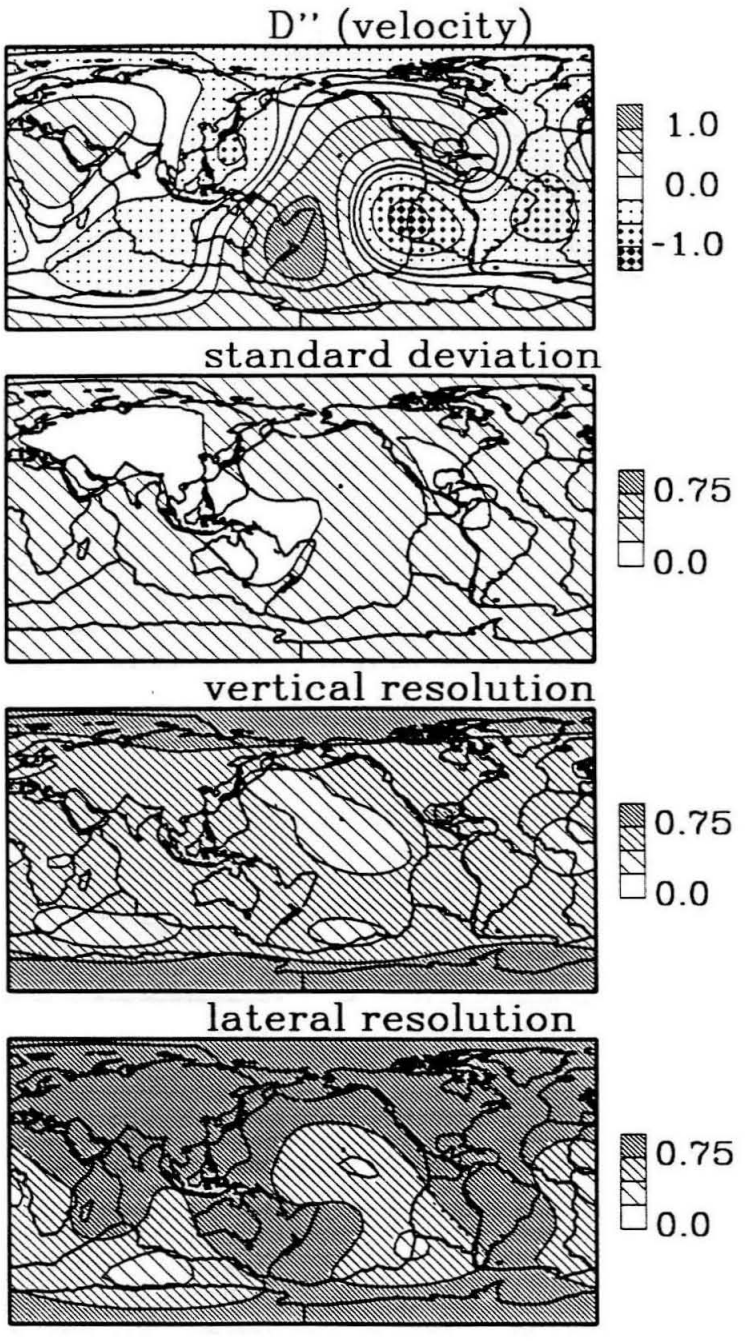

Figure 2.19. Results for D'' velocity variations. Data were corrected for inner-core anisotropy. All summary rays were included.

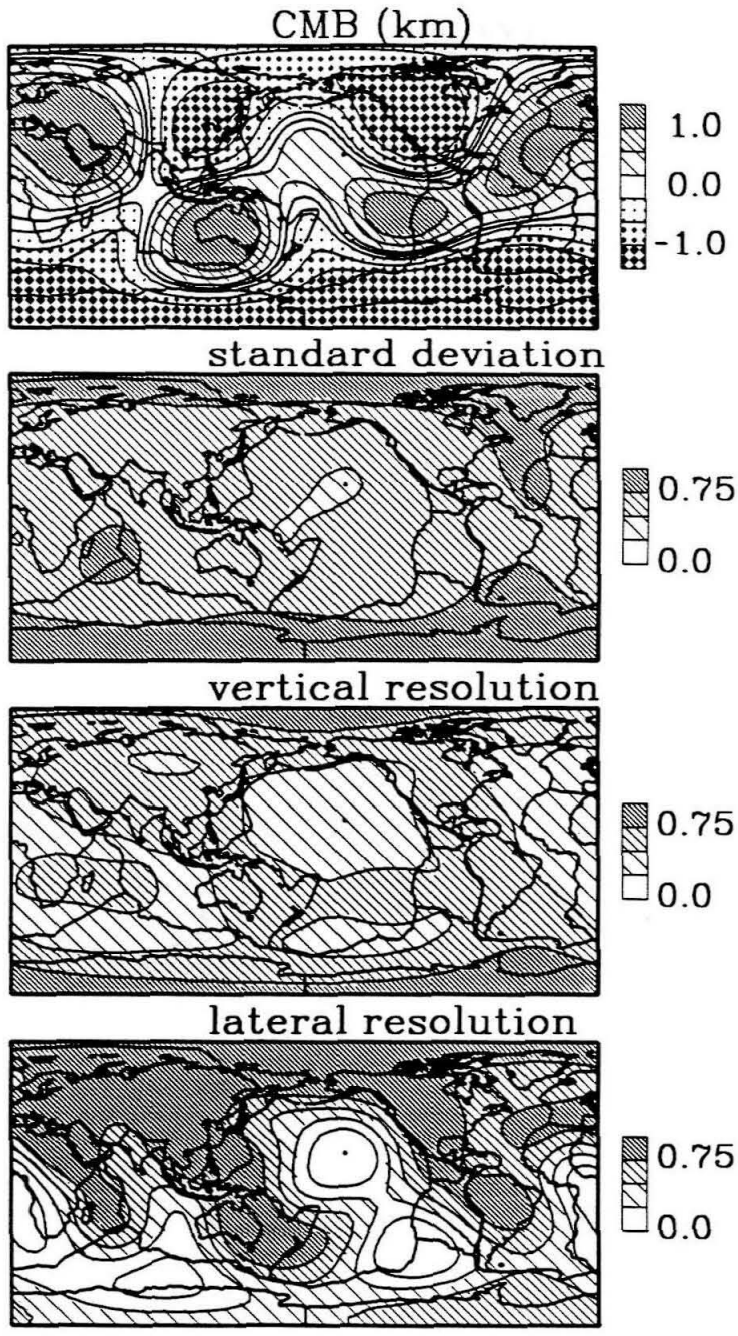

Figure 2.20. Results for CMB topography. Data were corrected for inner-core anisotropy. All summary rays were included.

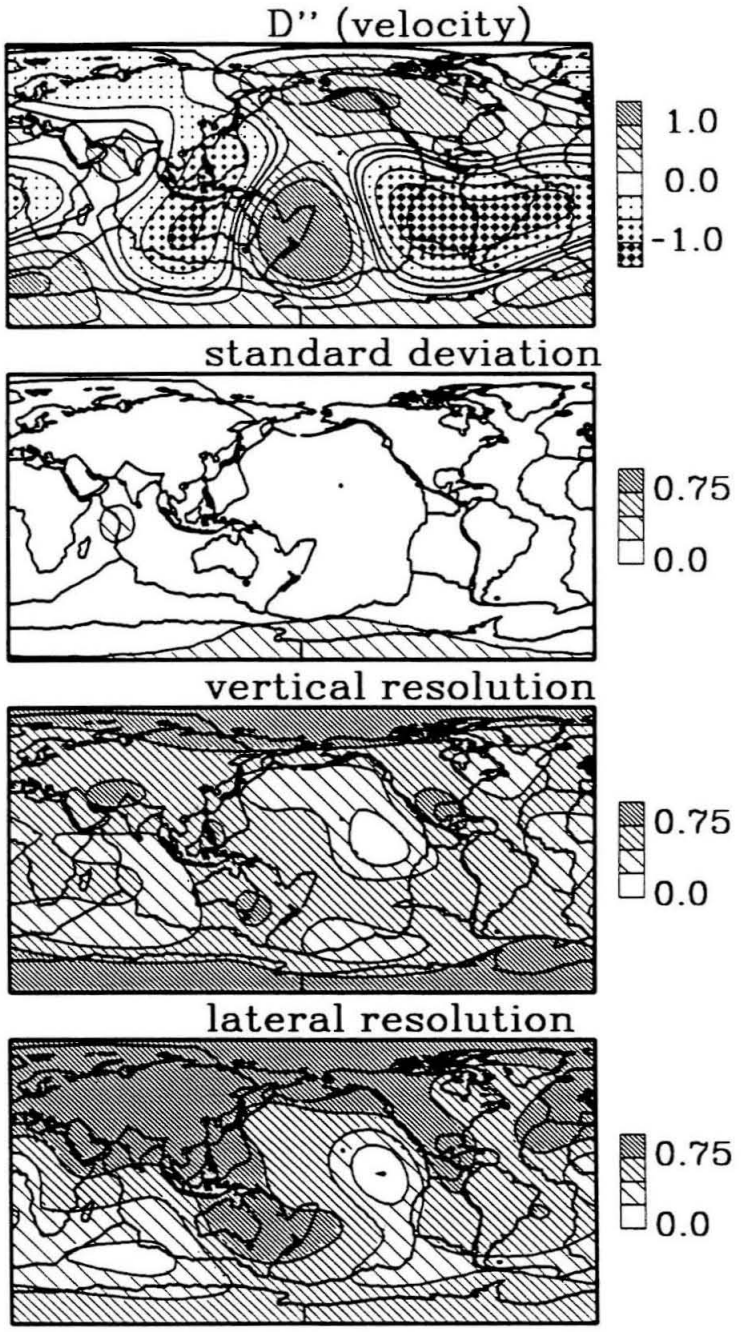

Figure 2.21. Results for D'' velocity variations. Data were corrected for inner-core anisotropy. All summary rays with at least 5 composite rays were included.

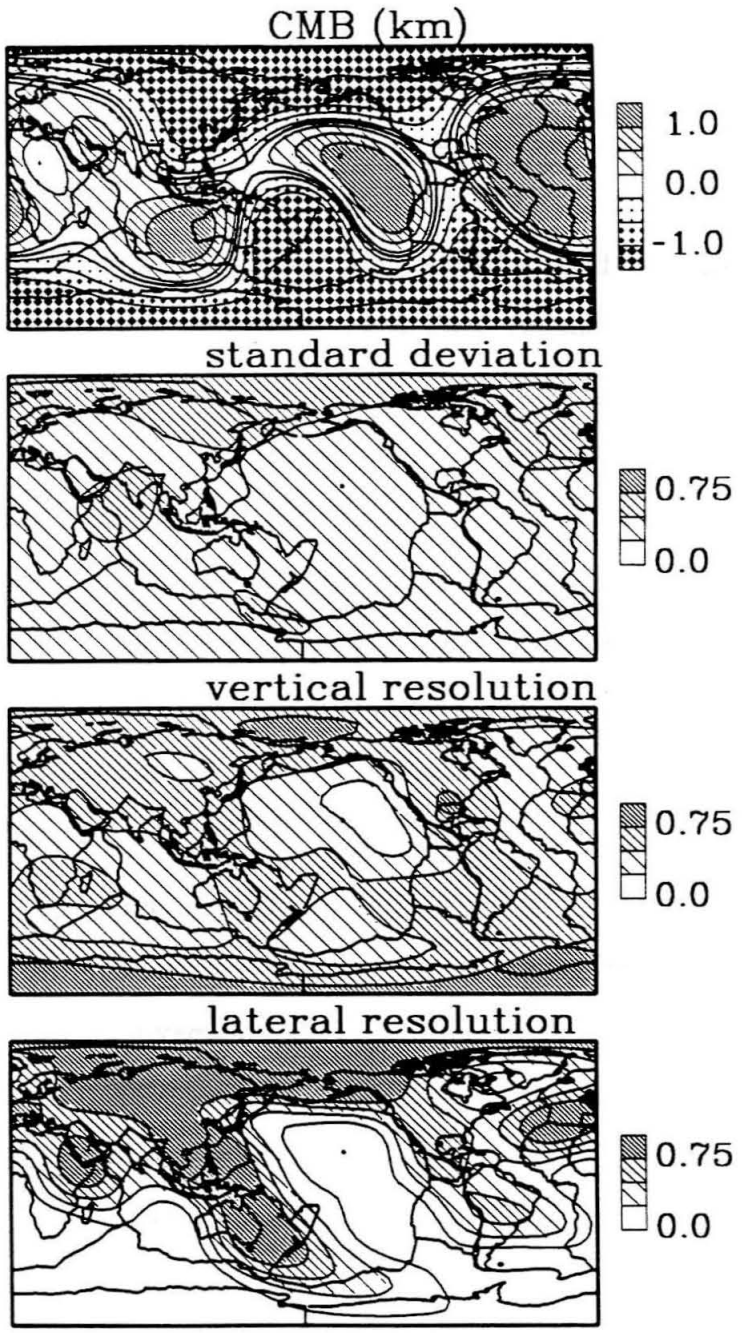

Figure 2.22. Results for CMB topography. Data were corrected for inner-core anisotropy. All summary rays with at least 5 composite were included.

topography; it is simply an example. All three models have a deep topographic low under New Zealand, a broad high under western Australia and the Indian Ocean, and a high near the East-Pacific Rise. However, the overall agreement is poor. In Table 2.5 we list the cross-correlation coefficients of all the models that we have discussed to this point. The models in Figure 2.14 correlate at the 0.35, 0.47, and 0.20 level, with the highest cross-correlation between our model and that of CJ. The highest correlation coefficients in the table are 0.57 between the PKPbc and PKPde models, 0.67 between the PKPbc, PKPde, and PKPef models on one hand and the All model on the other, and related correlations. The model of CJ correlates with our PKPef model at the 0.64 level, but at -0.24 with its other counterpart, the PKPab model. The model of MD correlates at the 0.18 level with our PKPbc model, but is slightly negatively correlated with its other counterpart, PcP.

Some of the discrepancies between the above CMB topography models may be explainable by structure immediately above the CMB in the D'' layer. We performed inversions of all subsets of data simultaneously for a two-layer structure at the CMB, including both topography and velocity anomalies in D''. The results are presented in Figures 2.15 through 2.22. Variance reductions obtained by these inversions are listed in Tables 2.3 and 2.4. Figure 2.15 shows the results for D'', when we have not corrected PKPdf (PKIKP) data for anisotropy, and include all summary rays in the inversion. The model has 2.5% peak-to-peak velocity variations. Note that we presume the thickness of this heterogeneous layer to be 200 km. In fact, we have no resolution to separate the product of the velocity anomaly and the layer thickness. Predictably, from the discrepancies between the CMB

Figures 2.23 - 2.34 Results from inversions for a three-layer structure at the CMB (CMB topography and D'' and D''' velocity variations). Top: Model of CMB topography in km or D'' or D''' velocity anomalies in percent relative deviation from the JB reference model as indicated at top. Contours are at 0.0, $\pm$ 0.4, $\pm$ 1.2, and $\pm$ 2.0 km or percent. Striped areas are positive (topographic highs or fast regions); dotted areas are negative (topographic lows or slow). Second from top: Square root of the diagonal elements of the covariance matrix of the model estimates. Contours are at 0.25, 0.50, and 0.75 km or percent. Densely striped areas are areas of much uncertainty. Second from bottom: Vertical resolution (unitless) as defined in text. Contours are at 0.25, 0.50, and 0.75. Densely striped areas are regions of good vertical resolution. Bottom: Lateral resolution (unitless) as defined in text. Contours are at 0.25, 0.50, and 0.75. Densely striped areas are regions of good resolution.

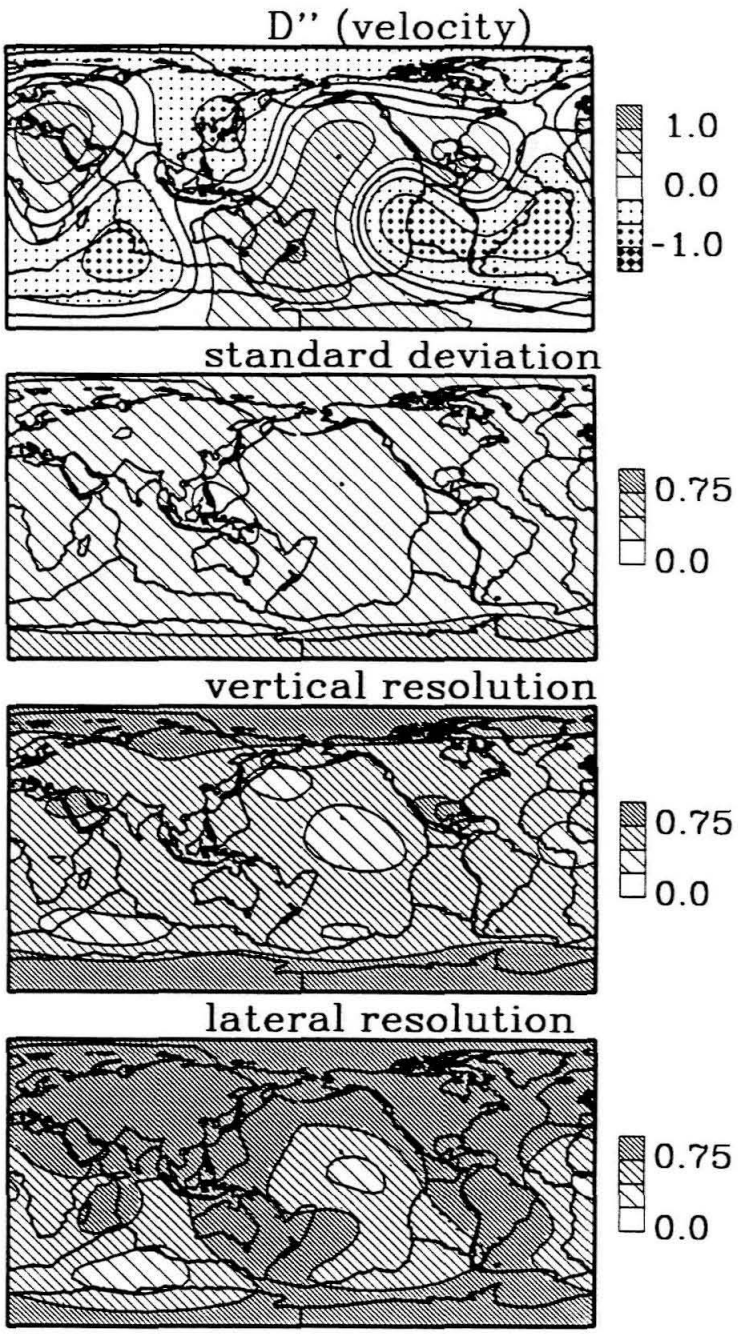

Figure 2.23. Results for D'' velocity variations. Data were not corrected for inner-core anisotropy. All summary rays were included.

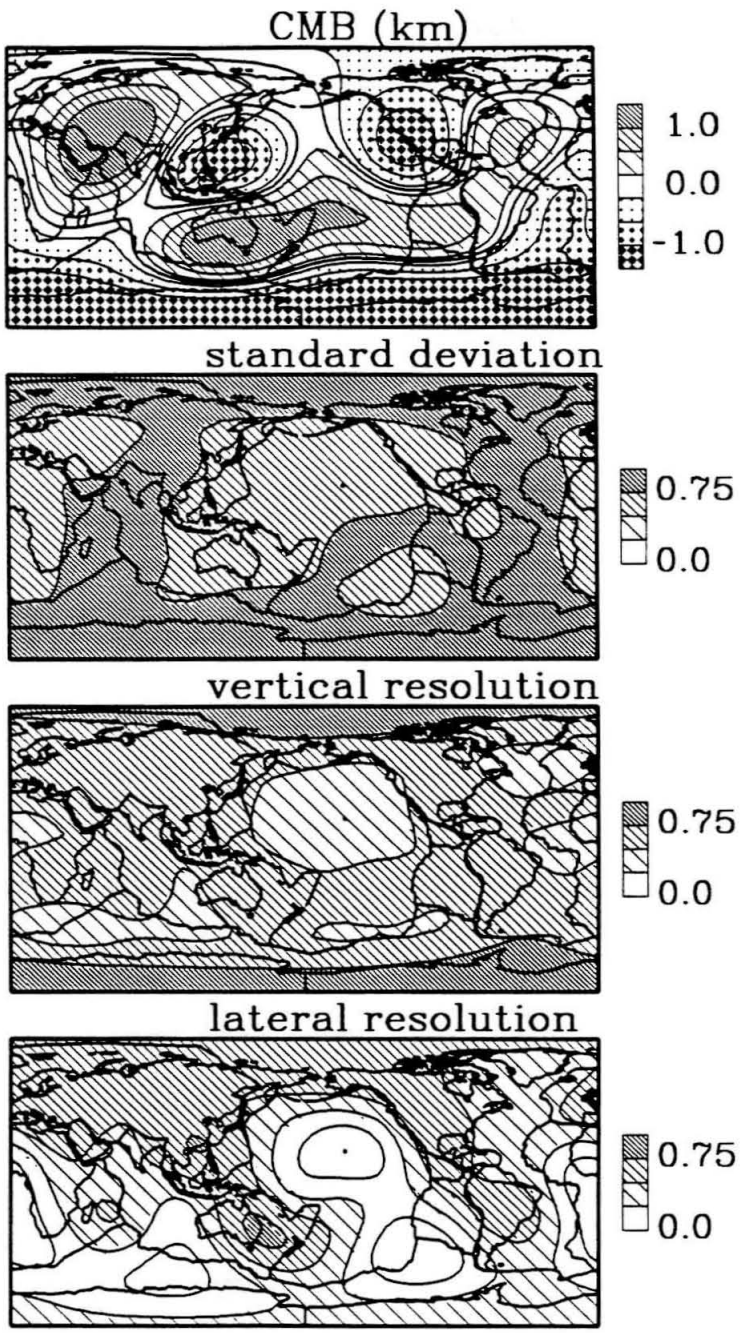

Figure 2.24. Results for CMB topography. Data were not corrected for inner-core anisotropy. All summary rays were included.

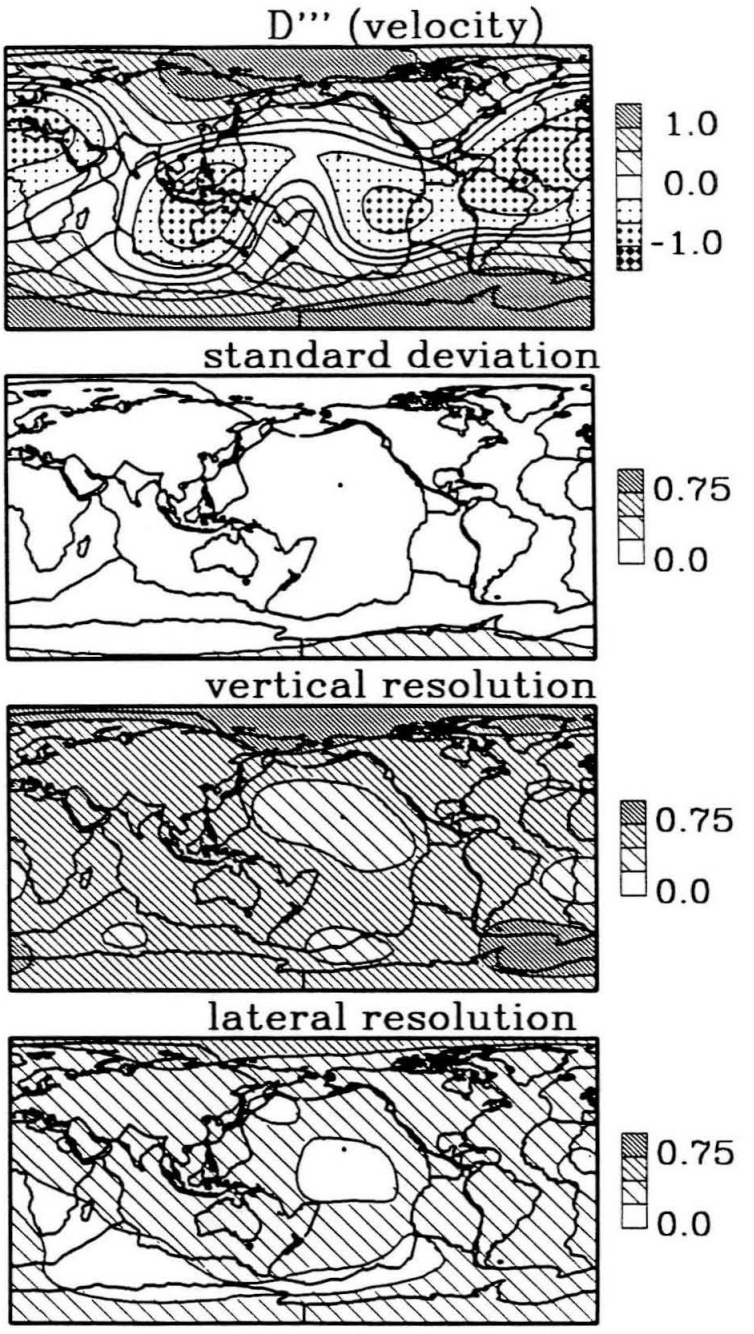

Figure 2.25. Results for D''' velocity variations. Data were not corrected for inner-core anisotropy. All summary rays were included.

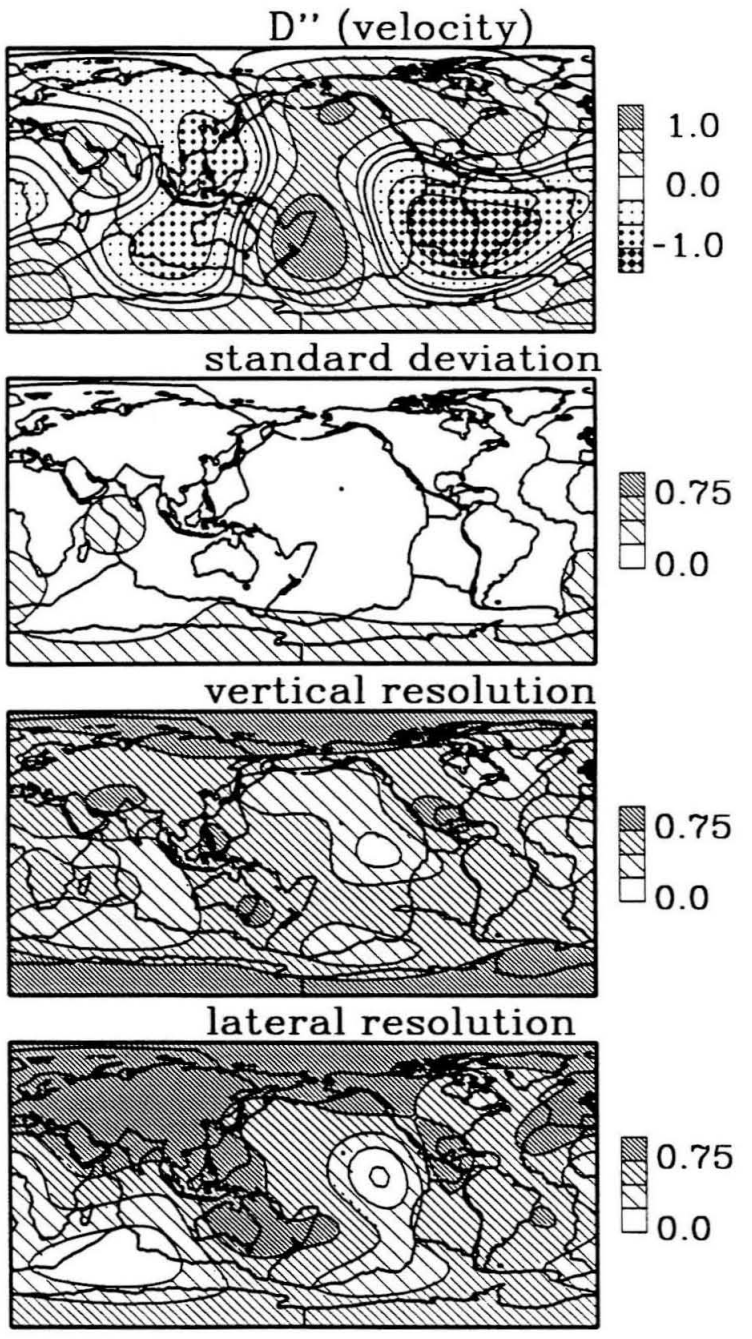

Figure 2.26. Results for D'' velocity variations. Data were not corrected for inner-core anisotropy. All summary rays with at least five composite rays were included.

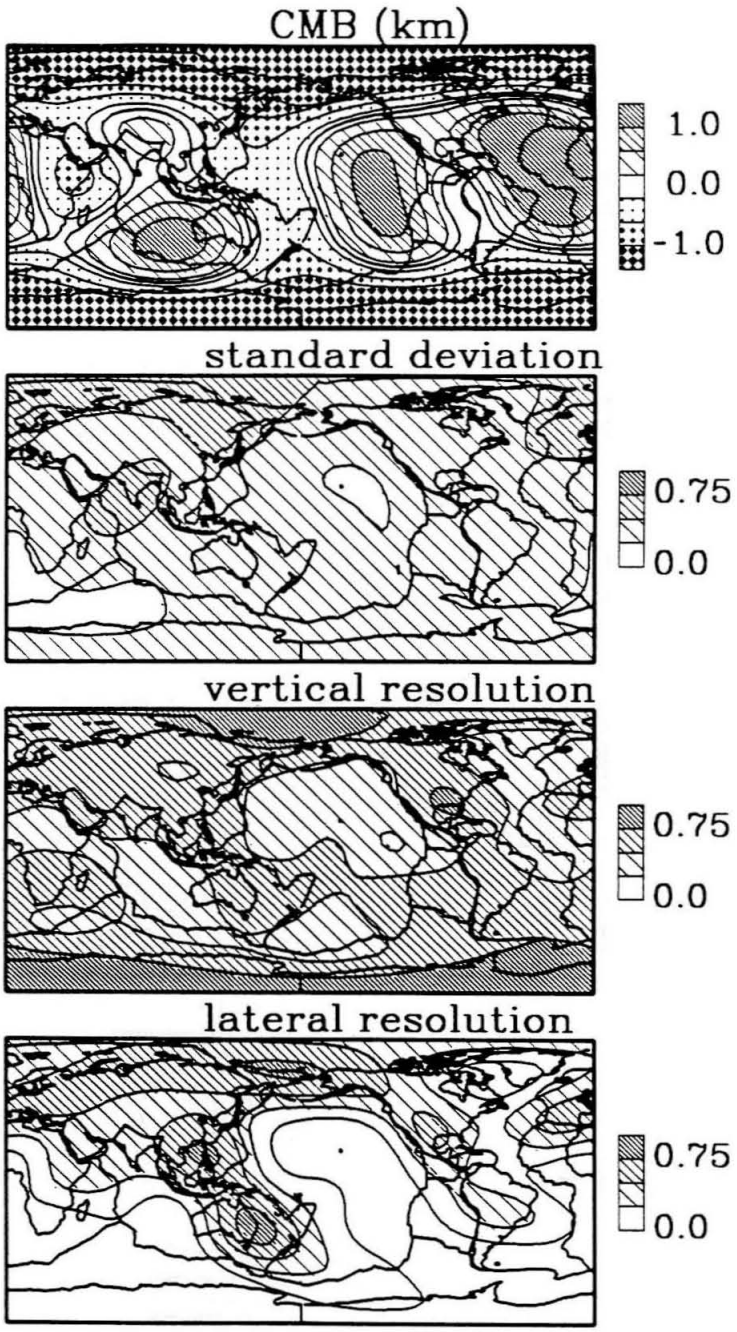

Figure 2.27. Results for CMB topography. Data were not corrected for inner-core anisotropy. All summary rays with at least five composite rays were included.

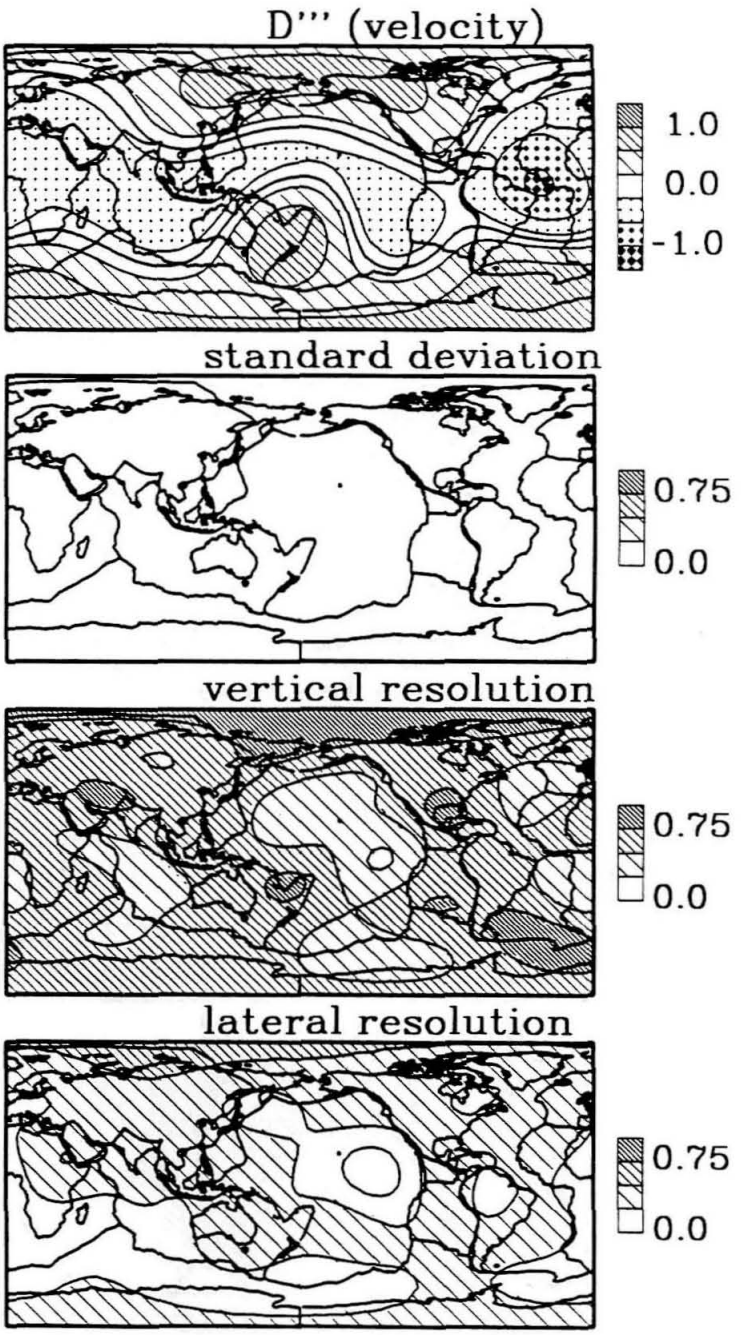

Figure 2.28. Results for D''' velocity variations. Data were not corrected for inner-core anisotropy. All summary rays with at least five composite rays were included.

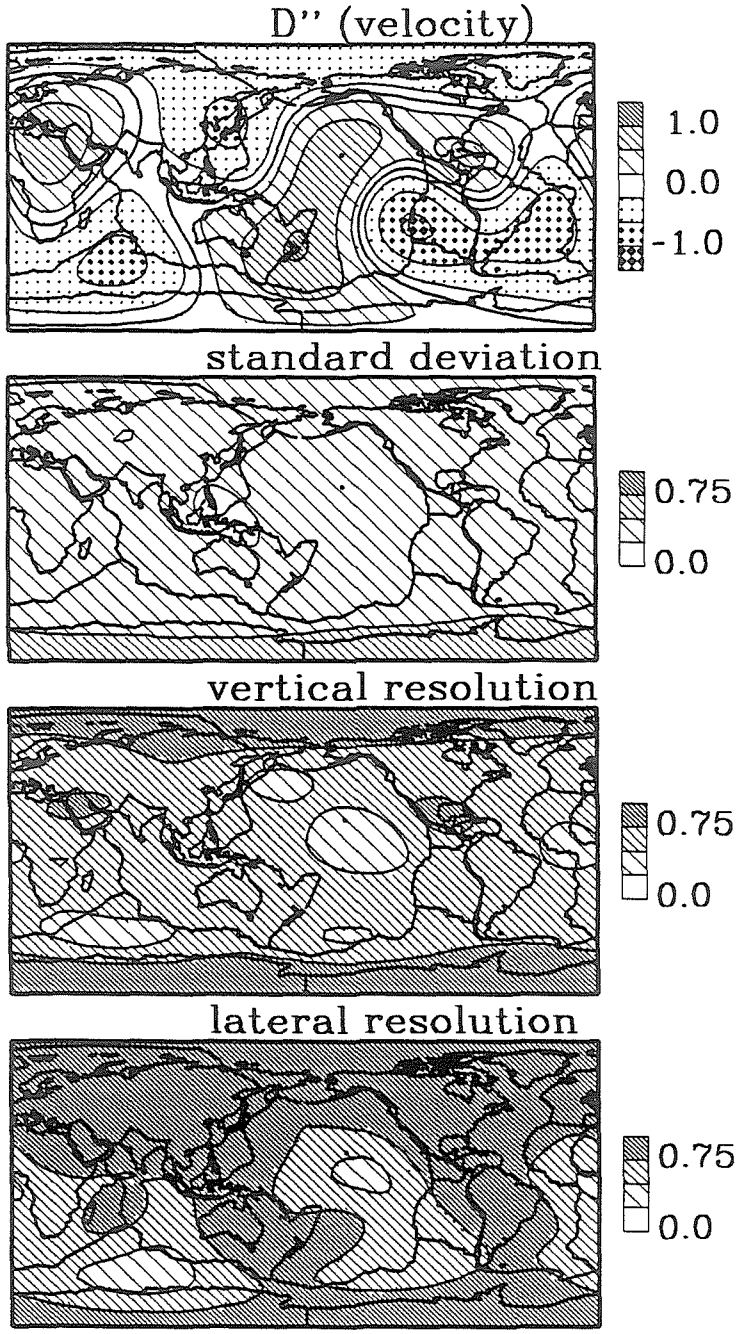

Figure 2.29. Results for D'' velocity variations. Data were corrected for inner-core anisotropy. All summary rays were included.

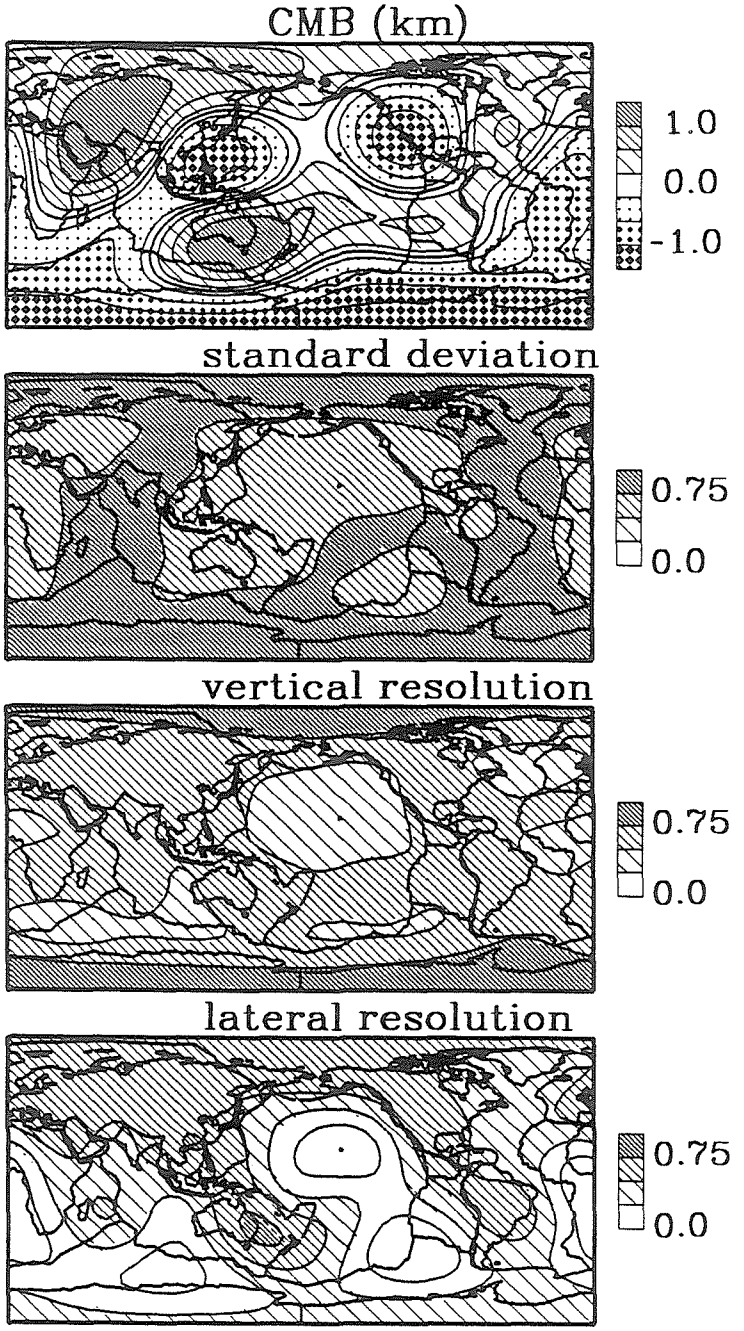

Figure 2.30. Results for CMB topography. Data were corrected for inner-core anisotropy. All summary rays were included.

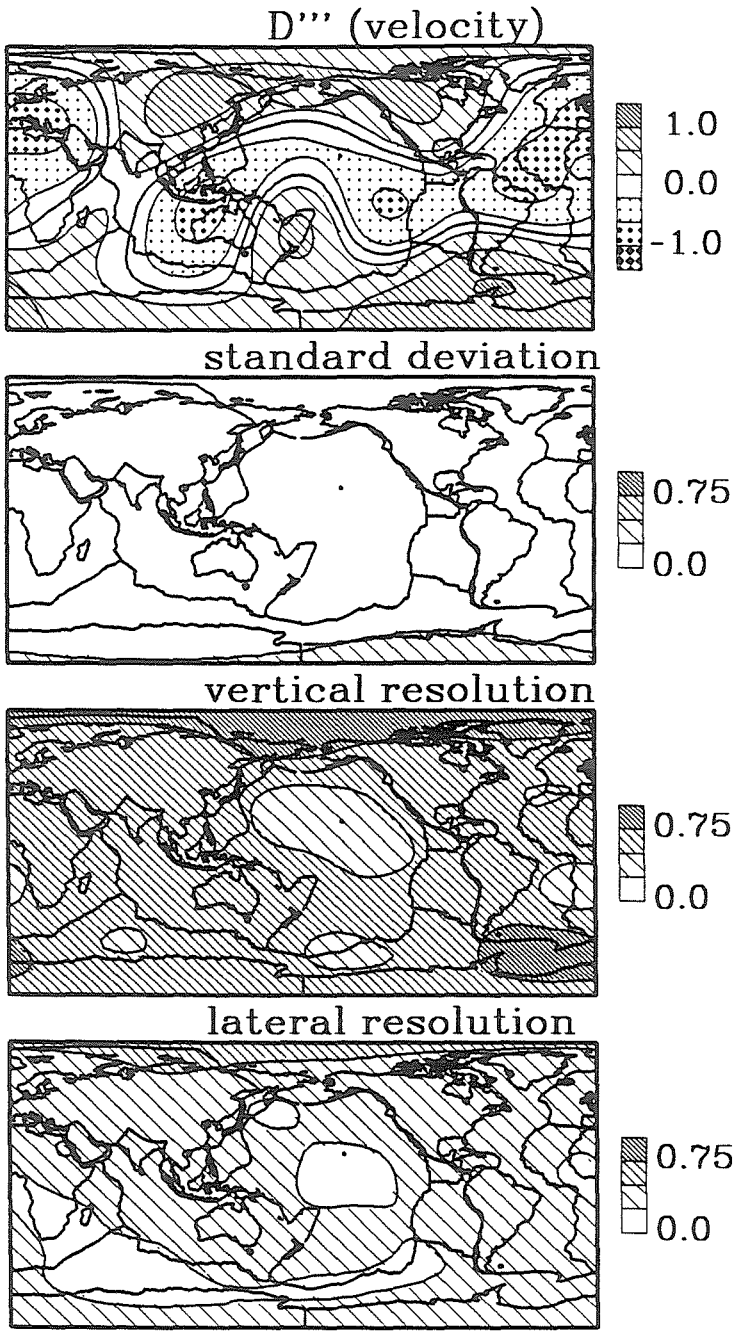

Figure 2.31. Results for D''' velocity variations. Data were corrected for inner-core anisotropy. All summary rays were included.

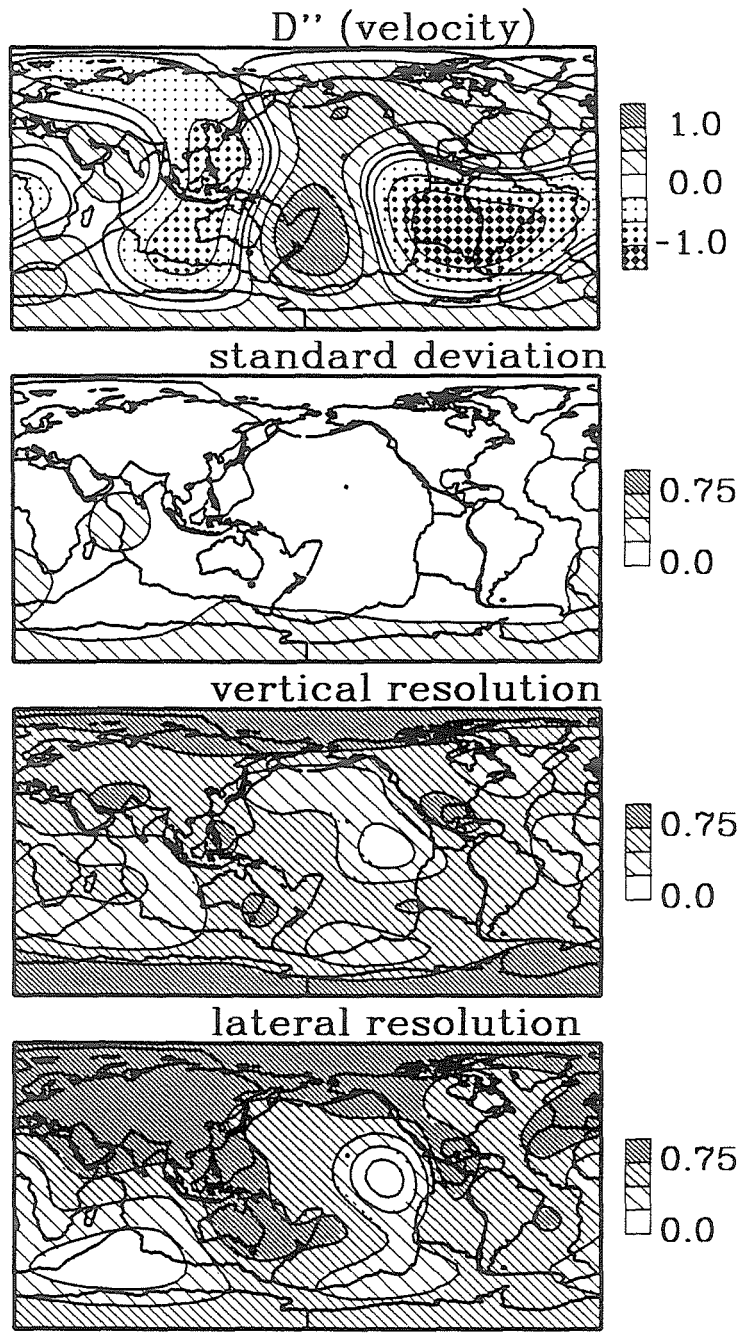

Figure 2.32. Results for D'' velocity variations. Data were corrected for inner-core anisotropy. All summary rays with at least five composite rays were included.

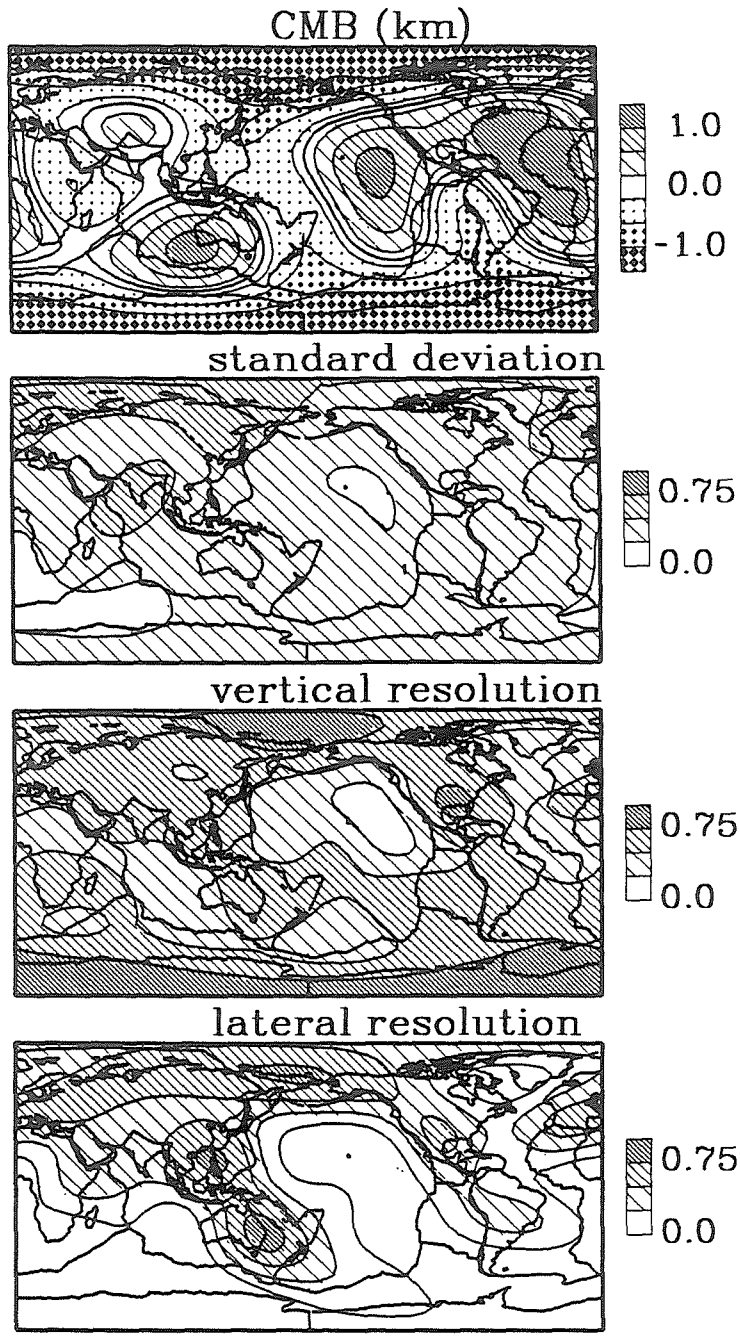

Figure 2.33. Results for CMB topography. Data were corrected for inner-core anisotropy. All summary rays with at least five composite rays were included.

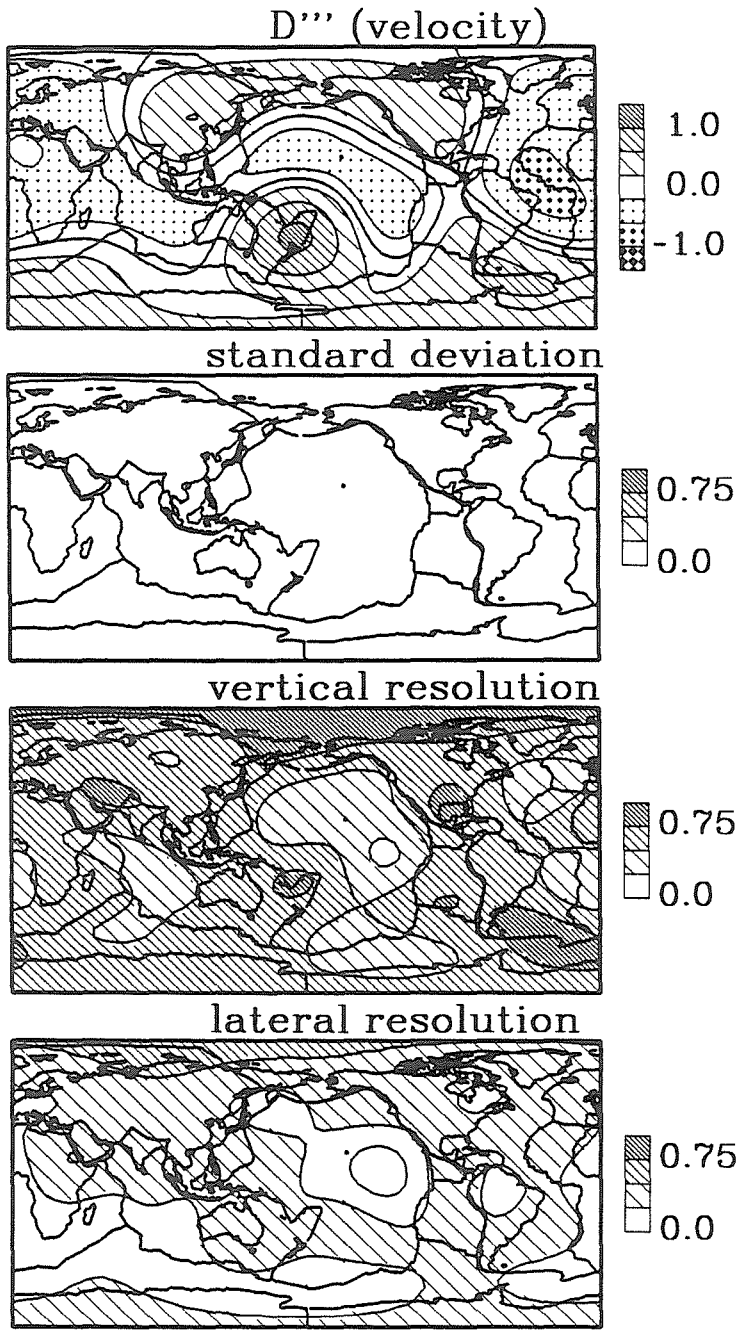

Figure 2.34. Results for D''' velocity variations. Data were corrected for inner-core anisotropy. All summary rays with at least five composite rays were included.

models, the model has a large, fast anomaly under New Zealand and an hourglass-shaped, slow anomaly under the East-Pacific Rice and S. America. The model far exceeds its standard error. Vertical resolution is reasonably good, particularly at the poles, and lateral resolution mimics the pattern of coverage by the data. Figure 2.16 shows the results for CMB topography, when anisotropy corrections have not been applied and all data are included. The peak-to-peak amplitude of this model is about 4 km. The model is dominated by a degree-two zonal pattern ($C_2^0 \approx 3.6\ km$), with saddle points under the Indian and western Pacific Oceans. Vertical resolution behaves much the same as for the D'' layer and lateral resolution mimics coverage density. Figures 2.17 and 2.18 are analogous to 2.15 and 2.16, except for that they are constructed from data with a minimum number of five rays per summary ray. The pattern in D'' is similar, but enhanced in amplitude. The pattern for CMB is also similar, but the New Zealand low is more pronounced. Figures 2.19 through 2.22 are analogous to Figures 2.15 through 2.18, except for that anisotropy corrections have been applied. This has little effect on the models. The models presented in Figures 2.15 - 2.22 yield variance reductions of the order of 5%, when all summary rays are included, and 20 - 25%, when data are required to be based on at least five picks.

CJ suggested that the core side of the CMB may contain regions of anomalous seismic velocities, while constituting only minor density anomalies, and would thus be stable in the low viscosity regime of the outer core. Stevenson (1988) suggested that the mantle and core may interact with each other by underplating of core material under the CMB, infiltration of core material into the mantle, and dissolution of mantle material by the core. This scenario could entail anomalous seismic velocities on the under side of

the CMB. We inverted our data (all data simultaneously) for a three-layer structure at the CMB, including topography on the CMB and velocity variations above and below. The results of that inversion are plotted in Figures 2.23 to 2.34. Variance reductions achieved by these inversions are listed in Tables 2.3 and 2.4. The models for D'' are only slightly altered from the two-layer solutions. On the other hand, the CMB models are changed from the two-layer case, particularly in the case of unselected data. Note that despite a significant increase in the number of degrees of freedom in these solutions from the two-layer case, the variance reduction of the data remains similar. This is particularly clear in the case of selected data, and indicates that the data do not prefer the addition of the D''' layer to the parameterization of the model. The models for the underside of the CMB, D''', have 2.5% peak-to-peak velocity variations, and are slow along the equator. The variance reduction for these models is about 8% (unselected data) and 25% (selected data).

2.5 Discussion and conclusions

Models of CMB topography based on different subsets of ISC core-data are inconsistent. Furthermore, our analysis of PcP, PKPbc, and PKPab data in terms of CMB topography does not agree well with results of previous studies with the same phases (MD and CJ). On the other hand, our analysis of PKPef data does agree well with previous workers. The inconsistencies that we observe between the various models indicate that their sources lie above the CMB, as possibly unaccounted for upper-mantle structure or D'' structure.

The core phases all have small take-off angles at the surface of the earth in their observable epicentral ranges. Their ray paths through the mantle are near radial and particularly PKPdf, but also to a lesser extent PKPbc, have little room to disperse within the mantle. PKPef data in the range from Δ 155^o to 180^o hit the CMB at a distance smaller than 7.5^o from the source or receiver. The range for the hit points of PKPde is 9.0^o to 11^o, for PKPbc 13^o to 21^o. For this reason, contamination from shallow structure in the travel-time residuals of core phases is more likely to map coherently on to the CMB than in the case of mantle P-waves used to map the lower mantle, where rays disperse widely around each source or receiver, and the residual, upper-mantle signal becomes incoherent relative to the model parameterization. The upper mantle is known to be strongly heterogeneous (e.g., Woodhouse and Dziewonski 1984). We present evidence in Chapter 4 of this thesis that implies a large difference in the overall level of heterogeneity between the upper and lower mantle. The simplistic method of station corrections or event/station statics may very well account insufficiently for the large, upper-mantle signal in the data. There is thus clearly a potential for significant contamination from upper-mantle structure in our results, which may account for some of the inconsistencies within them. We present in Chapter 5 of this thesis evidence that the mantle may, in fact, completely mask the structure of the CMB from the eyes of travel times.

The strong structure of the upper mantle and the straight connection of PKP rays of the surface of the earth with the CMB may also explain some of the discrepancies between our results and the results of previous workers with partly equivalent data. MD used shallow events only, while we use events from all source depths. MD used the entire BC branch as defined by PREM

(Dziewonski and Anderson 1981), while we use a much smaller JB BC branch, which remains a first arrival for more of its range. MD used station corrections and relocated events, CJ used station corrections, but did not relocate, while we compute iteratively static corrections for events and stations. These different procedures to filter out the effects of shallow structure may account for differences in results. A number of decisions are made in the processing of the data in regard to how to window out potentially poor data. These decisions are considerably different in the three above studies. That could help explain some of the differences in results.

Models obtained by simultaneous inversion of all the compressional phases in the ISC catalog, that are sensitive to CMB structure, are lower in amplitude (5 km peak-to-peak) than previously published models (CJ and MD) and correlate only marginally with those models. Consistent features of these models (see Figures 2.6, 2.10, 2.12, and 2.13) include topographic highs under western Australia and the Indian Ocean, under the East Pacific Rise, and under the central Atlantic Ocean. Consistent topographic lows lie under southeastern Asia, under N. America, under New Zealand, and under the South pole. Discounting the major topographic low under New Zealand, which might be due to slab contamination, the model becomes similar to the predicted CMB topography of Hager et al. (1985). This would imply direct coupling of mantle flow and CMB topography.

Models consisting of a two-layer structure at the CMB, including D'' velocity anomalies and CMB topography, require 2.5% peak-to-peak variations in the D'' layer and about 4 km topography on the CMB. This model of D'' heterogeneity assumes a thickness of 200 km for the heterogeneous layer. It should be noted that this heterogeneity is relative to a model

containing degrees 1 through 3 of the model of Clayton and Comer (1983). This is roughly equivalent to previous estimates of heterogeneity in D'' (e.g., Dziewonski 1984, Young and Lay 1988). In Chapter 4 of this thesis we present a stochastic estimate of the heterogeneity level in D'' of the order of 0.4% rms. This would be equivalent to about 1.2% peak-to-peak velocity variations. The present level of heterogeneity in D'' is thus a mere factor of two different from our stochastic estimate. The consistent features of these models (see Figures 2.15 through 2.22) include fast D'' anomalies under New Zealand, the South pole, and N. America, and slow D'' anomalies under the East-Pacific Rise, S. America, and the south-central Atlantic Ocean, and under southeastern Asia, the East Indies, and the Indian Ocean. A band of topographic highs align not far from the equator under Australia, under the north-central Atlantic, under the East-Pacific Rise, and under Arabia. The consistent topographic lows are under the poles, under eastern Asia, under N. America, and under New Zealand.

Morelli et al. (1986) and Woodhouse et al. (1986) suggested an anisotropic model for the inner core on the basis of travel times of PKPef-waves and the splitting of some normal modes. The proposed anisotropy is transverse anisotropy, symmetric about the earth's rotation axis. We see the same pattern in antipodal PKIKP data (PKPef). However, we also see hints of a similar pattern in PKPde and PKPbc data, and when inverting all our data simultaneously, we see a C_2^g component in our maps, despite correcting PKPef data for the anisotropic model of Shearer et al. (1988) (see Figures 2.12 and 2.13). We also observe that those of the PKPef data that hold the strongest anisotropic effect (if that is what it is) are from polar paths, which are somewhat lacking in redundancy. We thus conclude that a part of the

anisotropic pattern in the travel-time residuals of PKPef-waves is poorly constrained and that the remaining portion of the pattern may at least in part be explained by a degree-two, zonal anomaly on the CMB.

Multiple layer structures at the CMB help explain inconsistencies between data when modeled in terms of CMB topography only. Such models require 2.5% peak-to-peak velocity variations in D'' and 4 km peak-to-peak undulations on the CMB with a strong degree-two, zonal pattern. A significant component of that pattern persists despite anisotropy corrections of PKIKP data. When allowing for a heterogeneous layer under the CMB it absorbs some of the degree-two zonal. In that case D'' structure remains unchanged, CMB topography is 3 km peak to peak and the underside layer has 2% velocity variations. The velocity anomalies in D'' do not appear to correlate with results from studies reviewed in the introduction to this chapter.

In light of the limited variance reduction, the inconsistencies among subsets of data, and the apparent correlation of at least some common features in the data that may be due to contamination from above, we remain in doubt about the truthfulness of the present models as descriptions of CMB structure.

3 CORE-MANTLE BOUNDARY STRUCTURE OR CORE ANISOTROPY?

3.1 Introduction

Since 1964, the travel-time picks (9 million) of some 3000 world-wide seismic stations have been catalogued in machine-readable form by the International Seismological Centre (ISC). While the majority of these picks (2/3) are of mantle P-waves, a substantial number (1/6) of compressional phases (PKP, PKIKP, PcP, and P-diffracted), that interact with the earth's core, have been recorded. The ISC data are noisy. The variance of random noise is of the order of seconds (see Chapter 4 of this thesis and Morelli and Dziewonski 1987). The structural signal is of the same order as the noise, so much redundancy is needed. We can hope to resolve only the earth's gross structure with these data, and a statistical appraisal is critical.

After concentrating on the mantle for the first half decade of availability of the ISC data (Clayton and Comer 1983 (see also Hager and Clayton 1989) and Dziewonski 1984), our attention has focused on the earth's core. The above studies agree on very large-scale features (degrees 2 and 3) (Hager et al. 1985). However, they differ in one aspect pertinent to the present study. Clayton and Comer's model includes a significant, but small, degree-two, zonal (C_2^0) term, while Dziewonski's model does not.

There have been a number of studies of the core-mantle boundary (CMB) using ISC data. Morelli and Dziewonski (1987) used PcP and PKPbc data to map CMB topography. Separate mappings of the two data sets resulted in fair agreement, indicating the absence of aspherical heterogeneity

at the top of the core. Furthermore, the agreement of their models may be used to argue that the present lower-mantle models are reasonably accurate. Their results do not include a significant C_2^0 term. Creager and Jordan (1986a and b) used PKPdf (actually PKPef) and PKPab. Their maps are dominated by a C_2^0 pattern and correlate at the 0.2 level with the results of Morelli and Dziewonski (1987). Furthermore, there is a large amplitude discrepancy between the two models. In Chapter 2 of this thesis we present yet another study of CMB topography using travel times of core phases from the ISC catalog. Our results do not agree with those of Morelli and Dziewonski (1987), Creager and Jordan (1986b), or internally. The differences in results could be due to structure within the core, structure at the CMB, structure near the earth's surface, or errors.

Poupinet et al. (1983) first reported a spheroidal term in PKIKP data. They found a 2 second differential travel time between fast regions at the poles and slow regions along the equator. They suggested a spheroidal pattern of heterogeneity in the vicinity of the inner-core boundary (ICB) to explain their observation. In a series of papers Morelli et al. (1986) and Woodhouse at al. (1986) explained this feature in the data, as well as some observations of normal mode splitting, by an axially symmetric, transversely anisotropic, inner-core model. Shearer et al. (1988) reanalyzed the travel-time data and got a technically different, but conceptually identical model to that of Morelli et al. (1986).

Ritzwoller et al. (1986) and Giardini et al. (1987) studied the splitting of normal modes sensitive to the structure of the core. Ritzwoller et al. (1986) explained their data by a 0.3% C_2^0 density anomaly in the outer core, and a 0.5% density anomaly at the base of the mantle. Giardini et al. (1987)

required strong zonal undulations at the inner- and outer-core boundaries as well as 5% heterogeneity in the inner core. They suggested anisotropy in the inner core as an alternative explanation.

In summary, a number of anomalously split normal modes (Masters and Gilbert 1981, Ritzwoller et al. 1986, Giardini et al. 1987) and the differential travel time between polar and equatorial paths in PKIKP (Poupinet et al. 1983) and PKPab (Creager and Jordan 1986a) require significant aspherical structure at or below the CMB. Much of these data could be explained by excess ellipticity of the CMB. Inner-core anisotropy is certainly another candidate explanation as well as heterogeneity within the core. Heterogeneity in the fluid outer core will, however, be difficult to justify in light of the arguments of Stevenson (1987), as velocity anomalies are likely to be associated with density anomalies. The heterogeneity in the inner core or at the inner-core boundary, that is required to explain the anomalous travel times of PKPef, is likely too large to be acceptable (Morelli et al. 1986).

We have conducted a search for a similar effect in the travel times of PKPbc to that found in PKIKP and PKPab data. While the results of Chapter 2 might reveal excess heterogeneity at the CMB (and there are hints of it there), they are hampered by inconsistency and errors. The philosophy that we employ here is to stack the data as densely as possible in order to still resolve the parameters of interest to us. It is not clear what the optimal way to extract information from the noisy ISC data might be. Dense stacking, where account is taken for the uneven geographical distribution of data, may reveal simple features in Earth structure that are obscured by the uncertainty and artifacts of complex inversion schemes.

3.2 Method and results

A simple way to search for a C_2^0 pattern in the travel times of any phase is to restrict oneself to longitudinal rays and to map the travel-time residual of each datum onto its turning point. We have isolated 6 data sets from ISC data from 1964 to 1982. These are 2 epicentral ranges of PKIKP (PKPef and PKPde) and PKPbc, PKPab, PcP, and P-diffracted. The data have been corrected for hydrostatic ellipticity (Dziewonski and Gilbert 1975) and station and event statics calculated from mantle P-waves (25^o –95^o). Data from events or stations with less than 50 picks were omitted. The data are referenced to the JB tables, but corrected for baseline shifts and linear trends in the average residual as a function of epicentral distance. Details of the selection, windowing, and processing of the data were the same as described in Chapter 2.2, except for that a mantle correction was not applied.

We compute summary rays on a 5x5^o equal area grid over the globe. The average residual is taken as the summary-ray datum. We then select all data with azimuth less than 15^o from north or south. Each datum is then projected onto its turning point and the data binned in terms of the latitude and longitude of their turning points. For each latitude bin we group the data within ten longitude windows, compute the average residual within each bin, and then average the estimates for the longitude bins. The northern and southern hemispheres are stacked. We have thus applied the summary-ray concept twice, at the earth's surface and at the turning point of rays. In this geometry the latitude of the turning point of rays is approximately the same as the angle between the ray itself and the rotation axis of the earth. Thus, if axially symmetric transverse anisotropy exists in the earth's core, it should be detected by this process. In fact, this stacking procedure is sensitive to all

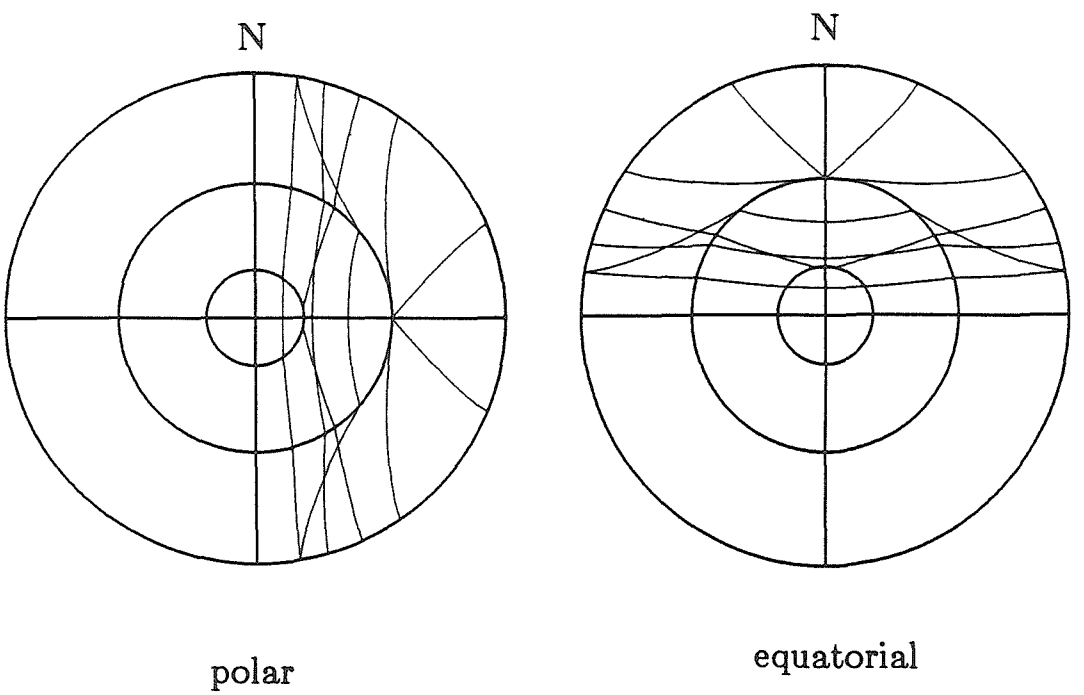

Figure 3.1. The ray geometry of the stacking experiment as described in the text. The rays are contained in great circle planes that are normal to the equator. Polar paths bottom parallel to the rotation axis of the earth, while equatorial paths turn parallel to the plane of the equator.

even-order, zonal harmonics. Figure 3.1 demonstrates the geometry of our stacking procedure.

Our results are presented in Figures 3.2 through 3.4. Figure 3.2 shows the results for PKPef (PKIKP1) and PKPde (PKIKP2) waves, which enter the inner core. The upper frames show the variation of the average stacked travel-time residual with the ray angle to the rotation axis. The lower frames show the number of summary rays contributing to each estimate. The total number of summary-ray data is indicated. The square on the side margin of the upper frames represents an average of summary-ray data, which are within 15^o from traveling in the plane of the equator. These results confirm the findings of Poupinet et al. (1983). A clear and simple trend is evident between polar (left) and equatorial (right) paths for near antipodal (PKPef) data. Polar paths are about 2 seconds faster than equatorial paths. Note, however, the large error bars at low angles and the low numbers of data. The PKPde (PKIKP1) data set is a much bigger one and yields better constrained estimates, and also a much smaller trend. The differential travel-time between polar and equatorial paths is about 0.5 second here. Figure 3.3 shows analogous results for the outer core phases. The PKPab data set exhibits a strong trend of the same sense as PKPef and PKPde data, but over a limited range of angles. This is a very small data set and uncertainties are large. The PKPbc data set is fairly large and renders reasonably stable averages. Here there is an apparent differential travel time between polar and equatorial paths of the order of 0.5 or 1.0 second. This observation is in contradiction with Shearer et al. (1988), who find no anisotropic effect in PKPbc data. They did not apply summary rays and their results are thus more susceptible to contamination from shallow

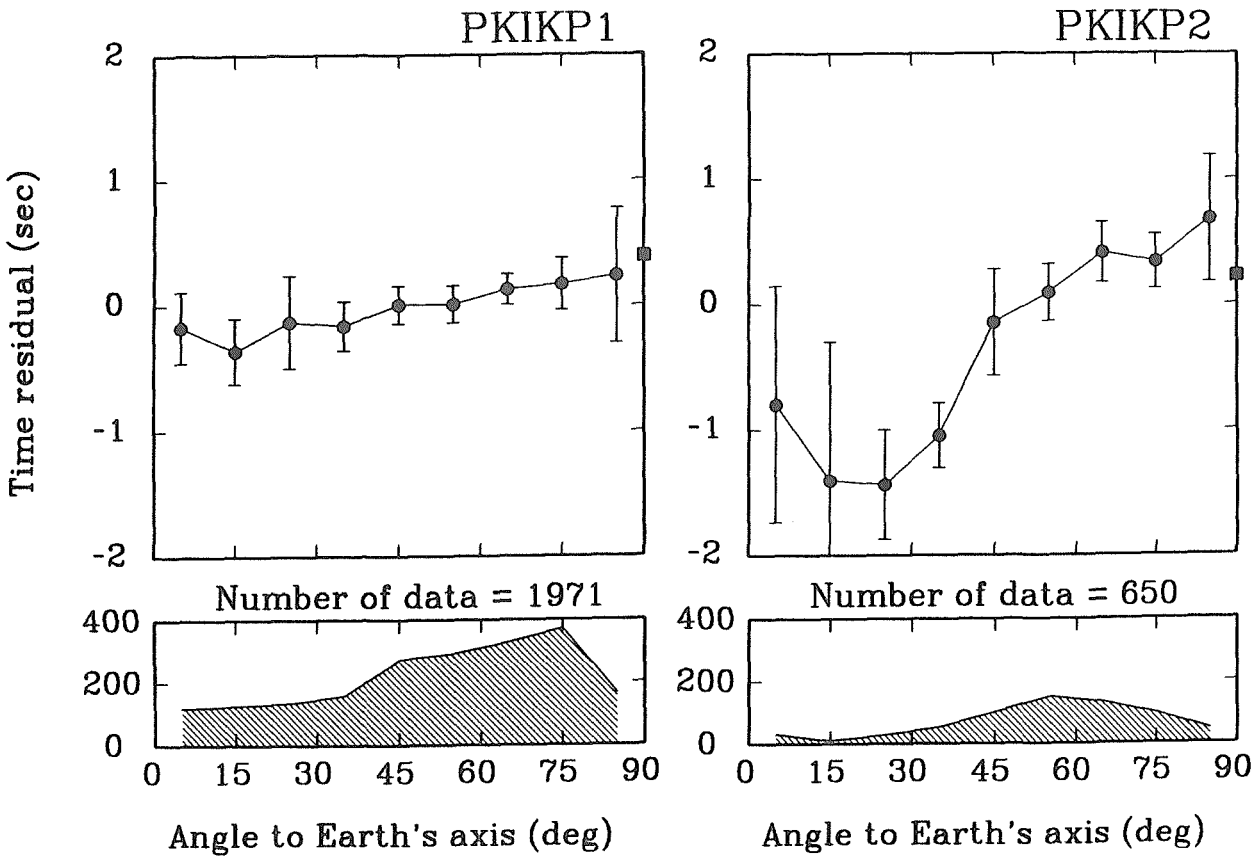

Figure 3.2. Results of the stacking procedure described in text for the inner-core phases, PKIKP (PKPdf). The error bars are two standard deviations, computed from the scatter. The lower frames show histograms of the numbers of summary rays contributing to each datum. (PKIKP1 = PKPde, PKIKP2 = PKPef).

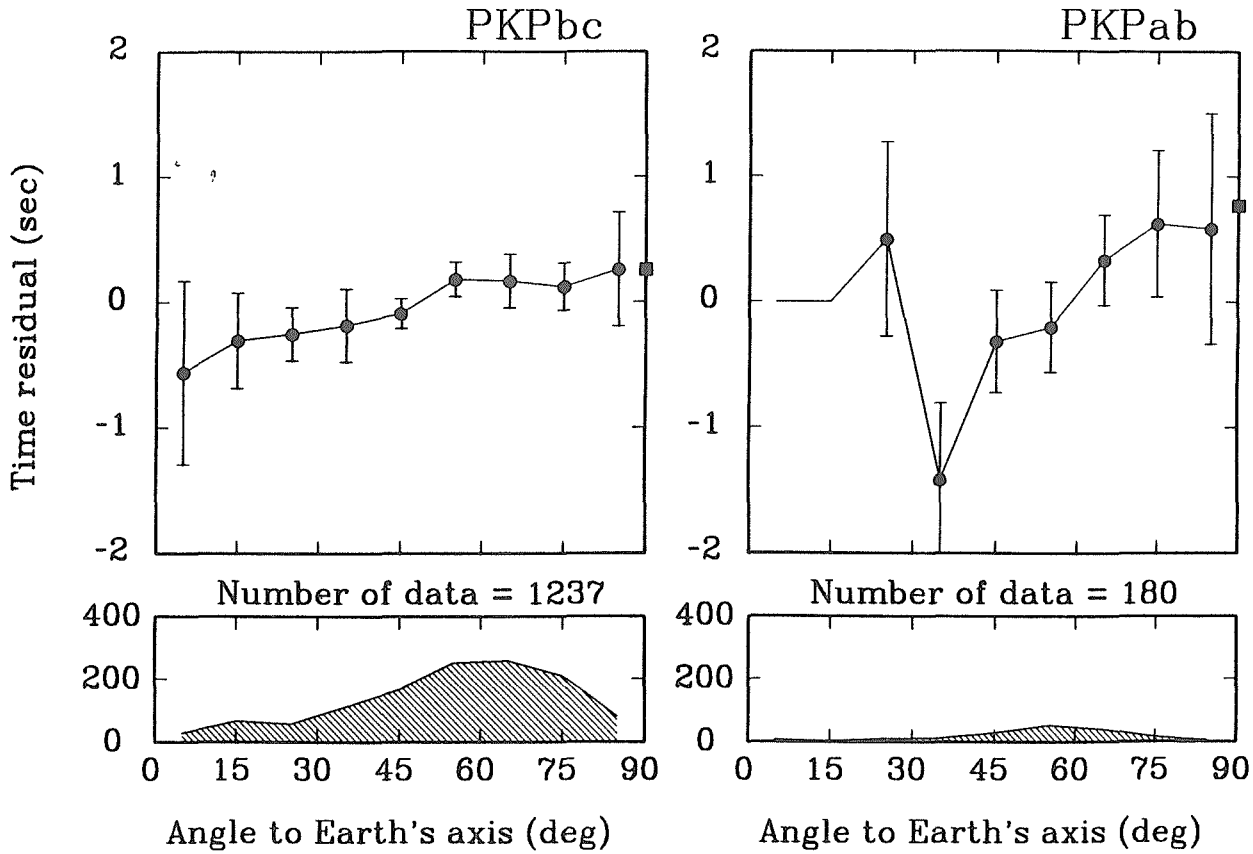

Figure 3.3. Results of the stacking procedure described in text for the outer-core phases, PKPab and PKPbc. The error bars are two standard deviations, computed from the scatter. The lower frames show histograms of the numbers of summary rays contributing to each datum (above).

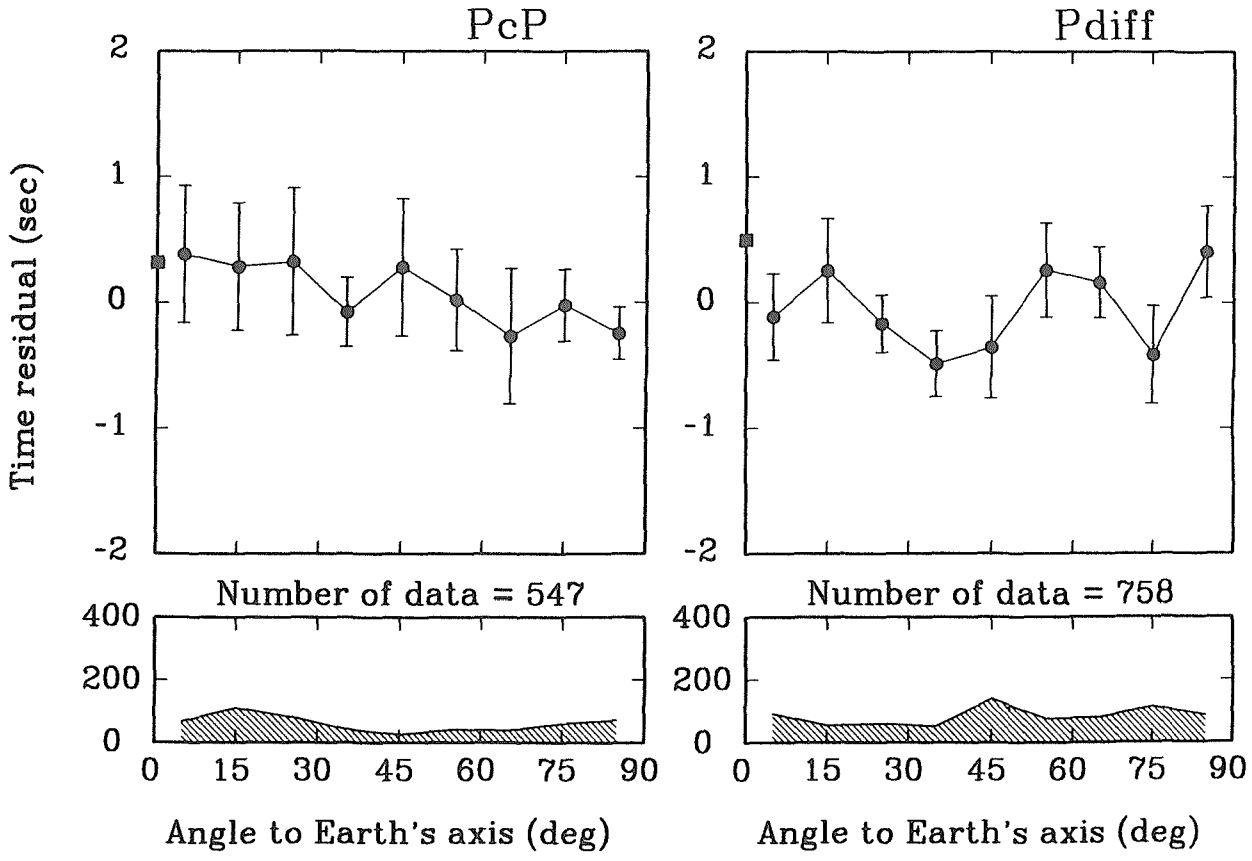

Figure 3.4. Results of the stacking procedure described in text for the mantle phases, PcP and Pdiff. The error bars are two standard deviations, computed from the scatter. The lower frames show histograms of the numbers of summary rays contributing to each datum (above).

heterogeneity. Figure 3.4 shows the results from PcP and P-diffracted data. Both sets are of intermediate size in terms of numbers of summary rays. The PcP data do, however, have relatively little redundancy within their summary rays. The behavior of P-diffracted is irregular, while PcP displays a weak, but poorly constrained trend (we could fit 0.0 through all of the error bars), with polar paths slower than equatorial paths. Note, however, that what we term polar PcP paths are rays that reflect off the CMB at the equator.

Subject to a stacking procedure that is designed to even the weight of geographical regions at the endpoints and turning points of rays, we observe an anisotropic pattern in the travel times of compressional core phases. Polar paths are fast relative to ray paths, either in the plane of the equator or turning parallel to it. The effect is strongest for near antipodal PKIKP and generally weakens as bottoming depth decreases. The exception to this is the PKPab data set, which yields the largest anomaly. As discussed earlier this estimate is poorly constrained and will be ignored later.

3.3 Modeling and discussion

To explain the patterns presented in Figures 3.2 through 3.4, we constructed a number of very simple models of heterogeneity at the CMB and anisotropy in the core. The parameters of the models were then adjusted in order to fit the data in Figures 3.2 - 3.4. The models we consider are the following:

1) CMB topography with a linear transition between polar and equatorial positions,

2) D'' velocity variations with a linear transition between polar and equatorial positions,

3) A combination of 1) and 2),

4) Axially symmetric transverse anisotropy in the core with $\cos(2\theta)$ transition between polar and equatorial directions, where θ is the angle a ray makes with the earth's rotation axis.

We allow for only two layers in model 4), i.e., the inner core and the bottom third of the outer core, or the inner core and the whole of the outer core, and assume a constant model within each layer. The inner-core anisotropic models of Morelli et al. (1986) and Shearer et al. (1988) do contain a $\cos(4\theta)$ component. There is a hint of $\cos(4\theta)$ behavior in the data in Figures 3.2 and 3.3, but it is hardly resolved given the error bars.

We can only assume that if core anisotropy is the cause of the above signal in the PKPef data set, it is also the cause of the similar, albeit weaker, signal in the PKPde and PKPbc data sets. That would require anisotropy in the outer core. Assuming the parameterization for core anisotropy described above, that would entail 0.5% anisotropy in the inner core and about 0.25% anisotropy in the lower third of the outer core, or equivalently 0.1% anisotropy throughout the outer core. The fit to the data by this model is presented in Figures 3.6 and 3.7. The PKPbc and PKPde data are well fit, but this model explains only a little over half the total effect in PKPef data. We could make the anisotropy stronger in the inner core and thus explain more of the PKPef signal by including a constant shift term. However, we point out that the data that we do not fit are relatively poorly constrained. The models that we have constructed for CMB structure are presented in Figure 3.5, in terms of the equivalent travel-time anomaly for antipodal

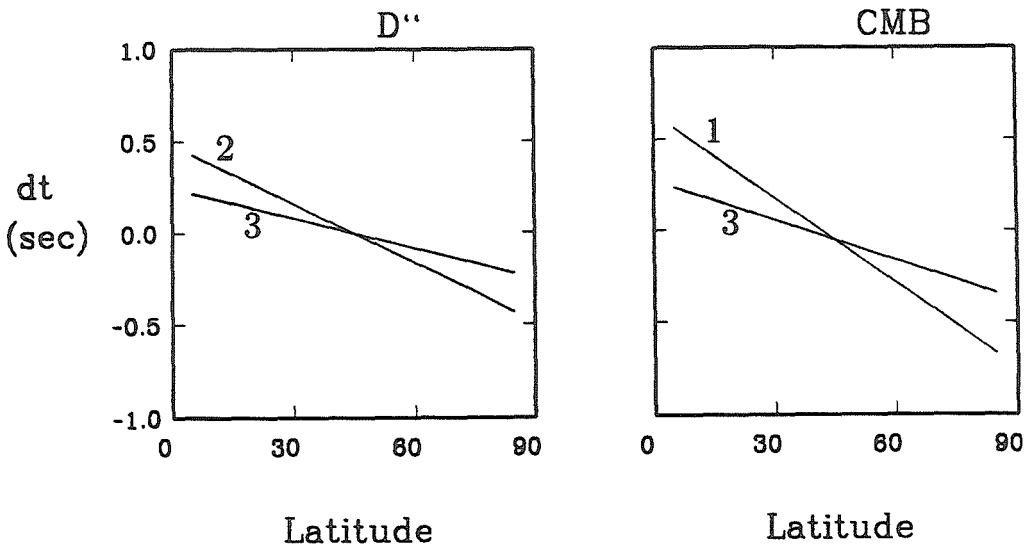

1) CMB topography only.
2) D" heterogeneity only.
3) 1 and 2 combined.
4) Anisotropy;
   inner core $> 0.5\%$;
   outer core $= 0.25\%$.

Figure 3.5. Models of structure in the CMB region obtained by forward modeling to explain the data in Figures 3.2, 3.3, and 3.4. The models are presented in terms of the equivalent travel-time anomaly of antipodal PKIKP-waves (multiply CMB models by 10.0 km/s to get topography, multiply D'' by 3.4%/s to get percent velocity variation, or by 0.5 km/s^2 to get absolute velocity anomaly (assuming a thickness of 200 km)). Model 1 considers CMB structure only, model 2 D'' structure only, and model 3 both. The fourth model considered is that of an anisotropic core, which has no effect on D'' or the CMB.

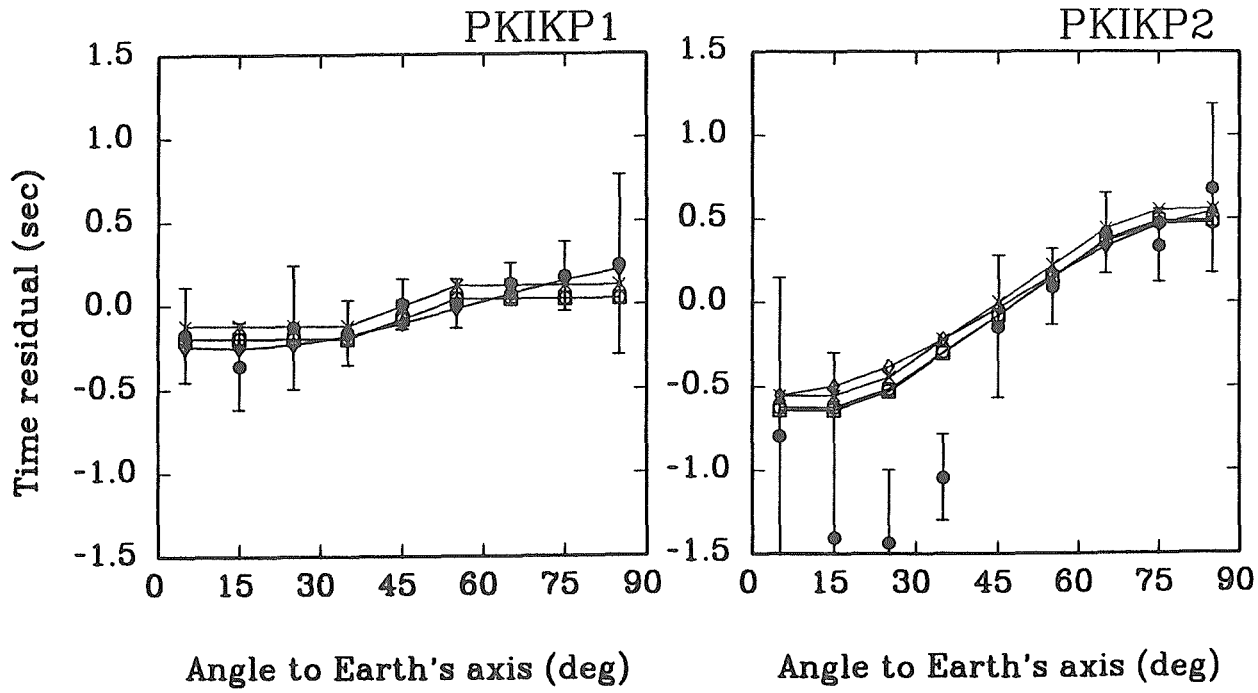

Figure 3.6. Fits to PKIKP data by the models presented in Figure 3.5. Solid circles represent the data (with two standard-deviations error-bars), boxes model 1 (CMB structure), exes model 2 (D'' structure), open circles model 3 (CMB and D'' structure), and diamonds model 4 (anisotropic core).

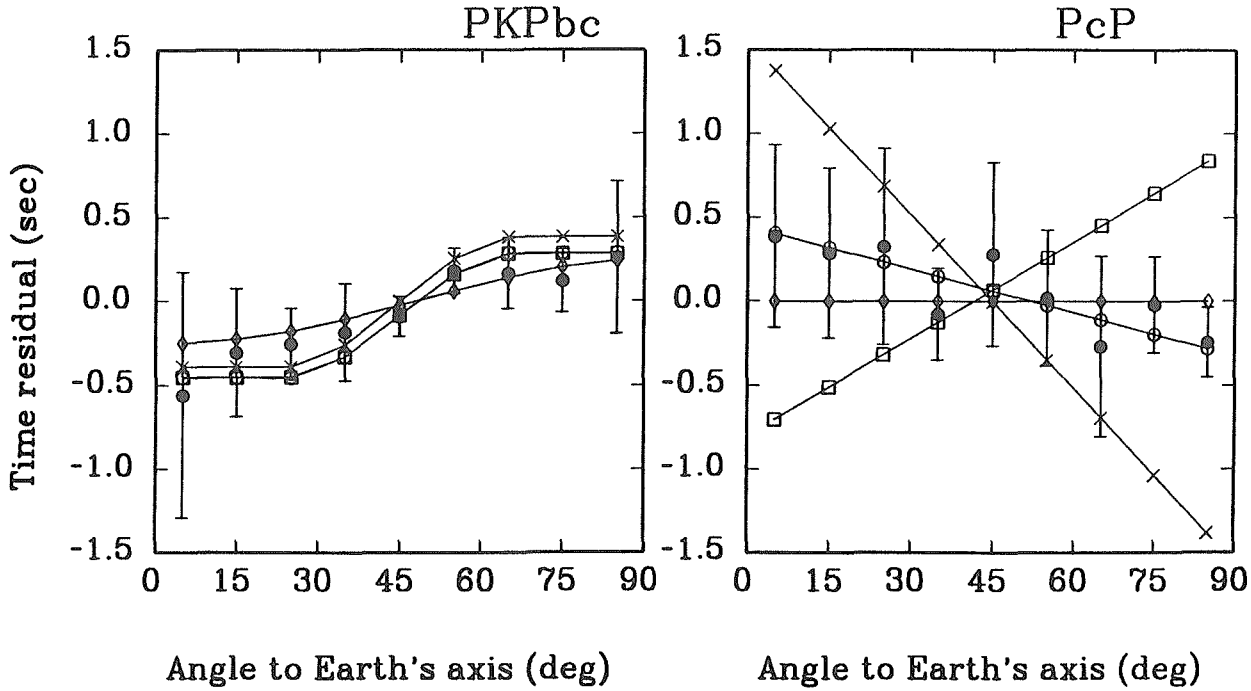

Figure 3.7. Fits to PKPbc- and PcP-data by the models presented in Figure 3.5. Solid circles represent the data (with two standard-deviations errorbars), boxes model 1 (CMB structure), exes model 2 (D'' structure), open circles model 3 (CMB and D'' structure), and diamonds model 4 (anisotropic core).

PKIKP, and the resulting fits in Figures 3.6 and 3.7. Model 1) of CMB topography has more than 1 second differential travel-time through the CMB. This model corresponds to about 12 km peak-to-peak topography, with a bulge on the equator and a low at the poles. It explains the PKPde and PKPbc data nicely and about as well as the above anisotropic model, but only about half the variation in PKPef. It does not explain the PcP data or PKPab and P-diffracted. Similarly, model 2) of D'' velocity variations has about 1 second differential, vertical travel-time through the CMB. This model corresponds to a differential, relative velocity-anomaly of about 3.5% (assuming a thickness of 200 km), with the equatorial region being slow, while the polar region is fast. This model fits the data very similarly to model 1). Model three has about 1.7% velocity variation in the D'' layer and a 5 km peak-to-peak topography. This model explains the PKP phases about as well as models 1) and 2), but now the trend in PcP is also explained. This is because the two effects of heterogeneity in D'' and CMB topography collaborate to affect PKP, but compete to affect PcP.

Admittedly the above PcP observation is weak. Furthermore, model 3) does not explain the PKPab and P-diffracted data and explains PKPef data only in part. The stacking procedure employed in this study is not specifically geared towards observing CMB structure, and the predicted PKPde and PKPbc data from models 1), 2), and 3) are much reduced from PKPef, because the stacking procedure for the PKPde and PKPbc phases is relatively insensitive to CMB structure. However, we refer to the models presented in Chapter 2 of this thesis, which entail a 4 km peak-to-peak CMB topography with a strong C_2^0 component and 2.5% velocity variations in D''. We also point out that the anisotropic pattern in PKPef data is

explainable in terms of CMB structure, less the poorly constrained polar paths.

If anisotropy is used as the sole explanation of the travel-time variations, then both the inner core and the outer core must be anisotropic. While 0.1% anisotropy in the outer core (0.25% if confined to the bottom third) cannot be ruled out, it certainly stretches the imagination to conceive of a mechanism. If outer-core anisotropy is rejected as a possibility, then some degree of heterogeneity near the CMB appears to be necessary. A model based on CMB topography alone explains most of the data. The violated data are PKPab, which are weak observations. A model that includes D'' heterogeneity also explains the (poor) PcP data. This model reduces the required CMB topography, which is in accord with length of day studies (Speith et al. 1986, Hide et al. 1989).

4 STOCHASTIC ANALYSIS OF GLOBAL, TRAVEL-TIME DATA

4.1 Introduction

Great advances have been made in recent years in the mapping of the aspherical structure of the earth's interior. One field that has contributed is global, travel-time tomography, invigorated by advances in inversion techniques, improved computing facilities, and improved data. This field has, however, raised considerable controversy; various model results agree only marginally if at all, and are met with some scepticism.

Most global, travel-time, tomography studies have utilized data from the International Seismological Centre (ISC) Catalogue, which contains over twenty years of worldwide, travel-time readings, more than nine million picks. Clayton and Comer (1983) (see also Hager and Clayton 1989) and Dziewonski (1984) used fifteen years of ISC P-wave data to map the lower mantle. Creager and Jordan (1986b) and Morelli and Dziewonski (1987) used compressional core-phases to map the core-mantle boundary. Morelli et al. (1986) and Shearer et al. (1988) used PKIKP-waves to map anisotropy in the inner core. These studies, together with surface-wave tomography, free-oscillation studies and long-period, body-wave synthesis provide important constraints on the style and scale of mantle convection, on the workings of the geodynamo, and on the evolution of the earth.

The concerns about results of global, body-wave tomography stem primarily from concerns about the ISC data. While serving well to map the overall seismicity of the earth, the uncertainty of measurement in the ISC data is high compared with the signal attributable to aspherical structure.

The data are contaminated by systematic errors that are due to misidentification of phases, earthquake mislocation, earthquake time-function complexity, and potentially biased picking. The geometrical coverage of the data is uneven, because of the clustering of seismic sources in tectonically active regions and the lack of recording stations in the oceans. The images may suffer from complex artifacts, which depend on the particular technique employed, because of the uneven coverage. The strong velocity variations in the crust and upper mantle are simplistically accounted for by station corrections. The severity of these problems is currently poorly understood.

In order to assess the quality of images obtained from the ISC data, it is important to have robust estimates of the level of random errors in the data. Random errors can be propagated through inversion schemes to estimate their effect (Davies and Clayton 1987). This, however, gives only a lower bound on the model uncertainty, as systematic errors and model-parameterization errors are ignored. It is not clear to what extent model amplitude exceeds random model-error in some of the previous studies. This will vary spatially within each model.

Systematic errors are perhaps the most serious limitation of the ISC data. The effect of phase mispicks can be dealt with by windowing out cross-overs in the travel-time curves. Gross errors are typically handled by excluding residuals exceeding a given value (4 - 5 seconds for compressional phases), thought to represent the maximum feasible structural signal. Beyond that, we are forced to assume that single station, single event, or regionally systematic errors get randomly mixed within the model. This assumption is better justified in a stochastic, spherically symmetric model than in a deterministic laterally varying model.

Because of the size of global, multidimensional, inverse problems and the level of redundancy needed to suppress random scatter in the ISC data, models have been parameterized as truncated expansions in terms of continuous, orthonormal functions (Dziewonski 1984, Morelli and Dziewonski 1987, and Morelli et al. 1986 used spherical harmonics and Legendre polynomials in depth) or in terms of discrete cells of fixed size (Clayton and Comer 1983, Humphreys et al. 1984, Zhou and Clayton 1989). This could give rise to significant truncation effects or aliasing of small-scale signal, and is particularly worrisome, since the variance reduction of previous studies has invariably been very low (5% - 15%). It is not clear if summary rays effectively filter out signal contributions from scales smaller than their lateral extent, because of the clustered geometry of both seismic sources and stations. It is not clear either that the remaining small-scale signal gets randomly mapped into the model. To understand this effect, we need to know the power spectrum of the structure beyond the truncation wavenumber or harmonic degree. Creager and Jordan (1986b) applied summary rays on a large scale (20^o x20^o) and thus obtained a much higher variance reduction than other studies. They employed an intrinsic, exponential, spatial filter in their stochastic-inverse scheme to suppress the aliasing problem.

It is well known from a variety of studies, ranging from array-scattering studies to surface-wave, tomography studies, that the earth's crust and upper mantle contain lateral velocity variations in excess of 5% on length scales ranging from tens to thousands of kilometers. This exceeds the level of heterogeneity in models of the earth's deep interior by an order of magnitude. Because of lack of resolution, teleseismic travel-time studies account for this region by applying static station (and event) corrections or by using

differential travel times (Creager and Jordan 1987). Since small-scale velocity variations may extend to considerable depths (e.g., Aki 1973, Flatte and Wu 1988), where the separation of teleseismic rays to the same station may exceed the correlation length of the medium, shallow small-scale signal is potentially mapped into models of the earth's deep interior. Again, a stochastic model describing the characteristic power spectrum of velocity variations provides sufficient information to study this effect synthetically.

We address some of these problems in this chapter through a statistical approach to the interpretation of the data. We have formulated the analysis of global, travel-time data in terms of the stochastic properties of the earth's heterogeneity pattern and random errors in the data. The formalism relates the coherency of travel-time residuals within bundles of rays (summary rays) of varying size to the spherical, harmonic, power spectrum of the slowness field of the medium. The measure of coherency is the variance within summary rays. It is estimated within bins in source depth, epicentral distance, and the scale size of the area that defines a summary ray. The variation of the variance with scale length contains information about the autocorrelation function or power spectrum of slowness perturbations within the earth. The variation with epicentral distance reflects the depth variation of the spectrum. The variance at infinitesimal scale length represents the incoherent component of the data (random errors). This stochastic approach allows for the separation of random variance (incoherent) from signal variance (coherent). It includes the entire volume through which the data pass, and it seeks to explain all the variance in the data. One can argue that spatially systematic errors in the ISC data are less likely to have a significant effect in this stochastic approach than in deterministic inversions, because global

averaging is applied. Nevertheless, the interpretation of incoherent variance as strictly random and coherent variance as being due to structure is an assumption. We do not address the problem of systematic errors in this study.

In our view, a stochastic model of the earth's aspherical structure may yield more robust, but less specific, conclusions than previous deterministic models. The loss of specificity inherent in the stochastic approach does, however, not lessen the usefulness of its conclusions as the modeling of mantle dynamics is still largely limited to idealized style or scale simulations.

4.2 Data processing

In order to estimate summary-ray variance as a function of epicentral distance, Δ, source depth, Z, and scale length, Θ, we construct equal area grids covering the earth's surface. The grids range in density from one cell, covering the entire surface of the globe, to one million cells. Eighteen different densities are used. The grids' cells are rectangular in latitude-longitude coordinates (see Figure 4.1). The grids possess a symmetry about the equator and the Greenwich longitudinal great circle. We use ellipticity-corrected (Dziewonski and Gilbert 1975) ISC residuals from events with at least fifty picks reported. We omit events located at the surface or at a source depth of 33 km, because the ISC assigns poorly located events to these depths. Travel-time residuals larger than 4 seconds in absolute value are omitted. The data are binned in 2^o windows of epicentral distance, ranging from 0 to 100^o and six windows of source depth; 0 to 30 km, 30 to 60 km, 60 to 100 km, 100 to 200 km, 200 to 450 km, and 450 to 650 km.

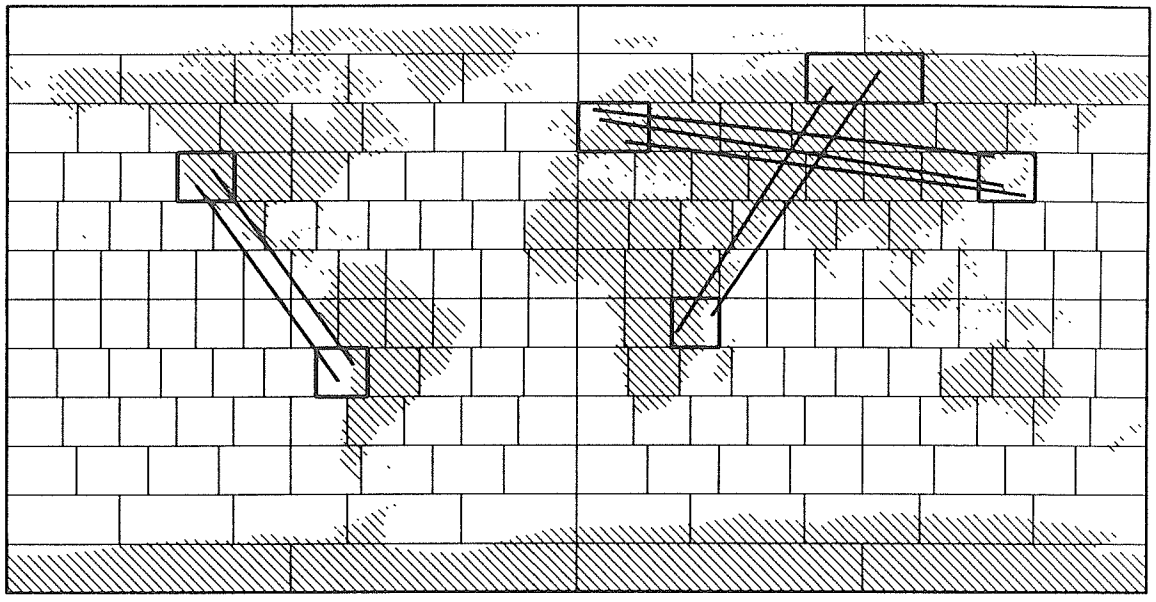

Figure 4.1. An example of the grids that we used to construct summary rays, and three schematic, sample summary rays. This grid has 192 cells or an angular measure of Θ=8.3^o. The three sample summary rays are of similar length and could contribute to the same Δ–Z–Θ bin.

A summary ray is defined as the collection of all the data that fall inside a given epicentral-distance window and a given source-depth window, and share both a source grid-cell and a receiver grid-cell (see Figure 4.1). The scale length is defined in terms of the scale angle, Θ:

$$\Theta = \cos^{-1}\left(1 - \frac{2}{N}\right),$$

where N is the total number of cells in the grid. If we consider a circular area centered on the north pole of a sphere and measure its size by the colatitude of its margin, Θ, its area is given by $2\pi(1-\cos\Theta)$. The grid cells in a grid with N cells are of area $4\pi/N$. Equating the two we get the above definition of the scale angle. The variance within the k-th summary ray is calculated as the variance of its residuals referenced to their mean.

$$\sigma_k^2 = \sum_{i=1}^{n_k} (\delta t_i - \overline{\delta t}_k)^2/(n_k - 1),$$

where n_k is the number of data in the k-th summary ray, δt_i are the individual time residuals and $\overline{\delta t}_k$ is the mean residual for the summary ray. A summary ray is included only if $n_k \geq 4$. The variance estimate for each scale, distance, and depth combination is taken to be the average of the variances of all the summary rays found for that combination. Finally, each grid is rotated four times in equal increments that span the width of the grid cells, and the variance estimates averaged. This is done to minimize the effects of spatially irregular ray populations. At the small scale end of the spectrum, $\Theta < 5^o$, estimates of variance based on fewer than 25 summary rays are omitted.

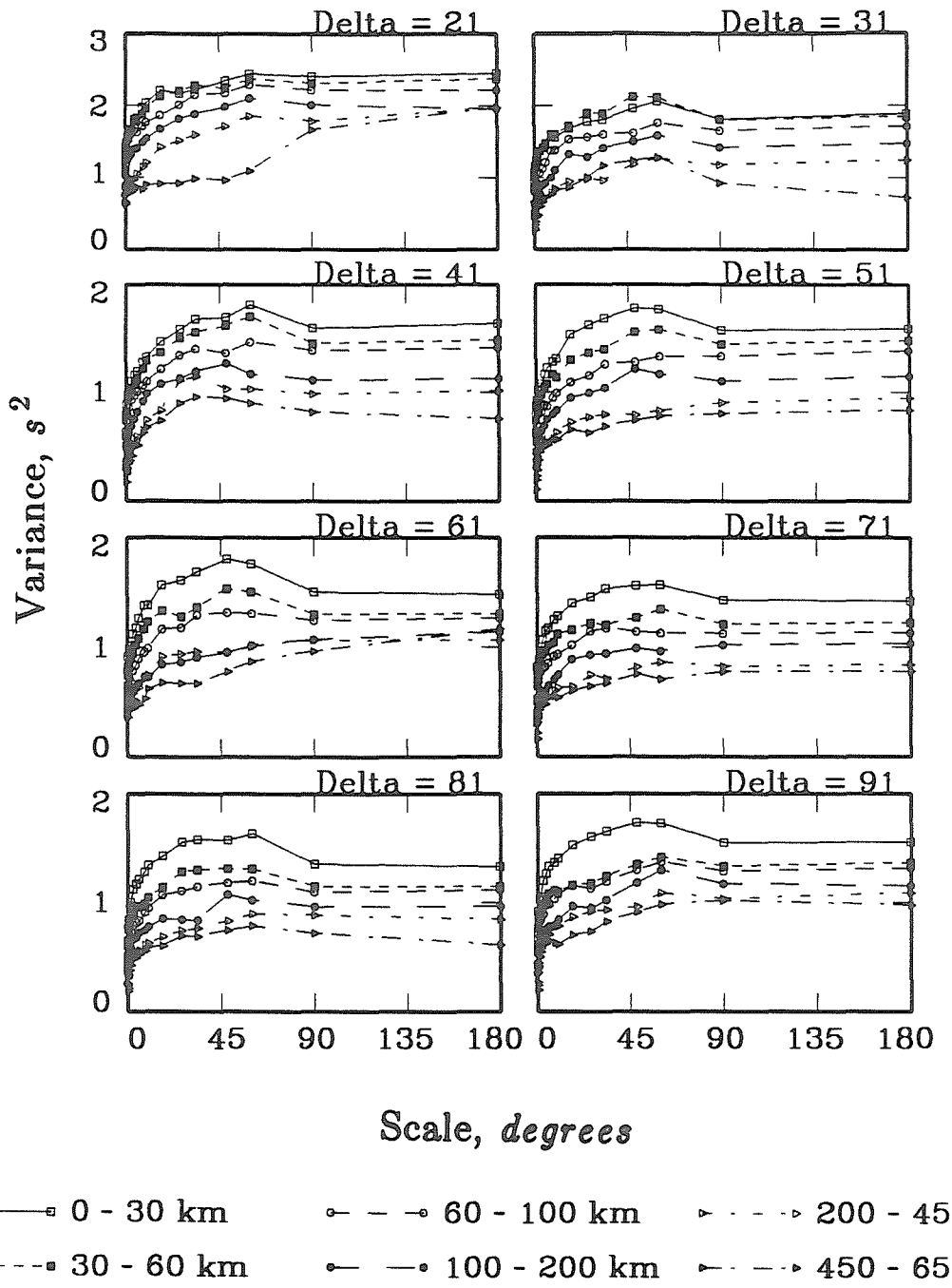

Figure 4.2. Samples of data as functions of scale in the distance range Δ=20° – 90° as indicated. The six curves in each frame represent the six depth bins. The shallowest depth bin consistently has the highest variance and the deepest one the lowest variance.

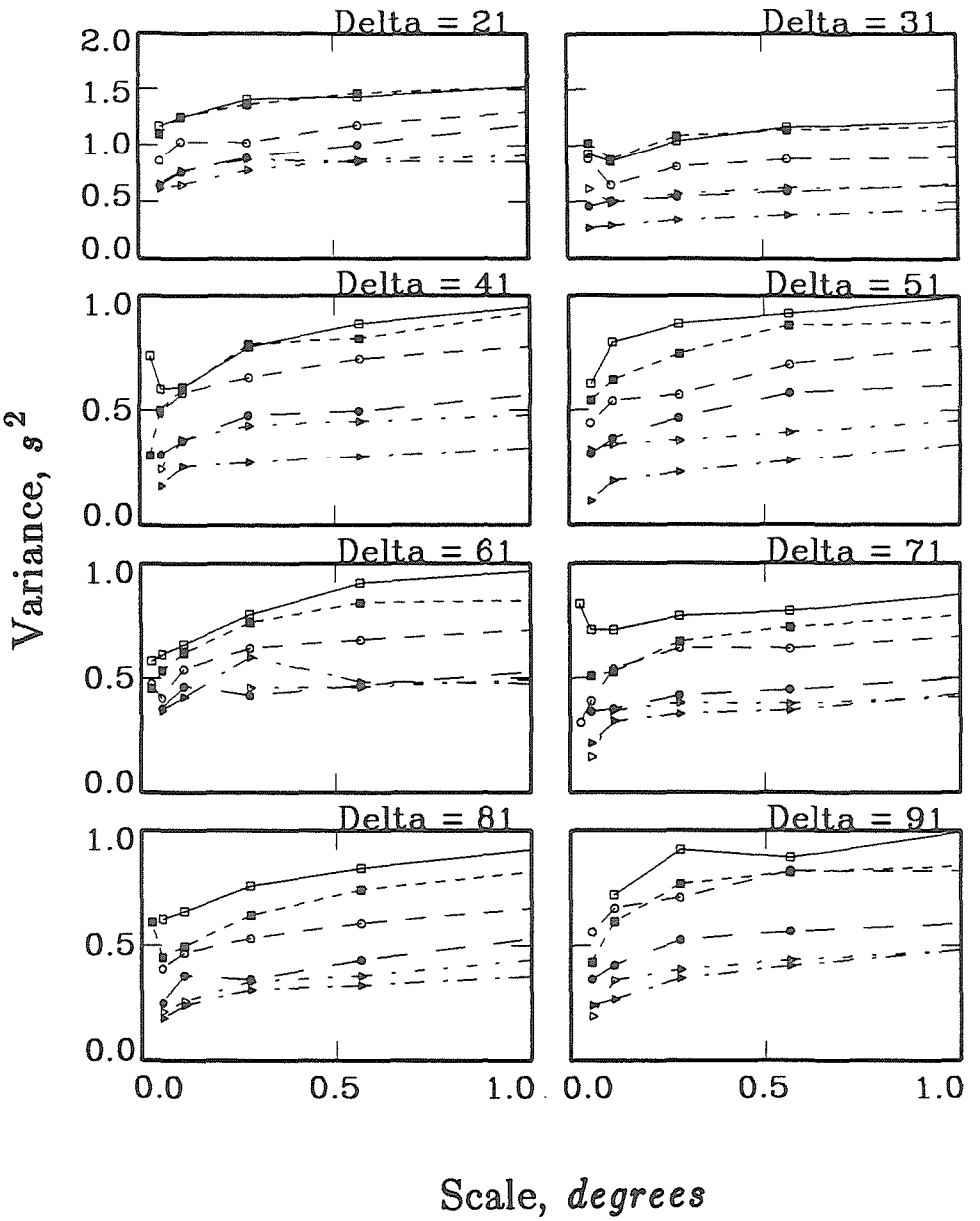

Figure 4.3. Same as Figure 4.2 except only showing the data at very small scales. Symbol legend same as in Figure 4.2.

A reference ray is ascribed to each Δ - Z bin. It is defined by the average epicentral distance and average source depth of the composite rays. A ray parameter is calculated by tracing through the JB (Jeffreys and Bullen) model.

The variance estimates are plotted as functions of scale length for each pair of Δ and Z. Some examples are shown in Figure 4.2. The behavior of the data is systematic. The curves rise rapidly at small scales and become relatively flat at large scales. The flat level of the curves invariably decreases with source depth. The behavior with epicentral distance is more complex. At teleseismic distances there is a gradual decrease with Δ out to about 90^o, where the variance starts to increase again. Figure 4.3 shows examples of the behavior at small scales. Extrapolation of the curves to vanishing scales does not yield a zero intercept with the variance (vertical) axis.

The overall behavior of the data is in accordance with the formalism developed in the following section. A nonzero intercept is expected because of picking errors, event mislocations, the finite binning of the data (particularly in source depth), and the lack of scale resolution at small scales. A finite correlation-length characterization of the medium predicts the general shape of the curves (see Figure 4.2). As the cross section of the summary ray tube increases, more and more component rays travel through uncorrelated slowness anomalies and the variance increases. As source depth increases the length of the path within the heterogeneous earth decreases and the variance decreases. If the earth were uniformly heterogeneous, the variance would increase as the total path length increased and hence as epicentral distance increased. The overall decrease in variance with epicentral distance at teleseismic distances thus implies that the strength of heterogeneity is

concentrated at shallow depths (see Figure 4.5). The small, but consistent, drop in variance at $\Theta = 60 - 90^o$ at shallow source depths does not fit in with the above scenario. We cannot explain this feature, but suggest that it is due to biases in sampling. While at small scales the sampling is dominated by continental and tectonic regions, oceanic regions come increasingly into play at large scales, but only at shallow source depths. If the small scale structure of oceanic crust and upper mantle is weaker than that of continental and tectonic regions, the above effect would be produced.

The intercepts of the individual curves in Figures 4.2 and 4.3 with the variance axis represent incoherent variance or random errors independent of the structure of the earth. We estimate the intercepts by a constrained linear extrapolation to the variance axis. We calculate a least-squares linear fit through the small-scale data ($\Theta < 1.5^o$), but constrain the slope to be inversely proportional to $\cos(i)$, where i is the angle of incidence for all curves at a common source depth; i.e., the curves that share a source-depth bin have a slope, b, described by the common constant, B, according to $b = B/cos(i)$. The behavior of the data at small scales is generally linear as is evident from Figure 4.3. We assume that the small-scale signal (the slope at the origin), is primarily accumulated at shallow depths, where the path length is inversely proportional to the cosine of the angle of incidence, hence the form of the constraint. The constraint is needed in order to minimize the effects of potential biases and errors at small scales. The resulting intercept estimates are plotted as a function of epicentral distance in Figure 4.4. The behavior is similar for all six source depth bins. The static variance peaks sharply in the triplication region ($15^o < \Delta < 25^o$), stays relatively flat at teleseismic distances, and increases beyond $\Delta = 85^o$, as the

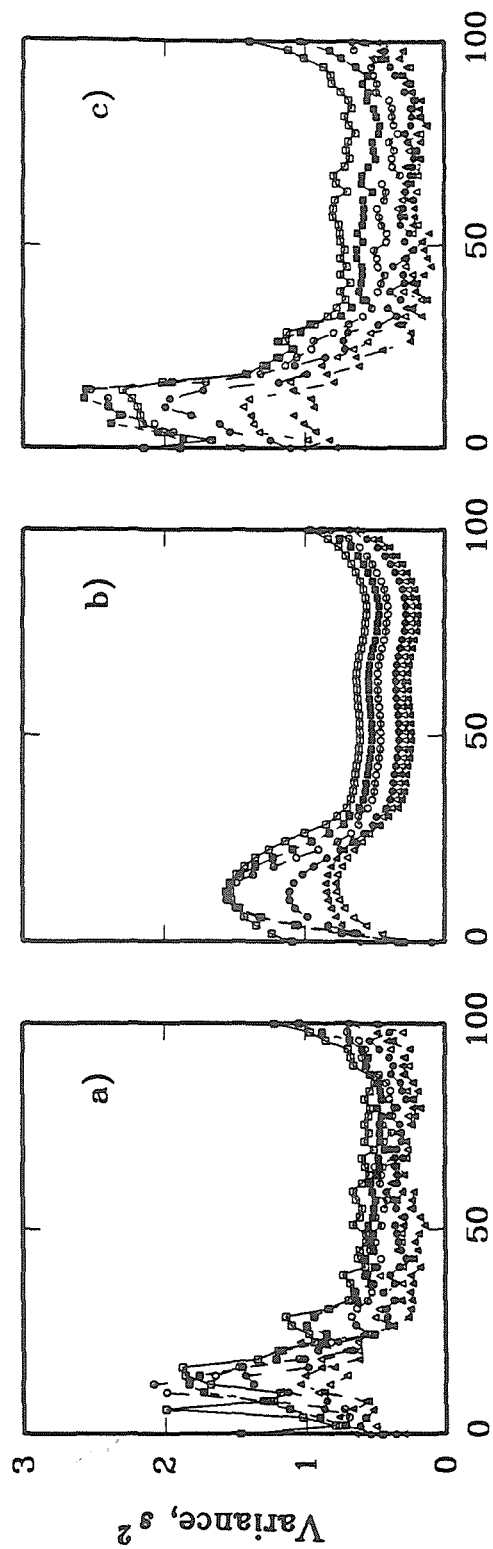

Figure 4.4. Estimates of intercepts or incoherent error variance as a function of epicentral distance. a) Independent estimates; b) Smoothed by polynomial fitting; c) Including systematic misfit of model to data (see Chapter 4.4). The six curves represent the six source-depth bins as before. Symbol legend same as in Figure 4.2.

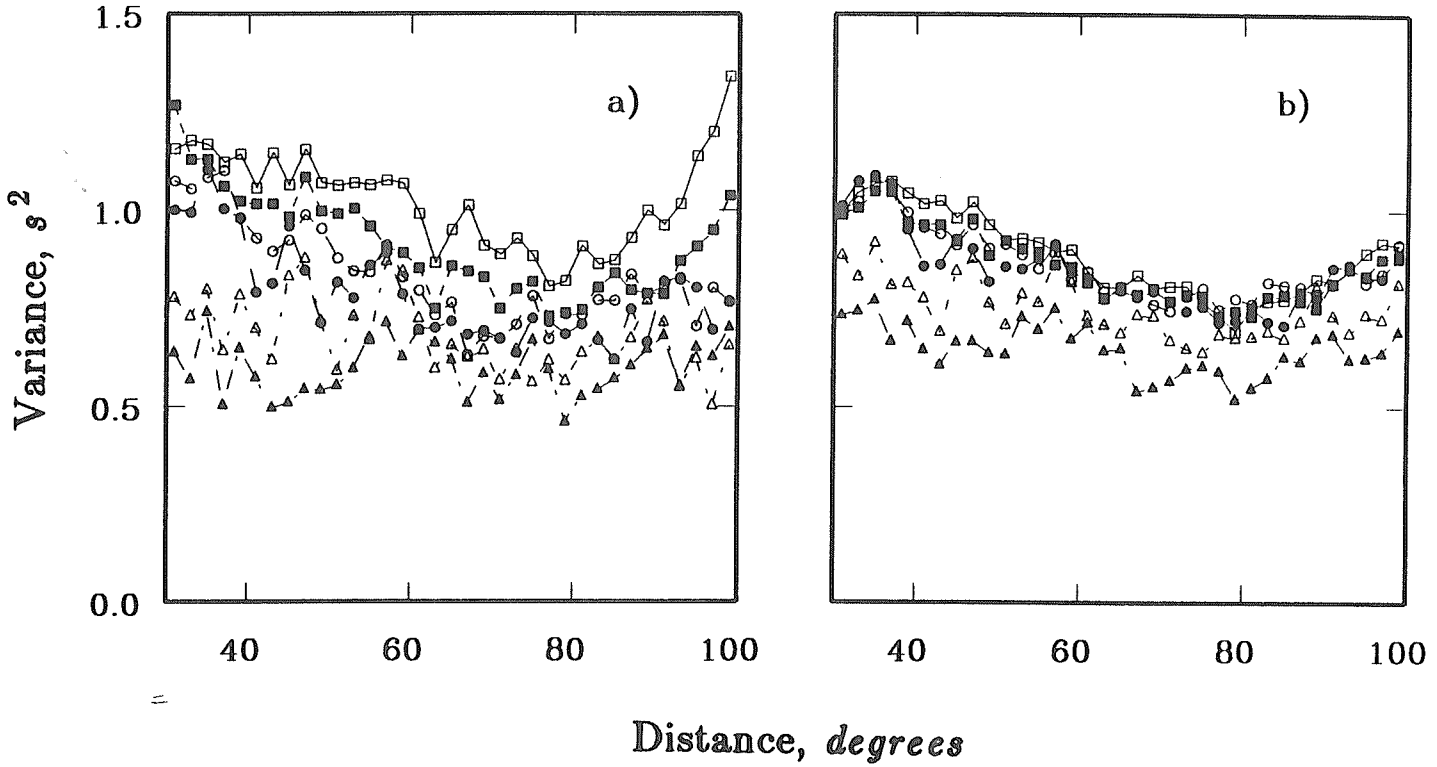

Figure 4.5. The asymptotic level of variance at large scales as a function of epicentral distance for the six depth bins. a) Using smoothed intercept estimates (Figure 4.4 b)); b) Using intercepts in Figure 4.4 c). Note the reduction in variance with source depth, the negative slope out to 80^o, and the positive slope beyond 85^o. Symbol legend same as in Figure 4.2.

travel-time curves for P- and PcP-waves merge. The static variance decreases with source depth. The behavior of the static variance with epicentral distance may be attributed to picking errors, since it is high where complexities occur on the travel-time curve. The behavior with source depth may be partially attributed to the variation of picking errors or location errors with depth, but is likely to have a contribution from the finiteness of the source-depth binning and the lack of scale resolution, because of the very fine structure of the earth (scale lengths of the order of tens of km).

We use the smoothed description of the intercepts as our estimates of random error (see Figure 4.4b). We then remove the random variance from the data. The remaining variance may be interpreted in terms of statistical measures of the earth's slowness field as formulated in the following section. Figure 4.5 summarizes the behavior of the reduced data with epicentral distance. Plotted is the asymptotic variance level at large scales.

4.3 Theory

The application of stochastic, structural modeling in seismology has been limited. It has been restricted to the analysis of dense array data, notably from LASA and NORSAR. A number of workers have applied the theory developed by Chernov (1960) to study the heterogeneous character of the lithosphere and upper mantle (e.g., Aki 1973, Capon 1974, Berteussen et al. 1975a and b). Flatte and Wu (1988) used a somewhat simpler approach based on the parabolic wave equation, which allows for more flexibility in the modeling. Frankel and Clayton (1986) used a synthetic approach to this problem, utilizing the finite difference method. Other problems that have

been analyzed with some success by stochastic means include the generation of coda by crustal heterogeneity (e.g., Aki and Chouet 1975, Gao et al. 1983a and b) and the generation of PKP precursors by heterogeneity near the core-mantle boundary (e.g., Doornbos and Vlaar 1973, Haddon and Cleary 1974).

We take a simpler approach to a greater volume of poorer data than the above studies, but apply many of the same concepts, i.e., those of a random medium. A full, wave-theoretical (scattering) formulation is inapplicable, since we are not dealing with single wavefronts. Yet, the diffraction effects described by scattering theory occur, since the data are travel-time readings off finite-frequency seismograms. The most important such effect is probably wavefront healing, which may be systematic in making the medium appear faster than its intrinsic properties imply (Wielandt 1987).

We take a somewhat simplistic, but pragmatic, attitude in regarding the finite wavelength property as an inherent limitation to the data, rendering them intrinsically insensitive to the small-scale features of the medium. The resulting characterization of the medium may then be interpreted as an apparent property, reflecting the true property intrinsically smoothed. This implies the existence of an inner scale of sensitivity of the data, which for short period teleseismic waves would be of the order of 10 km.

Our approach is a ray theoretical approach, which may be regarded as an adaptation of the linearized inverse problem of travel-time residuals to the concepts of stochastic analysis. It is designed to retrieve information about the earth's mantle slowness-field from travel-time data as compiled in the previous section. First we develop a formalism for a Cartesian, infinite world in some detail and then adapt that to the finite, spherical earth.

Consider the earth to contain a random function, $\delta U(\mathbf{x})$, of small slowness perturbations. Let δU be characterized by an autocorrelation function, $R(\mathbf{x},\mathbf{y})$. Here $\mathbf{x}$ is a position vector within the earth and $\mathbf{y}$ is the displacement vector between two arbitrary points. Assume that the statistics of $\delta U(\mathbf{x})$ are isotropic and spherically symmetric, such that $R(\mathbf{x},\mathbf{y}) = R(r, y)$, where r is distance from the earth's center and y is the length of the vector $\mathbf{y}$. Next consider a projection of the medium on to the earth's surface by means of curvilinear integrals to be specified later, i.e., that we have a random function $\delta t(\xi)$, where ξ is the position vector on the surface. Let this function be characterized by the autocorrelation function $T(\xi,\eta)$, where η is a displacement vector. Since δU is isotropic and spherically symmetric, we can assume that δt is isotropic and stationary, if the mapping of δU to δt is one to one or uniformly random. Thus, $T(\xi,\eta) = T(\eta)$, where η is the length of the displacement vector η. We need to estimate the scatter within a sample of circular area $A = \pi a^2$ of δt, i.e., the variance of all samples within A referenced to the mean of the area.

Assume that the global mean of δt is zero. Then the variance is

$$\sigma^2(a) = E\left\{ \left(\delta t(\xi) - \overline{\delta t}(a) \right)^2 \right\} = E\left\{ \delta t^2(\xi) \right\} - E\left\{ \overline{\delta t}^2(a) \right\}. \qquad (4.1)$$

Here $E\{\}$ stands for the statistical expectation over A and $\overline{\delta t}(a)$ for the mean of δt within A. The first term in Equation 4.1 is simply the global variance of δt; i.e.,

$$E\left\{ \delta t^2(\xi) \right\} = T(0). \qquad (4.2)$$

The second term in Equation 4.1 is the variance of the mean

$$E\left\{\overline{\delta t}^{\,2}(a)\right\} = E\left\{\left\{\frac{1}{\pi a^2}\int_A b_a(\xi)\delta t(\xi)d\,\xi\right\}^2\right\}$$

$$= \frac{1}{\pi^2 a^4}\int_A\int E\left\{\delta t(\xi_1)\delta t(\xi_2)\right\}E\left\{b_a(\xi_1)b_a(\xi_2)\right\}d\,\xi_1 d\,\xi_2 \qquad (4.3)$$

$$= \frac{1}{\pi^2 a^4}\int_A\int T(\,|\,\xi_1-\xi_2\,|\,)B(a\,,\,|\,\xi_1-\xi_2\,|\,)d\,\xi_1 d\,\xi_2,$$

where $b_a(\xi)$ is a scaled sampling function (an irregular 2D comb function).

$$b_a(\xi) = \frac{\pi a^2}{N}\sum_{i=1}^{N}\delta(\xi_i) = \frac{1}{\eta_a}\sum_{i=1}^{N}\delta(\xi_i),$$

where N is the number of measurements within the region A, η_a is the average sample density within A, and ξ_i are the sample positions. We can equivalently think of b_a as a normalized, random sample-density. The function $B(a\,,\rho)$ is then the autocorrelation of the sampling density. By separating the expectation of the sampling and the structure, we have assumed that the two are independent. In other words, it is assumed that the source and receiver locations are not correlated with structural anomalies. This assumption is suspect for subduction events.

Consider a point $\xi_1 = P$ a distance s from the center of A, and all points ξ_2 a distance ρ from P, within A (see Figure 4.6). If $\rho < (a - s)$, the points ξ_2 span a whole circle. If $(a - s) < \rho < (a + s)$, the angle ϕ is excluded. The cosine rule gives

$$a^2 = s^2 + \rho^2 - 2s\,\rho\cos(\theta). \qquad (4.4)$$

Thus, the arc spanned by the points ξ_2 is of length $2\theta = 2\pi$, if $0 < \rho < a$ and $0 < s < (a - \rho)$, and

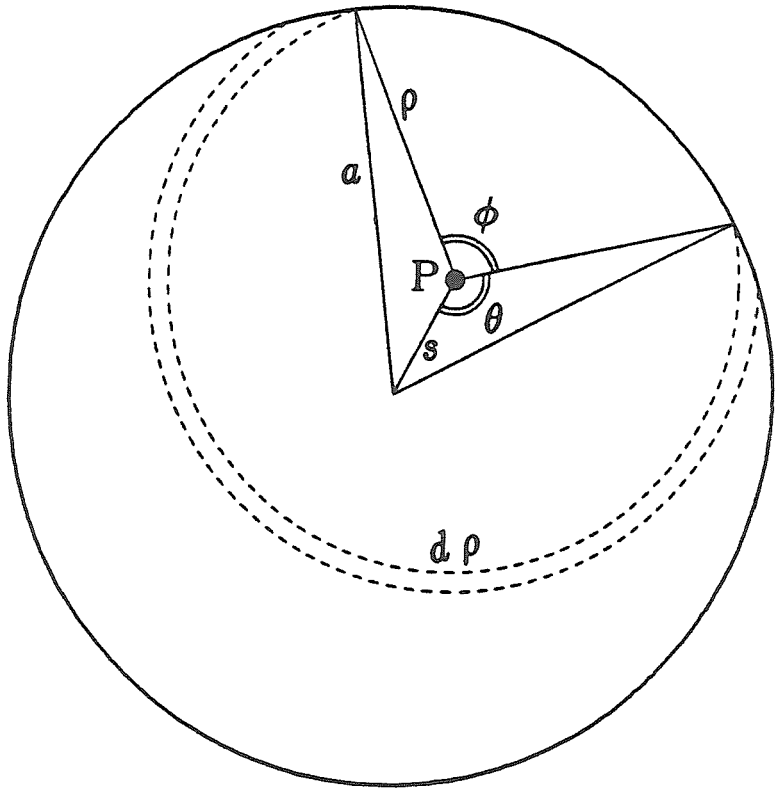

Figure 4.6. Geometrical definitions of the parameters used in the derivation of Equation 4.6.

$$2\theta = 2\cos^{-1}\left\{\frac{s^2 + \rho^2 - a^2}{2\rho s}\right\},$$

if $0 < \rho < a$ and $(a - \rho) < s < a$, or if $a < \rho < 2a$ and $(\rho - a) < s < a$. Since δt is isotropic, T is a function of ρ only, and assuming that the sampling density is isotropic, we can rewrite Equation 4.3 as

$$E\left\{\overline{\delta t}^2(a)\right\} = \frac{1}{\pi^2 a^4}\left[\int_0^a 2\pi\rho T(\rho)B(a,\rho)d\rho \int_0^{a-\rho} 2\pi s ds\right.$$

$$+ \int_0^a 2\pi\rho T(\rho)B(a,\rho)d\rho \int_{a-\rho}^{a} 2\cos^{-1}\left\{\frac{s^2 + \rho^2 - a^2}{2\rho s}\right\} s ds \qquad (4.5)$$

$$\left. + \int_a^{2a} 2\pi\rho T(\rho)B(a,\rho)d\rho \int_{\rho-a}^{a} 2\cos^{-1}\left\{\frac{s^2 + \rho^2 - a^2}{2\rho s}\right\} s ds\right],$$

which after simple, but tedious algebra simplifies to

$$E\left\{\overline{\delta t}^2(a)\right\} = \int_0^{2a} w(a,\rho)T(\rho)B(a,\rho)d\rho, \qquad (4.6)$$

where

$$w(a,\rho) = \frac{4}{\pi a^2}\left[\cos^{-1}\left\{\frac{\rho}{2a}\right\} - \frac{\rho}{2a}\left\{1 - \left\{\frac{\rho}{2a}\right\}^2\right\}^{\frac{1}{2}}\right]\rho.$$

Equation 4.6 describes the variance of the average $\overline{\delta t}$ over area of radius a. It is informative to consider a few simple cases. Assume that the sampling is uniform. Then $B = 1$. If the autocorrelation is a constant within the area, $T(\rho) = T_0$, the variance of the mean is T_0. This is expected, since in this case δt is constant within the area, and comparing randomly selected areal

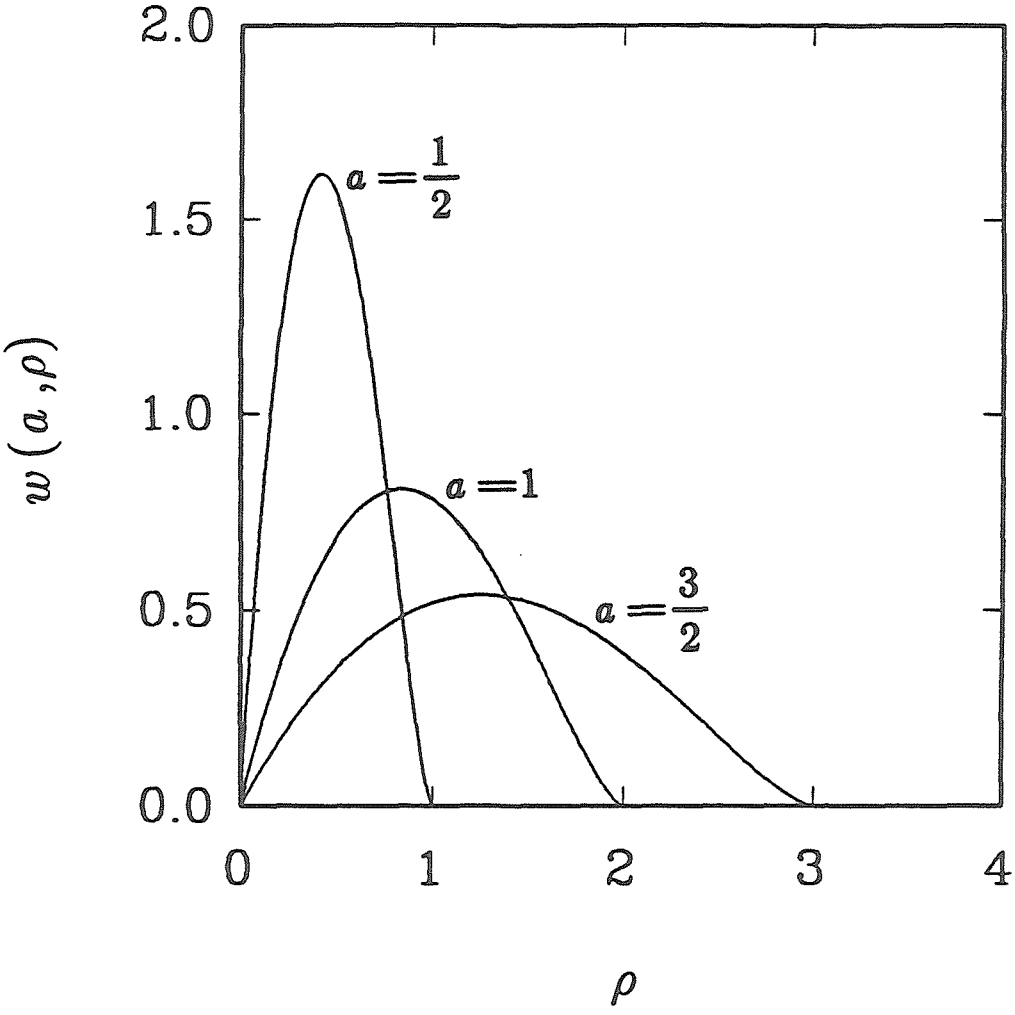

Figure 4.7. The weighting functions in Equation 4.6, $w(a,\rho)$, for a few choices of scale length.

averages is equivalent to comparing randomly selected points on δt. The variance of the averages should thus be the variance of the function itself, $T(0) = T_0$. From the above it is clear that if $T(\rho)$ has a zero derivative at the origin, we get

$$E\left\{ \overline{\delta t}^2(0) \right\} = T(0). \tag{4.7}$$

Another interesting example is a completely uncorrelated δt function; i.e., $T(\rho) = \delta(\rho)/\rho$, where δ represents the Dirac delta function. In this case the variance of the averages decays as the inverse of the area (analogous to the $1/N$ decay in the case of discrete sampling, where N is the number of samples).

Figure 4.7 shows some examples of the weighting functions of Equation 4.6, $w(a,\rho)$. Their integral is unity and they go to zero at the endpoints $(0,2a)$. They peak just below the center of their domain. Thus, when averaging uniformly over a circle of radius a, the main contribution to the variance is from a scale length of $\rho = a$.

Substituting Equations 4.2 and 4.6 into Equation 4.1 we get

$$\sigma^2(a) = T(0) - \int_0^{2a} w(a,\rho) T(\rho) B(a,\rho) d\rho \tag{4.8}$$

$$= \int_0^{2a} w(a,\rho) B(a,\rho) \left[T(0) - T(\rho) \right] d\rho,$$

since

$$\int_0^{2a} w(a,\rho) B(a,\rho) d\rho = 1,$$

as wB is the probability density of sample spacing within a circular region of radius a. Equation 4.8 describes the variance within area $A = \pi a^2$, referenced to the mean within A.

At this point we have a tool to relate our observations of the variance within summary rays to the autocorrelation function of the travel-time function. We need to express that in terms of the autocorrelation of the medium. In order to do that we must idealize the summary-ray geometry, i.e., assume a specific, deterministic or random geometry for the rays that contribute to a summary ray.

We calculate the variance of summary rays subject to fine binning in both source depth and epicentral distance. Thus, even when the averaging area becomes large, the ray parameter, and hence the ray geometry, stays relatively constant within each summary ray. Consequently, the contributing summary rays are not dominated by fans of rays stemming from a single receiver or a single event, except at the smallest scale lengths. It is thus reasonable to assume that all the rays have the same ray parameter and randomly distributed end points in the two grid-cells that define the summary ray. This implies that the rays are approximately parallel and simply shifted horizontally relative to each other. We can write

$$\delta t(\xi) = \int_{ray} \delta U(\mathbf{x}) dS. \tag{4.9}$$

Thus,

$$T(\rho) = E\Big\{\delta t(\xi_1)\delta t(\xi_2)\Big\} = \int_{ray_1}\int_{ray_2} E\Big\{\delta U(\mathbf{x}_1)\delta U(\mathbf{x}_2)\Big\} dS_1 dS_2 \tag{4.10}$$

$$= \int_{ray_1}\int_{ray_2} R(|\mathbf{x}_1 - \mathbf{x}_2|) dS_1 dS_2.$$

If we assume that the statistics of δU are a weak function of position within the earth and that the correlation length is small compared to the radius of curvature of the rays, we can think of the rays as locally straight and the autocorrelation function as locally constant. If ρ is the horizontal distance between two rays, i, the angle of incidence and ϕ, the angle the ray-displacement vector makes with the ray azimuth, then the minimum distance between the two rays is (see Figure 4.8)

$$d = \rho\sqrt{\cos^2(\phi)\cos^2(i) + \sin^2(\phi)}. \tag{4.11}$$

If we fix our attention to the point P_1 on ray 1 at Z and define S as ray length along ray 2, passing through 0 at P_2, the point on ray 2 that is closest to P_1, i.e., distance d away, we can write

$$\tau = \sqrt{d^2 + S^2}. \tag{4.12}$$

Hence,

$$| S | = \sqrt{\tau^2 - d^2} \tag{4.13}$$

and

$$| dS | = | dS_2 | = \frac{\tau d\tau}{\sqrt{\tau^2 - d^2}}. \tag{4.14}$$

The integral over dS_2 (ray 2) in Equation 4.10 can then be translated into an integral over τ, taken from d to ∞.

$$T(\rho) = 2 \int_{ray_1} \int_{d}^{\infty} \frac{\tau R(\tau) d\tau}{\sqrt{\tau^2 - d^2}} dS_1. \tag{4.15}$$

According to Equation 4.11 the close point, d, depends on the azimuth of the ray-displacement vector. For nearly vertical rays, $\theta = 0$, we have $d \approx \rho$. At the turning point the deviation of d from ρ is at its maximum

with $d = |\sin\phi|\rho$, which on the average is $d = 2\rho/\pi$. The variation of d is thus not a strong effect, particularly if the correlation length is large or the level of heterogeneity is small at the turning point, and we will simply approximate d by ρ.

If we now assume that the autocorrelation function of the medium is Gaussian, $R(\tau) = R_0 e^{-\tau^2/\alpha^2}$, we can simplify Equation 4.15.

$$T(\rho) = 2\int_{ray}\int_{\rho}^{\infty} R_0 \frac{\tau e^{-\tau^2/\alpha^2} d\tau}{\sqrt{\tau^2 - \rho^2}} dS = \sqrt{\pi}\int_{ray} R_0 \alpha e^{-\rho^2/\alpha^2} dS. \qquad (4.16)$$

This result holds approximately for many choices of an autocorrelation function, provided it does not have strong side lobes; i.e., the structure of the medium must not have a strong periodic component. Stated in a slightly different form, Equation 4.16 becomes

$$T(\rho) \approx C\int_{ray} x_{1/2} R(\rho) dS, \qquad (4.17)$$

where $x_{1/2}$ is the half-width of $R(\tau)$, $(R(x_{1/2}) = 0.5R(0))$, and C is a constant of order 2.0. For a Gaussian autocorrelation function, Equation 4.17 holds exactly and the constant is $C = \sqrt{\pi/\ln 2} = 2.129$.

If R_0 and α are constant along the ray path we get

$$T(\rho) = \sqrt{\pi} R_0 \alpha S e^{-\rho^2/\alpha^2}, \qquad (4.18)$$

which agrees with the transverse autocorrelation of phase of Chernov (1960) in the high-frequency limit. Chernov derived his results by a wave-theoretical approach and showed that when the wave parameter, $D = \dfrac{4S}{k\alpha^2}$, is not negligibly small ($D \ll 1$), diffraction effects (wavefront healing) cannot be ignored. (Here k stands for wavenumber, S for path length and α for

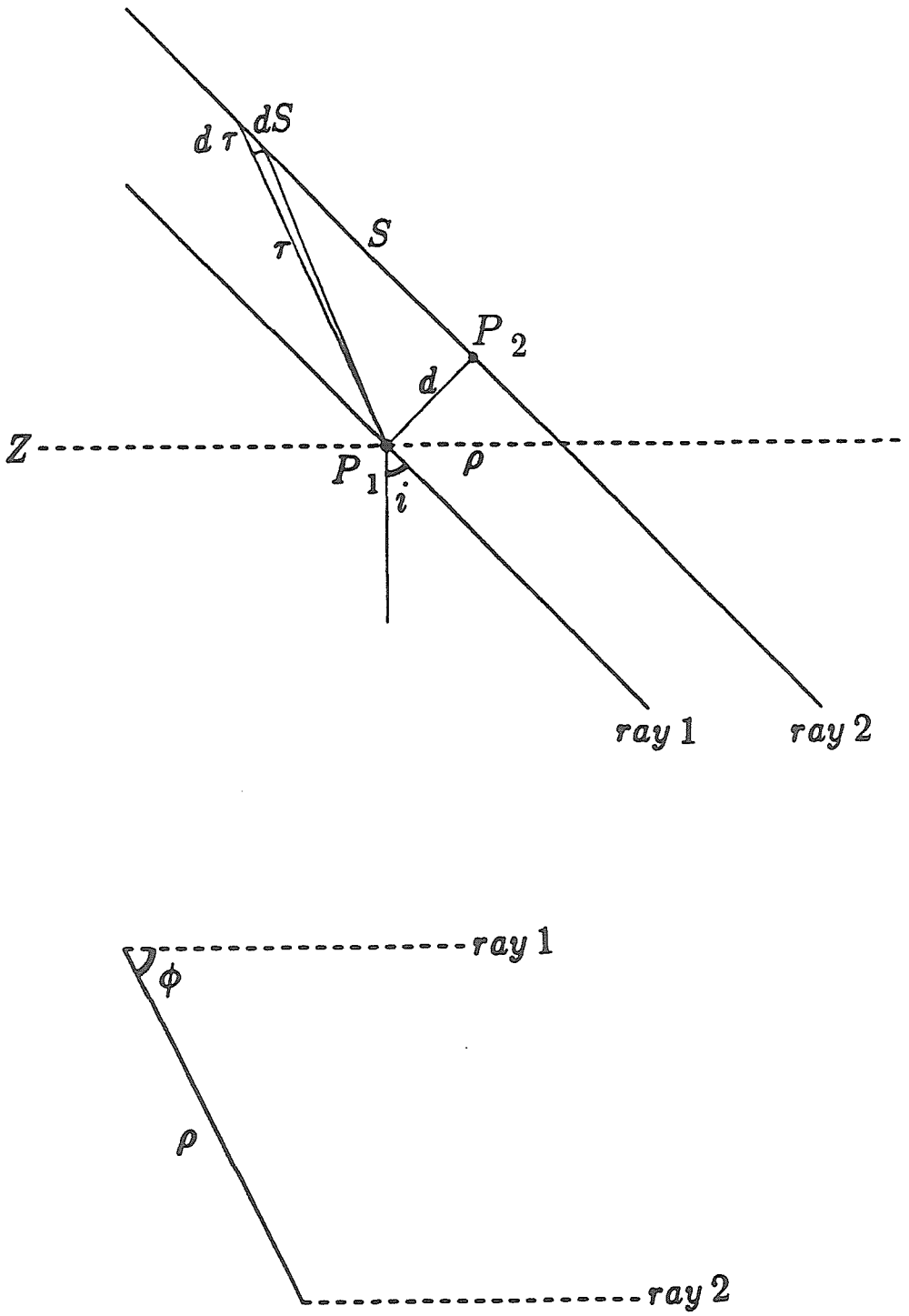

Figure 4.8. Geometrical definitions of the parameters used in the derivation of Equation 4.17. The top panel is a vertical cross section, the lower one a map view.

correlation length.) Wavefront healing describes a physical smoothing process on a single wavefront. We do not isolate single wavefronts in this study and cannot account for this effect properly.

We can combine Equations 4.8 and 4.17 to write the observables directly in terms of the parameters that we seek, namely, $R(r,\tau)$

$$\sigma^2(a) = C\int_{ray} x_{1/2}(r)\left[R(r,0) - \int_0^{2a} w(a,\rho)B(a,\rho)R(r,\rho)d\rho\right]dS \quad (4.19)$$

$$= C\int_{ray} x_{1/2}(r)\int_0^{2a} w(a,\rho)B(a,\rho)\left[R(r,0) - R(r,\rho)\right]d\rho dS.$$

The above formulation assumes the earth to be Cartesian and flat. It is applicable to localized studies. For the present global study we need to account for the finiteness and sphericity of the earth.

Let the medium be perturbed by

$$\delta U(r,\theta,\phi) = \sum_{l=0}^{\infty}\sum_{m=-l}^{l} A_{lm}(r)Y_{lm}(\theta,\phi), \quad (4.20)$$

where $Y_{lm}(\theta,\phi)$ are fully normalized spherical harmonics and θ is colatitude, ϕ is longitude and $A_{lm}(r)$ are harmonic coefficients varying with earth radius.

$$Y_{lm}(\theta,\phi) = \left(\frac{2l+1}{4\pi}\frac{(l-m)!}{(l+m)!}\right)^{\frac{1}{2}} P_l^m(\cos\theta)e^{im\phi}, \quad (4.21)$$

where P_l^m are the associated Legendre functions. We take the harmonic coefficients to be independent, random functions of depth. We can then define an autocorrelation function in terms of the power-spectral coefficients of the structure, Q_l. By definition,

$$Q_l = \frac{1}{(2l+1)} \sum_{m=-l}^{l} A_{lm} A_{lm}^* = E\left\{ A_{lm} A_{lm}^* \right\} \tag{4.22}$$

for a given set of surface spherical harmonics. Here the $*$ represents the complex conjugate. Allowing for some coherency in the harmonic pattern with depth, we thus define:

$$E\left\{ A_{lm}(r_1) A_{pq}^*(r_2) \right\} = Q_l \left[\frac{r_1 + r_2}{2} \right] f\left(| r_1 - r_2 | \right) \delta_{lp}\, \delta_{mq}\,, \tag{4.23}$$

where f describes the depth correlation and δ is the Kroenecker delta operator. Thus, correlating the travel-time residuals for two rays we get:

$$E\left\{ \delta t_1 \delta t_2 \right\} = E\left\{ \int_{ray_1} \int_{ray_2} \sum_{l=0}^{\infty} \sum_{m=-l}^{l} \sum_{p=0}^{\infty} \sum_{q=-p}^{p} A_{lm}(r_1) A_{pq}^*(r_2) \right. \tag{4.24}$$

$$\left[\frac{2l+1}{4\pi} \frac{(l-m)!}{(l+m)!} \right]^{\frac{1}{2}} \left[\frac{2p+1}{4\pi} \frac{(p-q)!}{(p+q)!} \right]^{\frac{1}{2}}$$

$$P_l^m(\cos\theta_1) P_p^q(\cos\theta_2) e^{im\phi_1} \left(e^{iq\phi_2} \right)^* dS_1 dS_2 \Big\}$$

$$= \int_{ray_1} \int_{ray_2} \sum_{l=0}^{\infty} \sum_{m=-l}^{l} Q_l \left[\frac{r_1 + r_2}{2} \right] f\left(| r_1 - r_2 | \right)$$

$$\frac{2l+1}{4\pi} \frac{(l-m)!}{(l+m)!} P_l^m(\cos\theta_1) P_l^m(\cos\theta_2) e^{im(\phi_1 - \phi_2)} dS_1 dS_2.$$

The latter identity comes about by substituting Equation 4.23 into Equation 4.24. Using the addition theorem for associated Legendre functions, we can simplify Equation 4.24 to

$$E\left\{ \delta t_1 \delta t_2 \right\} = \frac{1}{4\pi} \int_{ray_1} \int_{ray_2} \sum_{l=0}^{\infty} (2l+1) Q_l(r) f(\delta r) P_l(\cos\lambda) dS_1 dS_2, \tag{4.25}$$

where

$$\cos\lambda = \cos\theta_1\cos\theta_2\cos(\phi_1-\phi_2) + \sin\theta_1\sin\theta_2$$

$$r = (r_1 + r_2)/2$$

$$\delta r = r_1 - r_2.$$

λ is the angular distance between two arbitrary points on the two rays. Equation 4.25 is analogous to Equation 4.10 for the Cartesian case, except that it is cast in the spectral domain. The integrand

$$\frac{1}{4\pi}\sum_{l=0}^{\infty}(2l+1)Q_l(r)f(\delta r)P_l(\cos\lambda)$$

may be thought of as an autocorrelation function for the medium. To proceed we make the same assumptions as before; the two rays stay parallel along their entire path, the statistics of the medium are isotropic, the statistics vary smoothly along the path, the propagation distance far exceeds the correlation length and the radius of curvature of the rays is much greater than the correlation length. We can then apply the same arguments as in Equations 4.13 through 4.18 to conclude that

$$T(\lambda) = \frac{C}{4\pi}\int_{ray} x_{1/2}(r)\sum_{l=0}^{\infty}(2l+1)Q_l(r)P_l(\cos\lambda)dS, \qquad (4.26)$$

where T is the autocorrelation of the travel-time residuals as they are mapped onto the earth's surface and λ is the horizontal, angular distance between the two rays.

We proceed in the same manner as in Equations 4.1 through 4.6 to derive the effect of areal averaging on a spherical surface. Let Θ represent the angular radius of the area at hand (if the area is centered on the pole, Θ is the colatitude of its margin). Let λ represent angular distance between two arbitrary points within the area. Then the area is

$$A = 2\pi(1-\cos\Theta),$$

and provided that $\Theta<\pi/2$, the areal weighting function w is

$$w(\Theta,\lambda) = \frac{\pi-4\cos\Theta\cos^{-1}\alpha+\cos^{-1}\beta_1+\cos^{-1}\beta_2}{2\pi(1-\cos\Theta)^2}\sin\lambda, \tag{4.27}$$

if $0<\lambda<\Theta$, and

$$w(\Theta,\lambda) = \frac{\pi-4\cos\Theta\cos^{-1}\alpha+\sin^{-1}\beta_1-\sin^{-1}\beta_2}{2\pi(1-\cos\Theta)^2}\sin\lambda,$$

if $\Theta<\lambda<2\Theta$, where

$$\alpha = \frac{\cos\Theta(1-\cos\lambda)}{\sin\Theta\sin\lambda},$$

$$\beta_1 = \frac{(1-\cos\lambda)(1+\cos\lambda-\cos\Theta(1+\cos\Theta))}{(1-\cos\Theta)\sin\Theta\sin\lambda},$$

and

$$\beta_2 = \frac{(1-\cos\lambda)(1+\cos\lambda+\cos\Theta(1-\cos\Theta))}{(1+\cos\Theta)\sin\Theta\sin\lambda}.$$

We have not found a closed-form solution for $\Theta > \pi/2$, except at $\Theta = \pi$, where the solution is $w(\pi,\lambda) = \frac{1}{2}\sin(\lambda)$. In that case this areal averaging kernel must be evaluated numerically. Some examples are shown in Figure 4.9.

We can now put together an expression relating the observable, $\sigma^2(\Theta)$, to the structural parameters that we seek for the spherical finite earth by combining Equations 4.8, 4.26 and 4.27.

$$\sigma^2(\Theta) = \tag{4.28}$$

$$\frac{C}{4\pi}\sum_{l=0}^{\infty}\int_0^{2\Theta}\int_{ray} w(\Theta,\lambda)B(\Theta,\lambda)(2l+1)x_{1/2}(r)Q_l(r)(1-P_l(\cos\lambda))dSd\lambda,$$

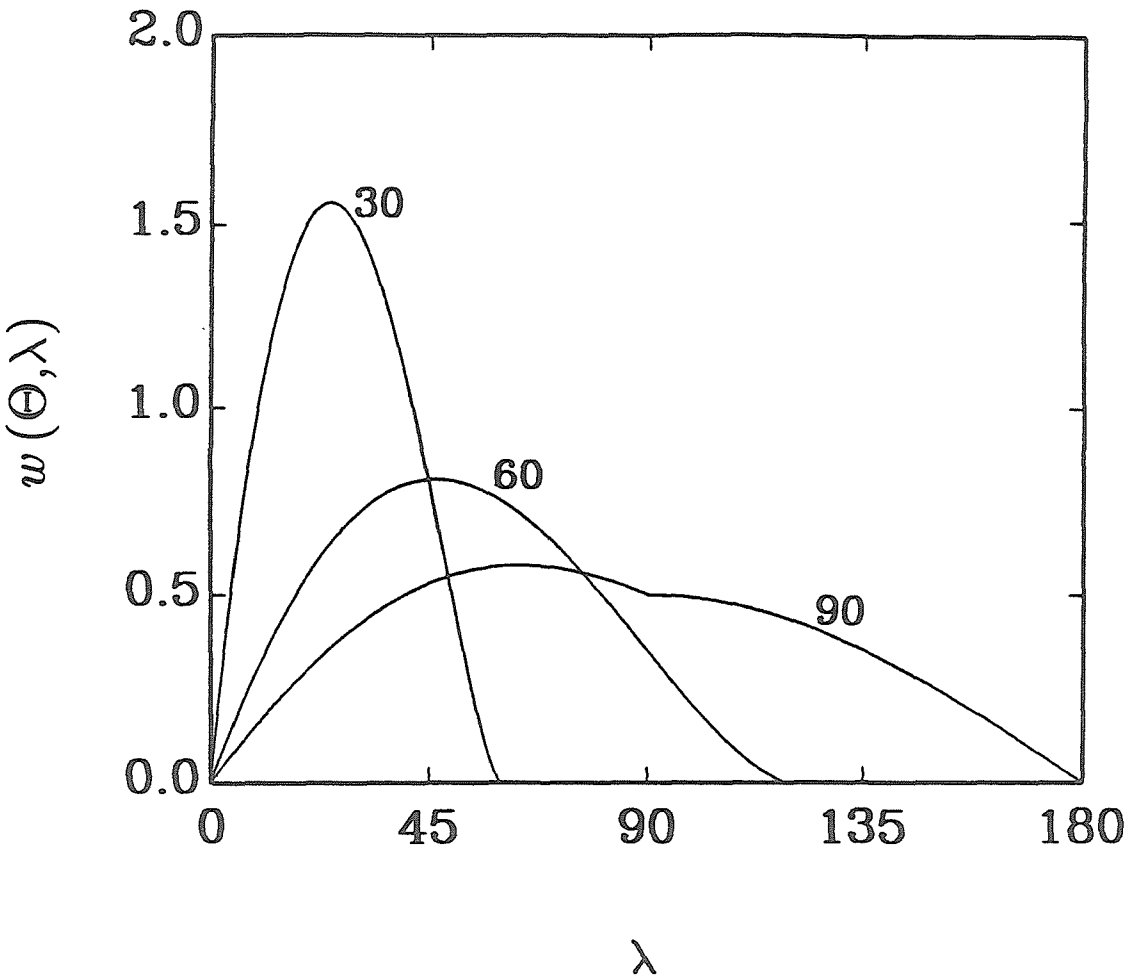

Figure 4.9. The weighting functions in Equation 4.27, $w(\Theta,\lambda)$, for a few choices of scale length. The curves are labeled by Θ (degrees).

which we can cast in matrix form as

$$\mathbf{D} = \mathbf{GXF}^T, \tag{4.29}$$

where

$$\mathbf{D}_{ij} = \sigma_i^2(\Theta_j),$$

$$\mathbf{G}_{ik} = \frac{dS_i}{dr}\Delta r_k,$$

$$\mathbf{F}_{jl} = \frac{C}{4\pi}\int_0^{2\Theta_j} w(\Theta_j,\lambda)B(\Theta_j,\lambda)(1 - P_l(\cos\lambda))d\lambda,$$

$$\mathbf{X}_{kl} = (2l+1)x_{1/2}(r_k)Q_l(r_k),$$

where we have transformed the ray integral to an integral over earth radius and then discretized that integral. The Δ–Z bins are indexed by i. The scale sampling is indexed by j. Earth radius and harmonic degree are indexed by k and l, respectively. Equation 4.29 describes a double, linear inverse problem in depth and harmonic degree (l). The matrix $\mathbf{D}$ contains the data. Each row of $\mathbf{D}$ represents the summary-ray variance as a function of scale for a given Δ–Z bin. $\mathbf{G}$ is a matrix of depth kernels. Each row of $\mathbf{G}$ represents the path length of the i–th ray (a reference ray, representative of the average ray geometry of the i–th Δ–Z bin) within the k–th depth bin of thickness Δr_k. $\mathbf{F}$ is a matrix of spectral kernels that relate the variance measurement at the j–th scale bin to the l–th harmonic degree. $\mathbf{X}$ is the unknown model matrix. Each row of $\mathbf{X}$ represents the product of the half-width and the power spectrum of the earth's slowness field at a given depth bin.

4.4 Inversion and results

Equation 4.29 in the previous section describes a linear inverse problem. The knowns are the data matrix, $\mathbf{D}$, and the kernel matrices, $\mathbf{G}$ and $\mathbf{F}$. The model matrix, $\mathbf{X}$, describing the product of the correlation length (autocorrelation half-width) and power spectrum of the slowness field as a function of depth, is unknown. We can isolate the individual columns of Equation 4.29 and solve the standard, vector inverse-problem

$$\mathbf{D}_{ij} = \mathbf{G}_{ik}\,\mathbf{Y}_{kj}, \tag{4.30a}$$

where

$$\mathbf{Y}_{kj} = \mathbf{X}_{kl}\,\mathbf{F}_{lj}, \tag{4.30b}$$

for the columns of $\mathbf{Y}$, and then transpose Equation 4.30b and solve it column by column for the columns of $\mathbf{X}^T$. This involves a matrix of standard, inverse problems. We opted to solve the inverse problem by simultaneous, damped least-squares for both dimensions of the solution.

$$\hat{\mathbf{X}} = \mathbf{G}^T \left(\mathbf{G}\mathbf{G}^T + \alpha^2\mathbf{I}\right)^{-1} \mathbf{D} \left(\mathbf{F}\mathbf{F}^T + \beta^2\mathbf{I}\right)^{-1} \mathbf{F}, \tag{4.31}$$

where the I's stand for identity matrices. The parameters α and β are the damping parameters, which are global in the sense that the same damping is applied to the entire solution. To apply the method of Backus and Gilbert (see Aki and Richards 1980, and references therein), which varies the damping internally to the solution, we would have to break up the problem as in Equation 4.30. That involves an unfeasible amount of computation. The damping parameters are thus chosen by a global trade-off of model errors and resolution. To form a solution for various choices of the damping parameters, it is efficient first to singular-value decompose the kernel matrices, $\mathbf{G}$

and $\mathbf{F}$.

$$\mathbf{G} = \mathbf{U}\Lambda\mathbf{V}^T . \tag{4.32}$$

$$\mathbf{F} = \mathbf{R}\Omega\mathbf{S}^T .$$

We can then transform Equation 4.31 to

$$\hat{\mathbf{X}} = \mathbf{V}\Lambda^T \left(\Lambda\Lambda^T + \alpha^2\mathbf{I}\right)^{-1} \mathbf{U}^T \mathbf{D}\mathbf{R} \left(\Omega\Omega^T + \beta^2\mathbf{I}\right)^{-1} \Omega\mathbf{S}^T . \tag{4.33}$$

Thus, as we vary the damping parameters, we need only invert the diagonal matrices

$$\left(\Lambda\Lambda^T + \alpha^2\mathbf{I}\right)$$

and

$$\left(\Omega\Omega^T + \beta^2\mathbf{I}\right).$$

We have chosen to parameterize the model finely and let the damping limit the degrees of freedom in the solution. This should yield a smooth solution and reduce discretization artifacts. We use 47 depth bins, 30 km thick at the surface and through the upper mantle and 100 km thick in the lower mantle, except at the very bottom where we use 30 km bins again. The inherent spectral resolution provided by the uneven sampling of the scale axis (see section 4.2) is such that the resolution length increases roughly linearly with harmonic degree. We thus decided to bin the spectral dimension parabolically. We use a total of 34 bins, of one degree width at low degrees and of 100 degrees width at high degrees. Beyond harmonic degree $l = 300$, a power-law decay is assumed for the spectrum, $Q_l \approx l^{-3}$ (note that the decay must be faster than l^{-2}; otherwise, an autocorrelation cannot be defined). Thus, we have about 1600 model parameters.

We use only data from teleseismic distances in the inversion. At distances less than $\Delta = 30^o$ the estimate of incoherent variance is unstable (see Figure 4.4). Furthermore, the idealization of the summary-ray geometry breaks down at short distances. We do not use data from scales smaller than $\Theta = 0.5^o$. At smaller scales fan summary rays dominate; i.e., the majority of contributing summary rays contain only one recording station, but multiple events. We thus include 210 variance curves and fifteen points on each curve (35 Δ-bins, 6 depth bins and 15 scale bins), or a total of 3150 data.

In order to form the spectral kernel matrix, $\mathbf{F}$, we need to estimate the distribution function, $B(\Theta,\lambda)$ (see Equation 4.29). We do this by compiling histograms of the frequency of spacings in the sampling of a given Δ-Z bin. This should be an estimate of the probability density of sample spacings, $w(\Theta,\lambda)B(\Theta,\lambda)$. We thus estimate B by normalizing the histograms by the known functions $w(\Theta,\lambda)$. The results for Δ=50^o, Z=0–30 km are plotted in Figure 4.10a. The behavior of B is similar for other Δ-Z bins. The generally linear behavior of B in the log-log domain implies a power-law distribution. The exponent of the distribution varies smoothly with scale, Θ. We take a smooth fit through the data in Figure 4.10a as a universal description of the sampling distribution for use in the calculation of the spectral kernels. Figure 4.10b shows a comparison of the theoretical kernels, using the above distribution (solid curves) and empirical kernels (symbols) evaluated by introducing a synthetic structure

$$Q_l(r) = \delta_{lk}\,\delta(r - r_o), \tag{4.34}$$

which should yield variance

$$\sigma^2(\Theta_j) = \frac{1}{2\pi}\int_0^{2\Theta_j} w(\Theta_j,\lambda)B(\Theta_j,\lambda)\left[1 - P_k(\cos\lambda)\right] d\lambda = \mathbf{F}_{jk}, \tag{4.35}$$

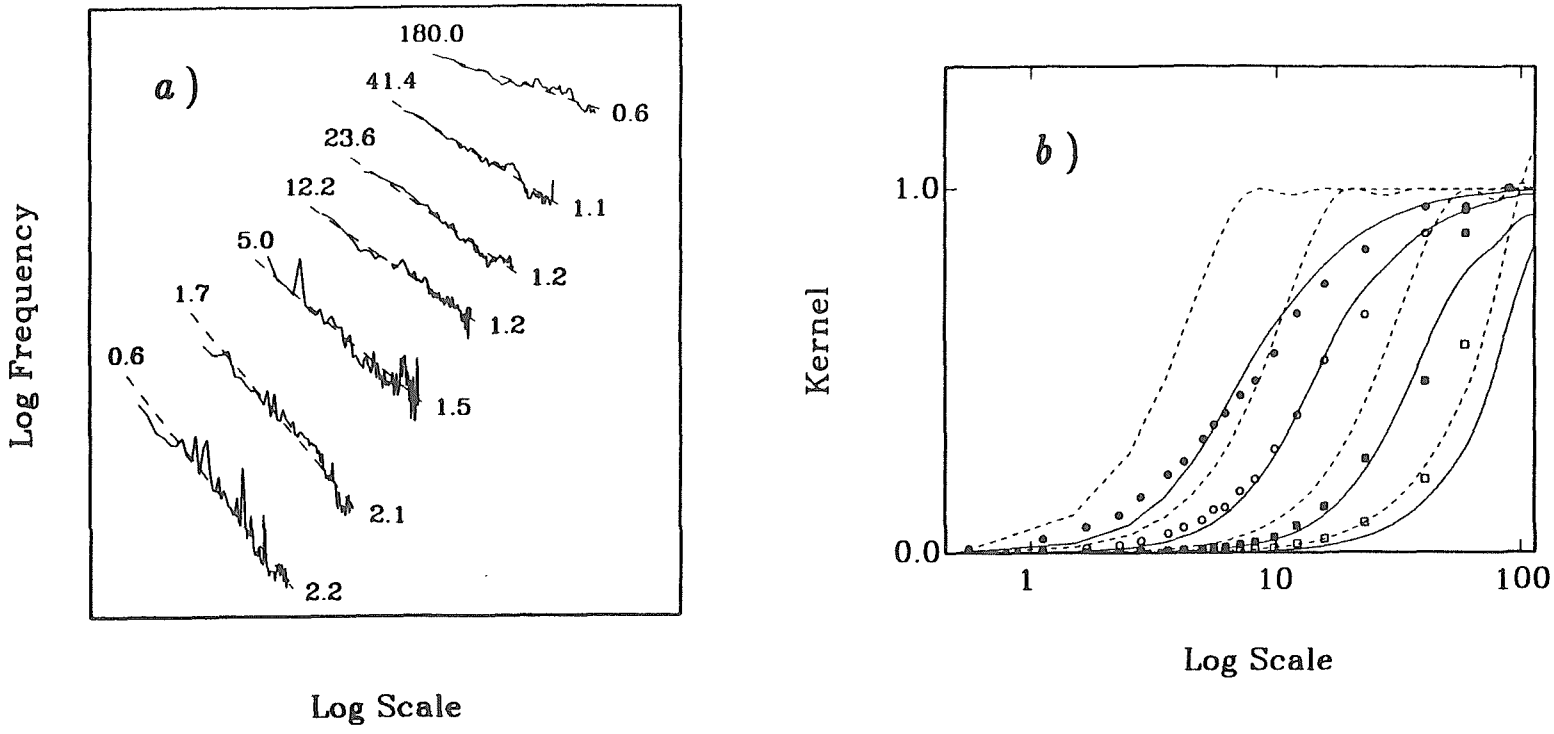

Figure 4.10. a) The autocorrelation of the sampling density, $(B(\Theta,\lambda))$, as evaluated empirically at $\Delta=50^o$ and $Z=0$–$30\ km$. The traces are labeled by the scale, Θ, above, and the best fitting slope below. b) Theoretical and empirical spectral kernels for a few harmonic degrees ($l=1,3,10,15$). Broken lines represent the theoretical kernels for uniform sampling, solid lines represent the theoretical kernels for the sampling in a) and symbols represent the empirical kernels evaluated by generating data from a synthetic structure (see Equation 4.35).

if our description of the data geometry holds. The fit of the theoretical kernels to the empirical kernels is good, except for low degrees and large scales. The goodness of this fit gives us confidence that we do not suffer significantly from the simplistic description of the data geometry in the formulation of this problem. For reference, the broken curves in Figure 4.10b show the theoretical kernels for uniform sampling ($B(\Theta,\lambda) = 1$). Clearly, the clustering of events and stations on the globe has a significant effect.

The damping parameters, α and β, were chosen to minimize a linear combination of resolution length in the two dimensions of the model and the model random-variance. Those measures of model goodness are global averages, because of the global nature of the damping in the damped least-squares technique. This is not an optimal way of solving the problem, as the inherent depth resolution in the sampling is quite uneven. This is because in using only teleseismic distances we have no rays bottoming in the upper mantle. The global damping thus causes an overemphasis on model error in the upper mantle and an overemphasis on model depth resolution in the lower mantle. It is unfeasible to tune the solution locally because of the size of the problem. For that same reason it is unfeasible to place nonnegativity constraints on the solution. Since the model is a power spectrum, it cannot physically take negative values.

The optimal global damping effectively reduces the number of degrees of freedom in the solution to about 100 (5 in the spectral dimension and 20 in the depth dimension). In other words, the model spectra at all depths are linear combinations of the same 5 eigenfunctions, and the depth variation of all spectral coefficients is a linear combination of the same 20 eigenfunctions. The resolution matrices in depth and the spectral dimension are shown in

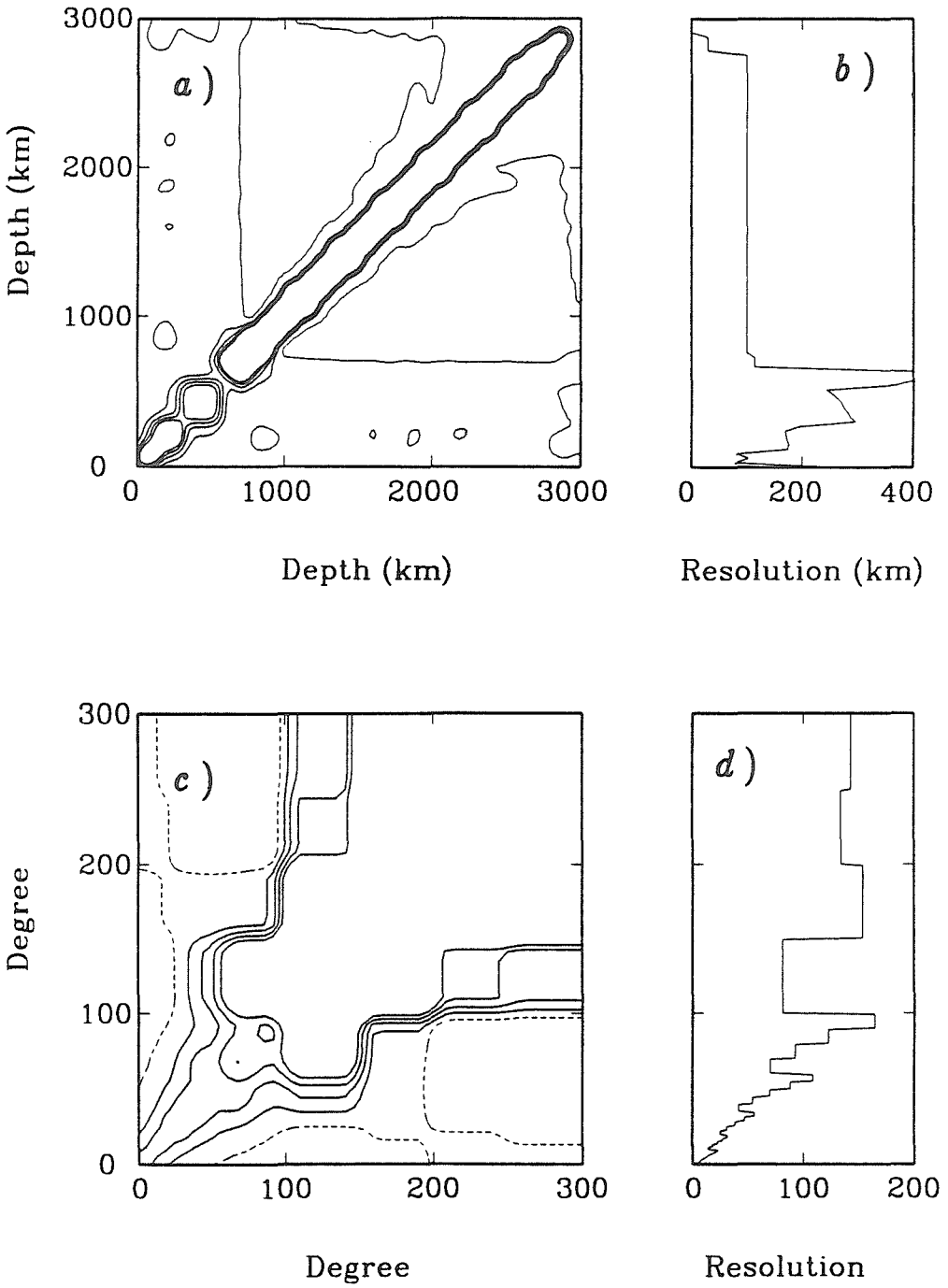

Figure 4.11. Contour maps of the resolution matrices for depth (a) and the spectrum (c). The small frames (b) and (d) show a simple measure of resolution length for each of the matrixes.

Figure 4.11 together with the derived resolution length. The resolution length is a simple measure of the width of the diagonal ridge of the resolution matrix and its off-centeredness. The resolution in depth is good throughout the lower mantle, but suffers from the lack of turning rays in the upper mantle, particularly in the transition zone, where the depth binning is coarse. The resolution in the spectral domain is poor and deteriorates rapidly with increasing harmonic degree, particularly beyond degree $l \approx 50$.

Figures 4.12 and 4.13 summarize the solution of the inverse problem, which we will refer to as model STP1 (Stochastic P-wave model). This solution explains 98% of the variance of the data (variance of estimates of travel-time variance). It should be noted, however, that the data are all positive. As they do not constitute a scatter about zero, the variance reduction may not be a fully appropriate measure of the goodness of fit. The rms (root-mean-square) value of the data is about 0.6 sec^2 and the rms value of the residual data is about 0.08 sec^2. About half of the residual rms value is due to systematic shifts of the data curves (Figure 4.2) relative to the predicted data. This discrepancy is best explained by error in the estimate of the intercept. We therefore absorb this component of the data misfit in the intercept and thus obtain a 99.5% variance reduction.

At large scales (high Θ) all of the spectral kernels, $\mathbf{F}$, take a value close to $\frac{C}{4\pi}$. Thus Equation 4.28 becomes

$$\sigma^2(\Theta) \approx \frac{C}{4\pi} \sum_{l=1}^{\infty} \int_{ray} (2l+1) x_{1/2}(r) Q_l(r) dS = C \int_{ray} x_{1/2}(r) \overline{Q}(r) dS \quad (4.36)$$

where $\overline{Q}$ is the total power of the slowness field at a given depth. We can thus invert directly for the product of the power and the autocorrelation

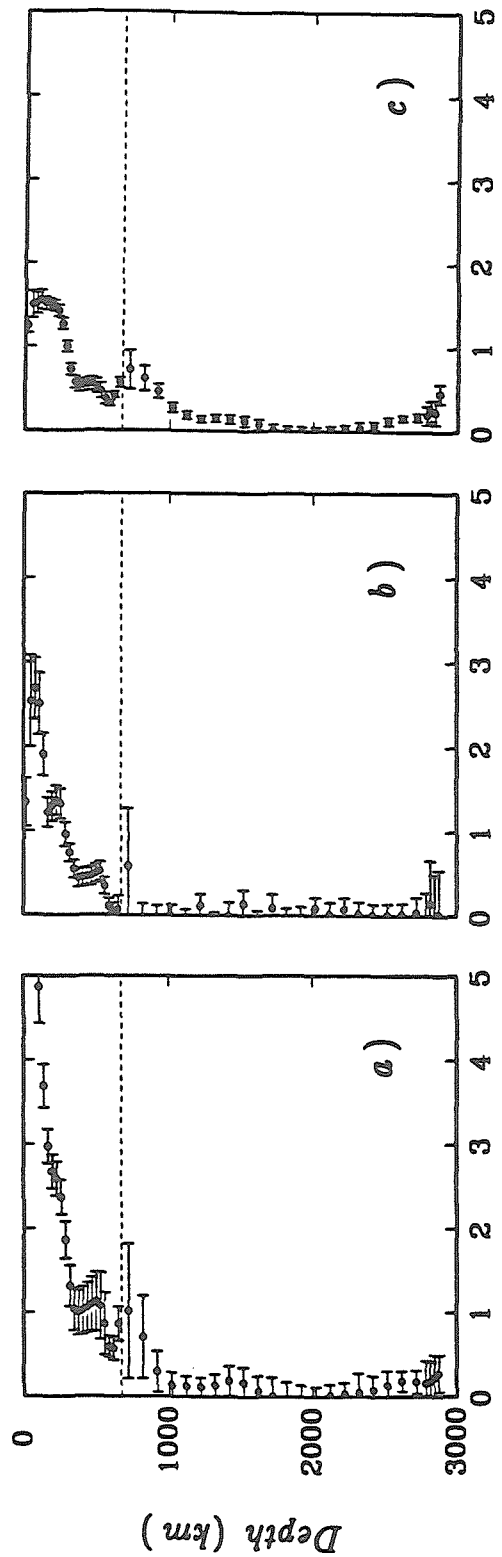

Figure 4.12. The product of power and autocorrelation half-width as a function of depth in the earth. a) The total power modeled by the inversion of Equation 4.36 (model STP). b) and c) The small-scale power ($l > 50$) and the large-scale power ($l < 50$), respectively, from the finely discretized inversion of Equation 4.29 (model STP1). Error bars are two standard deviations.

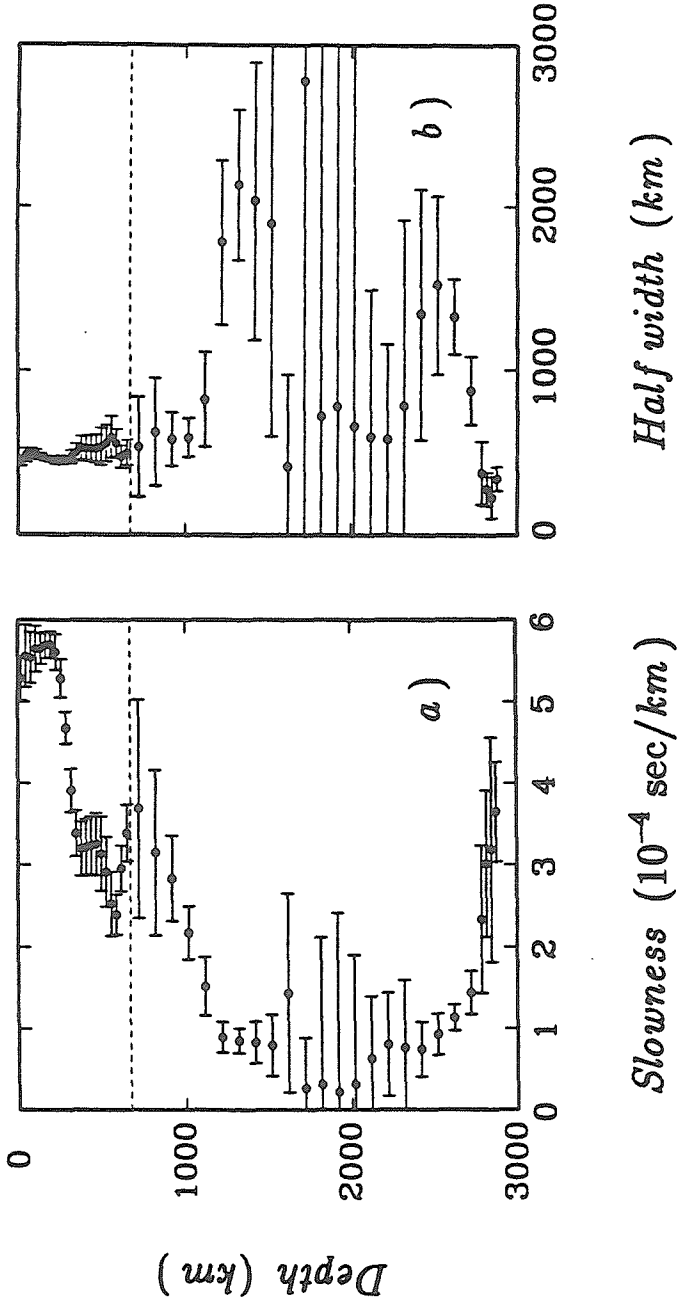

Figure 4.13. a) The standard deviation of long wavelength slowness variations as a function of depth. b) The autocorrelation half-width as a function of depth (l <50) according to model STP1. Error bars are two standard deviations.

half-width by taking the asymptotic level of the variance at large scales as our data (see Figure 4.5). The result of that inversion is shown in Figure 4.12a, and we will refer to it as model STP. The power is strongly concentrated in the top 200 or 300 km of the earth, drops to marginally resolvable values in the lower mantle and increases slightly at the base of the mantle. Because of the poor resolution in the spectral dimension, we cannot hope to resolve the shape of the power spectrum at high harmonic degrees. We do, on the other hand, have some resolution at low harmonic degrees. We therefore separate the power spectra into a small scale ($l > 50$) part and a large scale ($l < 50$) part. The integral power (multiplied by the half-width) of the two parts of the spectra in model STP1 is shown in Figure 4.12 b and c. Much of the total power in the upper mantle is in the small-scale structure, while the small-scale power in the lower mantle is not distinguishable from zero. The large-scale power is concentrated in the upper mantle, but appears to prefer finite power in the lower mantle and accounts for the slight increase in power at the base of the mantle. Figure 4.13 shows the results of our attempt to separate the power and the half-width of the large-scale spectrum. This was done by constructing the autocorrelation of the slowness field from the power spectrum and measuring the half-width of it. Taking that measure for granted, we normalized the solution by it, yielding an estimate of the actual power. This is a somewhat dangerous game to play in the upper mantle, as there the small-scale structure contains considerable power. Thus, the half-width of the low-passed autocorrelation may not be the true half-width; i.e., it may be an overestimate. Hence, the estimate of power in the upper mantle may be underestimated.

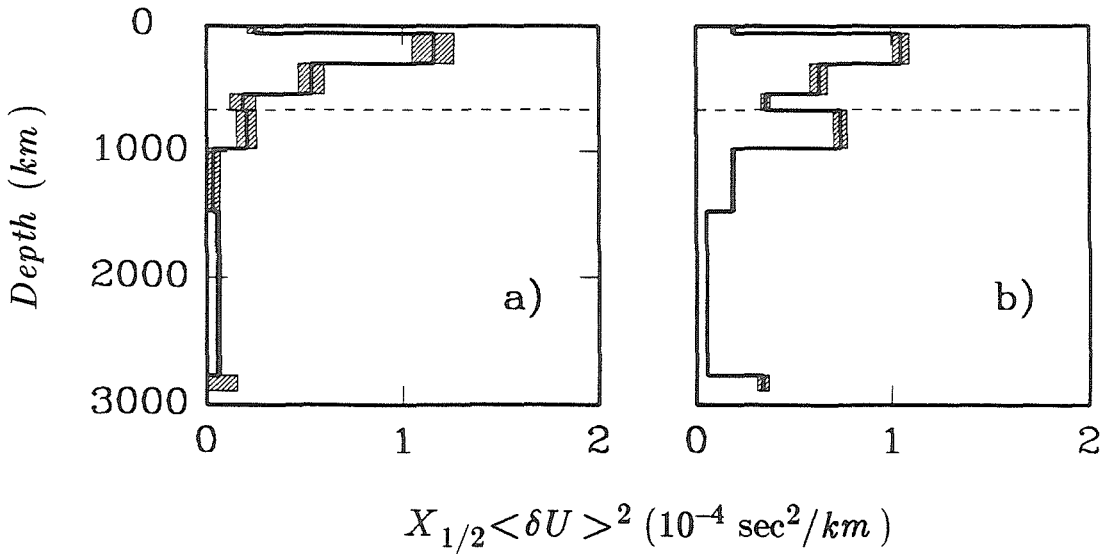

Figure 4.14. The product of autocorrelation half-width and the power of the slowness field as a function of depth according to model STP2. a) Small-scale power ($l > 50$), b) large-scale power ($l < 50$). Error bars are two standard deviations.

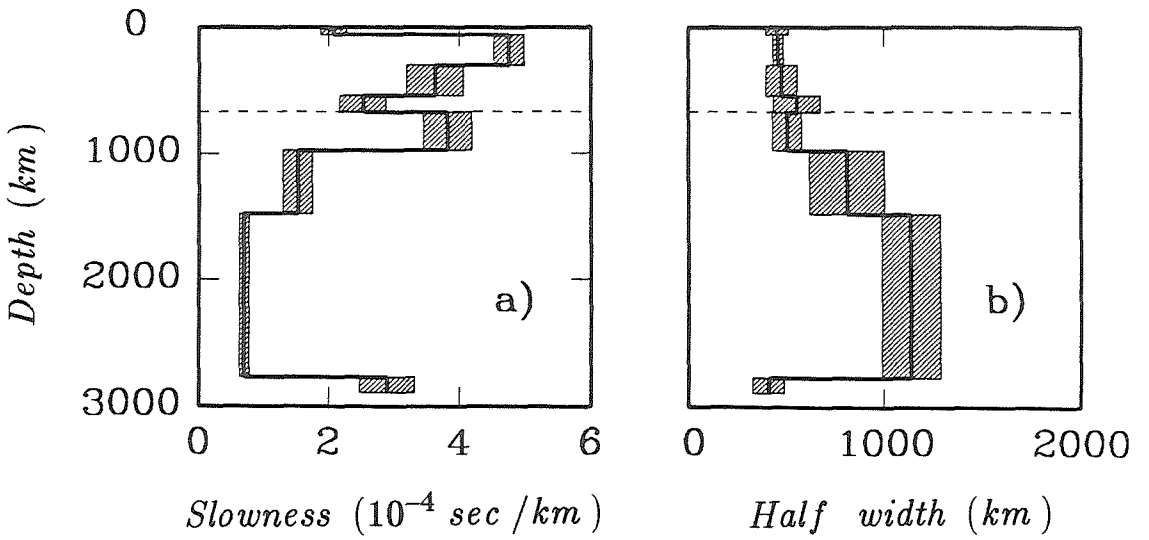

Figure 4.15. a) The standard deviation of long wavelength ($l < 50$) slowness variations as a function of depth according to model STP2. b) The auto-correlation half-width (Model STP2). Error bars are two standard deviations.

Model STP1 is hampered by relatively large errors in the lower mantle. We would prefer to smooth the solution more in depth in the lower mantle to obtain a better estimate of the correlation length and power. To achieve that we bin the depth dimension less densely and repeat the inversion. Figures 4.14 and 4.15 summarize the results that we get when using eight depth-layers, three in the lower mantle. We will refer to these results as model STP2. The quality of fit to the data is comparable to that for model STP1. 97% of the data variance is explained. Again, much of the residual variance is due to systematic shifts of individual data curves, which we attribute to the random-variance estimate. Hence, the variance reduction is improved to 99.3%. This model explains 75% of the rms value of the data that was left out of the inversion ($\Delta < 30^o$). Figures 4.4 c) and 4.5 b) show the incoherent variance estimates and the asymptotic, large-scale variance with the systematic data misfits included, based on model STP2. The features of model STP2 are similar to the main features of model STP1. Small scale power is concentrated at shallow depth and is small in the lower mantle. This may be in part due to diffraction effects. If small-scale structure existed in the lower mantle, the wavefront perturbations resulting from it would heal as the wave propagated to the surface. The large-scale spectrum is also concentrated in the upper mantle, but maintains a finite power in the lower mantle and shows a sharp increase in power in the deepest depth bin, about 150 km above the core-mantle boundary. Most of these general features are evident in the raw data. The variance decreases with epicentral distance out to about 85^o (see Figure 4.5), indicating strong shallow heterogeneity. The increase in variance beyond $\Delta \approx 85^o$ implies an increase in power at the base of the mantle. One feature in the data goes unexplained by the model. For

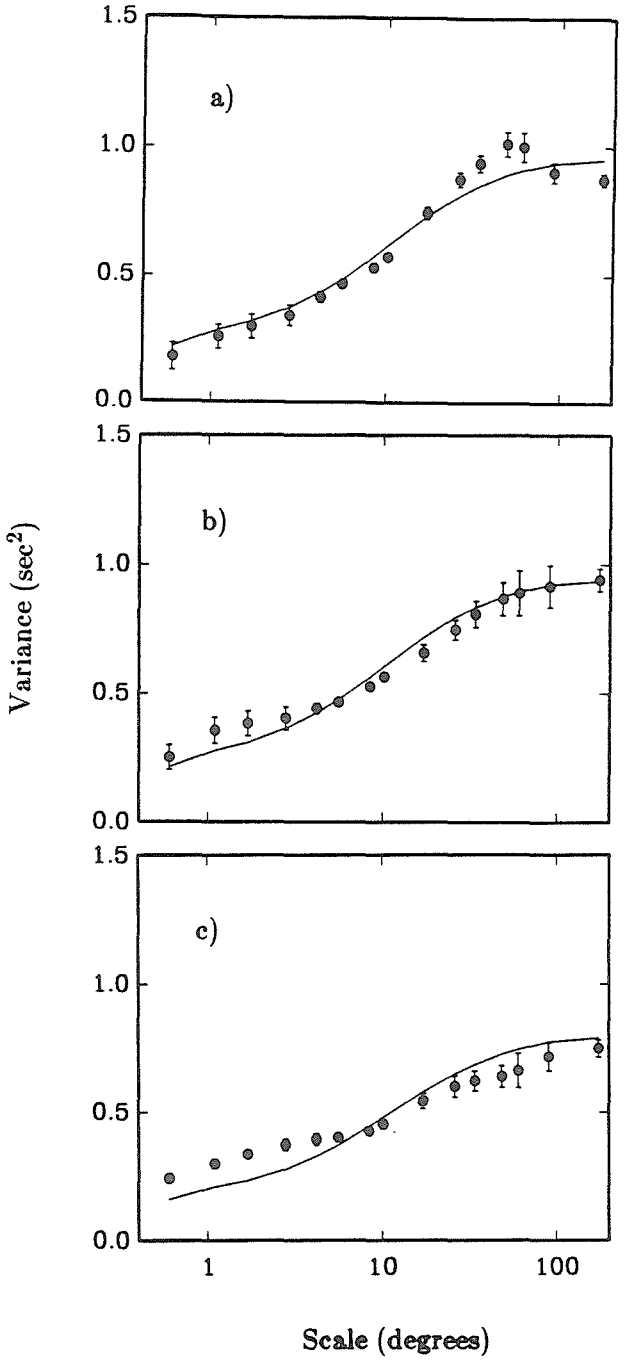

Figure 4.16. Examples of data fit by the model STP2. a) $\Delta = 51^o$, first depth bin; b) $\Delta = 51^o$, third depth bin; c) $\Delta = 51^o$, fifth depth bin. Dots are data with two standard-deviation error-bars. The curves are predicted data.

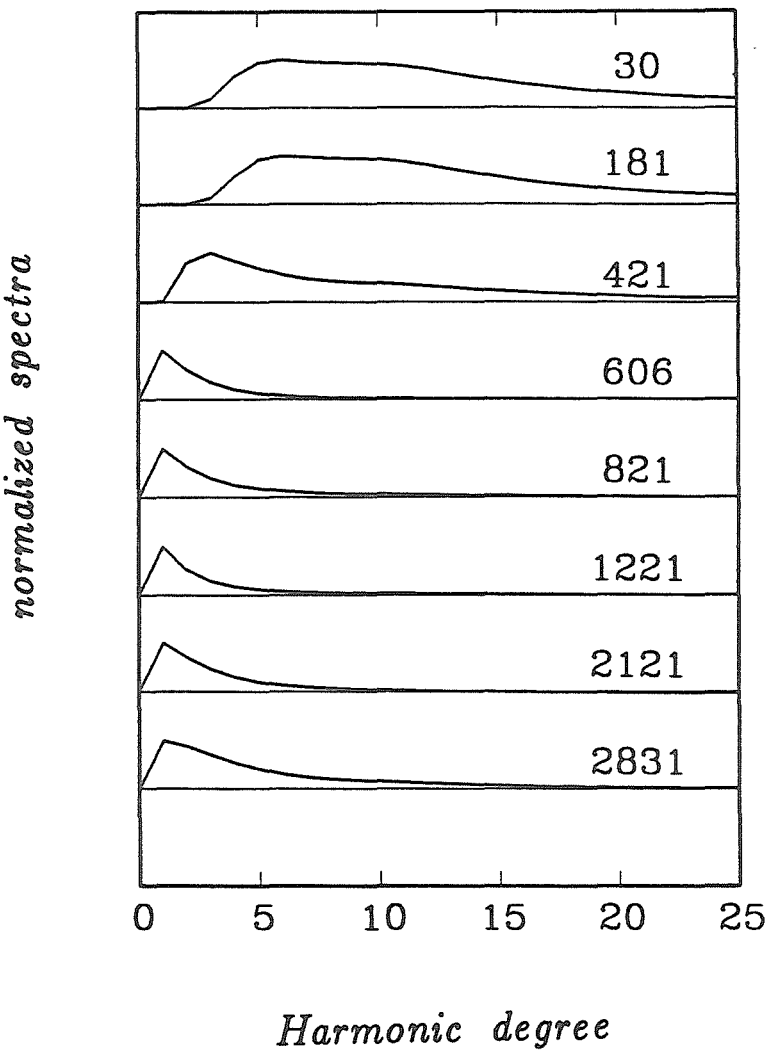

Figure 4.17. The normalized power spectra of model STP2 in the eight depth layers of the model. The central depth of each layer is indicated. The zeroth power coefficient is assumed to be zero. The shallow spectra contain an artifact at the lowest degrees that is due to features of the data that are discussed in the text.

shallow source depths the variance drops consistently at Δ=60–90°. This requires a negative power in the lowest harmonics at shallow depths, which is unphysical. This feature in the data may be due to some systematic effect in the sampling geometry at large scales, where Figure 4.10 demonstrates that our idealization of the data geometry fails.

Figure 4.16 shows some examples of the fit to the data obtained by model STP2. Plotted logarithmically is the variance versus scale. The error bars are two standard deviations. The overall fit is not satisfactory with respect to the error estimates ($\chi^2 \approx 15N$, $N = 3150$). This may indicate improper error estimates or problems with the applied formalism. The oscillation of the data curve in Figure 4.16 a) at large scales is a feature that cannot be explained by the formalism.

Figure 4.17 shows the spectra of the eight depth bins of model STP2, normalized to their maxima. The spectra are plotted out to harmonic degree $l = 25$. The median depth of each bin is indicated. The negative power coefficients of the lowest few degrees at shallow depths have been set to zero and a narrow Gaussian filter applied across the spectra. The zeroth power coefficient is assumed to be zero, since the data, as they are processed, are not sensitive to it. The greatest change in the power spectrum appears to occur between a depth of 400 and 600 km. Above that depth the spectra maintain strong power to degrees l = 10–15 and have a slowly decaying tail. Below a depth of 400 to 600 km, the power is strongly concentrated at the lowest degrees. The deepest depth bin has a noticeably larger tail than the ones above it. In comparing Figures 4.15 and 4.16, the low-degree spectra and the estimates of correlation half-width, respectively, we notice an apparent inconsistency at depths of 600 and 800 km. The spectra at these

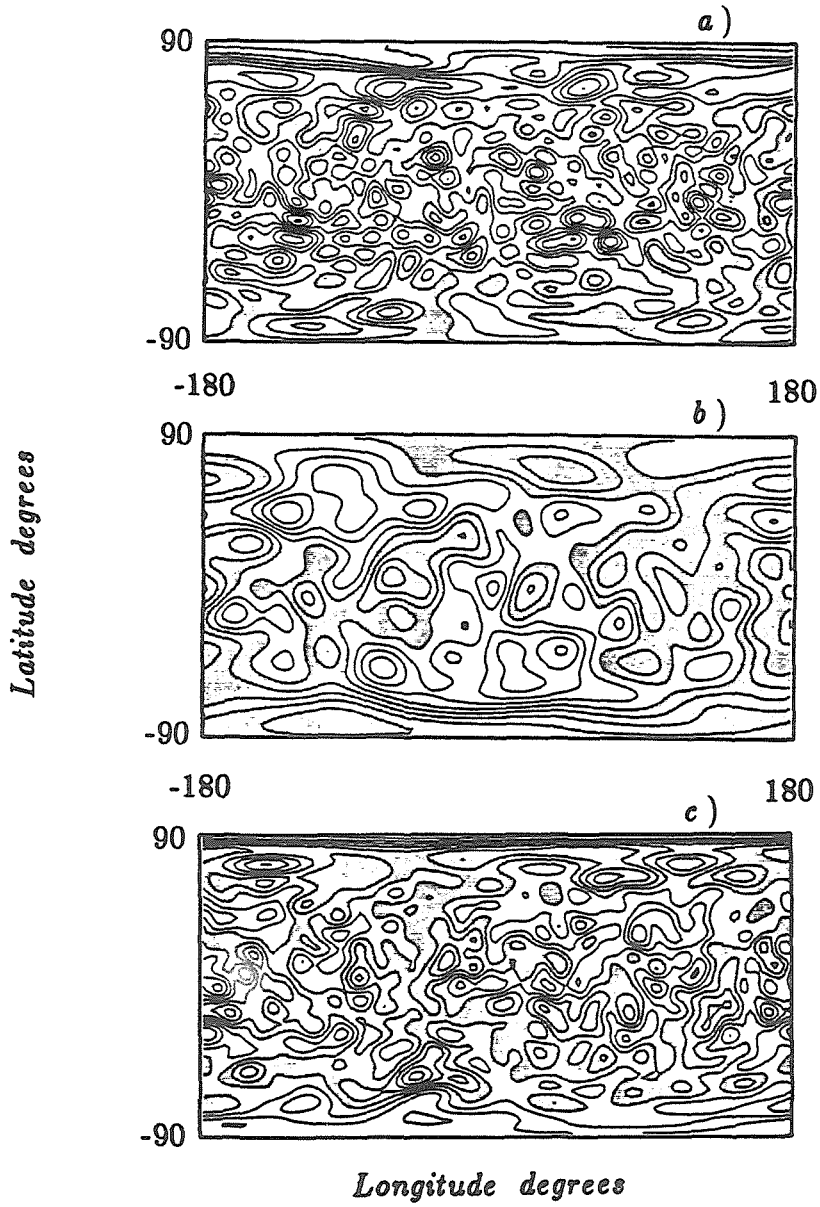

Figure 4.18. Synthetic maps of slowness variations calculated by a random selection of harmonic coefficients according to the power spectra of model STP2 at various depths. a) Upper mantle, $Z \approx 200$. b) Lower mantle, $Z \approx 2000$. c) Bottom of mantle, $Z \approx 2800$. The maps are projections of a spherical shell, linear in latitude and longitude, similar to a Mercator projection. Positive anomalies are shaded.

depths look more like the ones below, while the estimated half-width is more similar to that of the bins above. This demonstrates how sensitive the estimate of autocorrelation half-width is to the tail of the spectrum, including beyond harmonic degree $l = 25$. The estimated spectra in the lower mantle decay rapidly and become negative at about harmonic degree $l = 15$, while the estimated spectra at depths of $Z = 600$ and 800 km have small, but positive tails beyond degree $l = 25$.

Figure 4.18 shows normalized synthetic maps of the slowness field at three different depths consistent with the power spectra of model STP2. The spectra were truncated at degree $l = 25$. Since the spectra in the upper mantle have strong power beyond $l = 25$, Figure 4.18a should be considered as filtered. Figure 4.18b and 4.18c demonstrate how the slowness field of the lower mantle and at the base of the mantle might look like according to our results.

The above results are intriguing and consistent with some other studies. The model STP, which describes the variation of the product of power and correlation length with depth, is the most robust set of information to be drawn from this approach. It may, however, suffer from regional biases in the upper mantle. This interpretation of the data assumes a representative sampling of a laterally statistically stationary field in the upper mantle, which is questionable. In the models STP1 and STP2 we attempt to use the information contained in the shape of the data curves, presented in Figure 4.2, to make statements about the power spectrum of the earth's slowness field. Because of the limited sampling in the scale dimension, the spectral resolution is poor (see Figure 4.11c and d). We can therefore not claim to map the shape of the spectrum with much certainty. However, broad

measures of the spectrum, such as the separation into small- and large-scale integral power are supported by the data. The least reliable quantity derived from the data is the correlation length, and thus also the standard deviation of the slowness field (separation of the product of correlation length and power). This measure is relatively sensitive to details of the power spectrum. Note, however, the small range of estimates (350 km - 1200 km) (see Figures 4.13b and 4.15b). Since the product of power and correlation length varies by orders of magnitude across the models, while the estimates of correlation length vary by a factor of four, the main features of the variation of power with depth should be resolved. The error in the estimate of power that is due to the error in the estimate of correlation length should be within a factor of two. Our ability to separate the product of correlation length and power is dependent on the assumption of statistical isotropy, particularly in regions where the sampling is dominated by rays of a given direction. This is the case in the upper mantle, where the rays are predominantly vertical. Thus, the shape of the spectrum is primarily dependent on lateral variations, while the amplitude depends on the vertical correlation length. Furthermore, the upper mantle contains significant small-scale power, which is ignored in the estimate of half-width presented in Figures 4.13 and 4.15. Thus, the estimate of power in the upper mantle is likely an underestimate.

4.5 Discussion and conclusions

The travel-time residuals of mantle P-waves as reported by the ISC catalogue have been analyzed in a statistical sense. This statistical approach yields estimates of spatially incoherent variance, presumably due to random

errors of measurement, and spatially coherent variance and its dependence on scale. The spatially coherent variance is most likely due to signal from the earth's heterogeneous interior. A formalism has been developed to translate the coherent variance into statistical measures of the earth's heterogeneity pattern. The formalism has been applied to the ISC P-wave data, yielding a statistical model of the heterogeneity pattern in the mantle of the earth.

The estimates of random-error variance correlate well with complexities on the travel-time curve for P-waves, i.e., their variation with epicentral distance. The estimates also exhibit a systematic decrease with source depth. Since we cannot measure the variance at vanishing scales, we are forced to extrapolate our observations. Their behavior at small scales (see Figure 4.3) is reasonably linear. The data do, however, show signs of convex behavior. This would imply the existence of heterogeneity on scales smaller than our smallest scale samples ($0.06^o \approx 6\ km$), which is comparable to one wavelength of short-period P-waves. For this reason the linear extrapolation used to estimate the incoherent variance may result in overestimates. If the strength of this invisible heterogeneity decays with depth, which is suggested by the data (the convexity is strongest at shallow depths), it could explain some of the source-depth variation in the error estimates (Figure 4.4). Furthermore, the finite binning in source depth may introduce an areally incoherent component to the variance. If heterogeneity exists on scales smaller than the differences in ray length within the source depth bins, it would contribute to the variance within summary rays, which would not vary with scale. We thus have a further reason to suspect the data presented in Figure 4.4 to be overestimates of random measurement errors. It is, however, reasonable to expect some variation of picking errors with source depth.

Shallow events likely occur in an environment of stronger small-scale heterogeneity than deep events, and they occur close to the earth's free surface. Thus, scattering effects are likely to render the first arrival of shallow events more emergent than that of deep events, making them more difficult to pick. Assuming that the depth variation of the incoherent variance is dominated by small-scale structure and finite-binning effects, we conclude that random errors for P-waves at teleseismic distances are given by the upper bound $\sigma \approx 0.5$ sec. The remaining signal variance in the data is of the order of $\sigma^2 \approx 1.0$ sec^2. Thus, the signal to random noise ratio in the teleseismic, ISC P-wave data is about $S/N \approx 2$. On the other hand, the incoherent variance at local and regional distances is of the order of 1.0 – 2.0 sec^2, while the signal variance is comparable or less. The signal to noise ratio at short distances is thus less than unity.

Statistical measures of the heterogeneity pattern of the mantle have been obtained, based on the formalism developed herein. Error analysis yields a reasonably high level of confidence in the results. However, some simplistic assumptions are made in the formalism, rendering the description of the forward problem somewhat questionable. A more complete description of the sampling geometry is called for. Incorporating the effects of, e.g., transversely anisotropic statistics could be useful, and further testing of some of the other assumptions is needed. We do, however, feel that these results should hold to within a factor of two.

The most striking feature of the profile of small-scale power is the sharp overall decay with depth. In fact, the level of small-scale heterogeneity in the lower mantle is not resolvably different from zero in model STP1 (see Figure 4.12b). This could result in part from diffraction healing effects; i.e.,

the propagation distance from the lower mantle to the surface may be great enough to allow the healing of small-scale phase perturbations from the lower mantle on a single wavefront. If we assume a correlation half-width of $X_{1/2} = 10$ km, suggested by array studies at, e.g., NORSAR and LASA (Aki 1973, Capon 1974), the shallow peak at depths less than about 150 km corresponds to small scale velocity anomalies of the order of 4%. This, and the depth extent, are consistent with the above small-scale array studies. It should be noted in this context that although oceanic events are included in this analysis, they are sparse and probably contribute little, particularly at small scales.

We have some spectral resolution at low harmonic degrees and can thus separate the product of half-width and slowness variance. Figures 4.13a and 4.15a show the standard deviation of large-scale slowness variations as a function of depth. The three most robust features in this profile are: 1) the high level of heterogeneity in the upper mantle; 2) the low level of heterogeneity in the lower mantle; 3) the thin layer of strong heterogeneity at the base of the mantle. Two interesting details are the sharp drop in the strength of heterogeneity at about 300 km and the extension of intermediate levels of heterogeneity through the 670 km discontinuity into the lower mantle. It should be noted, however, that this is where the depth resolution is worst in the models. In terms of percent velocity variations (one standard deviation) this profile yields 0.5% at the top, 0.3% in the transition region and into the lower mantle, less than 0.1% in the lower mantle and 0.3% at the base of the mantle. Figures 4.13b and 4.15b show the variation of the correlation half-width with depth. It stays at about 500 km in the upper mantle, increases gradually to 1100 km in the lower mantle and drops

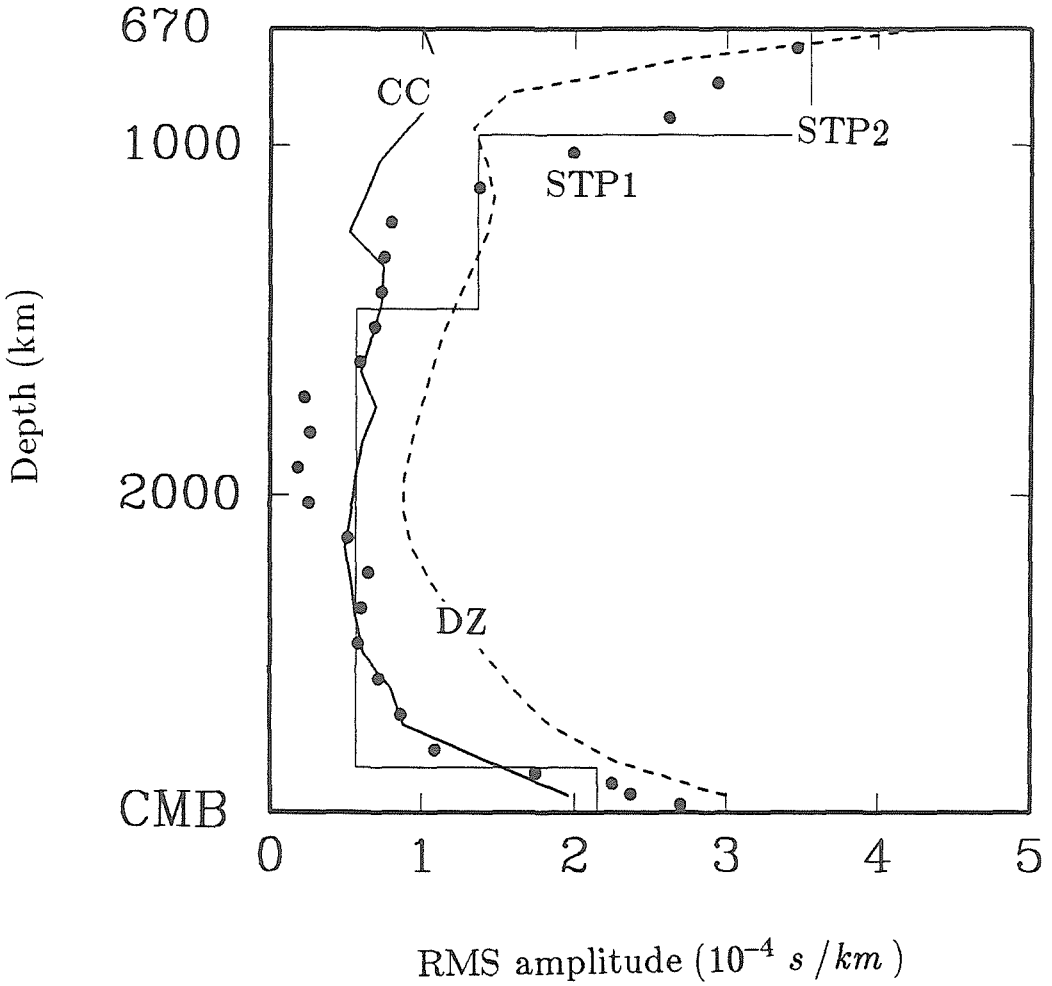

Figure 4.19. Comparison of the variation of power with depth in the lower mantle according to models STP1 and STP2, and the models of Dziewonski, (1984) [DZ] and Clayton and Comer (1983) [CC]. The CC model has been low-passed at harmonic degree 6.

sharply to about 350 km at the base of the mantle. These measures of the model in the upper mantle are based on the low-passed autocorrelation ($l < 50$). Thus the estimate of heterogeneity strength is an underestimate and the estimate of correlation length an overestimate. The general features of our results (models STP1 and STP2) are consistent with a number of previous studies. The variation of power with depth is similar to the P-wave models of Clayton and Comer (1983) (CC) and Dziewonski (1984) (DZ) (see Figure 4.19) and the S-wave model of Tanimoto (1989). The features in the lower mantle are similar to the model of Dziewonski, e.g., the apparent minimum in power at a depth of 2000 km (see Figure 4.13b). His model does, however, have a somewhat higher amplitude (by a factor of ≈ 2) throughout the lower mantle. A correlation half-width of 1000 km in the lower mantle corresponds to a spectral band-width of about $l = 7$ (assuming a Gaussian autocorrelation). This is comparable with the truncation harmonic degree of Dziewonski ($l = 6$). A full description of the boundary-layer half-widths of 350 km and 500 km would require a harmonic expansion beyond degree $l = 10$. Thus our STP models do not agree spectrally with the model of Dziewonski (1984). If the structure contains significant power beyond harmonic degree 6, truncating the model parameterization at that degree may result in significant aliasing effects. Comparison with a low-passed depiction of the model of Clayton and Comer is also favorable. Here the amplitude level is very similar to our results for depths greater than 1200 km. A large discrepancy is, however, present above that depth. Some of the discrepancies between our models and earlier deterministic models could be explained by the mapping of upper-mantle structure into the lower mantle. Our stochastic approach is not devoid of that problem, but is likely to suffer less from it

than three-dimensional models. Another potential contributor to amplitude discrepancies is our assumption of isotropic statistics.

All three models shown in Figure 4.19 have similar behavior at the base of the mantle. The relative slowness variations increase to 0.3 - 0.5% a few hundred km above the core mantle boundary. Our STP models have a sharper transition and a thinner D''. There is a marked difference in the modeled spectral content, however. The DZ model and the CC model as shown in Figure 4.19 contain only the six lowest harmonics, whereas the STP models claim a correlation length of 350 km and a significant spectral tail beyond degree 10. The STP models thus fall in between the deterministic (DZ,CC) models and the scattering models obtained from PKP precursors (e.g., Haddon and Cleary 1974), which yield 1% rms slowness variations on a characteristic scale of 30 km. We still have an order of magnitude discrepancy. It is, however, interesting to note that the product of slowness power and correlation length in our STP models agrees well with that of Haddon and Cleary. Our estimate of correlation length in D'' of 350 km contradicts the 1000 km estimate of Creager and Jordan (1988) for the structure of the core-mantle boundary region from PKP-waves.

A comparison of the present stochastic model with other studies cannot be as direct for the upper mantle as for the lower mantle, since a global P-wave model for the upper mantle is not available, and our presentation of the upper mantle may be obscured by the strong presence of small-scale heterogeneity. The drop in power at a depth of about 300 km is consistent with the results of surface-wave tomography (e.g., Woodhouse and Dziewonski 1984, Tanimoto 1987 and 1988), the results of long-period, body-wave synthesis (e.g., Helmberger et al. 1985) and upper-mantle, S-wave tomography (Grand

1987). Those studies are, however, primarily sensitive to large-scale S-wave velocity and report variations of the order of 5%, which correlate well with surface tectonics. Our models have about 0.5% velocity variations in the upper mantle from large scales (>400 *km*). This value is ambiguous, since it is based on an estimate of correlation length from a low-passed autocorrelation function. It is thus an underestimate. Nevertheless, this value is the integral strength of heterogeneity over a broad spectrum. Compared with 5% S-wave velocity variations over less than 10 harmonic degrees, there is a clear discrepancy. It is likely that we are in effect blind to the large-scale, strong variations between oceans and continents, because of the strongly biased distribution of sources and receivers over the globe. In fact, our upper-mantle models prefer negative power at the lowest harmonics in the upper mantle because of an unexplained feature in the data, possibly related to this distribution bias.

Some of our results have a bearing on the potential resolution of body-wave tomography. Our finding that the lower mantle is devoid of small-scale structure is encouraging. If true, we can get away with coarse parameterization of mantle models. Our finding that the signal-to-noise ratio of teleseismic ISC P-wave data exceeds unity by a factor of two is also encouraging. It demonstrates the value of the ISC data. We find the upper mantle to be two orders of magnitude more heterogeneous than the lower mantle (in terms of the product of power and characteristic scale), including strong structure at small scales. This inherent property of the earth will remain a problem for body-wave tomography in spite of improved instrumentation and picking procedures. It is as if we are examining the earth's interior through a very irregular glass window (random phase screen).

Some of our results may be used to make qualitative inferences about mantle dynamics. In the steady-state, Bernard-convection scenario, Jarvis and Peltier (1986) find that the convective boundary layers have a very narrow, low-degree spectrum of lateral temperature variations, while the interior of convection cells possess a relatively broad spectrum. This contradicts our finding of a decrease in correlation length towards the extremes of the mantle. In particular, it suggests that the D'' layer may be a chemical layer with independent convection, or lateral variations in seismic structure because of chemical heterogeneity. The possibly more realistic large aspect ratio, time-dependent, convection scenario of Weinstein et al. (1989) produces a much more chaotic temperature distribution, including transient secondary convection. This mode of convection better justifies our assumption of isotropic statistics than does simple steady state high Rayleigh number convection. Plumelike boundary-layer instabilities do, however, remain a prominent feature of the temperature field. The present stochastic approach is ill equipped to describe the effect of such features on the slowness field. In particular, our conclusion that the lower mantle does not possess significant small scale power ($l > 10$) seems to contradict the existence of confined plumes in the lower mantle, since such features would introduce small-scale structure at feasible Rayleigh numbers.

Since the binning of source depth is primarily what gives us depth resolution in the upper mantle, and deep events are restricted to subducting slabs, our upper-mantle model may be strongly biased to the regional structure of subduction zones. The upper mantle part of our model may be most properly interpreted in terms of the structure of subducting slabs as they penetrate the upper mantle. The extension of intermediate levels of

heterogeneity into the lower mantle could be interpreted in terms of slabs penetrating the 670 km velocity discontinuity rather than as a manifestation of a boundary layer.

Inversion of the structural signal in the data yields models that concentrate heterogeneity strongly in the upper mantle. The product of correlation length and power drops by about two orders of magnitude from the surface of the earth to the lower mantle. About half of this quantity in the upper mantle is due to small-scale features (<300 *km*). The lower mantle is devoid of small-scale structure. It contains 0.1% velocity variations at a characteristic scale of about 1000 *km*. This corresponds to a spectral band-width of $l \approx 7$. The D'' layer at the bottom 100 - 200 km of the mantle shows up as a distinct layer in our results. It has 0.3% velocity variations at a characteristic scale of 350 km. The top of the lower mantle contains 0.3% velocity variations on a scale of 500 km and also contains some small-scale power.

These results are somewhat preliminary, since some aspects of the technique are not fully tested and some potential improvements have not been tried out. We feel, however, that the overall agreement with earlier studies and the successful explanation of all the variance in the ISC data prove the usefulness of this approach.

5 A SYNTHETIC STUDY OF GLOBAL, TRAVEL-TIME TOMOGRAPHY

5.1 Introduction

The International Seismological Centre (ISC) Catalogue contains over twenty years of worldwide, arrival-time readings and event locations. This database of more than nine million picks has been used to map the heterogeneous structure of the earth's deep interior on a global scale. Clayton and Comer (1983) and Dziewonski (1984) used fifteen years of ISC mantle P-wave data to map the lower mantle. Creager and Jordan (1986) and Morelli and Dziewonski (1987) used compressional core phases to map the core-mantle boundary. Morelli et al. (1986) and Shearer et al. (1988), used PKIKP-waves to map anisotropy in the inner core. These studies, if successful, together with surface-wave tomography, free-oscillation studies, and long-period, body-wave synthesis, would provide important constraints on the style and scale of mantle convection, on the workings of the geodynamo, and on the evolution of the earth.

There are, however, some concerns about the ISC data. The uncertainty of measurement is high compared with the signal attributable to aspherical structure. The data are contaminated by potentially systematic errors that are due to misidentification of phases, earthquake mislocation, earthquake time-function complexity, and potentially biased picking. The geometrical distribution of the data is uneven, because of the clustering of seismic sources in tectonically active regions, the lack of recording stations in the oceans, and the inactive picking of many secondary phases at numerous stations. The

images may suffer from complex artifacts, which depend on the particular technique employed, because of the uneven coverage. The strong small-scale velocity variations in the earth's outermost layers are simplistically accounted for by station corrections. The severity of these problems is currently poorly understood.

We attempt in this chapter to assess the quality of images of the lower mantle and core-mantle boundary (CMB) obtained from ISC data, by a synthetic test. In order to do that we need reasonable heterogeneous velocity models for the mantle as well as estimates of errors in the data. We draw our information from the results of crustal-scattering studies (e.g., Aki 1973), from the results of surface-wave tomography (upper mantle) (e.g., Woodhouse and and Dziewonski 1984, and Tanimoto 1987, 1988, and 1989), from previous lower-mantle, body-wave studies (i.e., Clayton and Comer 1983 (see also Hager and Clayton 1989), and Dziewonski 1984) (hereafter referred to as CC and DZ, respectively), and from the results of Chapter 4 of this thesis, for errors and statistical measures of the structure.

5.2 Method

The earth is a three-dimensional (3D) object containing 3D heterogeneity. To address the potential problems of lower-mantle, travel-time studies fully, the full 3D problem should be treated. This entails a great volume of computation in order to include small-scale structure in the crust and upper mantle, and because of the vast number of individual observations over the globe. We thus reduce the problem size by taking a sample, two-dimensional (2D) great-circle cross-section of the earth. Our choice of cross

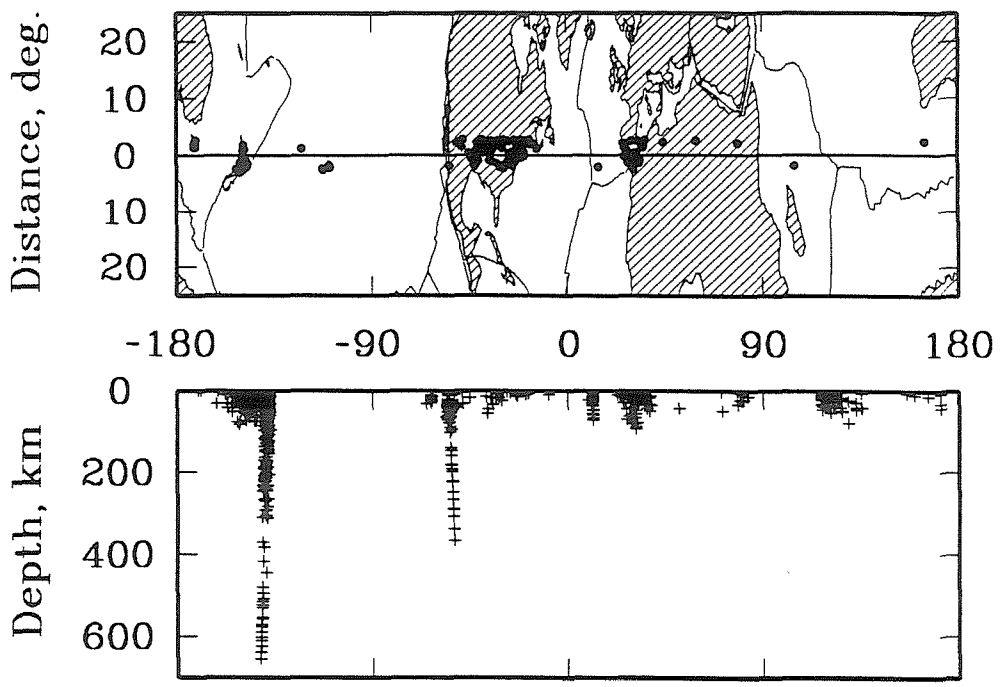

Figure 5.1. The distribution of stations and events used in synthetic case 1 (C1). The stations are selected from the ISC catalog within a distance of 2.5 degrees from the great circle drawn in the top frame. The events are selected in the same manner from the ISC catalog, except that events are added in the two subduction zones (Tonga/New Zealand and Mexico/N. America) to mimic the depth distribution of events in the entire ISC catalog. The great circle represents the cross section of the upper-mantle model DSXRG of Tanimoto (1988).

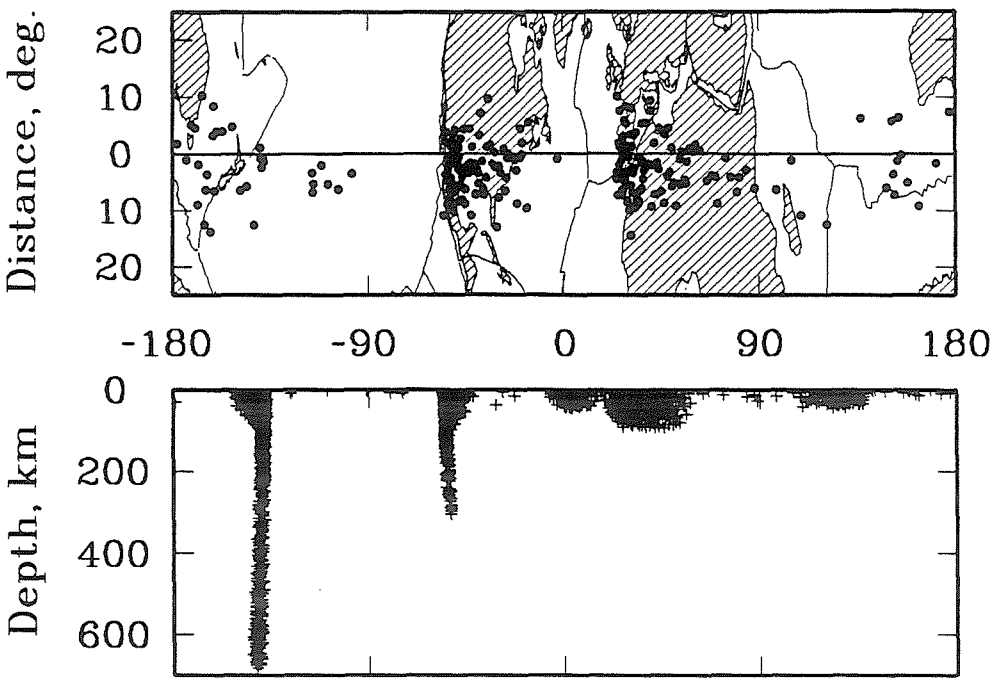

Figure 5.2. The distribution of stations and events used in synthetic case 2 (C2). Both distributions are entirely artificial and constructed to mimic a) the depth distribution of events in the ISC catalog, b) the lateral distribution of events and stations among a partition of the earth's surface into tectonic regions, and c) the clustering characteristics of stations and events in the ISC catalog. Stations are given a random distribution about the reference great circle for plotting purposes only.

section is shown in Figures 5.1 and 5.2 together with the distributions of events and stations used. Its normal vector is given by $45^o\ N$ latitude and $135^o\ E$ longitude. This great circle crosses two continents, one with abundant station coverage (N. America), the other with sparse station coverage (Africa). The continents cover about 30% of the great circle. It crosses two subduction zones, one major and deep (Fiji-Tonga), the other minor and shallow (Mexico). It crosses two midocean ridges, the North Atlantic ridge and the Indian Ocean ridge. The sparseness of recording stations and seismicity in the Pacific and Indian Oceans mimics the sparseness of sampling of the southern hemisphere of the globe in the 3D case.

It is impossible to design a 2D sample cross section of the earth that is strictly analogous to the full 3D problem. The aspects of the distribution of structure and data that one would like to mimic are:

1) The overall redundancy in the data relative to the characteristic scales of the structure.

2) The redundancy in the data relative to the number of model parameters.

3) The clustering characteristics of the data.

4) The biases in the geometrical data distribution relative to strong structural features in the earth.

5) The characteristic scale and strength of earth structure as it varies with depth.

We infer the characteristics of earth structure from current models for the crust and upper and lower mantle. We constructed two case examples of the geometrical distribution of data. Case 1 (C1) is based on the ISC data in the

vicinity of the above specified, sample great circle, but is lacking in the level of redundancy relative to the parameterization of the models we solve for. Case 2 (C2) is a completely artificial distribution of stations and events, but has comparable levels of redundancy in terms of numbers of data relative to numbers of model parameters, to the 3D problems solved by CC and DZ.

The station distribution in case C1, shown in Figure 5.1, was constructed by including all stations reporting more than 50 picks to the ISC catalog between 1964 and 1986, which are within 2.5^o from the great circle. We then added five stations to fill in uncharacteristically big gaps in the distribution. This yields 164 stations.

The seismicity distribution in case C1, shown in Figure 5.1, was constructed by including all the events reported to the ISC between 1964 and 1986 by at least 50 stations, which are within 2.5^o from the great circle. We then define Benioff-Wadati zones as linear features at Tonga (New Zealand) and Mexico and collapse the seismicity in their vicinity onto them (4/5) and in the back arc region (1/5). The Benioff-Wadati zones are given finite widths (100 - 300 km) and the events are distributed normally (Gaussian distribution laterally) within them. We then added events at depth in both subduction zones to mimic the depth distribution of seismicity according to the ISC catalog. The artificial subduction zones inserted into the distribution are not meant to resemble the actual zones the great circle crosses, but to mimic typical subduction zones. The number of events in this distribution is 1024.

If the geometrical distribution of data in the ISC catalog were uniform, model space were cubic, and the model parameterization isotropic, the 3D problem would scale to 2D by taking the 2/3 root of the number of data.

This is the criterion we used to determine the number of data in case C1. We selected the desired number of picks randomly, assigning probabilities proportional to the number of picks in the ISC catalog for each event and station included in this case. The resulting number of picks is about 26000.

Figure 5.2 shows the distribution of stations and events in case C2. We divided the great circle into tectonic provinces (subduction, tectonic, midocean ridges, intraplate). The sizes of the provinces were determined such that the proportion of the great circle length categorized by a given tectonic type was the same as the proportion of the earth's surface area categorized as that same type. We then assigned earthquake loci at random within the tectonic provinces according to the relative numbers of events within each tectonic province type in the ISC catalog. The depth was assigned at random such that the ISC depth distribution for the given tectonic type in the ISC catalog was satisfied. The lateral position was assigned at random according to a Gaussian distribution around the axes of subduction zones and midocean ridges, but a uniform distribution in tectonic and intraplate regions. The stations were selected at random from uniform deviates in oceanic intraplate regions, not at all at midocean ridges, from uniform deviates in tectonic and subduction regions, and from a decaying distribution on the continents away from adjacent tectonic or subduction zones. The total number of events and stations was selected such that the reduction from the number of events and stations in the ISC catalog was approximately the square root of the reduction of the number of generated picks from the number of picks in the ISC catalog. The number of P-wave picks was determined in this case such that the ratio of picks to model parameters is the same as in the case of CC for analogous model parameterization. The picks were distributed among the

	ISC	I	II
stations	1,650	164	245
events	25,000	1,024	4,981
P-picks	3,000,000	26,024	120,000
P-srays	100,000	987	3,671
PcP-picks	35,000	1,331	1,327
PKPab-picks	20,000	941	734
PKPbc-picks	400,000	4,677	15,509
PKPdf-picks	500,000	6,356	16,493

Table 5.1. Numbers of events, stations, and picks of various phases in the ISC catalog (1964-1986) and the two synthetic cases set up in this study. I refers to C1, II to C2.

station-event pairs that fall in any given epicentral distance window such that the epicentral distance distribution in the ISC data was satisfied. The number of stations, events, and picks in this case is 245, 4981, and 120000, respectively.

Table 5.1 shows a count of the number of picks of some of the compressional phases reported to the ISC between 1964 and 1986, as well as the number of stations and events with more than 50 picks in the same period. No windowing of crossovers of travel-time branches, or selection according to maximum travel-time residual has been applied. The P-data include everything between epicentral distances of 25^o and 95^o. PKPbc picks are counted, assuming that 85% of all PKP picks between distances of 143^o and 154^o are PKPbc (Anderssen and Cleary 1980). The remaining 15% are counted as PKPdf. Numbers of stations, events, and picks of all the compressional phases used in this study in both synthetic cases (C1 and C2) are also given in Table 5.1.

We constructed three basic models. Model UML is a model of large-scale slowness variations in the upper mantle. Model UMS is a model of small-scale slowness variations in the crust and upper mantle. Model LM is a model of slowness variations in the lower mantle.

Shallow heterogeneity in the earth is known to correlate well with surface tectonics on large scales and thus the distribution of data in the ISC catalog. There is therefore potential for the bias of lower-mantle models from shallow heterogeneity. The best global models of shallow heterogeneity come from surface-wave tomography (e.g., Woodhouse and Dziewonski 1984, Tanimoto 1987 and 1988). These studies are primarily sensitive to shear-velocity variations. We took the DSXRG model of Tanimoto (1988) as the

basis for our UML model. For a Poisson solid with correlated velocity variations (S- and P-wave), travel-time residuals scale with slowness perturbations. Observations of the ratio of S- to P-wave station corrections are generally close to 4 seconds (e.g., Hales and Doyle 1967, Souriau and Woodhouse 1985), although Romanowicz and Cara (1980) suggest that this high ratio may be an artifact for USA stations. To convert the DSXRG model to a viable compressional-velocity model, we thus scaled it by a factor of 1/4 in terms of slowness. We took the same great-circle cross-section of the model as was used in constructing the event and station distributions in case C1 (see Figure 5.1). We then inserted slablike anomalies at Tonga (New Zealand) and Mexico, that coincide with the Benioff-Wadati zones in the data distribution. These anomalies are Gaussian in the lateral dimension of widths 100 - 300 km and have a maximum strength of relative velocity variation of 5%. This is in accord with seismic studies of slab structure (Mitronovas and Isacks 1971 and Suyehiro and Sacks 1979) and thermal modeling of slabs (e.g., Schubert et al. 1975). The width was increased linearly with depth, and the relative strength decreased linearly with depth to 2.5%. We also inserted spherical, Gaussian, slow anomalies in the back-arc regions at a depth of 200 km with a radius of 100 km and maximum strength of 2.5%. These structures are similar to features in the Hellenic model of Spakman et al. (1988). These slab features are not large scale in the lateral dimension, but they are strong structural features, which correlate with the data distribution. Model DSXRG of Tanimoto (1988) includes harmonic degrees up to $l = 8$. The results of Chapter 4 of this thesis indicate that above a depth of 400 km significant power extends beyond that scale. Given the results presented in Chapter 4 we added randomly selected harmonic components to model UML

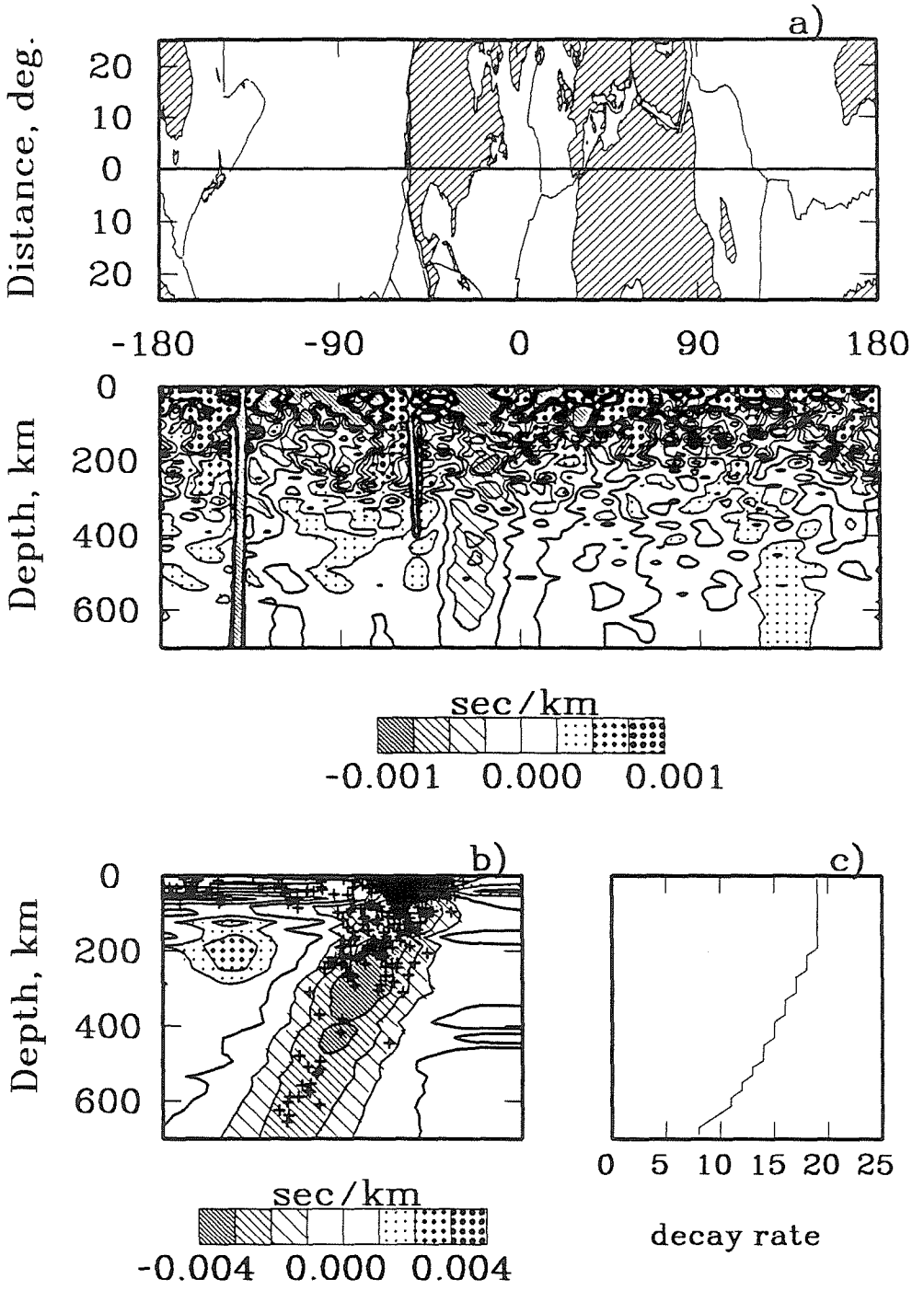

Figure 5.3. The large-scale, upper-mantle model (UML) used for both C1 and C2. It was constructed from a great-circle cross-section of model DSXRG of Tanimoto (1988). This shear-velocity model was scaled by a factor of one-quarter in terms of slowness. We then inserted artificial slab-structures into it (at New Zealand and Mexico), and, finally, appended the power spectrum of the model according to the decay rates presented in c), given here as the harmonic-degree half-width of the spectrum. Figure b) shows an enlargement of the New Zealand subduction zone and its seismicity.

consistent with a Gaussian decay of the power spectrum with a half-width of $l = 10 - 15$. The resulting model, UML, is plotted in Figure 5.3a. The structure near the Tongan slab is highlighted in Figure 5.3b. The imposed spectral decay beyond degree $l = 8$ is shown in Figure 5.3c.

Model UMS is meant to describe the small-scale structure of the upper mantle. Localized scattering studies at dense arrays (e.g., NORSAR and LASA) indicate that in the top 150 km of the earth the small-scale velocity structure is characterized by 5% variations on a characteristic scale of 10 km (e.g., Aki 1973). The results of Chapter 4 are consistent with this. We took the results presented in Chapter 4 for the variation of small-scale power with depth in the upper mantle, assumed a correlation length of 10 km and constructed the UMS model accordingly (see Figure 5.4). This was done by parameterizing the model at a 10 km scale and selecting incoherent random numbers for the model parameters from a Gaussian distribution with standard deviation as a function of depth according to Figure 5.4.

Global models of slowness heterogeneity in the lower mantle agree to within a factor of two on the rms (root-mean-square) level of heterogeneity (see Figure 4.19). The models of CC, DZ, Tanimoto (1989) (S-velocity), and our results from Chapter 4 agree on an rms low in the central lower mantle and an increase towards both the core-mantle boundary (CMB) and the upper mantle. These studies are also consistent with a characteristic scale length of heterogeneity throughout much of the lower mantle of the order of 1000 km. We took the results from Chapter 4 for the power and correlation length of slowness variations in the lower mantle and constructed a model accordingly. The construction was done by generating an incoherent random field at a parameterization interval of 1^o (60 - 100 km). We then convolved

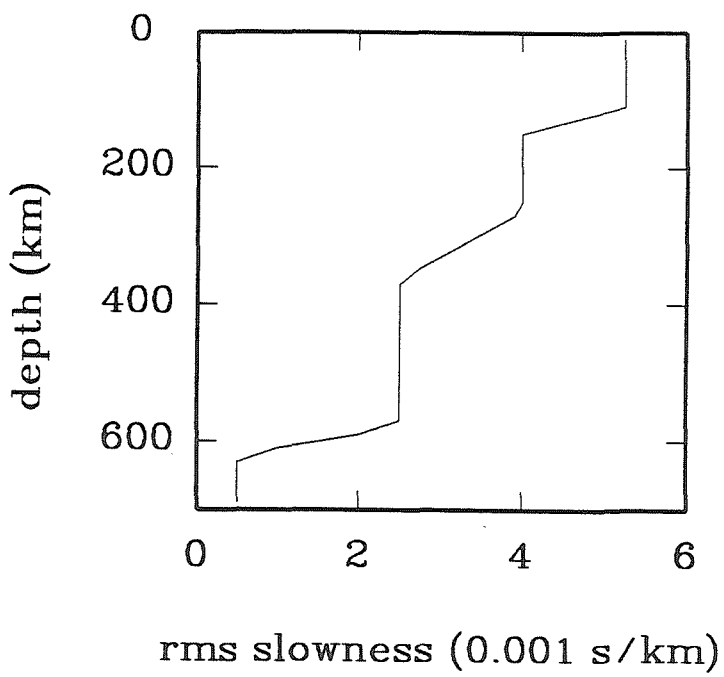

Figure 5.4. The small-scale upper-mantle model (UMS) used for both C1 and C2. It was constructed by a random process yielding a model of 10 km correlation length and rms level as a function of depth as shown here.

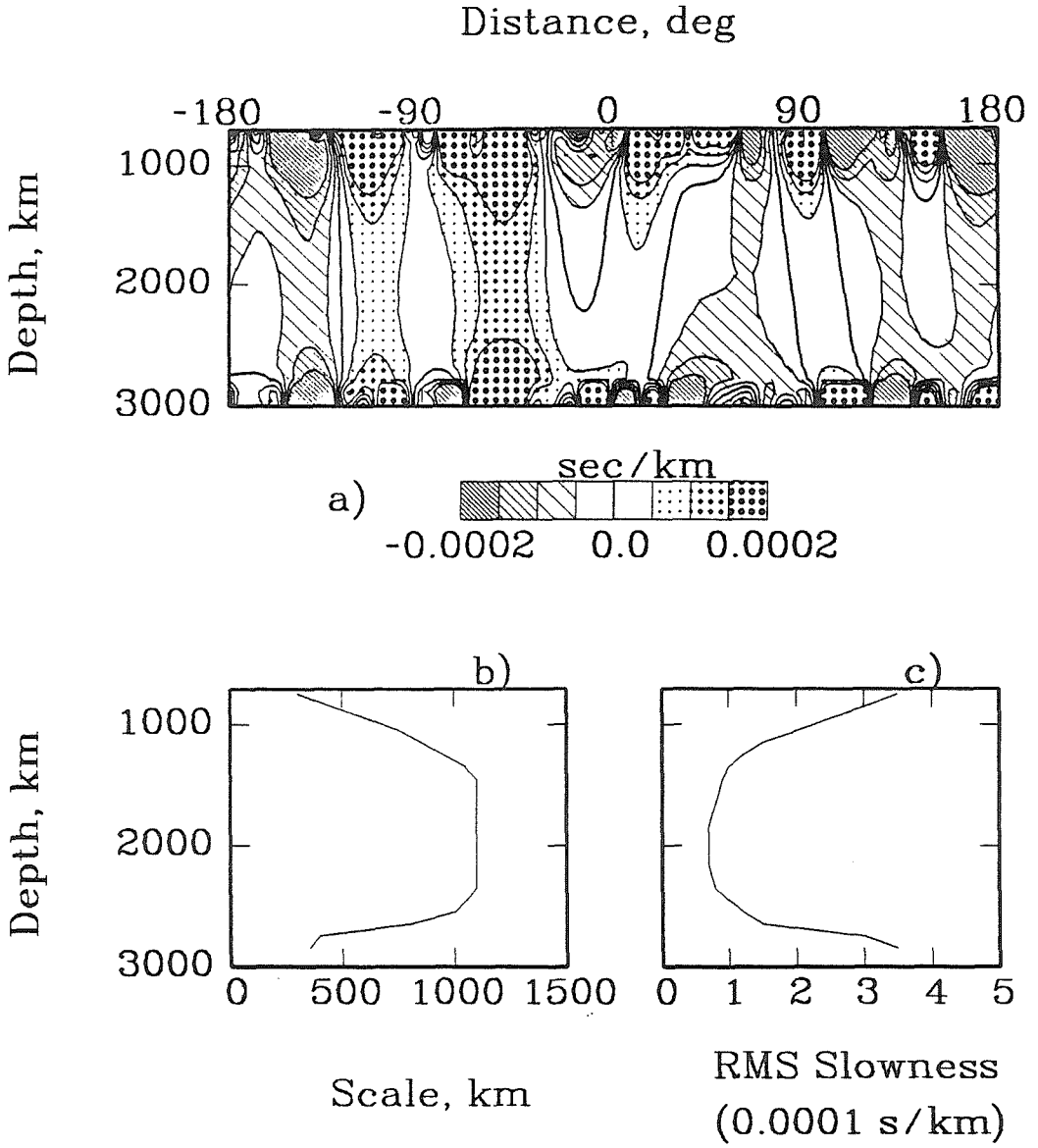

Figure 5.5. The lower-mantle model (LM) used for both C1 and C2. a) A contour map of the model. b) The variation of correlation length with depth. c) The variation of the rms level of the model as a function of depth. The model was constructed by an incoherent, random, number generator, then smoothed according to b), and, finally, the amplitude was adjusted according to c).

that field with a Gaussian function of width varying with depth according to the specified correlation length. Power was then adjusted according to the results of Chapter 4 depth layer by layer. The resulting model, LM, is shown in Figure 5.5a. The variation of correlation length with depth is shown in Figure 5.5b, and the variation of the rms level of heterogeneity with depth in Figure 5.5c.

We used the spherically symmetric, reference velocity-model of Jeffreys and Bullen (JB) (Jeffreys, 1939) and power-law ray-tracing (see Bullen, 1979) to construct ray geometries. The above models were densely parameterized by small constant value cells and they integrated along the rays according to the simple, linearized, ray-theoretical, travel-time integral

$$\delta t = \int_{ray} \delta u ds ,$$

where δt stands for travel-time residual, δu for slowness perturbation and ds for incremental length along the ray.

Finally, we took the estimates of error in the ISC P-wave data from Chapter 4 of this thesis (see Figures 4.4 and 5.6) and added to the data randomly generated numbers with variance according to Figure 5.6. The data then consist of four distinct contributions: from models UML, UMS, LM, and from random errors. The variances of the individual contributions to all the data are shown in Tables 5.2 and 5.3 for cases C1 and C2, respectively. The two tables are similar except for the difference in UML contributions to the PKPab and PKPbc data sets. This could be coincidental, as the relative distribution of these data to the UML model is quite different.

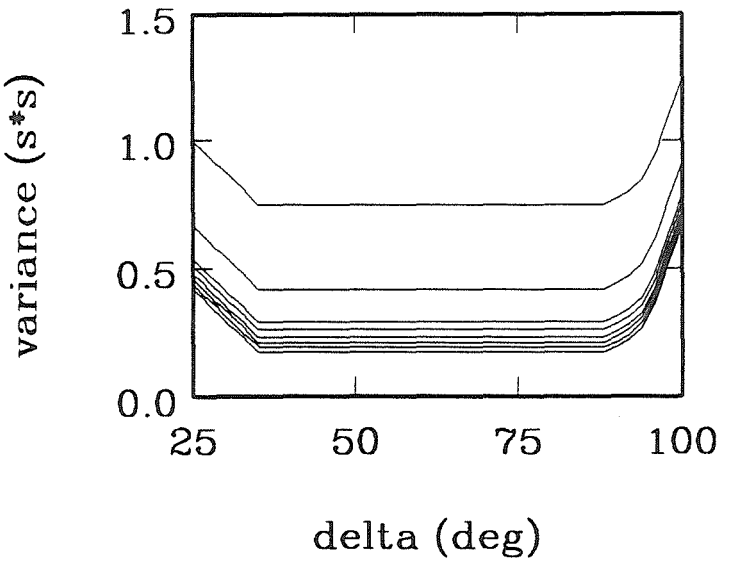

Figure 5.6. The variation of random-error variance with epicentral distance and source depth for the P-wave data. The different curves represent different source depths, with the highest variance for shallow events, and the variance monotonically decreasing with source depth. The eight curves are at 100 km increments in depth.

phase	UML	UMS	LM	ERR	TOT
P	0.82	0.20	0.24	0.72	2.11
PcP	0.96	0.14	0.16	0.87	2.03
PKPab	0.49	0.12	0.38	0.94	1.99
PKPbc	0.53	0.13	0.06	0.93	1.73
PKPdf	0.78	0.12	0.14	0.87	2.08

Table 5.2. Variances of the various contributions to the different data sets constructed in synthetic case C1. UML represents contributions from the upper-mantle UML model. UMS stands for contributions from the upper-mantle mantle UMS model. LM stands for contributions from the lower-mantle LM model. ERR stands for contributions from random errors. TOT refers to the total variance of each data set prior to relocations or static corrections.

phase	UML	UMS	LM	ERR	TOT
P	0.90	0.22	0.34	0.63	2.21
PcP	0.87	0.15	0.21	0.86	1.98
PKPab	1.10	0.13	0.20	0.96	2.33
PKPbc	1.13	0.14	0.16	0.84	2.22
PKPdf	0.96	0.14	0.19	0.84	2.21

Table 5.3. Variances of the various contributions to the different data sets constructed in synthetic case C2. UML represents contributions from the upper-mantle UML model. UMS stands for contributions from the upper-mantle UMS model. LM stands for contributions from the lower-mantle LM model. ERR stands for contributions from random errors. TOT refers to the total variance of each data set prior to relocations or static corrections.

The ISC travel-time residuals are given relative to the JB model and event locations made by the ISC with teleseismic compressional data (mantle P-waves and PKIKP-waves). Some studies have referenced the travel-time data to the PREM model and appropriately relocated the events. The use of teleseismic data to locate events can introduce significant errors in location because of small-scale lateral structure, particularly around the event, that may introduce spatially systematic errors in the travel-time residuals. We therefore relocate all events laterally, based on the synthetic data that we compute, based on what are exact locations. The initial location in the relocation is the exact location. We relocate only laterally, because of the unresolved trade-off of origin time and source depth, because of the use of teleseismic data only. We use our synthetic data sets for P-waves and PKIKP-waves in the relocation (These are the first arrivals at almost all distance ranges). The results of the relocation are shown in Figure 5.7 for both cases (C1 and C2). The patterns of relocations are quite similar for the two cases, largest for the subduction events, and of the order of 20 km where largest. This is similar to the results of Mitronovas and Isacks (1971), Engdahl et al. (1977), and Fujita et al. (1981) for real subduction-zone events. A ten km relocation introduces an error of up to the order of 1 second (mantle velocity is of the order of 10 km/sec).

The next step in the data processing was applying static station and event corrections, using the method of CC. This was done by an iterative scheme, where first the average residual for each event is explained by an event correction, then having corrected the data for the event correction, the average residual of each station is attributed to a station correction and removed. This cycle is repeated until convergence is reached. The event

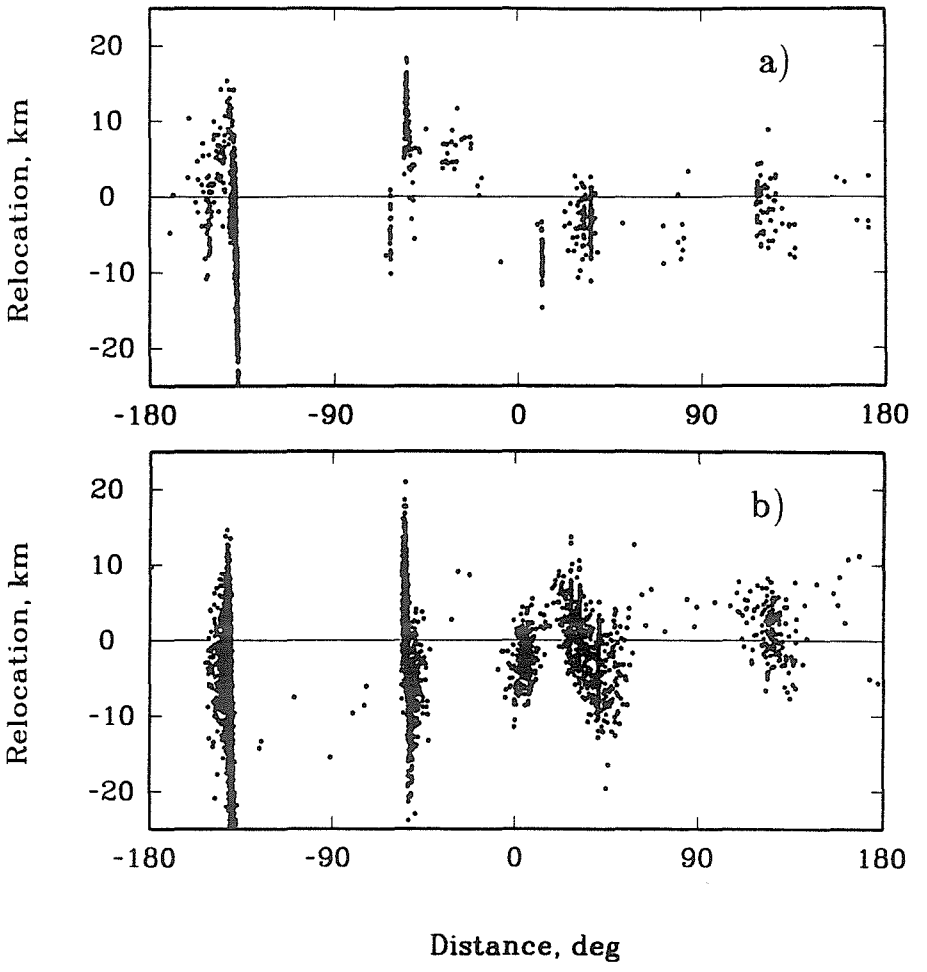

Figure 5.7. The results of lateral relocations of the events a) used in case C1, b) used in case C2. The relocation is one-dimensional and plotted in km. The sign indicates whether the events were relocated clockwise or counter-clockwise.

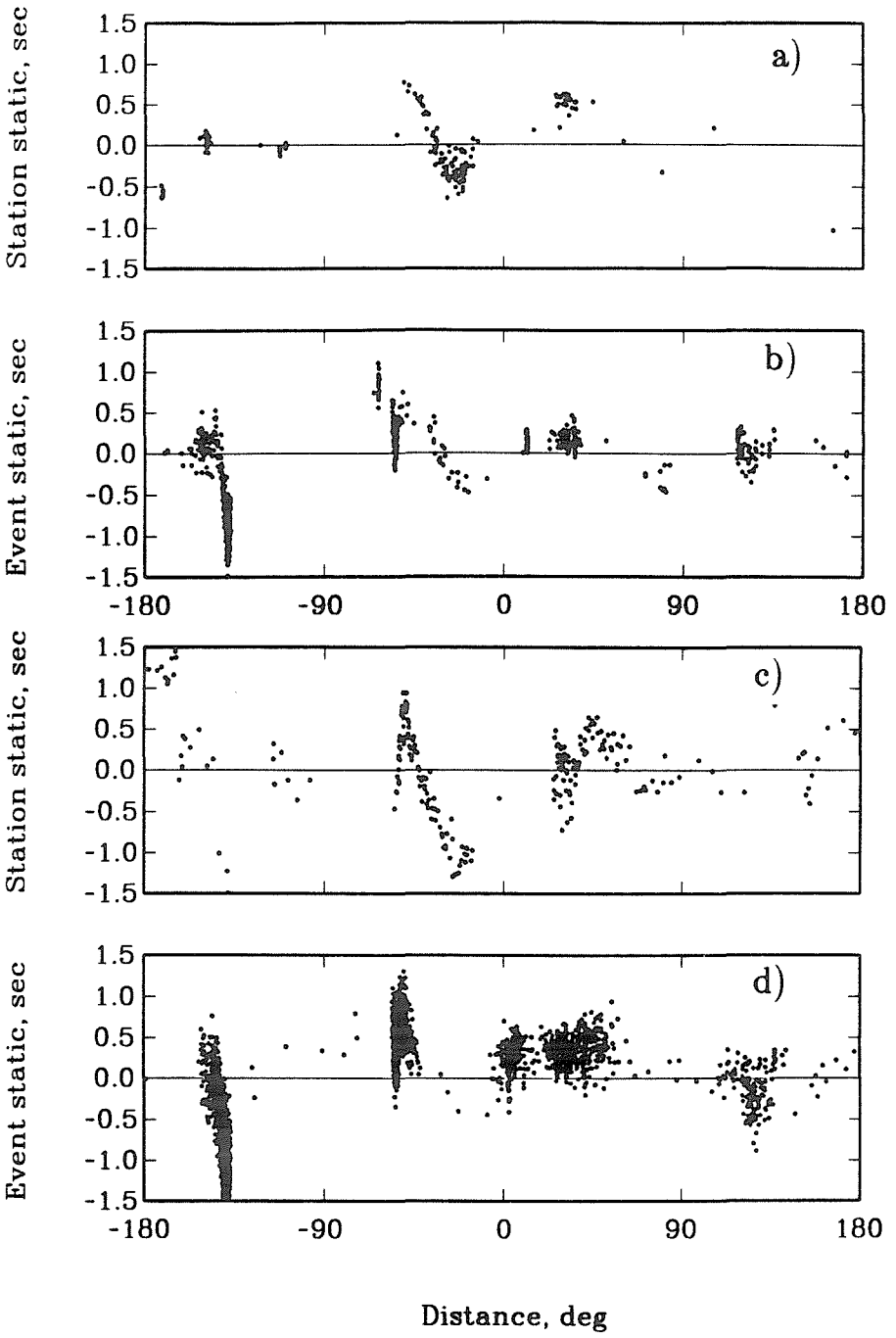

Figure 5.8. Event and station static corrections a) and b) for case C1, c) and d) for case C2. Both are plotted in seconds and against position along the reference great circle. Note the similarities between the two cases and the apparent correlation with the main features of model UML.

correction is roughly equivalent to relocation in depth and origin time. The results of the statics are shown in Figure 5.8 in the same format as the relocation results. Figure 5.8a shows the individual station statics in case C1 as a function of position along the great circle; Figure 5.8b shows the event static corrections in case C1 as a function of great-circle position; Figure 5.8c shows the station statics in case C2, and Figure 5.8d the C2 event statics. Event statics are generally negative in the Tonga subduction zone, particularly within the slab, and in the Mexican subduction zone event statics are negative relative to a positive regional trend. The Mexican subduction zone is immersed in a regional slow anomaly. The patterns of event and station statics are similar for both cases C1 and C2. The shallow fast anomaly under N. America is associated with negative event and station statics. The shallow, slow anomaly under the western margin of N. America coincides with positive station and event statics. The positive corrections in the eastern Atlantic and African region are due to an overall slow upper mantle. Thus the static corrections correlate well with the strongest features of model UML. This is what one hopes for, as the statics are the simplistic way lower-mantle, travel-time studies typically attempt to account for upper-mantle structure.

The final step in the data processing was the formulation of summary rays (see, e.g., Dziewonski 1984). In order to reduce the volume of the inverse problem and to give regions at the earth's surface a more equal weight in the inversion for lower-mantle structure, previous studies have applied the summary-ray concept. The earth's surface is divided into patches of uniform size, and all rays with endpoints within common patches are lumped together. Those rays have similar travel paths through the lower

mantle (and core) and thus sample deep, large-scale anomalies similarly. They may pick up a variable signal from small-scale, shallow structure, which will cancel. Furthermore, if a large number of rays pass through a shallow seated anomaly, its effect is given reduced weight by collapsing all the rays into a single summary ray. The density of coverage in the lower mantle is evened. We applied summary rays at a scale of 5^o in case C2 as did CC and DZ, but at a scale of 2.5^o in case C1 in order to adjust the level of redundancy (relative number of summary-ray data and model parameters). The number of summary rays for P-waves was 760 and 3670 for cases C1 and C2, respectively.

Finally, we inverted our processed, synthetic P-wave data sets for structure in the lower mantle, using similar procedures to those applied by CC and DZ. This involves two significantly different inversion techniques (which yield significantly different results). The technique of DZ expands the model in terms of a small number of continuous, orthonormal basis functions and applies a standard least-squares method to solve for the coefficients of each function. The functions used are the five lowest-order Legendre polynomials in depth and the 7 lowest-degree spherical harmonics laterally. We will hereafter refer to this technique as THE (truncated harmonic expansion). The technique of CC divides the model into discrete boxlike cells, assumes a constant slowness perturbation within each cell, and applies an iterative back-projection inversion scheme to solve for a large number of model parameters. We will hereafter refer to this technique as BP (back-projection). Our adaptation of the THE method uses 5 Legendre polynomials to expand the depth variation and a truncated (at $l = 6$) discrete Fourier transform to expand the lateral variation (spherical harmonics in the plane of

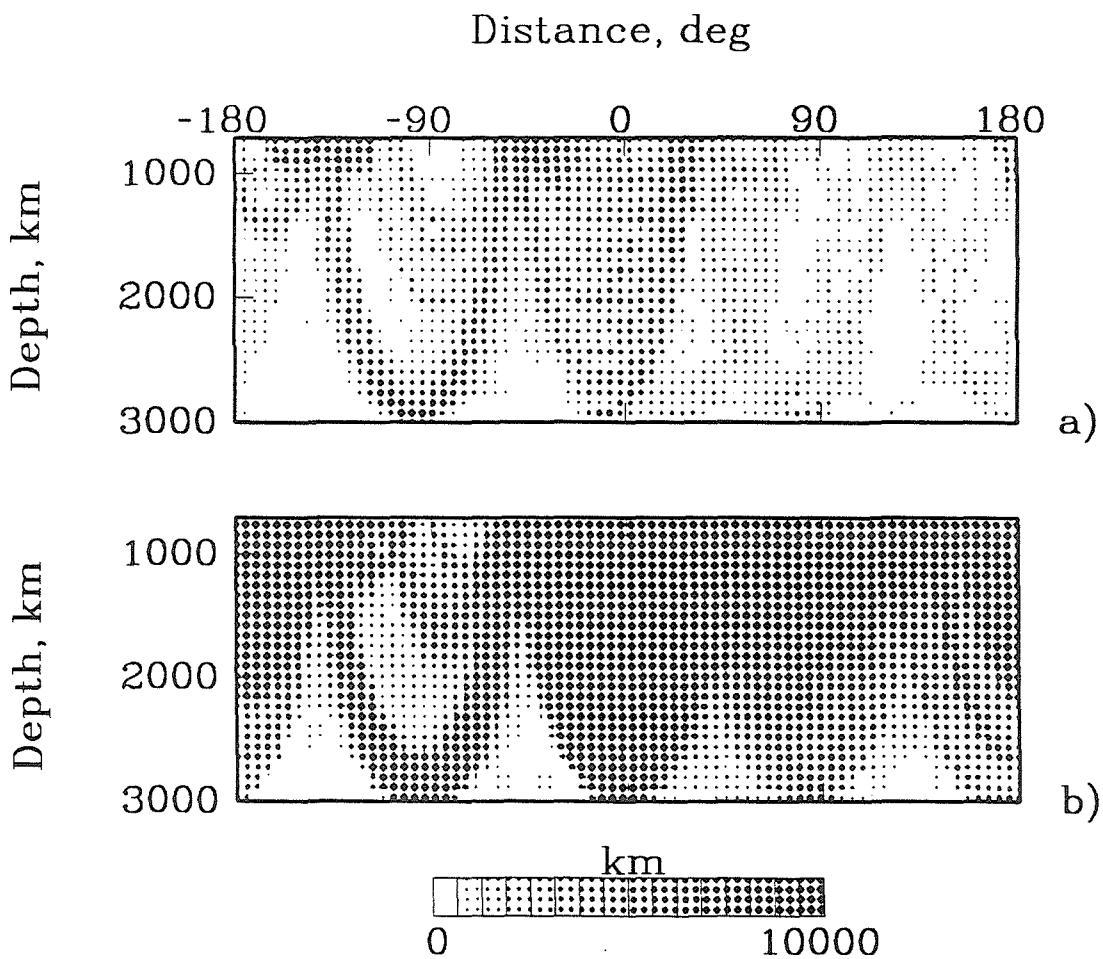

Figure 5.9. Hitcounts in the lower mantle a) for case C1, b) for case C2. Here hitcount is presented in terms of the total path length within each model cell in the discrete parameterization of the BP method.

the equator). This level of parameterization is equivalent to that used by DZ for the 3D earth. The level of parameterization in the BP method is also kept equivalent to that used by CC. The binning interval in depth is 100 km and in the lateral dimension is 5^o. The damping parameter used in the application of the BP method is $\mu = 50$ km, or the same used by CC in their global inversion. In applying the BP method we used data from all source depths, while in applying the THE method we used only data from shallow events ($Z < 50$ km). All comparisons of the results of the two methods and with the LM model are done with equally parameterized models. The THE parameterization is the sparsest one. The BP and LM models (finely discrete) were expanded a posteriori, out to degree 10 and using 8 depth polynomials, by a least-squares fit. Only those parameters equivalent to those used in THE are included.

Figure 5.9 shows the ray coverage in the lower mantle in cases C1 and C2 in terms of the total, ray path-length within each model cell in the BP parameterization. The coverage is considerably better in the C2 case, since the total number of summary rays is about five times greater. The coverage is relatively poor at the base of the mantle in both cases. Rays from Tongan events to American stations give an illusion of reasonable coverage under the Pacific. However, this densely covered path is not crossed by many other paths.

5.3 Results

The results of the inversion of the P-wave data set, which includes all contributions of signal and error, by both the BP and THE methods are shown in Figures 5.10 and 5.11 for cases C1 and C2, respectively. The center frame shows the LM model for reference. The contouring is the same for all models. It is clear from these figures that the success of the inversion is marginal. The BP model is lacking in power at the top of the lower mantle relative to LM in both cases C1 and C2. The THE model has excessive power throughout the lower mantle relative to LM in both cases. The visual correlation of the models is reasonable at best and poor at the top and bottom, particularly in case C1. Figures 5.12 through 5.15 show the standard deviation (root-mean-square anomaly) of the models and their depth by depth correlation. Analogous parameters for the 3D results of CC (model CC) and DZ (model DZ) are shown for reference. Figure 5.12 includes harmonic degrees 1,2 and 3 and shows the results in case C1. The behavior of the rms slowness is similar for the 2D synthetic case and the 3D case. The DZ model is consistently about a factor of two higher in amplitude than the CC model and the THE model is about a factor of 2 bigger than model BP. The power in model BP falls closer to the power of model LM than does the power of model THE. Models CC and DZ correlate consistently positively at this parameterization, but at a relatively low level of $R \approx 0.6$. The correlation of models BP and THE is also consistently positive and somewhat higher, $R \approx 0.7$. However, each of the models correlate significantly worse with the LM model. In particular, the correlation goes to zero or negative values at the top and bottom of the lower mantle. Figure 5.13 shows harmonic degrees 1 through 6 of the results from case C1. The behavior of rms slowness is still

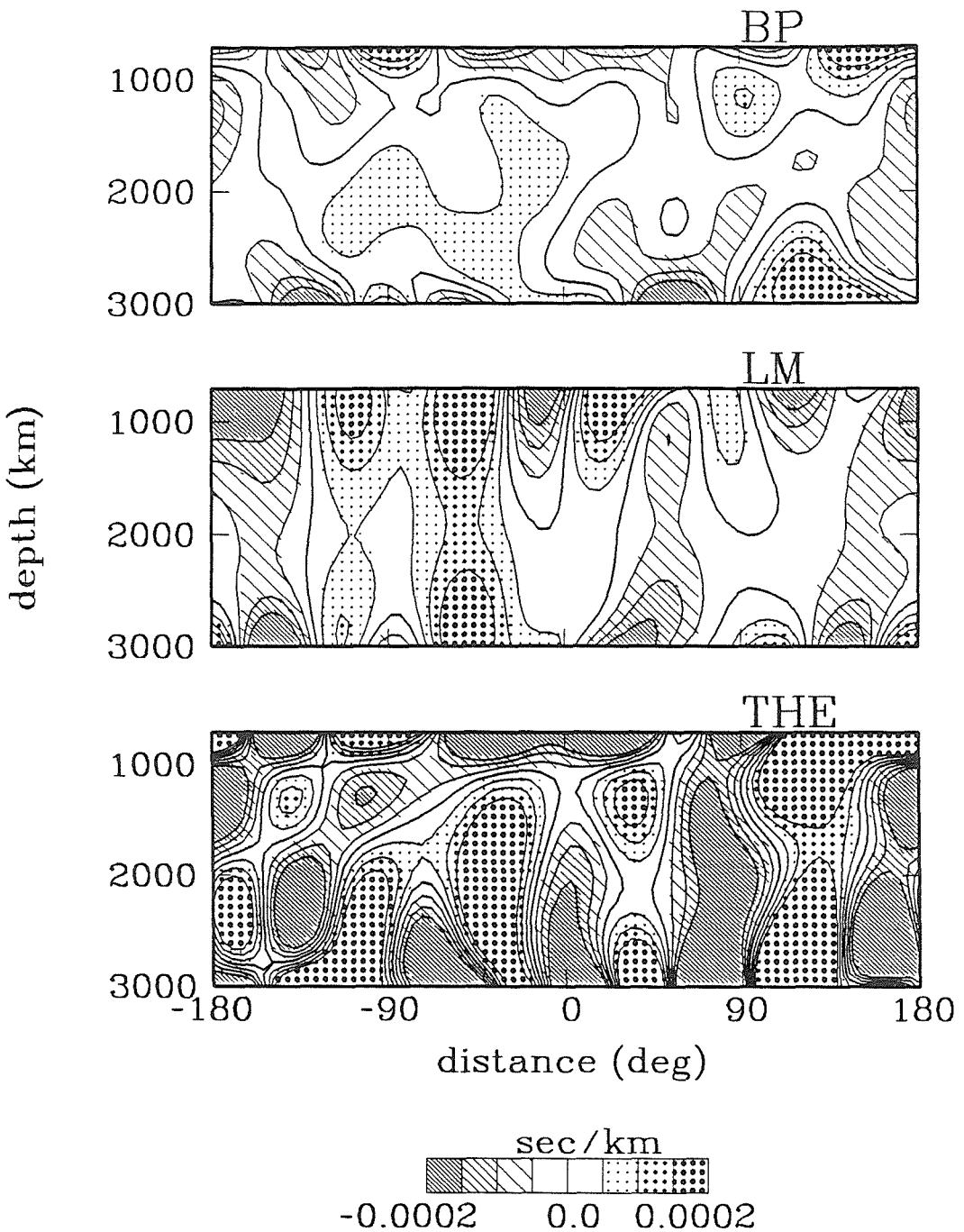

Figure 5.10. The result of inversion for structure in the lower mantle by the BP and THE methods for case C1. The LM model is plotted for reference.

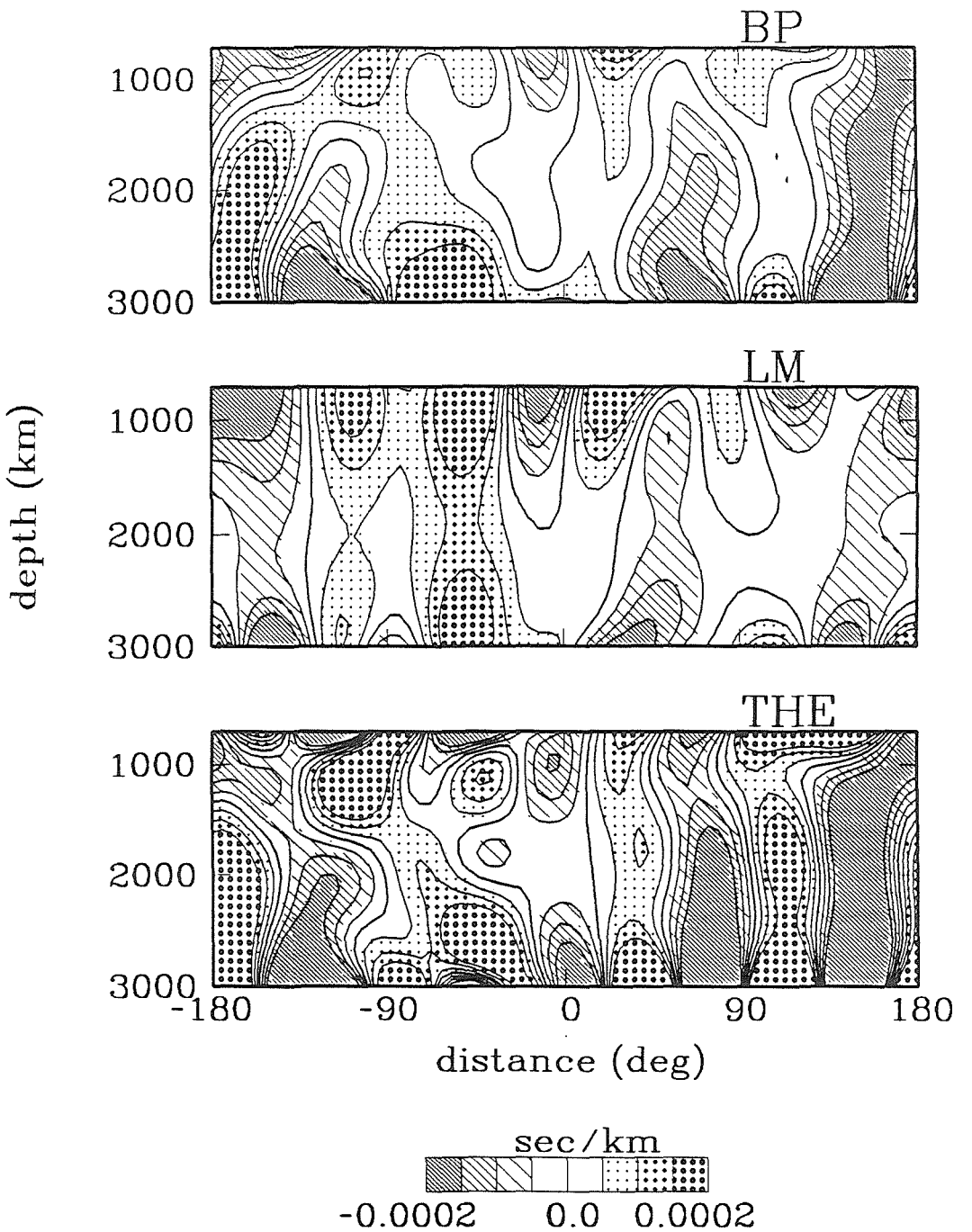

Figure 5.11. The result of inversion for structure in the lower mantle by the BP and THE methods for case C2. The LM model is plotted for reference.

Figures 5.12 - 5.15. The variation of the rms level of slowness anomalies and correlation coefficients as functions of depth in the lower mantle. In a) we plot the rms level of models CC (solid line) and DZ (dashed line). In c) we plot the correlation coefficient of models CC and DZ. In b) the solid line represents the BP model, the dashed line the THE model and the doubly dashed line the LM model. In d) the solid line is the correlation between BP and THE, the dashed line the correlation between BP and LM and the doubly dashed line the correlation between THE and LM.

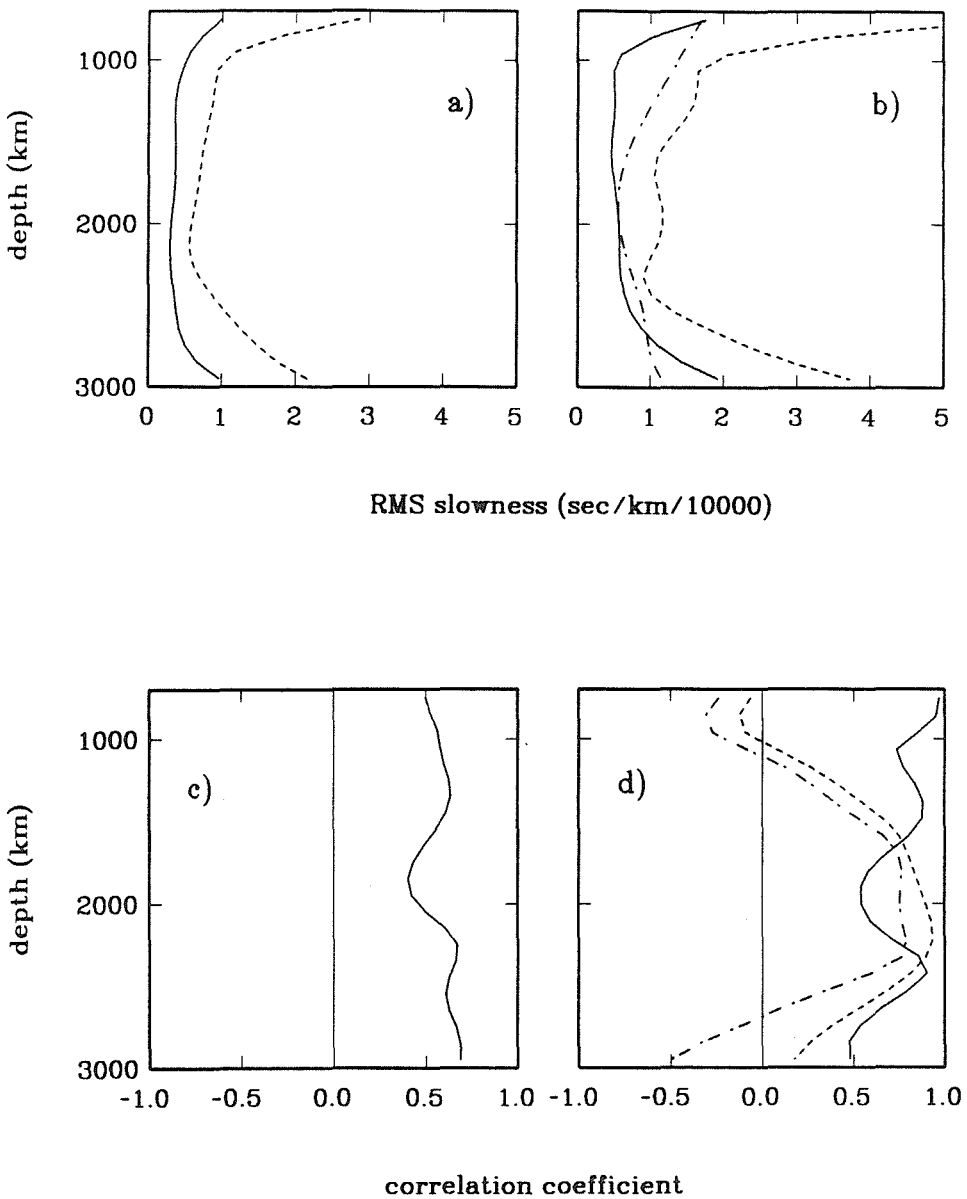

Figure 5.12. Case C1. Degrees 1 through 3.

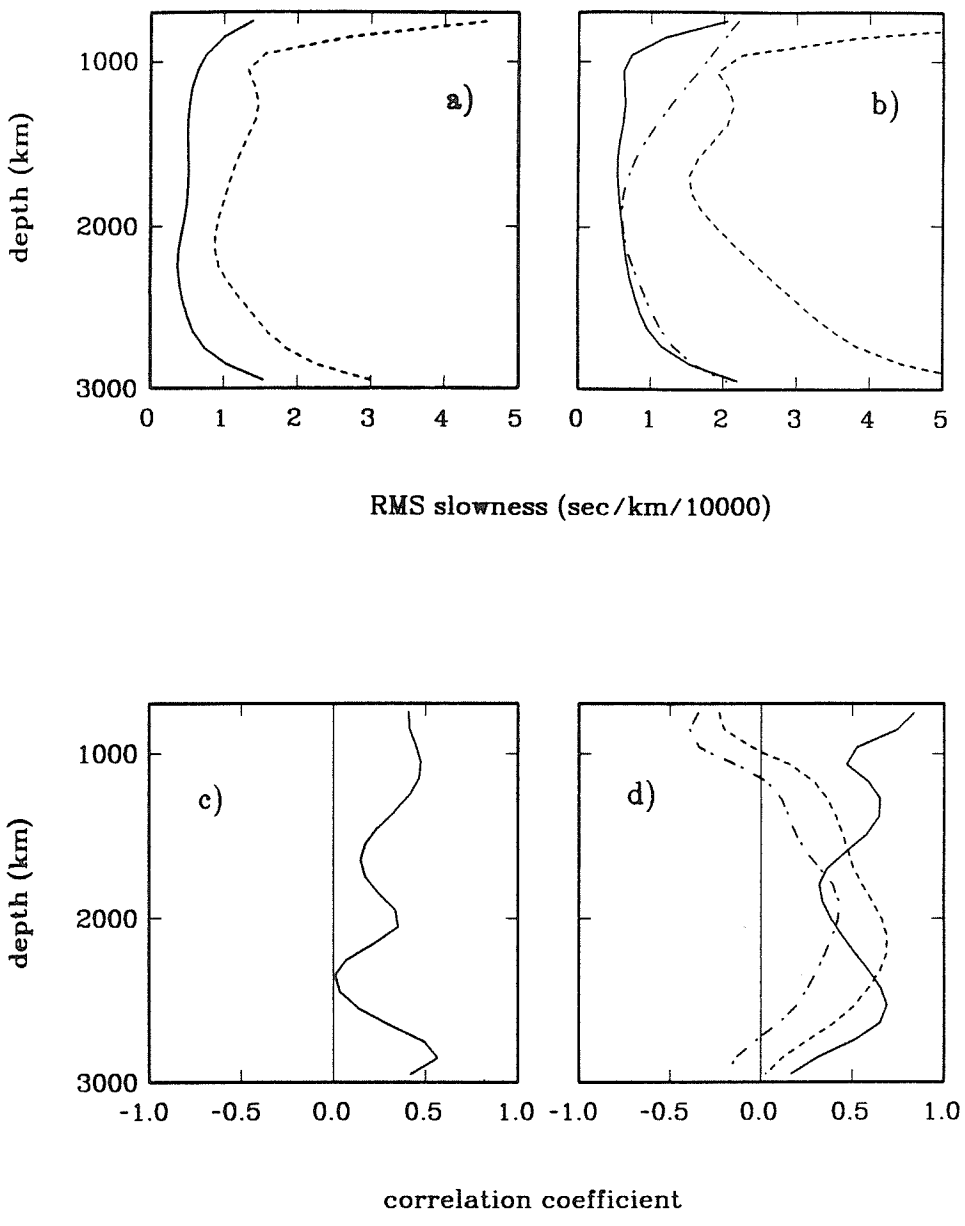

Figure 5.13. Case C1. Degrees 1 through 6.

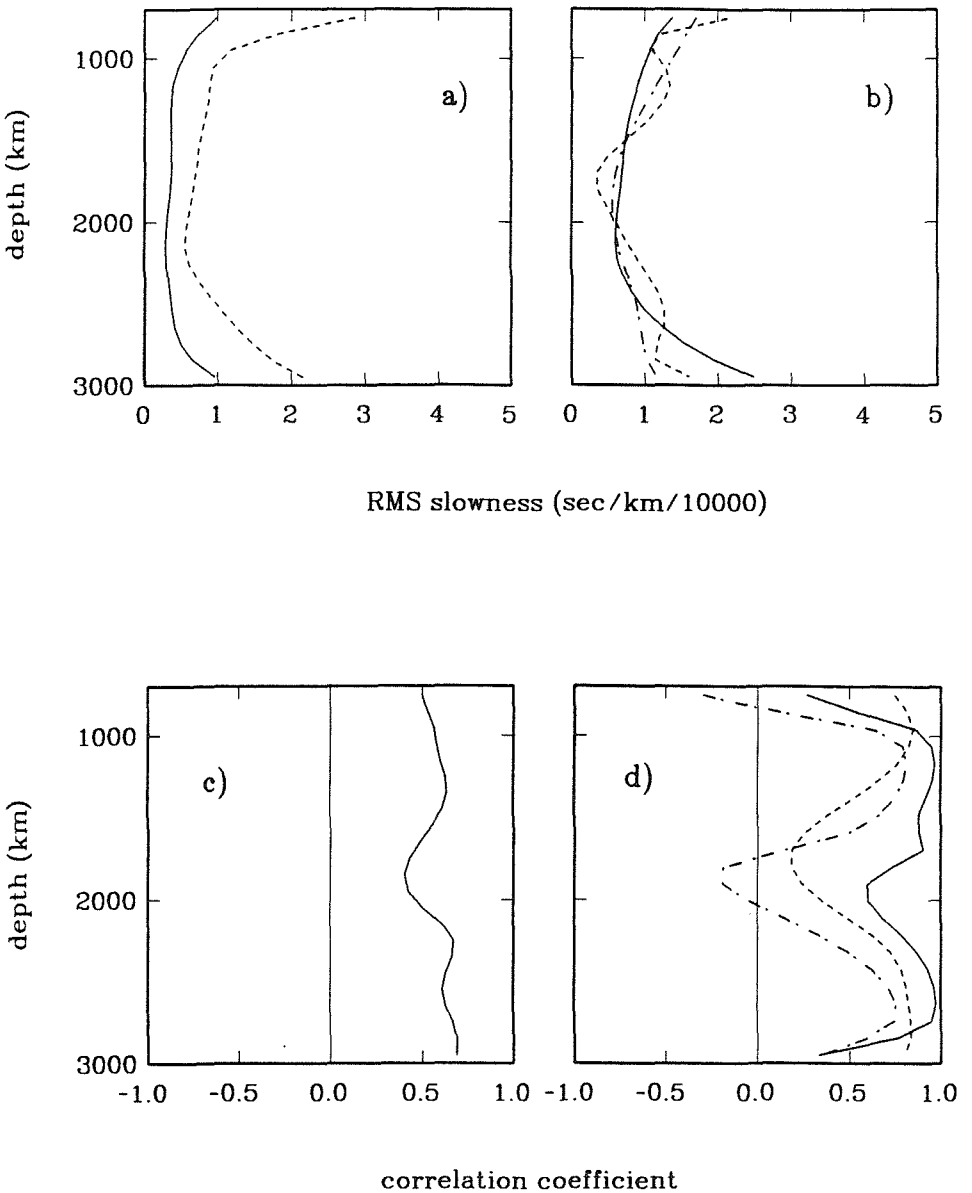

Figure 5.14. Case C2. Degrees 1 through 3.

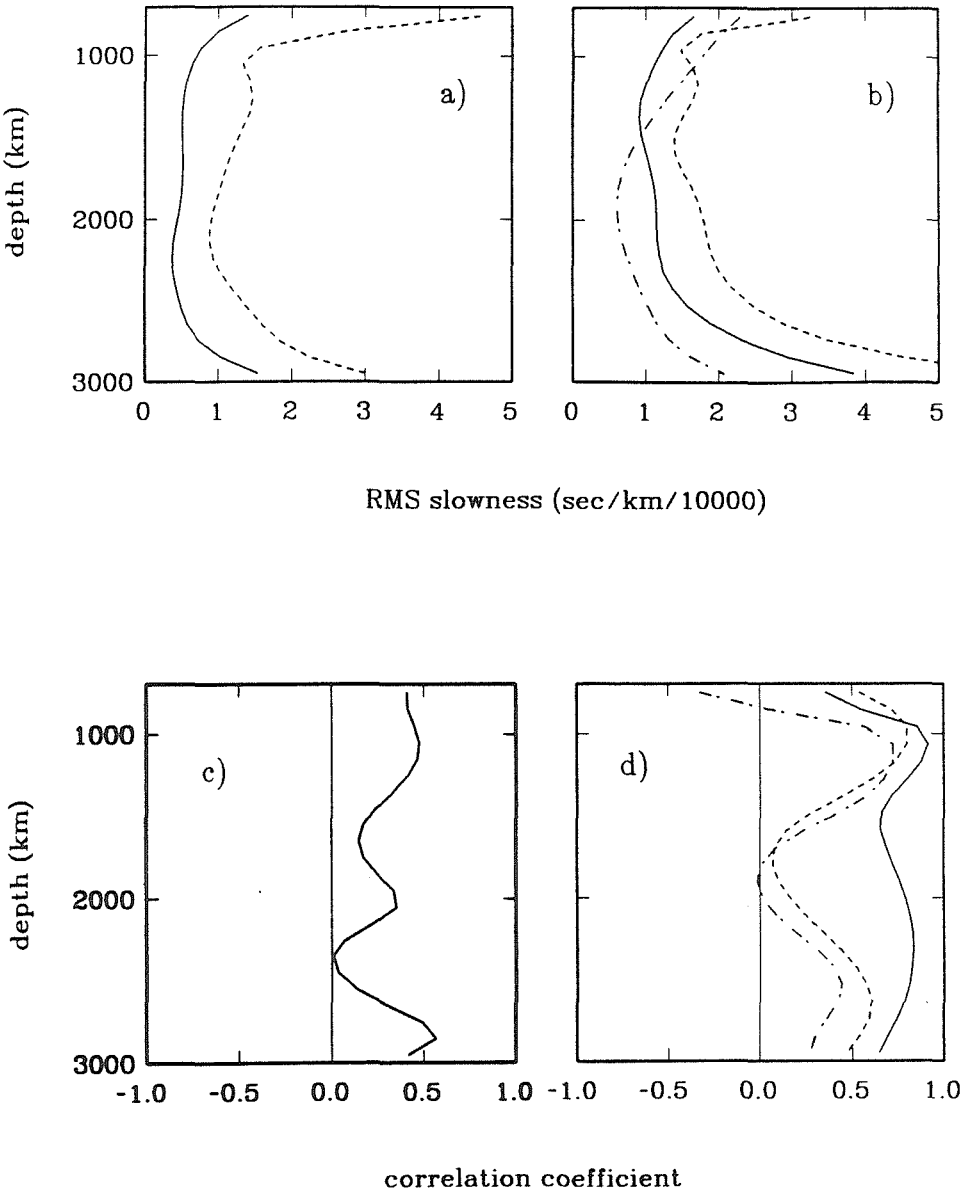

Figure 5.15. Case C2. Degrees 1 through 6.

similar for the 2D and 3D cases. The amplitude discrepancy between THE and BP is in this case magnified over the discrepancy between DZ and CC. The correlation of CC and DZ on one hand, and BP and THE on the other is still positive overall and somewhat higher in the latter case. Figure 5.14 shows degrees 1,2, and 3 for case C2. In this case the rms slowness is similar for all of LM, BP, and THE. The correlation of BP and THE is very high throughout much of the lower mantle, drops towards the top and bottom and drops slightly in the lower mantle. The correlation of models BP and THE with LM is in this case low in the center of the lower mantle and remains positive at the top and bottom, while dropping somewhat. Figure 5.15 shows degrees 1 through 6 of the results from case C2. Here the amplitude discrepancy between BP and THE reappears, but in the lower part of the lower mantle both models overestimate the rms slowness of the LM models significantly. The correlation of THE and BP is similar to Figure 5.14, only slightly reduced. The higher correlation of BP and THE than CC and DZ in both cases C1 and C2 may be an indication that the problems with the data are underestimated in this 2D synthetic example. Bear in mind, however, that the 3D expansion up to degree 6 involves 48 parameters, while the 2D expansion up to degree 6 involves only 12. The lower the number of parameters the more likely random components in the field correlate. This discrepancy may be a manifestation of this numbers effect. The BP model correlates significantly better with the LM model than does the THE model. This may be due to the lower level of parameterization, i.e., aliasing, or that in the application of the THE method we used only shallow events ($Z < 50$ km), as did DZ. Shallow data are more evenly distributed than deep data, but contain larger random errors (see Chapter 4) and pick up a higher

contribution from upper-mantle structure. On the other hand, deep events may be more likely to be poorly located because of the strong lateral velocity anomalies of subducting slabs.

We can apply a significance test to the correlation coefficient similar to the student T-test or the χ^2-test. The correlation coefficient of two N-long strings of numbers taken from the same Gaussian distribution follows a distribution that approaches a Gaussian distribution at high N. The standard deviation of this distribution behaves as $\sigma = 1/\sqrt{N}$. Thus, we calculate that the overall correlation of models CC and DZ for harmonic degrees 1-3 and 1-6 is about the 2σ level. The probability that this correlation is coincidental is very low (2.5%). We calculate that the correlation of models BP and THE is about 1.7σ in case C1 and about 2.0σ in case C2. The probability that this correlation is coincidental is about 4.5% and 2.5%, respectively. Thus, the lower correlation in the 3D case is actually more significant than the higher correlation in the 2D C1 case and about as significant as the correlation is the 2D C2 case. In both cases the correlation is highly significant. That is not necessarily to say that the noncoincidental cause of the correlation is lower-mantle structure. In fact, the poorer correlation of the BP and THE models with LM than with each other implies that it is not so. The problem evidently lies in the data values rather than in their spatial distribution.

To estimate the effect of the lack of coverage in the lower mantle on the resolution of this problem, we tried inverting data containing contributions from the lower mantle only (no upper mantle, no errors). The correlations of the results of that inversion are shown in Figure 5.16 (case C1, harmonic degrees 1-6). The correlation is nearly perfect down to a few hundred km

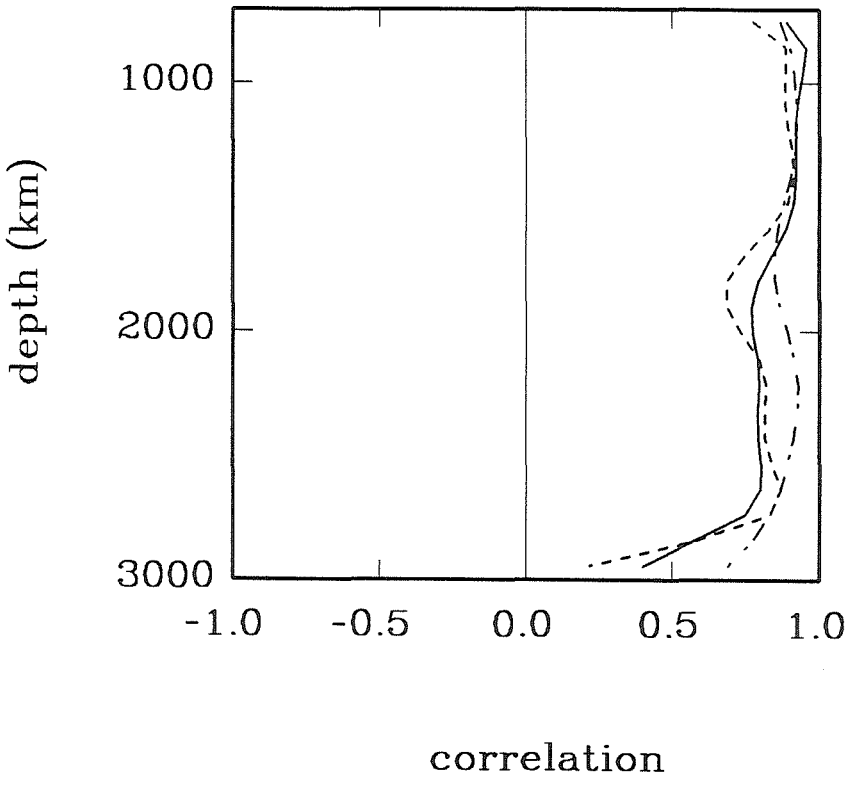

Figure 5.16. The correlation of the LM model with models computed by the BP and THE methods from data generated from the LM model only. (No upper mantle structure, no errors, no relocations, no statics.) The solid line is the correlation of models BP and THE, the dashed line the correlation between models BP and LM, and the doubly dashed line the correlation between models THE and LM.

above the CBM. This demonstrates that the data spatially resolve the lower-mantle structure at the present parameterization.

Figures 5.17 and 5.18 show the rms amplitude (left column) and correlation with LM of models obtained by the BP method from various combinations of the individual contributions to the data for cases C1 and C2, respectively. The top pairs of frames are the same as in Figures 5.13 and 5.15. The lower four pairs are from data excluding one or more contributions as indicated. REL refers to data excluding relocation errors. Here little is changed at the top of the model, but the correlation is significantly improved at depth in the C1 case. The correlation is somewhat improved in case C2. ERR refers to data excluding random errors and contributions from small-scale, upper-mantle structure. Again the effect is small at the top of the model, but is much improved at depth in case C1 and at central lower-mantle depths in case C2. The correlation a few hundred km above the CMB is reduced in case C2 but increased at the very base of the mantle. A common effect of excluding random errors is the reduction in the rms amplitude at the base of the mantle for both cases C1 and C2. This implies that the increase in power at the base of the mantle may be at least in part due to a combination of poor coverage there and large errors in the data. UML refers to data excluding contributions from the UML model. In case C1 the correlation is improved at the top of the lower mantle, but reduced at central depths. There is remarkably little effect in case C2. LM refers to data excluding contributions from the lower mantle. The correlation is low, but significantly negative at the top and positive at central depths in case C1. In case C2 this is reversed. This indicates that in these particular synthetic cases the geometrical distribution of data and upper-mantle structure are

Figures 5.17 - 5.18. Rms slowness variations and correlation with the LM model for the results of BP inversions of various data sets. "All" refers to data including all contributions; "rel" refers to data excluding event relocations; "err" refers to data with random errors excluded; "uml" refers to data with contributions from the UML model excluded; "lm" refers to data with contributions from the LM model excluded. Scales are the same as in Figures 5.13 through 5.16.

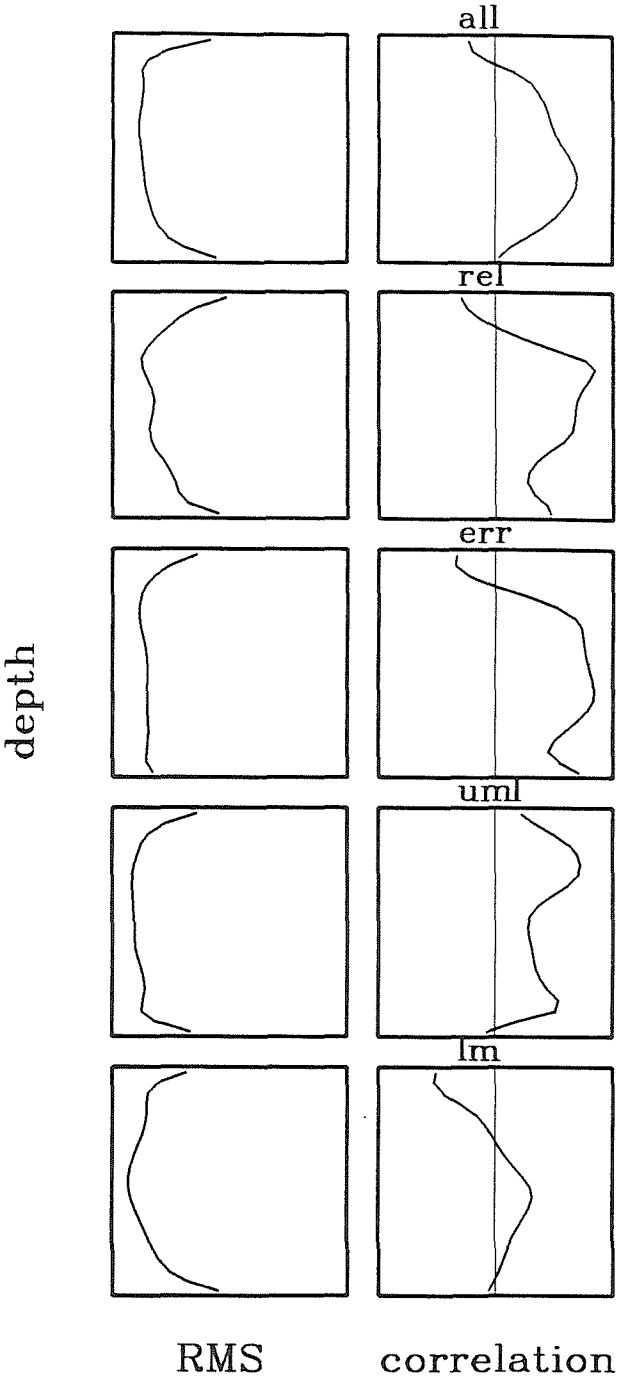

Figure 5.17. Case C1. Degrees 1 through 6.

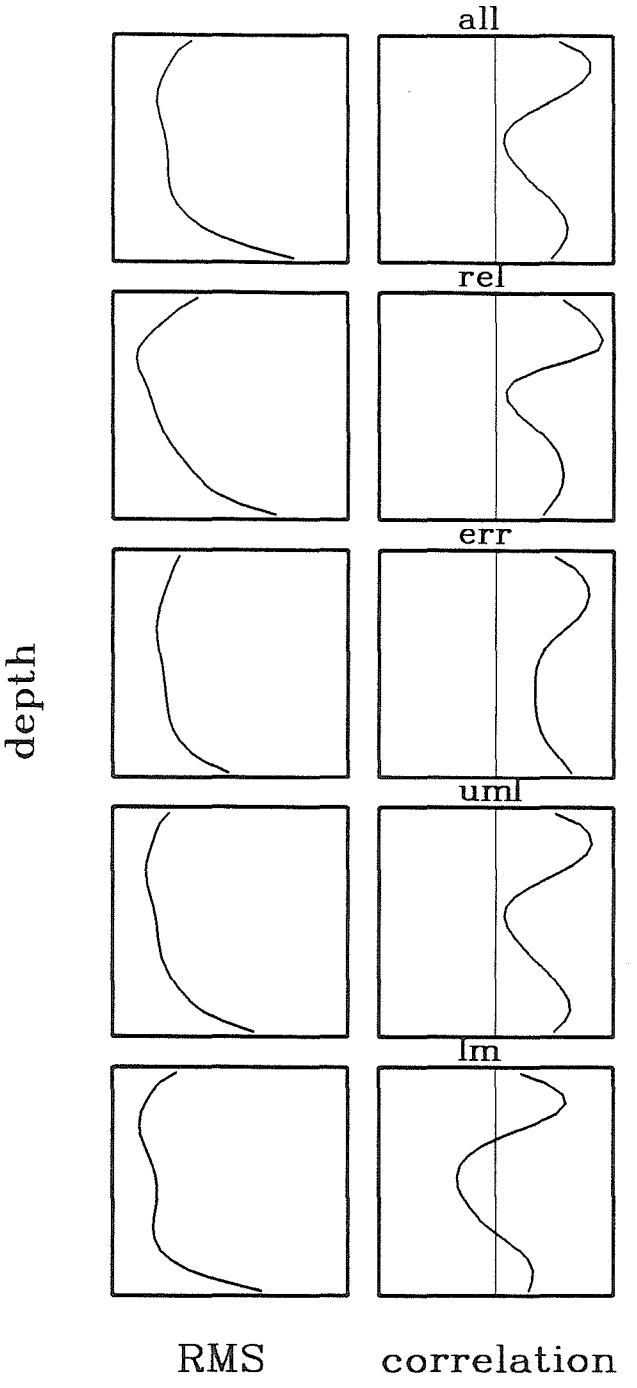

Figure 5.18. Case C2. Degrees 1 through 6.

such that pervasive effects manifest themselves throughout the mantle. In case C1 the positive correlation in the LM case at central depths is consistent with the reduced correlation in the UML case from ALL. The depth profile of correlation in the C2-LM case is quite similar to that of C2-ALL, except for a constant shift. This constant shift of about 0.3 may be a better measure of the correlation between the BP model and the LM model, which is actually due to the signal from the LM model. Note how little effect the exclusion of the various components of the data has on the rms amplitude depth profiles. The only notable difference appears to be the effect of random errors on rms amplitude at the base of the mantle. The overall differences between cases C1 and C2 are only slight. The variation of rms amplitude is similar for the two cases, despite a factor of 5 difference in overall redundancy. The behavior of correlation with depth is quite different in the two cases, while the overall level of correlation is similar. This points at the sensitivity of the artifacts of these inversions to the specifics of the distribution of data and its relation to the structure, and indicates the need for a full-fledged 3D synthetic test of global, travel-time tomography.

Figures 5.19 and 5.20 show the results of inverting for CMB structure using the various core data-sets. The data were generated using the same upper- and lower-mantle structures as the P-wave data, the same relocation errors, but estimates of random error obtained by a stochastic approach similar to that applied in Chapter 4, yielding error variance of about 1 sec^2 for all of the core data-sets. The core data contain no contribution from the CMB or below it. Each frame represents the result for one particular phase. The bottom frame shows the result from a simultaneous inversion of all the phases, with all summary rays given equal weights. The inversion technique

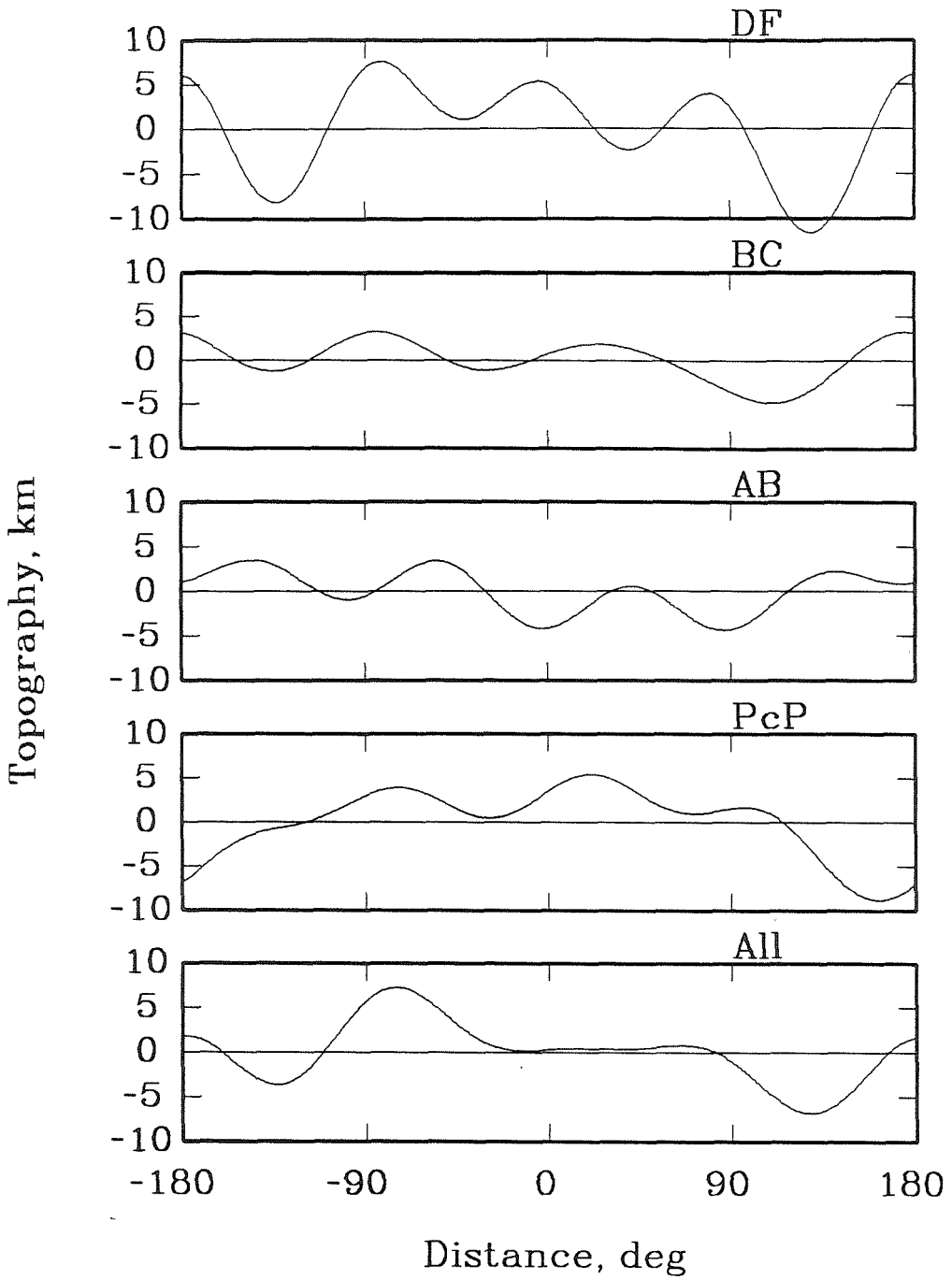

Figure 5.19. Topography of the CMB (degrees 1 - 4) from inversions of compressional, core-wave data sets as indicated. Case C1.

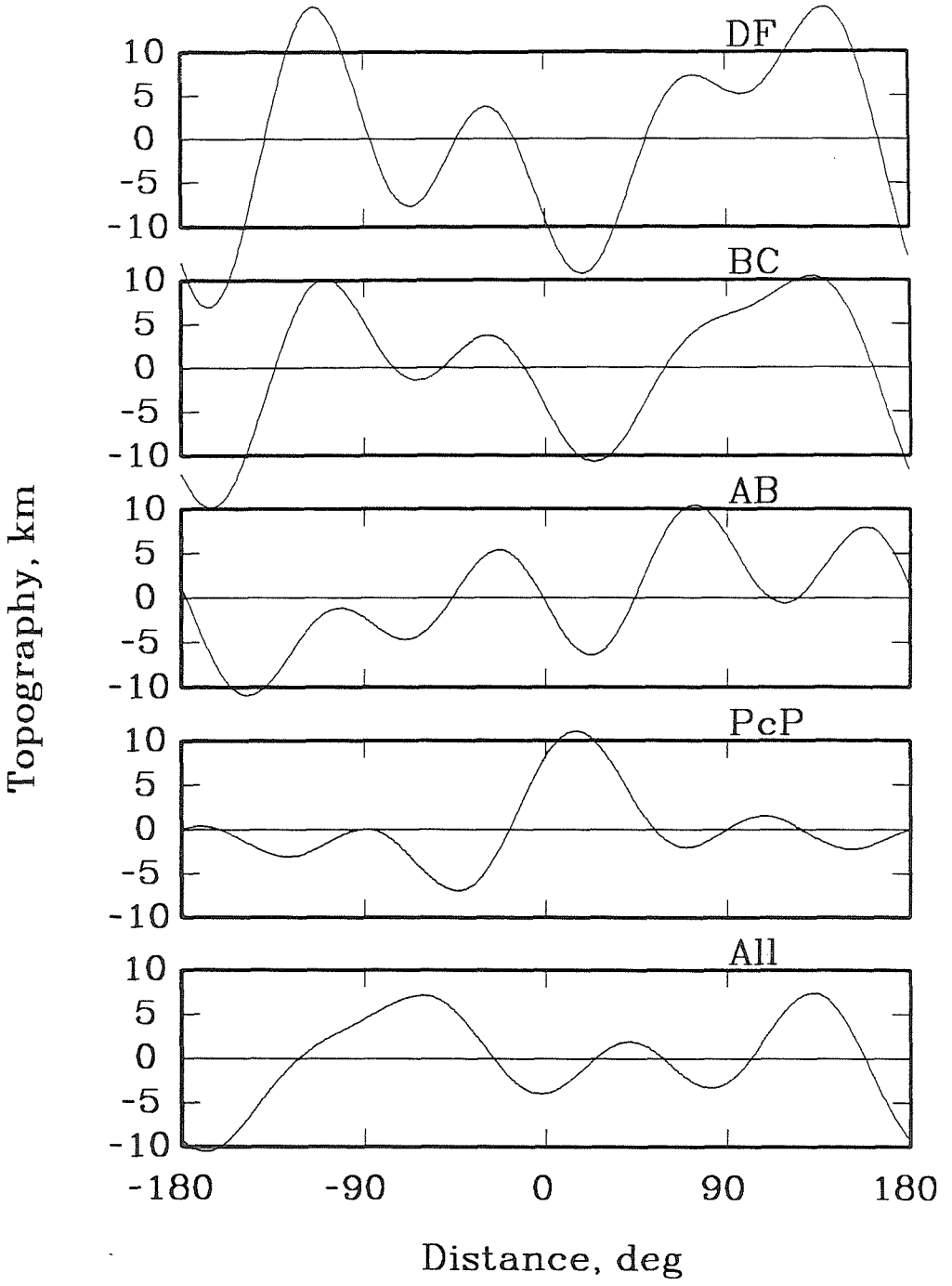

Figure 5.20. Topography of the CMB (degrees 1 - 4) from inversions of compressional, core-wave data sets as indicated. Case C2.

used was damped least squares. The model parameterization in the inversion included harmonic degrees up to and including degree 8, and the inversion solves for the harmonic coefficients (Fourier coefficients) much like Morelli and Dziewonski (1987) did. The figures include only degrees 1 through 4. The overall peak-to-peak amplitude of these patterns is fairly consistently of the order of 10 to 20 kilometers for all the phases, highest for PKPdf (PKIKP), despite the fact that this is the biggest data set. Also note that in general the topography is higher in case C2 than in C1, in spite of the higher degree of redundancy in case C2. This implies that the uncertainty of models of the CMB obtained from ISC travel-time data is at this level of parameterization of the order 5 to 10 km, and that this uncertainty is less related to random errors in the data than to spatially coherent errors, such as relocation errors and upper-mantle structure, that statics do not account for.

5.4 Discussion and conclusions

The overall conclusion of this study is a negative one. Our results indicate that the usefulness of the ISC data for mapping the aspherical structure of the earth's deep interior is limited. It should be pointed out, however, that this kind of synthetic study is only as good as the information that goes into it. We have used a specific model of lateral velocity variations for the upper mantle, which we claim has a large detrimental effect on lower-mantle inversion. How realistic is this model? We have used a specific model for the lower mantle. How realistic is it? Are our estimates of error reasonable? Is our modeling of event-location errors appropriate? We have simplified a 3D problem to a 2D problem. How would our conclusions be changed if we were

able to set up a 3D synthetic study? Are there any effects in the ISC data that we have left out? We think that our choices of inputs into this synthetic study stand to reason, but that a number of the parameters chosen should have the effect of underestimating problems of lower-mantle, travel-time inversion.

A number of reports of surface-wave tomographic studies have been published (e.g., Nakanishi and Anderson 1984, Woodhouse and Dziewonski 1984, Nataf et al. 1986, and Tanimoto 1987 and 1988). These studies agree satisfactorily, although not impressively. Furthermore, they agree with regional, body-wave-synthesis studies (e.g., Helmberger et al. 1985) and regional, tomographic studies using S-waves (Grand 1988). The level of large-scale, shear-wave heterogeneity in the upper mantle is consistently estimated at about 5% and the pattern consistently correlates with surface tectonics. As to the scaling of the shear-wave model of Tanimoto (1988) to construct a realistic P-wave model, this is done on the basis of P/S-wave station correction ratios (e.g., Hales and Doyle 1967 and Souriau and Woodhouse 1985). We take the value of 4, which is at the upper end of the range of values obtained by researchers. Using a smaller ratio would increase the strength of the upper-mantle structure and make the problems introduced by it more severe. We extended the spectra of the model beyond degree 8 based on the results of Chapter 4, but in a decaying manner and only out to about degree 15. We inserted slab structures into the model, but conservatively chose a maximum amplitude of the slab anomaly at 5%. We dispersed the Benioff-Wadati seismicity throughout the several hundred km thick slab anomaly, whereas it could be more focused within the slab and thus cause larger event mislocations.

The model we used for the lower mantle was based on previous deterministic and stochastic studies of the lower mantle using the ISC data (CC, DZ, and Chapter 4 of this thesis). As we have demonstrated in this study, these studies suffer from upper-mantle contamination and random errors. Both problems could insert undue power into the models. We thus expect the amplitude of the lower-mantle model to be too high rather than too low. Reducing its amplitude would effectively reduce the relative signal contribution from the lower mantle and thus serve to make the problems more severe.

The main source of errors in the data was assumed to be random in this study. There is reason to expect the ISC data to contain some level of spatially systematic errors that are due to phase mispicks, etc. Systematic errors do not cancel upon stacking as random errors do and thus more effectively obscure images obtained from the data. (We attempt to model the spatially coherent errors that are due to relocation errors in this study.)

The static event- and station-correction results in our 2D synthetic tests (see Figure 5.8) correlate well with the main structural features in the upper-mantle model, UML. This is in general agreement with studies of station corrections from ISC data (e.g., Dziewonski and Anderson 1983). Our results for the lateral relocations of events (see Figure 5.7) yield maximum relocations in slab regions of the order of 20 km. This is consistent with slab event-relocation studies (e.g., Fujita et al. 1981) and indicates that our modeling of location errors in the ISC data is reasonable.

We cannot make inferences about the possible differences between these 2D synthetic test cases and a 3D synthetic study based on the actual data geometry in the ISC catalog. The extension of the spectra of model DSXRG did assume random phase to construct model UML. It is likely that at least

some of the power in the upper-mantle structure at degrees 10 - 15 is due to components that serve to sharpen the transitions between the larger-scale anomalies and thus are correlated in phase. It is not clear what effect this might have on our results, although they are probably minor.

We argue above that the effects of upper-mantle structure and data errors on lower-mantle, travel-time inversion may be underestimated. The checks that we have to compare with the 3D models of CC and DZ, namely, their correlation and amplitude as compared to the correlation and amplitude of our models BP and THE, are similar, however. The significance of the overall level of correlation is about the same in our 2D synthetic cases as in the 3D case. Furthermore, the amplitude depth profiles are similar, and the factor-of-two amplitude discrepancy between the two models is reproduced. Correlation of our inversion results with the input model, LM, is consistently positive in at least parts of the lower mantle. Inspection of Figures 5.10 and 5.11 shows that some of the input structures are successfully modeled. This indicates that lower-mantle, travel-time inversions for aspherical structure are, in fact, partially successful.

Hager et al. (1985) presented comparisons between the large-scale geoid pattern and that predicted from the results of CC and DZ through a dynamic, mantle-flow model for a few, simple, mantle-rheology models. The comparison is impressive for harmonic degrees 2 and 3 and those rheology models that render the geoid largely insensitive to upper-mantle structure and structure at the base of the mantle. The sensitivity kernels are in these cases negative throughout the lower mantle. Thus this comparison involves a large degree of smoothing in depth. It is because of this smoothing that the geoid patterns, that are predicted from models CC and DZ, correlate much

better than the analogous patterns in the models themselves. The same is likely to hold for the correlation of the predicted geoids with the observed (or residual) geoid versus the correlation of the structural models with the true structure of the lower mantle. In the results of our synthetic tests, the inversion results from both methods (BP and THE) correlate positively with the input model (LM) in the depth range where the geoid kernels are large. Thus a similar calculation to that of Hager et al. (1985) would yield similar results.

We attempt to discern the cause of the partial failure of the inversion results of the BP method to correlate with the input LM model in Figures 5.17 and 5.18. The interpretation of the figures is not clear. The effect of random errors appears to be significant and greater at depth in the models, where the level of redundancy in the ray coverage is generally less than at the top of the lower mantle. The same is true for the effect of relocations in case C1. In case C1 contamination from upper-mantle structure appears to be greatest at the top of the lower mantle. The insensitivity of the amplitude-versus-depth profiles to omitting components of the data (see Figures 5.17 and 5.18), including contributions from lower-mantle structure, casts a doubt on recent lower-mantle results, including some of the results of Chapter 4 of this thesis.

The amplitude ratio of the DZ and CC models is reproduced in THE and BP models. In case C1 the ratio is about the same at degrees 1,2, and 3, but higher when degrees 4,5, and 6 are included. In case C2 the ratio of THE to BP is close to unity for degrees 1,2, and 3, but about 2 (same as DZ to CC) when degrees 4,5, and 6 are included. In both cases the relative ratio increases at the higher degrees, which approach the truncation degree of THE and DZ. This may indicate that the excess power in the THE and DZ results

is due to aliasing. In other words, power belonging to harmonic degrees that are not included in the model parameterization may leak into the model parameters corresponding to scales that are comparable to the truncation scale.

Our estimate of uncertainty of travel-time-based maps of the CMB is of the order of 5 or 10 km. This is about the peak-to-peak amplitude of recent studies of the CMB from travel times (e.g., Chapter 2). If this estimate is correct, recent results for the CMB are completely obscured. This level of error is high enough to draw a cloud of doubt over even the prominent, large scale, degree-two, zonal harmonic pattern in PKIKP data and thus models of inner-core anisotropy.

In closing, we suggest on the basis of the present results, that while the ISC data have a reasonably high signal to noise ratio (including small-scale, structural signal in the signal) of the order of 2 for teleseismic P-waves (see Chapter 4), and a good enough spatial distribution to resolve earth structure at the parameterization of say Dziewonski (1984) (see Figure 5.16), greater care must be taken to account for shallow structure. We need good, detailed models for the strongly heterogeneous upper mantle and good locations for the events used.

6 SUMMARY

While the four basic chapters of this thesis are somewhat independent, they have one common goal. We have tried to map core-mantle boundary (CMB) structure using travel-time data provided by the International Seismological Centre (ISC), and have tried to understand how reliable our maps are. The quality of maps of the CMB is dependent on the characteristics of lower-mantle structure and how well it is mapped by recent studies. Lower-mantle maps are, in turn, dependent on the characteristics of crustal and upper-mantle structure and on how well the data are corrected for it. Of course data errors affect the success of our modeling of both the lower mantle and the CMB. We have thus been faced with the following questions:

1) What are the errors in the ISC data?

2) What are the characteristics of crustal and upper-mantle structure?

3) What are the characteristics of lower-mantle structure?

4) How well can we map the structure of the lower mantle using ISC travel times?

5) How well can we map the structure of the core-mantle boundary (CMB) using ISC travel-time data?

6) If we can map CMB structure with any degree of accuracy, then what is it?

7) Is the large, degree-two, zonal pattern in the travel times of antipodal PKIKP-waves necessarily best explained by inner-core anisotropy as has been suggested?

In Chapter 4 we try to answer questions 1, 2, and 3. In Chapter 5 we seek an answer to questions 4 and 5. Chapter 2 addresses questions 6 and 7 and

Chapter 3 addresses question 7.

The answer to question 1 (Q1) is summarized in Figure 4.4 in what we consider fairly robust estimates of random errors in the ISC data. The error variance is of the order of 0.2 to 1.0 sec^2 and varies with epicentral distance and the source depth of earthquakes in a sensible fashion.

Our answer to Q2 in Chapter 4 is somewhat obscured by artifacts in our data. A lot of other studies have addressed this same question and come up with answers much like ours (surface-wave tomography, crustal scattering). This region of the earth appears to contain very strong heterogeneity over a wide range of scales. The heterogeneity is strongly concentrated at shallow depths.

Our answer to Q3 in Chapter 4 also agrees to some degree with previous studies (lower-mantle tomography and scattering studies). This region of the earth appears to have much lower levels of heterogeneity than the overlying upper mantle and crust, particularly at intermediate depths.

These answers to questions 1,2, and 3 are necessary prerequisites for addressing Q4 and Q5. In Chapter 5 we use the results of Chapter 4 and other studies to design synthetic tests to address Q4 and Q5. Our conclusions are that travel-time data may be used to map lower-mantle structure with some success, but that the uncertainty of CMB models obtained from ISC travel times is of the order of 5 or 10 km.

Our results in Chapter 2 for the structure of the CMB are in general of amplitude comparable to or less than the above error estimate. This would imply that we cannot hope to model this structure with these data (Q6). The inconsistencies of the results in Chapter 2 for different subsets of the ISC data support that conclusion. Furthermore, the positive correlation of

residuals in regions of dense coverage among the various data sets implies possible contamination from above. Assuming that this is due to upper mantle structure is consistent with our results in Chapters 4 and 5. Lower mantle structure might contaminate CMB structure, but probably much less so than upper mantle structure, because of the large difference in the level of heterogeneity.

Our answer to Q7 (Chapters 2 and 3) is that the C_2^g component of antipodal PKIKP data (PKPef) is also present in PKPde and PKPbc data, albeit weaker. Thus, at least a part (1/2) of this feature in the data must be explained by heterogeneity or anisotropy above the inner core. Our preferred explanation is heterogeneity close to the CMB. The large errors in CMB maps according to the results of Chapter 5 (degrees 1 through 4) may allow us to write off this feature as erroneous or from shallow sources. This would, however, contradict some free-oscillation data.

Despite the problems for lower-mantle modeling and failure of CMB modeling, the ISC data remain one source of valuable information about the aspherical structure of the earth's interior. It is possible, even likely, that the ISC data will become more useful to map earth structure with improved upper-mantle models (great advances are being made in surface-wave tomography and long-period, body-wave synthesis with digital data sets) and more selective procedures in the data processing. We suggest that corrections for strong, structural features near the earth's surface, such as subducting slabs, including relocations, by means of inserting idealized bodies into the reference model, may improve the performance of lower-mantle modeling with travel-time data. The use of local event-locations, using intra-plate events only, or using only impulsive picks (this is often indicated in the ISC data) may also

enhance performance. Constraining the inversion of travel-time data for lower-mantle structure by means akin to the method applied in Chapter 2, on the basis of auxiliary information (such as the results of Chapter 4) may be helpful.

We are somewhat uncertain about our results in Chapter 5, because of our 2D approximation to a 3D problem. It would be useful to do the analysis in Chapter 5 using the actual 3D data distribution of the ISC catalog. This would involve vast amounts of computer time, but is doable. Furthermore, that would enable synthetic testing of the method applied in Chapter 4. It would be useful to test a number of classes of lower-mantle models, including idealized models based on convection simulations.

7 REFERENCES

Aki, K., 1973. Scattering of P Waves under the Montana Lasa, *J. Geophys. Res.*, **78** ,1334-1346.

Aki, K., and B. Chouet, 1975. Origin of coda waves: Source, attenuation and scattering effects, *J. Geophys. Res.*, **80** , 3322-3342.

Aki, K., and P.G. Richards, 1980. *Quantitative seismology, theory and methods,* W.H. Freeman and Company, San Francisco, California, USA.

Alexander, S.S, and R.A. Phinney, 1966. A study of the core-mantle boundary using P-waves diffracted by the Earth's core, *J. Geophys. Res.*, **71** , 5943-5958.

Anderssen, R.S., and J.R. Cleary, 1980. Estimation of PKP times from ISC data, *Phys. Earth Planet. Inter.*, **23** , 207-214.

Berteussen, K.A., A. Christoffersson, E.S. Husebye, and A. Dahle, 1975a. Wave-scattering theory in analysis of P-wave anomalies at NORSAR and LASA, *Geophys. J. R. astr. Soc.*, **42** , 403-417.

Berteussen, K.A., E.S. Husebye, R.F. Mereu, and A. Rau, 1975b. Quantitative assessment of the crust-upper mantle heterogeneities beneath the Gauribidanur seismic array in southern India, *Earth Planet. Sci. Lett.*, **37** , 326-332.

Bolt, B.A., 1962. Gutenberg's early PKP observations, *Nature,* **196** , 122-124.

Bolt, B.A., 1964. The velocity of seismic waves near the earth's center, *Bull. Seismol. Soc. Am.*, **54** , 191-208.

Bolt, B.A., 1970. PdP and PKiKP waves and diffracted PcP waves, *Geophys. J. R. Astron. Soc.*, **20** , 367-382.

Bolt, B.A., 1972. The density distribution near the base of the mantle and near the earth's center, *Phys. Earth Planet. Inter.*, **5** , 301-311.

Bolt, B.A., M. Niazi, and M.R. Somerville, 1970. Diffracted ScS and the shear velocity at the core boundary, *Geophys. J. R. Astron. Soc.*, **19** , 299-305.

Brown, J.M., 1986. Interpretation of the D'' zone at the base of the mantle: Dependence on assumed values of thermal conductivity, *Geophys. Res. Lett.*, **13** , 1509-1512.

Bullen, K.E., 1979. *An introduction to the Theory of Seismology* (3rd ed.), Cambridge University Press, Cambridge, U.K.

Bullen, K.E., 1949. Compressibility-pressure hypothesis and the earth's interior, *Mon. Not. R. Astron. Soc.*, **5** , 355-368.

Capon, J., 1974. Characterization of crust- and upper-mantle structure under Lasa as a random medium, *Bull. Seis. Soc. Am.*, **64** , 235-266.

Capon, J. and K.A. Berteussen, 1974. A random-medium analysis of crust- and upper-mantle structure under NORSAR, *Geophys. Res. Lett.*, **1** , 327-328.

Chang, A.C., and J.R. Cleary, 1978. Scattered PKKP: Further evidence for scattering at a rough core-mantle boundary, *Phys. Earth Planet. Inter.*, **24** , 15-29.

Chernov, L.A., 1960. *Wave propagation in a random medium,* McGraw-Hill, New York, New York, USA.

Clayton, R.W. and R.P. Comer, 1983. A tomographic analysis of mantle heterogeneities from body-wave travel-times, *EOS, Trans. Am. Geophys. Union,* **64** , 776.

Cleary, J.R., 1969. The S velocity at the core-mantle boundary, from observations of diffracted S, *Bull. Seismol. Soc. Am.*, **59** , 1399-1405.

Cleary, J.R., and R.A.W. Haddon, 1972. Seismic-wave scattering near the core-mantle boundary: A new interpretation of precursors to PKP, *Nature,* **240** , 549-551.

Cormier, V.F., 1985. Some problems with S, SKS and ScS observations and implications for the structure of the base of the mantle and outer core, *J. Geophys.*, **57** , 14-22.

Creager, K.C. and T.H. Jordan, 1984. Slab penetration into the lower mantle, *J. Geophys. Res.*, **89** , 3031-3049.

Creager, K.C., and T.H. Jordan, 1986a. Large-scale structure of the outermost core from P_{DF} and P_{AB} travel times, *EOS Trans. Am. Geophys. Union,* **67** , 311.

Creager, K.C. and T.H. Jordan, 1986b. Aspherical structure of the core-mantle boundary from PKP travel times, *Geophys. Res. Lett.*, **13** , 1497-1500.

Creager, K.C. and T.H. Jordan, 1987. Differential travel-time constraints on core-mantle boundary structure, *EOS, Trans. Am. Geophys. Union,* **68** , 1487.

Creager, K.C. and T.H. Jordan, 1988. PKP tomography of the core-mantle boundary: Scale lengths of heterogeneities, *EOS, Trans. Am. Geophys. Union,* **69** , 1306.

Davies, G.F, and M. Gurnis, 1986. Interaction of mantle dregs with convection: Lateral heterogeneity at the core-mantle boundary, *Geophys. Res. Lett.*, **13** , 1517-1520.

Davies, J.H. and R.W. Clayton, 1987. Error analysis of a shear-wave, mantle tomographic inversion, *EOS, Trans. Am. Geophys. Union,* **68** , 1376.

Davies, J.H., O. Gudmundsson, and R.W. Clayton, 1988. Errors and small-scale structure inferred from areal statistics of ISC residuals, *Seism. Res. Lett.,* **59** , 40.

Doornbos, D.J., and N.J. Vlaar, 1973. Regions of seismic-wave scattering in the earth's mantle and precursors to PKP, *Nature,* **243** , 58-61.

Doornbos, D.J., 1974. Seismic-wave scattering near caustics, *Nature,* **247** , 352-353.

Doornbos, D.J., 1978. On seismic-wave scattering by a rough core-mantle boundary, *Geophys. J. R. Astron. Soc.,* **53** , 643-662.

Doornbos, D.J., and E.S. Husebye, 1972. Array analysis of PKP phases and their precursors, *Phys. Earth Planet. Int.,* **5** , 387-399.

Doornbos, D.J., and J.C. Mondt, 1979a. Attenuation of P and S waves diffracted around the core, *Geophys. J. R. Astron. Soc.,* **57** , 353-379.

Doornbos, D.J., and J.C. Mondt, 1979b. P and S waves diffracted around the core and the velocity structure at the base of the mantle, *Geophys. J. R. Astron. Soc.,* **57** , 381-395.

Doornbos, D.J., 1980. The effect of a rough core-mantle boundary on PKKP, *Phys. Earth Planet. Inter.,* **21** , 351-358.

Doornbos, D.J., 1983. Present seismic evidence for a boundary layer at the base of the mantle, *J. Geophys. Res.,* **88** , 3498-3505.

Doornbos, D.J., S. Spiliopoulos, and F.D. Stacey, 1986. Seismological properties of D'' and the structure of a thermal boundary layer, *Phys. Earth Planet. Inter.,* **41** , 225-239.

Dziewonski, A.M., and Don L. Anderson, 1981. Preliminary reference Earth model (PREM), *Phys. Earth Planet. Inter.*, **25** , 297-356.

Dziewonski, A.M., and Don L. Anderson, 1983. Travel times and station corrections for P waves at teleseismic distances, *J. Geophys. Res.*, **88** , 3295-3314.

Dziewonski, A.M., and F. Gilbert, 1975. The effect of small, aspherical perturbations on travel times and a re-examination of the corrections for ellipticity, *Geophys. J. R. Astron. Soc.*, **44** , 7-16.

Dziewonski, A.M., 1984. Mapping the lower mantle: Determination of lateral heterogeneity in P velocity up to degree and order 6, *J. Geophys. Res.*, **89** , 5929-5952.

Dziewonski, A.M., and J.H. Woodhouse, 1987. Global images of the earth's interior, *Science,* **236** , 37-48.

Engdahl, E.R., N.H. Sleep, and M.T. Lin, 1977. Plate effects in north Pacific subduction zones, *Tectonophysics,* **37** ,95-116.

Flatte, S.M., 1983. Wave propagation through random media: contributions from ocean acoustics, *Proc. IEEE,* **71** , 1267-1294.

Flatte, S.M., and R.S. Wu, 1988. Small-scale structure in the lithosphere and asthenosphere deduced from arrival time and amplitude fluctuations at NORSAR, *J. Geophys. Res.*, **93** , 6601-6614.

Frankel, A., and R.W. Clayton, 1986. Finite difference simulations of seismic scattering: Implications for propagation of short-period seismic-waves in the crust and models of crustal heterogeneity, *J. Geophys. Res.*, **91** , 6465-6489.

Frasier, C.W., and D.K. Chowdhury, 1974. Effect of scattering on PcP/P amplitude ratios at LASA from 40–84^o distance, *J. Geophys. Res.*, **79** , 5469-5477.

Fujita, K., E.R. Engdahl, and N.H. Sleep, 1981. Subduction-zone calibration and teleseismic relocation of thrust-zone events in the central Aleutian Islands, *Bull. Seismol. Soc. Am.*, **71** , 1805-1828.

Gao, L.S., N.N. Biswas, L.C. Lee, and K. Aki, 1983a. Effects of multiple scattering on coda waves in three-dimensional medium, *Pure Appl. Geophys.*, **121** , 3-15.

Gao, L.S., L.C. Lee, N.N. Biswas, and K. Aki, 1983b. Comparison of the effects between single and multiple-scattering on coda waves for local earthquakes, *Bull. Seis. Soc. Am.*, **73** , 377-389.

Garnero, E., D. Helmberger, and G. Engen, 1988. Lateral variations near the core-mantle boundary, *Geophys. Res. Lett.*, **15** , 609-612.

Giardini, D., X.D. Li, and J.H. Woodhouse, 1987. Three-dimensional structure of the earth from splitting in free-oscillation spectra, *Nature*, **325** , 405-411.

Gradshteyn, I.S., and I.M. Ryzhik, 1980. *Table of integrals, series and products, Corrected and enlarged edition*, Academic Press, New York, New York, USA.

Grand, S.P., 1987. Tomographic inversion for shear velocity beneath the North American plate, *J. Geophys. Res.*, **92** , 14065-14090.

Gubbins, D., and M. Richards, 1986. Coupling of the core dynamo and mantle: Thermal or topographic? *Geophys. Res. Lett.*, **13** , 1521-1524.

Gudmundsson, O., R.W. Clayton, and Don L. Anderson, 1986. CMB topography inferred from ISC PcP travel times, *EOS, Trans. Am. Geophys. Union,* **67** , 1100.

Gudmundsson, O., R.W. Clayton, and Don L. Anderson, 1987. Is there anisotropy in the outer core?, *EOS, Trans. Am. Geophys. Union,* **68** , 1378.

Gudmundsson, O., J.H. Davies, and R.W. Clayton, 1988. Stochastic analysis of global, travel-time data, *EOS, Trans. Am. Geophys. Union,* **69** , 1308.

Gudmundsson, O., J.H. Davies, and R.W. Clayton, 1989. Stochastic analysis of global, travel-time data; Mantle heterogeneity and random errors in the ISC data, *submitted to Geophys. J.*

Gutenberg, B., 1914. Uber Erdbebenwellen, VII A., *Nachr. Ges. Wiss. Gottingen, Math. Phys. Klasse,* 1-52 and 125-176.

Gutenberg, B., and C.F. Richter, 1939. On seismic waves, *Beitr. Geophys.,* **54**

Haddon, R.A.W., and J.R. Cleary, 1974. Evidence for scattering of seismic PKP-waves near the mantle-core boundary, *Phys. Earth Planet. Int.,* **8** , 211-234.

Haddon, R.A.W., and G.G.R. Buchbinder, 1986. Wave-propagation effects and the Earth's structure in the lower mantle, *Geophys. Res. Lett.,* **13** , 1489-1492.

Haddon, R.A.W., and G.G.R. Buchbinder, 1987. S-wave scattering by 3-D heterogeneities at the base of the mantle, *Geophys. Res. Lett.,* **14** , 891-894.

Hager, B.H., R.W. Clayton, M.A. Richards, R.P. Comer, and A.M. Dziewonski, 1985. Lower-mantle heterogeneity, dynamic topography and the

geoid, *Nature,* **313** , 541-545.

Hager, B.H., and R.W. Clayton, 1989. Constraints on the structure of mantle convection using seismic observations, flow models, and the geoid, *in press*

Hales, A.L., and H.A. Doyle, 1967. P and S travel-time anomalies and their interpretation, *Geophys. J. R. Astron. Soc.,* **13** , 403-415.

Helmberger, D.V., G. Engen, and S. Grand, 1985. Upper-mantle cross-section from California to Greenland, *J. Geophys.,* **58** , 92-100.

Hide, R., R.W. Clayton, B.B. Hager, M.A. Spieth, and C.V. Voorhies, 1989. Topographic core-mantle coupling and fluctuations in the Earth's rotation, *in preparation.*

Humphreys, E., R.W. Clayton, and B.H. Hager, 1984. A tomographic image of mantle structure beneath southern California, *Geophys. Res. Lett.,* **11** , 625-627.

Husebye, E.S., D.W. King, and R.A.W. Haddon, 1976. Precursors to PKIKP and seismic-wave scattering near the mantle-core boundary, *J. Geophys. Res.,* **81** , 1870-1882.

Jarvis G.T., and W.R. Peltier, 1986. Lateral heterogeneity in the convecting mantle, *J. Geophys. Res.,* **91** , 435-451.

Jeanloz, R., X. Li, E. Knittle, and Q. Williams, 1988. Ultrahigh P-T experiments, the core-mantle boundary and geomagnetic variations: A new electromagnetism of the Earth, *EOS Trans. Am. Geophys. Union,* **69** , 1403.

Jeffreys, H., 1939. The times of P, S, and SKS and the velocities of P and S, *Mon. Not. R. Astron. Soc.,* **4** , 498-533.

King, D.W., R.A.W. Haddon, and J.R. Cleary, 1974. Array analysis of precursors to PKIKP in the distance range 128° to 142°, *Geophys. J. R. Astron. Soc.*, **37** , 157-173.

Lay, T., and D.V. Helmberger, 1983a. The shear-wave velocity-gradient at the base of the mantle, *J. Geophys. Res.*, **88** , 8160-8170.

Lay, T., and D.V. Helmberger, 1983b. A shear-velocity discontinuity in the lower mantle, *Geophys. Res. Lett.*, **10** , 63-66.

Lay, T., and D.V. Helmberger, 1983c. A lower-mantle, S-wave triplication and the shear-velocity structure of D'', *Geophys. J. R. Astron. Soc.*, **75** , 799-838.

Lay. T, 1986. Evidence for a lower-mantle, shear-velocity discontinuity in S and sS phases, *Geophys. Res. Lett.*, **13** , 1493-1496.

Lee, R.C., and L.R. Johnson, 1984. Extremal bounds on the seismic velocities in the earth's mantle, *Geophys. J. R. Astr. Soc.*, **77** , 667-681.

Loper, D.E., 1984. The dynamical structures of D'' and deep plumes in a non-Newtonian mantle, *Phys. Earth Planet. Inter.*, **34** , 57-67.

Masters, G., and F. Gilbert, 1981. Structure of the inner core inferred from observations of its spheroidal shear modes, *Geophys. Res. Lett.*, **8** , 569-571.

Menke, W., 1986a. Effect of heterogeneities in D'' on the decay rate of P_{diff}, *J. Geophys. Res.*, **91** , 1927-1933.

Menke, W., 1986b. Few 2-50 km corrugations on the core-mantle boundary, *Geophys. Res. Lett.*, **13** , 1501-1504.

Mitronovas, W., and B.L. Isacks, 1971. Seismic-velocity anomalies in the upper mantle beneath the Tonga-Kermadec island arc, J. Geophys. Res.,

76 ,7154-7180.

Mondt, J.C., 1977. SH waves: Theory and observations for epicentral distances greater than 90 degrees, *Phys. Earth Planet. Inter.*, **15** , 46-59.

Morelli, A., A.M. Dziewonski, and J.H. Woodhouse, 1986. Anisotropy of the inner core inferred from PKIKP travel times, *Geophys. Res. Lett.*, **13** , 1545-1548.

Morelli, A., A.M. Dziewonski, 1987. Topography of the core-mantle boundary and lateral homogeneity of the liquid core, *Nature,* **325** , 678-683.

Mula, A.H., 1981. Amplitudes of diffracted long-period P and S waves and the velocities and Q structure at the base of the mantle, *J. Geophys. Res.*, **86** , 4999-5011.

Mula, A.H., and G. Muller, 1980. Ray parameters of diffracted long-period P and S waves and the velocities at the base of the mantle, *Pure Appl. Geophys.*, **118** , 1272-1292.

Muller, G., 1973. Amplitude studies of core phases, *J. Geophys. Res.*, **78** , 3469-3490.

Nakanishi, I., and D.L. Anderson, 1984. Measurements of mantle wave-velocities and inversion for lateral heterogeneity and anisotropy, 2. Analysis by the single-station method, *Geophys. J. R. Astron. Soc.*, **78** , 573-617.

Nataf, H.H., I. Nakanishi, and D.L. Anderson, 1986. Measurements of mantle wave-velocities and inversion for lateral heterogeneities and anisotropy 3. Inversion, *J. Geophys. Res.*, **91** , 7261-7307.

Nolet, G. (Ed.), 1987. *Seismic tomography,* Elsevier, Dordrecht, Netherlands.

Papoulis, A., 1965. *Probability, random variables and stochastic processes,* McGraw-Hill, New York, New York, USA.

Powell, C.A., and A.S. Meltzer, 1984. Scattering of P-waves beneath Scarlet in southern California, *Geophys. Res. Lett.,* **11** , 481-484.

Poupinet, G., R. Pillet, and A. Souriau, 1983. Possible heterogeneity of the earth's core deduced from PKIKP travel times, *Nature,* **305** , 204-206.

Richards, P.G, 1974. On the adequacy of plane-wave reflection/transmission coefficients in the analysis of seismic body waves, *Bull. Seism. Soc. Am.,* **66** , 701-717.

Ritzwoller, M., G. Masters, and F. Gilbert, 1986. Observations of anomalous splitting and their interpretation in terms of aspherical structure *J. Geophys. Res.,* **91** , 10203-10228.

Ritzwoller, M., G. Masters, and F. Gilbert, 1988. Constraining aspherical structure with low-degree interaction coefficients: Application to uncoupled multiplets, *J. Geophys. Res.,* **93** , 6369-6396.

Romanowicz, B.A., and M. Cara, 1980. Reconsideration of the relations between S and P station anomalies in North America, *Geophys. Res. Lett.,* **7** , 417-420.

Ruff, L.J., and D.V. Helmberger, 1982. The structure of the lowermost mantle determined by short-period P-wave amplitudes, *Geophys. J. R. Astron. Soc.,* **68** , 95-119.

Sacks, I.S., 1967. Diffracted P-wave studies of the earth's core, 2. Lower-mantle velocity, core size, lower-mantle structure, *J. Geophys. Res.,* **72** , 2589-2594.

Sacks, I.S., J.A. Snoke, and L. Beach, 1979. Lateral heterogeneity at the base of the mantle revealed by observations of amplitudes of PKP phases, *Geophys. J. R. Astron. Soc.*, **59** , 379-387.

Schlittenhardt, J., J. Schweitzer, and G. Muller, 1985. Evidence against a discontinuity at the top of D'', *Geophys. J. R. Astron. Soc.*, **81** , 295-306.

Schubert, G., D.A. Yuen, and D.L. Turcotte, 1975. Role of phase transitions in a dynamic mantle, *Geophys. J. R. Astron. Soc.*, **42** , 705-735.

Sengupta, M.K., and M.N. Toksoz, 1977. Three-dimensional model of seismic-velocity variation in the earth's mantle, *Geophys. Res. Lett.*, **3** , 84-86.

Sengupta, M.K., R.E. Hassell, and R.W. Ward, 1981. Three-dimensional seismic-velocity structure of the earth's mantle using body-wave travel-times from intra-plate and deep-focus earthquakes, *J. Geophys. Res.*, **86** , 3913-3934.

Shearer, P.M., K.M. Toy, and J.A. Orcutt, 1988. Axi-symmetric Earth models and inner-core anisotropy, *Nature*, **333** , 228-232.

Simon, R.B., 1981. *Earthquake interpretations: A manual for reading seismograms,* William Kaufmann Inc, Los Altos, California, USA.

Souriau, A., and J.H. Woodhouse, 1985. A worldwide comparison of predicted S-wave delays from a three-dimensional upper-mantle model with P-wave station corrections, *Phys. Earth Planet. Inter.*, **39** , 75-88.

Spakman, W., M.J.R. Wortel, and N.J. Vlaar, 1988. The Hellenic subduction zone: A tomographic image and its geodynamic implications, *Geophys. Res. Lett.*, **15** , 60-63.

Speith, M.A., R. Hide, R.W. Clayton, B.H. Hager, and C.V. Voorhies, 1986. Topographic coupling of core and mantle and changes in the length of day, *EOS Trans. Am. Geophys. Union,* **67** , 908.

Stacey, F.D., and D.E. Loper, 1983. The thermal boundary-layer interpretation of D'' and its role as a plume source, *Phys. Earth Planet. Inter.,* **33** , 45-55.

Stevenson, D.J., 1987. Limits on lateral density and velocity variations in the earth's outer core, *Geophys. J. R. Astron. Soc.,* **88** , 311-319.

Stevenson, D.J., 1988. Infiltration, dissolution and underplating: Rules for mixing core-mantle cocktails, *EOS Trans. Am. Geophys. Union,* **69** , 1404.

Suyehiro, K., and I.S. Sacks, 1979. P- and S-wave velocity anomalies associated with the subducting lithosphere determined from travel-time residuals in the Japan region, *Bull. Seismol. Soc. Am.,* **69** , 97-114.

Tanimoto, T., 1987. The three-dimensional, shear-wave structure in the mantle by overtone waveform-inversion. I, Radial-seismogram inversion, *Geophys. J. R. astr. Soc.,* **89** , 713-740.

Tanimoto, T., 1988. The 3D shear-wave structure in the mantle by overtone waveform-inversion. II, Inversion of X waves, R waves and G waves, *Geophys. J. R. astr. Soc.,* **93** , 321-333.

Tanimoto, T., 1989. Long-wavelength, S-wave velocity structure throughout the mantle, *submitted to Geophys. J.*

Tatarski, V.I., 1961. *Wave propagation in a turbulent medium,* McGraw-Hill, New York, New York, USA.

Weinstein S.A., Olson, P.L. & Yuen, D.A., 1989. Time-dependent, large-aspect-ratio thermal convection in the Earth's mantle, *preprint.*

Wielandt, E., 1987. On the validity of the ray approximation for interpreting delay times, in Nolet, G. (Ed.), *Seismic tomography,* Elsevier, Dordrecht, Netherlands.

Williams, Q., R. Jeanloz, J. Bass, B. Svendsen, and T.J. Ahrens, 1987. The melting curve of iron to 250 gigapascals: A constraint on the temperature at the Earth's center, *Science,* **236** , 181-182.

Woodhouse, J.H., and A.M. Dziewonski, 1984. Mapping the upper mantle: Three-dimensional modeling of Earth structure by inversion of seismic waveforms, *J. Geophys. Res.,* **89** , 5953-5986.

Woodhouse, J.H., D. Giardini, and X.D. Li, 1986. Evidence for inner-core anisotropy from free oscillations, *Geophys. Res. Lett.,* **13** , 1549-1552.

Wright, C., 1973a. Observations of multiple core reflections of the PnKP and SnKP type and regional variations at the base of the mantle, *Earth Planet. Sci. Lett.,* **19** , 453-460.

Wright, C., 1973b. Array studies of P phases and the structure of the D'' region of the mantle, *J. Geophys. Res.,* **78** , 4965-4982.

Wright, C., 1975. The origin of short-period precursors to PKP, *Bull. Seism. Soc. Am.,* **65** , 765-786.

Wright, C., and J.A. Lyons, 1975. Seismology, $dT/d\Delta$ and deep mantle convection, *Geophys. J. R. Astron. Soc,* **40** , 115-138.

Wright, C., and J.A. Lyons, 1981. Further evidence for radial anomalies in the lower mantle, *Pure Appl. Geophys.,* **119** , 137-162.

Wright, C, K.J. Muirhead, and A.E. Dixon, 1985. The P-wave velocity structure near the base of the mantle, *J. Geophys. Res.*, **90** , 623-634.

Wu, R.S., and K. Aki, 1985. Elastic wave scattering by a random medium and the small-scale inhomogeneities in the lithosphere, *J. Geophys. Res.*, **90** , 10261-10273.

Young, C.J., and T. Lay, 1987a. Evidence for a shear velocity discontinuity in the lower mantle beneath India and the Indian Ocean, *Phys. Earth Planet. Inter.*, **49** , 37-53.

Young, C.J, and T. Lay, 1987b. The core-mantle boundary, *Ann. Rev. Earth Planet. Sci.*, **15** , 25-46.

Young, C.J, and T. Lay, 1988. The core shadow-zone boundary and lateral variations of the P velocity structure of the lowermost mantle, *submitted to Phys. Earth Planet. Inter.*

Zhang, J., and T. Lay, 1984. Investigation of a lower-mantle, shear-wave triplication using a broadband array, *Geophys. Res. Lett.*, **11** , 620-623.

Zharkov, V.N., P.B. Karpov, and V.V. Leontjev, 1985. On the thermal regime of the boundary layer at the bottom of the mantle, *Phys. Earth Planet. Inter.*, **41** , 138-142.

Zhou, H.W., and R.W. Clayton, 1989. P- and S-Wave Travel-Time Inversion for Subducting Slab under the Island Arcs of the Northwest Pacific, *submitted to J. Geophys. Res.*

Appendix: Some manipulations of matrix-inverse theory

We present in this appendix some manipulations of matrix-inverse theory. Some are directly relevant to the methodology of this thesis. Others are related to some of the suggestions in Chapter 6. We have arrived at these manipulations (some are trivial) without direct reference to the work of others. Suffice it to point to Aki and Richards (1980), and references therein for background information.

Consider a linear inverse problem of the form:

$$\mathbf{t} = \mathbf{G}\mathbf{m} + \delta\mathbf{t}, \tag{A1}$$

where $\mathbf{t}$ are data, $\delta\mathbf{t}$ are data errors, $\mathbf{m}$ is the unknown model, and $\mathbf{G}$ is a matrix of kernels. A model estimate is constructed by a linear combination of the data.

$$\hat{\mathbf{m}} = \mathbf{A}\mathbf{t}, \tag{A2}$$

where $\mathbf{A}$ can be thought of as an inverse operator to $\mathbf{G}$. We can compute the data that the model estimate ($\hat{\mathbf{m}}$) predicts by

$$\hat{\mathbf{t}} = \mathbf{G}\hat{\mathbf{m}} = \mathbf{G}\mathbf{A}\mathbf{t}. \tag{A3}$$

Thus, the data misfit is:

$$d\mathbf{t} = \mathbf{t} - \hat{\mathbf{t}} = (\mathbf{I} - \mathbf{G}\mathbf{A})\mathbf{t}, \tag{A4}$$

where $\mathbf{I}$ is the identity matrix. Often, the inverse problem is solved by minimizing some norm of the data misfit, i.e., the elements of the matrix $\mathbf{A}$ are determined such that this norm is at its minimum. If one chooses to minimize the L_2 norm, $\mathbf{A}$ becomes the least-squares inverse. If one chooses to minimize a linear combination of the L_2 norms of the data misfit and the model estimate, the damped least-squares inverse results. One can in

principle employ any linear constraint, akin to the minimization of the model itself, to the solution of this linear inverse problem.

Consider a set of linear constraints on the model:

$$\hat{\mathbf{r}} = \mathbf{D}\hat{\mathbf{m}} = \mathbf{DAt}. \tag{A5}$$

We want to minimize the data misfit and $\hat{\mathbf{r}}$.

$$Q = d\,\mathbf{t}^T d\,\mathbf{t} + \alpha^2 \hat{\mathbf{r}}^T \hat{\mathbf{r}}, \tag{A6}$$

where α is a trade-off parameter that prescribes the relative importance placed on fitting the data and minimizing the constraints. One can write Q as:

$$Q = \mathbf{t}^T \left[\mathbf{I} - 2\mathbf{A}^T\mathbf{G}^T + \mathbf{A}^T \left[\mathbf{G}^T\mathbf{G} + \alpha^2\mathbf{D}^T\mathbf{D}\right]\mathbf{A}\right]\mathbf{t}.$$

Differentiating Q with respect to the elements of $\mathbf{A}$ we get:

$$\frac{\delta Q}{\delta a_{kj}} = 2t_j \left[(\mathbf{G}^T\mathbf{G} + \alpha^2\mathbf{D}^T\mathbf{D})\mathbf{A} - \mathbf{G}^T\right]_k \mathbf{t}, \tag{A7}$$

where $[\mathbf{M}]_k$ represents the k-th row of the matrix $\mathbf{M}$. Setting Equation A7 equal to zero to minimize yields for all k and j:

$$\left(\left(\mathbf{G}^T\mathbf{G} + \alpha^2\mathbf{D}^T\mathbf{D}\right)\mathbf{A} - \mathbf{G}^T\right)\mathbf{t} = 0. \tag{A8}$$

In order to satisfy this for arbitrary $\mathbf{t}$, we get:

$$\mathbf{A} = \left[\mathbf{G}^T\mathbf{G} + \alpha^2\mathbf{D}^T\mathbf{D}\right]^{-1}\mathbf{G}^T. \tag{A9}$$

Compare this to the stochastic inverse

$$\mathbf{A}_{st} = \left[\mathbf{G}^T\mathbf{C}_d^{-1}\mathbf{G} + \mathbf{C}_m^{-1}\right]^{-1}\mathbf{G}^T\mathbf{C}_d^{-1}, \tag{A10}$$

where $\mathbf{C}_d$ and $\mathbf{C}_m$ are the data- and model-covariance matrices, respectively. Assuming that $\mathbf{C}_d = \alpha^2\mathbf{I}$, i.e., that the data errors are independent and all

drawn from the same distribution (same variance), we get:

$$\mathbf{A}_{st} = \left[\mathbf{G}^T\mathbf{G} + \alpha^2\mathbf{C}_m^{-1}\right]^{-1}\mathbf{G}^T. \qquad \text{(A11)}$$

This is exactly the same form as derived above, with $\mathbf{C}_m$ equated with $[\mathbf{D}^T\mathbf{D}]^{-1}$. Thus, applying linear constraints to the model is equivalent to assuming a specific form for the covariance of the model. One can always determine the model-covariance matrix that is analogous to specified linear constraints, but one cannot uniquely determine a set of constraints that are analogous to a specified model-covariance matrix. Note, that in general, one assumes a smooth model-covariance matrix. Any equivalent set of constraints will be rough, because of the inverse relationship of the two. For example, applying a Gaussian model-covariance matrix to a one-dimensional, periodic model is equivalent to minimizing a combination of the zeroth and second derivatives of the model, if one consideres only a symmetric set of constraints in the continuous model space limit (this equivalence is easily calculable from the singular-value decomposition of $\mathbf{C}_m$ and simply involves replacing the singular values by their inverse, square roots). This analogy between the model covariance of the stochastic inverse and linear constraints that are applied in a least-squares sence to the solution of an inverse problem is useful, because in practice the stochastic inverse is often applied, whereas it is in many ways simpler to think of it in terms of linear constraints.

If we set $\mathbf{D} = \mathbf{I}$, i.e., minimize the model itself, the analogous model-covariance matrix is $\mathbf{C}_m = \mathbf{I}$ and we have the damped least-squares inverse.

Equations A9, A10, and A11 are written in a form that involves the inverse of a model-by-model matrix. One can equivalently write them in terms of the inverse of a data-by-data matrix. For example, Equation A10 is

equivalent to

$$\mathbf{A}_{st} = \mathbf{C}_m \mathbf{G}^T \left[\mathbf{G}\mathbf{C}_m \mathbf{G}^T + \mathbf{C}_d \right]^{-1}. \tag{A12}$$

One need only cross multiply by the inverse brackets of equations A10 and A12 to show this. Equation A12 is the more common form of the stochastic inverse, but the less practical one. This is because, in general, one has fewer model parameters than data. Thus, Equation A10 involves the inverse of a smaller matrix. In addition, it allows one to avoid the computer storage of data-space arrays, by performing data-space matrix-multiplications on the fly as data and their kernels are read one by one.

Equations A9, A10, A11, and A12 may be further manipulated. For example, Equation A11 may be rearranged as:

$$\mathbf{A} = \left[\mathbf{C}_m \mathbf{G}^T \mathbf{G} + \alpha^2 \mathbf{I} \right]^{-1} \mathbf{C}_m \mathbf{G}^T, \tag{A13}$$

which is the form applied in Chapter 2 of this thesis. Also, Equation A9 may be rearranged as:

$$\mathbf{A} = \mathbf{D}^{-1} \left[\mathbf{H}^T \mathbf{H} + \alpha^2 \mathbf{I} \right]^{-1} \mathbf{H}^T, \tag{A14}$$

where $\mathbf{H} = \mathbf{G}\mathbf{D}^{-1}$, if $\mathbf{D}$ is invertible. In general, $\mathbf{D}$ will be a square, near-diagonal matrix with a well defined inverse.

Since the model-covariance matrix is always symmetric and positive definite, it may be decomposed as

$$\mathbf{C}_m = \mathbf{V}\Lambda\mathbf{V}^T, \tag{A15}$$

where the matrix $\mathbf{V}$ contains its eigenvectors, and Λ is a diagonal matrix of positive eigenvalues. One can thus define the square root of $\mathbf{C}_m$ as

$$\mathbf{S}_m = \mathbf{V}\lambda\mathbf{V}^T, \tag{A16}$$

where $\lambda_{ii} = \sqrt{\Lambda_{ii}}$. Hence, $\mathbf{C}_m = \mathbf{S}_m \mathbf{S}_m = \mathbf{S}_m^2$ and $\mathbf{S}_m$ is equivalent to $\mathbf{D}^{-1}$. Thus, Equation A14 may be written as

$$\mathbf{A} = \mathbf{S}_m \left[\mathbf{H}^T \mathbf{H} + \alpha^2 \mathbf{I}\right]^{-1} \mathbf{H}^T, \tag{A17}$$

where $\mathbf{H} = \mathbf{G}\mathbf{S}_m$. This manipulation is interesting in that less the premultiplication by $\mathbf{S}_m$ Equation A17 takes the exact form of the damped, least-squares inverse of the transformed inverse problem:

$$\mathbf{t} = \mathbf{H}\mathbf{m} = \mathbf{G}\mathbf{S}_m \mathbf{m}. \tag{A18}$$

The transformation involves the smearing of the kernels of $\mathbf{G}$ with the smooth operator $\mathbf{S}_m$. Equation A17 shows how it is not equivalent to smooth an unconstrained solution a posteriori on one hand, and constraining a solution in the sence of the stochastic inverse on the other.

Equation A17 may be of some practical value. Remember, that the iterative, back-projection, inversion scheme converges to the damped least-squares inverse (see Comer and Clayton, unpublished manuscript). Thus, provided that $\mathbf{S}_m$ is not too smooth, Equation A16 may be used to constrain a large, linear inverse problem. If $\mathbf{H}$, which is less sparse than the kernel matrix $\mathbf{G}$, is still manageably sparse, one can use back projection to solve the inverse problem with $\mathbf{H}$, and then convolve the solution with $\mathbf{S}_m$. This would be approximately equivalent to applying linear constraints, as derived above, to the solution.